THE ASTROPHYSICAL JOURNAL

AN INTERNATIONAL REVIEW OF SPECTROSCOPY AND ASTRONOMICAL PHYSICS

NOVEMBER 1950

THE EFFECT OF PRESSURE BROADENING OF SPECTRAL LINES ON RADIATIVE EQUILIBRIUM TEMPERATURE . . . . . John Avery 345

THE THEORY OF THE FLUCTUATIONS IN BRIGHTNESS OF THE MILKY WAY . . . . . & Chandrasekhar 355

THE THEORY OF THE FLUCTUATIONS IN BRIGHTNESS OF THE MILKY WAY. II . . . . . Chandrasekhar 370

ON THE DOPPLER BROADENING OF ABSORPTION LINES FORMED IN MULTIPLE INTERSTELLAR CLOUDS 395

ON TURBULENCE IN THE ATMOSPHERES OF THE SUN AND STARS 414

TURBULENCE AND THE CURVE OF GROWTH 426

THE ORBITAL MOTION OF GIANT BINARY STARS 437

DIFFUSE REFLECTION BY PLANETARY ATMOSPHERES 448

ON EMISSION BANDS IN THE INFRARED SPECTRUM OF THE NIGHT SKY 466

PHOTOELECTRIC MAGNITUDES AND COLORS OF STARS IN SELECTED AREAS 57, 61, AND 68 . . . . . Joel Stebbins, A. E. Whitford 469

PHOTOELECTRIC INVESTIGATIONS OF THE WOLF-RAYET BINARY HD 192641 474

THE LIGHT-CURVE OF UX MONOCEROTIS . . . . . W. A. Hiltner, O. Struve 486

THE SPECTRUM OF R AQUARII, 1936-1946 511

W. P. BOND'S WORK ON BETA CANIS MAJORIS 520

A STUDY OF THE SPECTROSCOPIC BINARY U CEPHEI 548

A CORRELATION BETWEEN THE SPECTROSCOPIC AND DYNAMICAL PROPERTIES OF THE LATE B- AND EARLY O-TYPE STARS 562

NOTES:

Notes on the Emission Spectrum of 17 Leporis 582

Tabular Velocities of the Inner Harvard Constellations 587

Notes on the Fluorescence-Protected Reactions in White Dwarf Stars 593

A Note on the Spectra of M 31 in the Ultraviolet 595

INDEX 597

THE UNIVERSITY OF CHICAGO PRESS

CHICAGO, ILLINOIS, U.S.A.

November 1950 Vol. 112, No. 3

THE ASTROPHYSICAL JOURNAL

AN INTERNATIONAL REVIEW OF SPECTROSCOPY AND ASTRONOMICAL PHYSICS

The Astrophysical Journal is published bimonthly by the University of Chicago at the University of Chicago Press, 5750 Ellis Avenue, Chicago 37, Illinois, during July, September, November, January, March, and May. Two volumes are published per year, one beginning with the January issue and the other beginning with the July issue. The subscription price is $6.00 per volume or $12.00 per year; the price of single copies is $3.00. (Orders for service of less than a volume will be charged at the single copy rate.) Postage is prepaid by the publishers on all orders from the United States and its possessions. No extra charge is made for postage to countries in the Pan American Postal Union. Postage is charged extra as follows: for Canada, 30 cents per volume, 40 cents per year (total $6.30 per volume, $12.40 per year); on single copies 5 cents (total $3.05); for all other countries in the Postal Union, 50 cents per volume, $1.00 per year (total $6.50 per volume, $13.00 per year), on single copies 10 cents (total $3.10). Subscriptions are payable in advance. Please make all remittances payable to The University of Chicago Press, in United States currency or its equivalent by postal or express money orders or bank drafts.

The following is an authorized agent:

For the British Empire, except North America and Australasia: The Cambridge University Press, Bentley House, 200 Euston Road, London, N.W. 1, England. Prices of yearly subscriptions and of single copies may be had on application.

Claims for missing numbers should be made within the month following the regular month of publication. The publishers expect to supply missing numbers free only when losses have been sustained in transit, and when the reserve stock will permit.

Business correspondence should be addressed to The University of Chicago Press, Chicago 37, Illinois.

Communications for the editors and manuscripts should be addressed to: W. W. Morgan, Editor of The Astrophysical Journal, Yerkes Observatory, Williams Bay, Wisconsin.

Line drawings and photographs should be made by the author, and all marginal notes such as co-ordinates, wave lengths, etc., should be included in the cuts. It will not be possible to set up such material in type.

One copy of the corrected galley proof should be returned as soon as possible to the editor, Yerkes Observatory, Williams Bay, Wisconsin. Authors should take notice that the manuscript will not be sent to them with the proof.

The cable address is "Observatory, Williamsbay, Wisconsin."

The articles in this journal are indexed in the *International Index to Periodicals*, New York, N.Y.

Applications for permission to quote from this journal should be addressed to The University of Chicago Press, and will be freely granted.

Microfilms of complete journal volumes are available to regular subscribers only and may be obtained at the end of the year. Orders and inquiries should be addressed to University Microfilms, 313 North First Street, Ann Arbor, Michigan.

Notice to subscribers: If you change your address, please notify us and your local postmaster immediately. The Post-Office does not forward second-class mail.

Entered as second-class matter, July 21, 1905, at the Post-Office at Chicago, Ill., under the Act of March 3, 1879. Acceptance for mailing at special rate of postage provided for in United States Postal Act of October 3, 1917, Section 1103, authorized February 26, 1925.

THE ASTROPHYSICAL JOURNAL

An International Review of Spectroscopy and Astronomical Physics

FOUNDED IN 1895 BY GEORGE E. HALE AND JAMES E. KEELER

VOLUME 112

JULY–NOVEMBER, 1950

THE UNIVERSITY OF CHICAGO PRESS
CHICAGO, ILLINOIS

CAMBRIDGE UNIVERSITY PRESS, LONDON

PUBLISHED JULY, SEPTEMBER, NOVEMBER, 1950

COMPOSED AND PRINTED BY THE UNIVERSITY OF CHICAGO PRESS
CHICAGO, ILLINOIS, U.S.A.

CONTENTS

NUMBER 1

THE AMOUNT OF POLARIZATION BY INTERSTELLAR GRAINS. H. C. van de Hulst . . . 1

PULSATION PROPERTIES OF GIANT-STAR MODELS. I. Epstein 6

RADIATIVE EQUILIBRIUM IN AN ATMOSPHERE IN WHICH PURE SCATTERING AND PURE ABSORPTION BOTH PLAY A ROLE. A. D. Code 22

RADIAL VELOCITIES, SPECTRAL TYPES, AND LUMINOSITY CLASSES OF 820 STARS. J. H. Moore and G. F. Paddock 48

ADDITIONAL STARS WHOSE SPECTRA HAVE A BRIGHT *Hα* LINE. Paul W. Merrill and Cora G. Burwell 72

STELLAR SPECTRA IN MILKY WAY REGIONS. II. A REGION IN CYGNUS. S. W. McCuskey and C. K. Seyfert 90

OH EMISSION BANDS IN THE SPECTRUM OF THE NIGHT SKY. II. A. B. Meinel 120

ON THE IDENTIFICATION OF THE 3670 A BAND OF THE C_2 MOLECULE. John G. Phillips . 131

FINE STRUCTURE OF N_2O BANDS IN THE INFRARED SOLAR SPECTRUM. Marcel V. Migeotte 136

PHOTOELECTRIC STUDIES. IV. COLOR-LUMINOSITY ARRAY FOR STARS IN THE REGION OF THE SUN. Olin J. Eggen 141

SPECTROGRAPHIC OBSERVATIONS OF W URSAE MAJORIS. Otto Struve and Henry G. Horak 178

SPECTROGRAPHIC OBSERVATIONS OF THE ECLIPSING BINARIES TW CASSIOPEIAE, TY PUPPIS, AND VV URSAE MAJORIS. Otto Struve 184

THE RADIAL VELOCITY OF GAMMA CASSIOPEIAE. Burke Smith and O. Struve 192

ON THE CHANGE OF PERIOD OF ECLIPSING VARIABLE STARS. Frank Bradshaw Wood . 196

NOTES

A NOTE ON ENERGY GENERATION. I. Epstein 207

ON THE TRANSITION PROBABILITIES OF C_2 SWAN BANDS. N. R. Tawde and J. M. Patel 210

APPARENT MAGNITUDES AND COLOR INDICES FOR SEVENTY-FOUR WHITE DWARFS AND DEGENERATE STARS. W. J. Luyten 212

THE SPECTRUM OF YY GEMINORUM (CASTOR C). O. Struve, G. Herbig, and H. Horak 216

THE SPECTRUM OF GP ORIONIS. William P. Bidelman 219

TWENTY-NINE NEW VARIABLE STARS IN THE GLOBULAR CLUSTER M 15. L. Rosino . 221

ZEEMAN SHIFTS FOR STELLAR DIPOLES AND QUADRUPOLES WITH INCLINED AXES. Martin Schwarzschild 222

REVIEWS 224

NUMBER 2

On the Determination of the Convergent Point of a Moving Cluster from Proper Motions. Archibald Brown 225

The Color-Magnitude Array for the Galactic Cluster NGC 2362. Harold L. Johnson 240

A Spectroscopic Comparison between High- and Low-Velocity F Dwarfs. Martin and Barbara Schwarzschild 248

A Spectrographic Study of HD 193576. Guido Münch 266

Observations of Solar Limb Darkening between 0.5 and 10.2 μ. A. K. Pierce, R. R. McMath, Leo Goldberg, and O. C. Mohler 289

Dynamics of Star Streaming. II. P. Stehle 299

Scattering by a Moving Electron Atmosphere and Its Effect on Spectral Lines. I. The Schuster Problem. Frank N. Edmonds, Jr. 307

Scattering by a Moving Electron Atmosphere and Its Effect on Spectral Lines. II. The Planetary Nebula Problem. Frank N. Edmonds, Jr. 324

The Thermodynamic Structure of the Outer Solar Atmosphere. II. Comment on Empirical Determinations of b_n and T_e. Richard N. Thomas 337

Superthermic Phenomena in Stellar Atmospheres. VI. Comment on Regions of Emission Fluctuation in the Solar Atmosphere. Richard N. Thomas 343

Theoretical Computations of Transition Probabilities for Electronic Spectra of C_2 and N_2^+. Harrison Shull 352

Notes

The Balmer Series and the Parallax of the Pleiades. G. R. Miczaika . . . 361

Revised Standards for Supergiants on the System of the Yerkes Spectral Atlas. W. W. Morgan and Nancy G. Roman 362

NUMBER 3

The Effect of Pressure Broadening of Spectral Lines on Atmospheric Temperature. John Strong and Gilbert N. Plass 365

The Theory of the Fluctuations in Brightness of the Milky Way. I. S. Chandrasekhar and G. Münch 380

The Theory of the Fluctuations in Brightness of the Milky Way. II. S. Chandrasekhar and G. Münch 393

On the Doppler Broadening of Absorption Lines by Turbulence and by Multiple Interstellar Clouds. Su-shu Huang 399

On Turbulence in the Atmospheres of the Sun and the Stars. Su-shu Huang . . 418

Turbulence and the Curve of Growth. Marshal H. Wrubel 424

The Apsidal Motion of Giant Binary Stars. Lloyd Motz 434

Diffuse Reflection by Planetary Atmospheres. Henry G. Horak 445

O_2 Emission Bands in the Infrared Spectrum of the Night Sky. A. B. Meinel . . 464

Photoelectric Magnitudes and Colors of Stars in Selected Areas 57, 61, and 68. Joel Stebbins, A. E. Whitford, and H. L. Johnson 469

Photometric Investigations of the Wolf-Rayet Binary CQ Cephei. W. A. Hiltner 477

The Light-Curve of UX Monocerotis. W. A. Hiltner, O. Struve, and P. D. Jose . 504

The Spectrum of R Aquarii, 1936–1949. Paul W. Merrill 514

W. F. Meyer's Work on Beta Canis Majoris. Otto Struve 520

A Study of the Spectroscopic Binary U Cephei. Robert H. Hardie 542

A Correlation between the Spectroscopic and Dynamical Characteristics of the Late F- and Early G-Type Stars. Nancy G. Roman 554

NOTES

Note on the Infrared Spectrum of 17 Leporis. Arne Slettebak 559

Radial Velocities of Six Stars Having Composite Spectra. William C. White, Jr. 559

Note on the Proton-Proton Reaction in White Dwarf Stars. T. D. Lee . . 561

A New Band System of N_2^+ in the Infrared Auroral Spectrum. A. B. Meinel . 562

Index 565

THE ASTROPHYSICAL JOURNAL

AN INTERNATIONAL REVIEW OF SPECTROSCOPY AND ASTRONOMICAL PHYSICS

VOLUME 112 NOVEMBER 1950 NUMBER 3

THE EFFECT OF PRESSURE BROADENING OF SPECTRAL LINES ON ATMOSPHERIC TEMPERATURE*

JOHN STRONG AND GILBERT N. PLASS
Johns Hopkins University
Received June 24, 1950

ABSTRACT

Pressure broadening causes lines in infrared absorption bands to have considerably greater half-widths in the lower layers of a planetary atmosphere than in the upper layers. As a result, radiation emitted upward from the wings of lines in the lower atmosphere is not strongly absorbed by the upper layers. Such radiation is thus free to escape to the cosmic cold. In this paper we calculate the net loss of heat by radiation from the various layers in the stratosphere, which is greater for the lower layers than for the upper layers. This affords a new basis for the explanation of the existence of the stratosphere.

The radiation budget for the stratosphere as a whole is reconsidered after these ideas and after new data on the transmission of the upper air first published herein. It is shown that the heat losses from the stratosphere by radiation from the 9.6 μ O_3, 15 μ CO_2, and 50 μ H_2O bands are approximately balanced by the heat gained from absorption of terrestrial radiation by these bands and by the absorption of solar radiation by O_3 in the ultraviolet.

INTRODUCTION

The effect of the pressure broadening of infrared lines on the transfer of radiation in our atmosphere has not been properly taken into account in previous calculations. The pressure broadening is not a minor correction to the older calculations but a major cause for the existence of the isothermal layer. It is to be anticipated that the thermal structure of planetary atmospheres is likewise controlled in large measure by the phenomena of pressure broadening of the lines in infrared absorption bands. This effect causes lower layers of the atmosphere to lose considerably more radiation to space than is the case when the line character of infrared absorption is ignored. Pressure broadening of these lines provides a stabilizing agency acting to suppress convection.

The three main problems of the stratosphere that have so far remained unexplained are, to quote D. Brunt, (1) ". . . the existence of the stratosphere, in which the temperature remains constant at all heights, or possibly slowly increases with height"; (2) ". . . in all latitudes there is a marked discontinuity of lapse rate at the tropopause . . ."; and (3) ". . . the temperature (near the base of the stratosphere) increases from the equator to the poles. . . ."

In Figure 1 we show the stratosphere divided into three physically and chemically homogeneous layers, in order to present our explanation of the first of these problems qualitatively. An average pressure and height have been ascribed to each of these layers.

* This work was supported in part by ONR.

The absorption lines shown are representative of a few lines in any of the bands of O_3, H_2O, or CO_2 which play a role in the radiative equilibrium of the stratosphere. Each line has a contour given by the Lorentz collision broadening formula,

$$k(\nu) = \frac{S}{\pi} \frac{a}{(\nu - \nu_0)^2 + a^2}, \tag{1}$$

where k is the absorption coefficient, S is the total intensity of the line, a is the half-width, and ν_0 is the center frequency of the line in wave numbers. According to the Lorentz theory, the half-width is inversely proportional to the time between molecular collisions which are capable of disrupting the phase of the absorbing oscillators. From

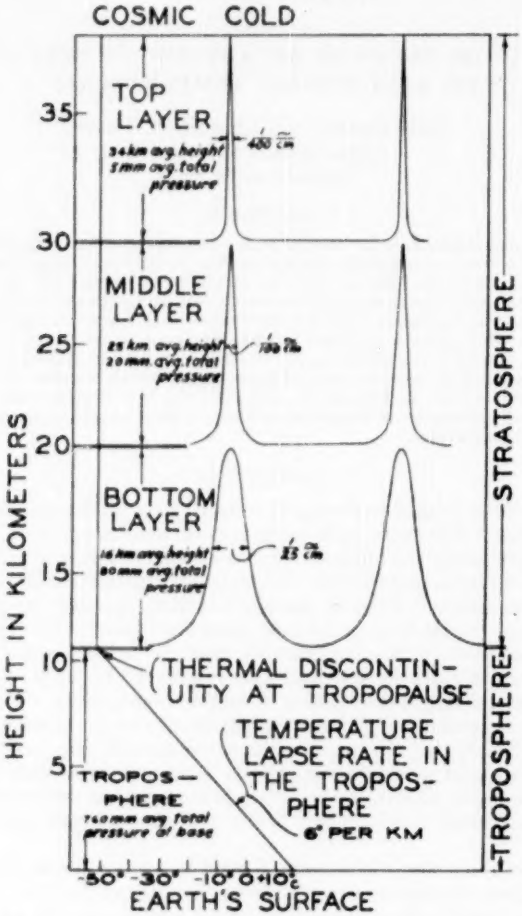

FIG. 1.—Line width, pressure, and temperature of the atmosphere. This figure illustrates the importance of line width for radiative cooling.

kinetic theory the half-width is proportional to the total pressure, since the temperature in the stratosphere is sensibly constant. In view of this the lines have half-widths which decrease with height proportional to the pressure, as has been indicated in Figure 1.

Qualitatively, it may be expected that the lowest layer represented in Figure 1 is cooled by radiation to the cosmic cold more strongly than are the upper layers because the pressure effect exposes the wings of the absorption lines in the lowest layers almost unobstructedly to the cosmic cold, while the radiations which are emitted near the line centers are strongly absorbed by higher layers. At the same time, the radiation loss from any layer is uncompensated by the warming radiations from lower layers, since such radiations from below are strongly absorbed in just those spectral regions where superior layers could collect them. These conclusions[1] agree with the quantitative theory given below.[2]

This strong differential radiative cooling of the lower layers in the stratosphere stabilizes its thermal structure so that vertical convection there becomes impossible. This differential radiative cooling, together with the oppositely distributed solar heating of the stratosphere by ozone, which is greater in upper layers, will explain the observed isothermal structure of the stratosphere.

The second of Brunt's unexplained facts about the stratosphere is apparent on consideration of the causes of vertical convection in the atmosphere. The motive power producing convection in the upper air is, in part, a result of lateral inhomogeneity of the water content of atmospheric layers. Moisture-laden air is lighter than dry air, owing to the lightness of the H_2O molecules as compared to N_2 and O_2. This density difference and differences in the heat content of different air masses can produce vertical convection. The observed lapse rate in the troposphere, due mainly to adiabatic cooling, is 6° C per kilometer. This cooling removes the moisture by condensation as the air rises. There is a height at which the water vapor is greatly attenuated by condensation and where it can no longer produce vertical convection, owing to the stabilizing effect of radiation cooling. One can also expect, at an appropriate height, that the radiation cooling can also stabilize an air mass initially warmer than the surrounding air. In either case, one would expect a sharp thermal discontinuity at the critical height where convection-producing agencies are first inactivated by our stabilizing infrared radiative transfer of heat. This hypothesis of the sudden change in lapse rate is supported by the fact that the height of a given temperature in the troposphere at low latitudes (say 0° in summer at 6 km) lies approximately at the same distance under the local tropopause (17 − 6 = 11 km) as that at which the same temperature at the pole lies under the polar tropopause (0° C at the surface in summer with tropopause at 10 km). One would expect this on the basis that the distance at which the tropopause lies above these 0° C layers is the same for both latitudes. This is presumed to be the distance for the lapse rate to condense out the water vapor characterizing a 0° C layer in the atmosphere to that critical concentration at which the stabilizing infrared radiation transfer just neutralizes convection.

The hypothesis presented here has no answer for the third of Brunt's unexplained facts. One would expect, however, that the greater vertical kinetic energy of air masses at low latitudes would be an important factor. As a consequence of this vertical component of motion, one would expect the vertical momentum at low latitudes to drive the convection higher there than it would otherwise go, with a resultant lower tropopause temperature and a sharper thermal discontinuity at the equator than at the pole.

The above speculations and remarks present, qualitatively, the influence of the pressure-broadening effect on the thermal structure of the stratosphere. We now proceed to show the infrared bands that are of importance in this connection, and we will then give a

[1] J. Strong, "The Infrared Atmospheric Transmission Problem," *Columbus Meeting Publication, ONR* (1948).

[2] For a preliminary report see G. N. Plass and J. Strong, *Phys. Rev.*, **78**, 334, 1950.

quantitative calculation of the heat loss from one of these bands to illustrate the manner in which the pressure effect plays its role.

DATA ON ABSORPTION IN THE INFRARED IN THE STRATOSPHERE

We are fortunate in having certain high-altitude measurements of the transmission characteristics of the upper atmosphere in the infrared which show the bands that are important for our considerations.

Figure 2 gives a curve representing the transmission of the atmosphere from 8 to 26 μ above 33,000 feet altitude.[3] A curve of the black-body emission for 220° K has been superimposed on this transmission-curve to show the importance of various spectral regions in stratosphere heat transfer. The transmission-curve shows that there are only three important regions in this range of wave lengths: the 9.6 μ region of the O_3 band; the 15 μ region of the CO_2 and O_3 bands, observed to be completely black around 15 μ; and the region beyond 17 μ due to the very strong pure rotation water lines.

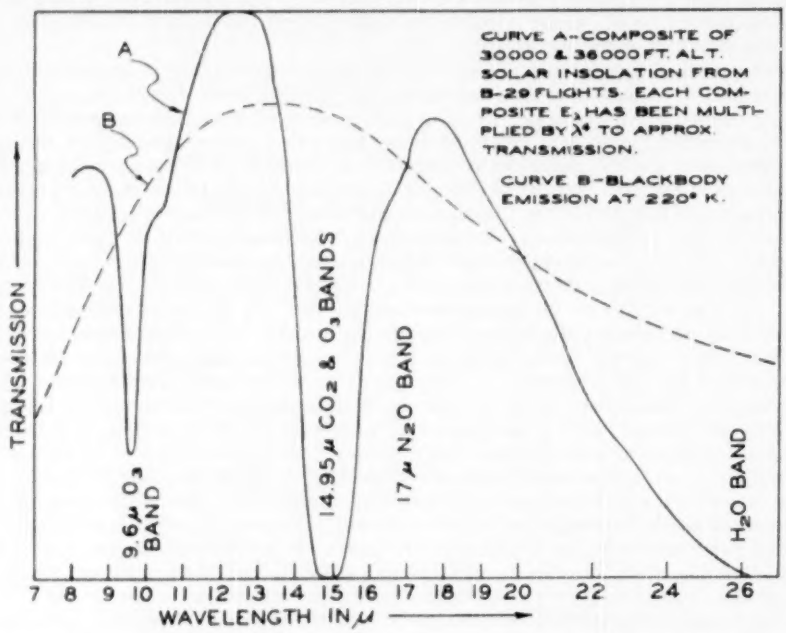

FIG. 2.—Transmission of the atmosphere in arbitrary units at 33,000 feet for solar radiation from 8 to 26 μ.

Further work is in progress at Johns Hopkins with the ONR 100-foot absorption cell. When this observational work is complete, we will have the necessary data for making a more detailed balance of the heat budget of the stratosphere than is now possible.

CALCULATION OF THE RADIATION LOSS

We calculate, below, the net loss of heat by radiation from a layer of the atmosphere

[3] These data were obtained in B-29 flights by the N.O.T.S. group of Roger Estey at Inyokern in co-operation with the Army Air Force and the Johns Hopkins group of John Strong.

at a prescribed height. For a particular radiating gas, the optical distance, u, from the top of the atmosphere, is defined by the equation

$$u = \int_z^\infty c\,\rho\,dz = \int_z^\infty \rho_r\,dz, \tag{2}$$

where the fractional concentration, c, is the ratio of the density of the radiating gas, ρ_r, to the total density, ρ. The positive direction of the vertical co-ordinate z is chosen upward. The absorption coefficient, $k = k(\nu, u)$, is a function of both frequency and height, since the pressure effect changes the half-width with height. The temperature of the radiating gas varies with height in the atmosphere. As a consequence of this variation, the black-body intensity in a straight beam, $I_b = I_b(\nu, u)$, is a function of both frequency and height. At a given frequency, let I_0 be the intensity of radiation entering the top of the atmosphere from the sun. Further, let I_1 be the known intensity of radiation crossing an imaginary boundary in the atmosphere at the height $u = u_0$. If this boundary is chosen at the earth's surface, then I_1 is the black-body intensity radiated from the surface. If this boundary is chosen at the tropopause, then I_1 is the radiation from the earth's surface plus that from the troposphere that crosses this boundary.

From the elementary differential equation for the transfer of radiation, it is found that the energy loss by radiation per unit area, solid angle, and time from a layer of thickness, du, at height determined by u, at an angle θ from the vertical, is

$$\begin{aligned} dR = \Big\{ \Big[I_b - I_0 + \int_0^u \frac{dI_b}{du'} \exp\Big(\int_0^{u'} k \sec\theta\, du'' \Big)\, du' \Big] \exp\Big(- \int_0^u k \sec\theta\, du' \Big) \\ + \Big[I_b - I_1 + \int_u^{u_0} \frac{dI_b}{du'} \exp\Big(\int_{u'}^{u_0} k \sec\theta\, du'' \Big)\, du' \Big] \\ \times \exp\Big(- \int_u^{u_0} k \sec\theta\, du' \Big) \Big\}\, k\, du\, d\Omega\, d\nu . \end{aligned} \tag{3}$$

The first term of equation (3) gives the black-body radiation loss from the given layer to the cosmic cold; the second represents the heat gain from incoming radiation from outer space; the third represents the heat exchange between the given layer of the atmosphere and higher layers because of temperature differentials which change the frequency at which the energy appears. Similarly, the fourth term gives the radiation loss from the given layer to the earth's surface and the part of the atmosphere below $u = u_0$; the fifth represents the heat gain from radiation originating at the earth's surface and in the atmosphere below $u = u_0$; and the sixth represents the heat exchanged because of temperature differentials between the given layer of the atmosphere and lower layers.

The detailed heat balance in the atmosphere can be computed from equation (3)[4] when the necessary experimental information is available. In order to solve this problem completely, the infrared spectroscopist must determine the value of the absorption coefficient as a function of frequency and density for the radiating gases. The meteorologists must determine the fractional concentration of the radiating gases and the density and temperature of the atmosphere as a function of height. Until more detailed data are available, we calculate the radiation loss from a layer of the atmosphere by means of certain simplifying assumptions. This enables us to reduce equation (3) to a very simple form (see eq. [18], below).

[4] A correction must be added to eq. (3) for the radiation scattered from the original direction. It is expected that this correction is very small for the stratosphere, but it could easily be appreciable near the surface of the earth, especially on overcast days. For a complete solution of the atmospheric heat-transfer problem, allowance must also be made for nonradiative processes, particularly convection and condensation. These effects are apparently important only in the lower layers of the atmosphere.

We now assume a model atmosphere which satisfies the following conditions: (1) The temperature is the same at all heights; (2) the total pressure decreases exponentially with height above the layer in which we are interested; (3) the fractional concentration of the radiating gas is constant with height; (4) the shape of the spectral lines is given by the Lorentz collision-broadening formula; (5) the half-width of the spectral lines is directly proportional to the total pressure; (6) at the highest pressure considered, the spacing between the lines is at least somewhat larger, on the average, than the width of the lines (i.e., the gas still obeys a square-root absorption law at this pressure).

These assumptions are reasonably well satisfied in the stratosphere for the radiations from the 15 μ CO_2 band and for the short wave-length lines of the 50 μ H_2O band. The above assumptions give the simple formulae which confirm our hypothesis quantitatively. These conditions can be modified in obvious ways to describe the transfer of radiation where different conditions prevail, as, for example, in the troposphere or in other planetary atmospheres.

According to assumption (2), the density of the atmosphere, ρ, is

$$\rho = \rho_0 \exp(-\beta z), \tag{4}$$

where z is the height, ρ_0 is the density at $z = 0$, and β is a constant equal approximately to 1.3×10^{-6} cm^{-1} for the stratosphere.

The density of the radiating gas, ρ_r, and its fractional concentration, c, are equal to the following expression by assumption (3):

$$\rho_r = c\rho = c\rho_0 \exp(-\beta z). \tag{5}$$

Since all the gases that contribute to the radiation balance of the atmosphere have small concentrations, the radiating gases will not be expected to exhibit an appreciable self-broadening effect. This simplifies the calculations, since the half-width in equation (6) is then independent of c and dependent only on the total pressure. This may not be true in some of the atmospheres of other planets where c is large.

According to assumptions (4) and (5), the absorption coefficient, k, is given as a function of frequency by equation (1), and the dependence of the half-width of the lines on the total pressure is given by

$$\alpha = a\rho = a\rho_0 \exp(-\beta z) = \frac{a\beta u}{c}, \tag{6}$$

where a is a constant and the optical distance, u, from the top of the atmosphere, is defined by equation (2). Note that the optical distance from the top of the atmosphere to a lower level, at height $z = 0$, equals $c\rho_0/\beta$.

We first calculate dR, the energy per unit area, solid angle, and time in a given wave-number interval, $d\nu$, which escapes from a layer of radiating gas of thickness, dz, to the cosmic cold. This is given by the first term of equation (3):

$$dR = I_b k \exp\left(-\int_z^\infty k\rho_r \sec\theta\, dz'\right) \rho_r dz d\Omega d\nu. \tag{7}$$

Because of assumption (5), the absorption coefficient is a function of the height, z. The remaining terms of equation (3), representing the exchange of radiation between the isothermal layer and the earth's surface and the remainder of the atmosphere, are small. These are considered later.

Substituting for the absorption coefficient, k, from equation (1) and the half-width from equation (6) and performing the indicated integration, equation (7) can be written in the form

$$dR = -I_b \cos\theta \frac{d}{du}\left[\frac{(\nu-\nu_0)^2}{(\nu-\nu_0)^2 + a^2\beta^2 c^{-2}u^2}\right] du\, d\nu d\Omega, \tag{8}$$

in which γ is a dimensionless constant, given by

$$\gamma = \frac{Sc}{2\pi a\beta \cos\theta}. \tag{9}$$

Equation (8) gives an expression for the radiation escaping from the atmosphere at an angle θ to the vertical that originates in a layer of given optical thickness. This equation has been plotted in Figure 3, for the particular value $\gamma = 29$ estimated for the 15 μ CO_2 band in our atmosphere. A consideration of this figure quantitatively confirms our earlier speculations on the influence of the pressure effect on the escaping radiation. The curves for the escaping radiation in a given frequency range, small compared to the line

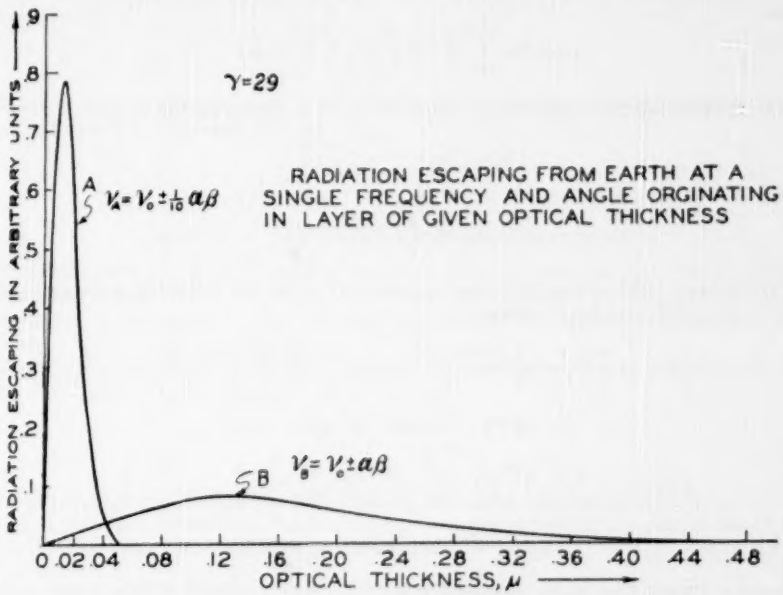

FIG. 3.—The radiation escaping from the atmosphere to the cosmic cold at a single frequency and given angle from the vertical that originates in a layer of given optical thickness.

breadth, first rise as the optical distance, or depth under the top of the atmosphere, increases from zero (owing to the increase in the emissivity with thickness). They then reach a maximum and finally decrease as the optical distance further increases (after the absorption coefficient of the higher layers becomes great enough effectively to shield the lower layers from the cosmic cold).

When the pressure effect is *not* taken into account, the above considerations apply for all frequency ranges in the spectrum. However, when the pressure effect is considered, Figure 3 shows that the lower layers are shielded by the upper layers only for the frequency range coinciding with the central part of the line (curve *A*); while, for the frequency ranges lying in the wings of the line, the upper layers absorb weakly, and radiation can escape from the lower layers without appreciable absorption (curve *B*). If our model isothermal atmosphere were infinitely deep, the radiation leaving at *any* frequency would be that of the black-body radiation, I_b. Thus the area under any of the

curves given by equation (8) has the constant value I_b. However, the full black-body intensity originates in our stratosphere only for frequencies near the center of a line, while in the frequency ranges lying between the lines and far from the line centers very little intensity comes from the stratosphere.

According to assumption (6), the total radiation emitted to the cosmic cold from a single spectral line of a layer of a given optical thickness is obtained by integrating equation (8) over all frequencies. We perform this integration by changing to the dimensionless variable $x = c(\nu - \nu_0)/a\beta u$, carrying out the indicated differentiation with respect to u, and assuming that I_b does not change appreciably over the width of the band. The result may be written in the form

$$dR = 2 I_b a \beta c^{-1} G(\gamma) \cos\theta \, du \, d\Omega , \tag{10}$$

where

$$G(\gamma) = \int_0^\infty \left[1 - \left(\frac{x^2}{x^2+1}\right)^\gamma\right] dx . \tag{11}$$

The definite integral occurring in equation (11) can be evaluated to give

$$G(\gamma) = \pi^{1/2} \frac{\Gamma(\gamma + \frac{1}{2})}{\Gamma(\gamma)} , \tag{12}$$

where

$$\Gamma(x) = \int_0^\infty y^{x-1} e^{-y} dy .$$

For physical applications, it is more convenient to use the following series expansions of $G(\gamma)$ for small and large values of γ:

$$G(\gamma) = \frac{\pi}{2}\left\{\frac{\gamma}{1!} - \frac{1}{2}\frac{\gamma(\gamma-1)}{2!} + \frac{1\cdot 3}{2\cdot 4}\frac{\gamma(\gamma-1)(\gamma-2)}{3!} - \ldots\right\} \tag{13}$$

$$\cong \pi\gamma \qquad \text{(valid for small } \gamma) ; \tag{13a}$$

and

$$G(\gamma) = \left(\frac{\pi\gamma^2}{\gamma+\frac{1}{2}}\right)^{1/2}\left(1 + \frac{1}{8}\frac{1}{\gamma+\frac{1}{2}} + \frac{3}{384}\frac{1}{(\gamma+\frac{1}{2})^2} + \ldots\right) \tag{14}$$

$$\cong \pi^{1/2}\gamma^{1/2} \qquad \text{(valid for large } \gamma) . \tag{14a}$$

The very simple expression given by equation (14*a*) is correct within 2 per cent for $\gamma > 5$.

It is important to notice that equation (10) does not depend on the variable u, but only on the constants I_0, a, β, c, and γ. Thus the amount of radiation escaping to the cosmic cold from a single spectral line is the *same* for all layers of the same optical thickness, du, regardless of their depth in the atmosphere. Since $du = -c\rho dz$, it follows that *the amount of radiation escaping from layers of the same thickness, dz, increases exponentially, the closer the layer is to the earth's surface.* This is the result of the relatively large amount of radiation starting from the wings of the spectral lines in a lower layer, which undergoes very little absorption by the upper layers.

In order to calculate the total radiation lost by a band of infrared lines to the cosmic cold, we multiply equation (10) by the total number of lines in the band, N. According to our assumption (6), the spacing between lines is somewhat larger than the width of the lines, and therefore the total radiation lost by the band is N times the loss from one line. If the pressure becomes so large that this assumption no longer applies, then the radiation lost is somewhat smaller than that calculated by the above procedure and, of course, cannot be greater than the black-body intensity in the given frequency interval.

Thus the total radiation escaping from the layer of thickness dz into the solid angle $d\Omega$ is

$$dR = 2NI_b a\beta c^{-1} G(\gamma) \cos\theta \rho dz d\Omega . \tag{15}$$

By integrating this equation from a given height z, where the density has the value ρ, to the top of the atmosphere,[5] we find, for the total radiation into the solid angle $d\Omega$,

$$dR = 2NI_b a\rho G(\gamma) \cos\theta d\Omega . \tag{16}$$

When $\gamma > 5$, $G(\gamma)$ can be replaced by the expression given in equation (14*a*) to a good approximation. With equation (9), the integration over the solid angle can be readily performed. In this case the total radiation escaping from the layer of thickness dz to the cosmic cold is

$$dR = \frac{4\pi}{3} 2^{1/2} NI_b \left(\frac{Sa\beta}{c}\right)^{1/2} \rho dz . \tag{17}$$

Integrating this equation over z, we find the total radiation escaping from the height z to the top of the atmosphere to be

$$R = \frac{4\pi}{3} 2^{1/2} NI_b \left(\frac{Sac}{\beta}\right)^{1/2} \rho . \tag{18}$$

APPLICATION TO 15 μ CO_2 BAND IN THE STRATOSPHERE

As an example of the application of equation (18), we compute the total amount of radiant heat lost from the stratosphere to the cosmic cold from the 15 μ CO_2 band. The combination of constants S, a, and N occurring in equation (18) can be determined from laboratory absorption experiments.

The square-root law of absorption applies to CO_2 absorption over a wide range of pressures. For this band the fractional absorption is

$$2.14N \frac{Sau^{1/2}}{\Delta\nu}, \tag{19}$$

where u is the optical distance traversed by the beam and $\Delta\nu$ is the wave-number interval covered by the measurements. For the appropriate pressure ranges, a plot of the experimentally determined fractional absorption against $u^{1/2}$ gives a straight line with a slope D, where

$$D = 2.14N \frac{Sa^{1/2}}{\Delta\nu} . \tag{20}$$

Substituting this expression in equation (18), we find

$$R = 2.76\rho \left(\frac{c}{\beta\rho_l}\right)^{1/2} DI_b\Delta\nu , \tag{21}$$

where ρ_l is the density used in the laboratory experiments which determined D as a function of wave number. We have used the absorption measurement of C. W. Peters[6] at 5-cm pressure for CO_2 in N_2 to determine D from 13 to 17 μ. We have taken the following values for the other constants in equation (21): $\rho = 1.7 \times 10^{-4}$ gm/cm^3 (density of atmosphere at 17 km, which is approximately the beginning of the stratosphere); $c = 2 \times 10^{-4}$ (estimated concentration of CO_2 in stratosphere); $\beta = 1.3 \times 10^{-6}$ cm^{-1}; I_b is

[5] Somewhere above 35 km the line width is dominated by Doppler broadening instead of by pressure broadening. Above these heights our calculations in this section lose their significance.

[6] C. W. Peters, *Infrared Absorption of Carbon Dioxide at 15 Microns* (diss.; Baltimore: Johns Hopkins University, 1949).

computed by assuming that the stratosphere has a constant temperature of 220° K.[7]

The fraction of the black-body radiation emitted from the stratosphere to the cosmic cold per unit wave-number interval as a function of wave number is shown in Figure 4. It should be noted that the CO_2 is completely black at the center of the band (as can also be observed in Fig. 2). The above equations are not strictly applicable at the center of the band because of the complete opacity and also because of the presence of the O_3 bands. However, the error due to these effects is probably no larger than other uncertainties in the present data.

From the area under the curve in Figure 4, the total radiation lost from the 15 μ CO_2 band to the cosmic cold is calculated to be 310 μcal/cm^2 sec. This should be regarded as a

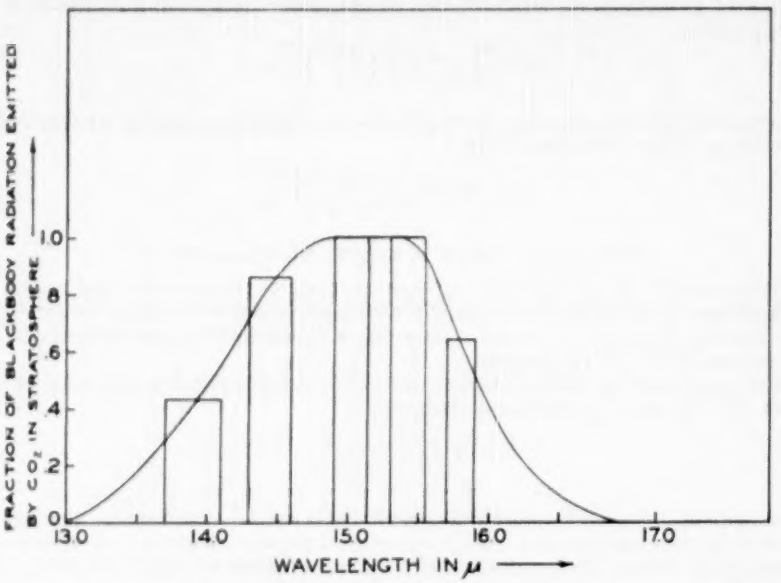

FIG. 4.—Radiation from the 15 μ CO_2 band in the stratosphere as a function of wave length in microns. The radiation is expressed as the fraction of total possible black-body radiation at the particular wave length. The rectangles are calculated from laboratory absorption measurements. The solid curve has been sketched as a possible representation of these data.

tentative value until it is possible to determine the constants in equation (21) more accurately. The radiation transfer by the CO_2 between the stratosphere and the troposphere is neglected, since it cancels in the first approximation. According to equation (18), the radiation exhausted from the atmosphere by the CO_2 increases as the square root of the concentration of CO_2. Since the atmosphere is at a lower temperature than the surface of the earth, the surface temperature rises as the CO_2 concentration increases.

The principal contribution of the CO_2 band to the heat balance is the loss of radiation to the cosmic cold. However, this band also exchanges radiation with the lower layers of the atmosphere and the earth's surface. Because of the higher temperature of the lower layers, the CO_2 in the stratosphere gains heat from this exchange. This is represented in

[7] From laboratory absorption experiments at both low and high pressures, the separate values of the constants S, a, and N can be estimated. From these experiments for the 15 μ CO_2 band we find that $\gamma \sim 30$, so that the use of eq. (18) instead of eq. (16) is justified.

the general heat-transfer equation (3) by the fourth and fifth terms. These terms are calculated in Appendix A. Since the incoming solar radiation is small compared to the outgoing radiation at 15 μ and since the temperature gradients over most of the stratosphere are assumed to be small, the second and third terms of equation (3) are neglected here. The sixth term for the heat exchange due to the temperature gradient in the troposphere gives a contribution that we have not calculated in this preliminary survey.

Since the line width increases with depth in the atmosphere, the pressure effect tends to prevent the exchange of heat with the warmer earth below. Since the pressure effect aids the escape of radiation to the cosmic cold, it is seen qualitatively that the gain in heat by a given layer in the stratosphere from the earth's surface is small compared to the loss of heat to the cosmic cold.

Taking the temperature of the earth's surface as 300° K, we find from equation (A5) that the heat gained from the earth's surface by the 15 μ band for the CO_2 in the stratosphere is 40 μcal/cm^2 sec. This assumes that an atmosphere at 220° K extends to the earth's surface. In addition, the stratosphere gains heat from the warmer gases of the troposphere (the sixth term of eq. [3]). From this term we estimate that the total heat gained by the stratosphere from the troposphere and the earth's surface combined is 60 μcal/cm^2 sec.

9.6 μ OZONE-BAND ABSORPTION AND EMISSION IN THE STRATOSPHERE

Since the ozone in the stratosphere is stratified, the concentration of ozone is certainly not a constant as the height is varied. Therefore, the previous equations, which assume a constant concentration, do not apply to ozone. We can, however, estimate the influence of O_3 on the heat budget of the stratosphere as follows:

From the transmission-curve in Figure 2, we assume that the 9.6 μ ozone band is a continuous absorption region about $\frac{1}{2}$ μ wide; its total absorption is $\frac{1}{2}$; its emission is half the intensity of a black body at 220° K. From these assumptions it follows immediately that the ozone loses 30 μcal/cm^2 sec to the cosmic cold and it sends another 30 μcal/cm^2 sec in radiation down to the earth's surface.

The black-body radiation from the earth's surface is absorbed by the 9.6 μ ozone band. Using the above assumptions about the ozone and taking 300° K for the temperature of the earth's surface, we find that the ozone is absorbing 190 μcal/cm^2 sec from the black-body radiation starting at the earth's surface. The 9.6 μ ozone band, therefore, adds a net amount, 130 μcal/cm^2 sec, to the heat budget of the stratosphere. This net absorption of heat is a result of the temperature of the ozone layer being lower than that of the earth's surface. It also depends on the troposphere being transparent to radiation around 9.6 μ.

50 μ H_2O BAND

Experimental studies of the absorption of this band in the region 10–30 μ, which will be adequate for the purposes of this calculation, are just now being carried out. It is uncertain whether the main absorption in this region is from lines or from the wings of very strong lines at 50 μ. Assuming the latter to be the case and taking the currently accepted values for the absorption from the wings, we show in Appendix B that there is much less absorption from 10 to 30 μ than is actually observed. This lends some support to the assumption that the individual lines primarily cause the absorption in this region.

Until further experimental studies are completed, we give only a very rough estimate of the loss of radiation from the water band. From the absorption-curve of Figure 2, it appears reasonable that the H_2O acts like a black body above about 25 μ. If we assume that all the black-body radiation leaving the earth above 28 μ comes from the 50 μ H_2O band, we find that the water vapor is exhausting about 780 μcal/cm^2 sec. If the H_2O band is completely black above 28 μ, it is able to absorb relatively less radiation from the earth's surface and troposphere than is the case for CO_2. We roughly estimate the heat gain from these sources by H_2O as 100 μcal/cm^2 sec.

RADIATION BALANCE IN THE STRATOSPHERE

The losses of heat in the stratosphere from the significant bands are collected in Table 1. The total heat loss from the stratosphere is 1150 μcal/cm^2 sec. This is balanced by heat

TABLE 1

RADIATION BALANCE IN THE STRATOSPHERE

	μcal/Cm^2 Sec
Heat loss:	
From 15 μ CO_2 and O_3 bands	310
From 9.6 μ O_3 band	60
From 50 μ H_2O band	(?)780
Total heat loss	1150
Heat gain:	
From sunlight absorbed by O_3	800
From earth's black-body radiation absorbed by O_3 at 9.6 μ	190
From earth's black-body radiation and exchange of radiation with troposphere by CO_2 at 15 μ	60
From same by H_2O at 50 μ	(?)100
Total heat gain	1150

gained from two major sources: (1) the absorption in the ultraviolet of the direct sunlight by the O_3 and (2) the absorption of the black-body radiation from the earth's surface and troposphere. The solar absorption can be estimated by assuming that the ozone absorbs one-twentieth the solar constant for two-fifths of the time. This gives 800 μcal/cm^2 sec. The agreement between heat lost and gained, shown in Table 1, should be accorded only qualitative significance; however, it indicates the relative importance of the various effects contributing to the heat balance.

With the present data it is not possible to discuss the heat balance at each level of the stratosphere separately. However, again we believe that the main features of the problem are now evident. From our previous discussion of the pressure effect, it follows that the heat lost from the CO_2 and H_2O bands comes largely from the lower layers of the stratosphere, and the net heat gained by the ozone will occur mainly at the levels of large ozone concentration, as well as in the lower layers. By the proper consideration of the pressure effect on the infrared bands, it follows that the lower layers of the stratosphere are expected to lose heat very much more rapidly than one would expect from calculations ignoring the pressure effect.

STABILITY OF THE STRATOSPHERE

If a given layer of the stratosphere becomes warmer or cooler than its surroundings, then its black-body radiation increases or decreases until equilibrium is restored. When layers at nonequilibrium temperatures are produced by atmospheric disturbances, it has been observed that they return to the equilibrium temperature within a period of a couple of days. We can calculate approximately the time required to return to equilibrium, since any layer loses heat at a rate proportional to f, the fraction of the total mass of the stratosphere which it contains (see eqs. [15]–[18]).

From Table 1 we find that a layer at the equilibrium temperature, T_0, loses heat at the rate $R = 1.15\ (10)^{-3} f$ cal/cm^2 sec. If the temperature of the layer is changed by a small

amount to T, the excess heat lost by radiation in the time dt is found from the Planck black-body law to be

$$dR = \sum_i \left[1 - \exp\left(\frac{-h c\nu_i}{kT}\right)\right]^{-1} \frac{h c\nu_i}{kT} R_i \frac{(T - T_0)\, dt}{T_0} = \epsilon R \frac{(T - T_0)\, dt}{T_0}, \tag{22}$$

where R_i is the heat loss from the given layer near the frequency ν_i and the summation is carried out over the three important bands. Equation (22) defines the quantity ϵ. From the data in Table 1 ϵ is found to be 2.9. This loss is equal to $\pm fCdT$, where $C = 20$ cal/°K cm² is the heat capacity of the layer and dT is the change in temperature in the time dt. Equating these two expressions and integrating, we find, for the expression giving the return to the equilibrium temperature,

$$T - T_0 = \text{(const.)} \exp\left(\pm \frac{\epsilon R t}{fCT_0}\right). \tag{23}$$

Substituting the numerical values for τ, the relaxation time for the return to equilibrium, we have $\tau = fCT_0/\epsilon R \backsim 1.3\ (10)^6$ sec $\backsim$15 days.

THE TROPOSPHERE

We have chosen to consider in detail the radiation balance in the stratosphere because the formulae are made simple by its isothermal character. However, in any problem involving the transfer of radiation through layers of gases with varying pressure or temperature, the varying width of the spectral lines with change in pressure or temperature is an important effect.

A simple qualitative consideration shows that the pressure effect also has an important influence on the transfer of radiation in the troposphere. Here, in bands where there is complete absorption at the centers of the band, radiations will be entrapped, like resonance radiation, and will not escape from the earth. However, the radiation in the wings of partially transparent atmospheric absorption lines will cause a greater net radiation loss from the lower layers of the tropopause than would have been expected previously. This has an important bearing on the meteorological problems of the troposphere and especially on the explanation of the observed lapse rate of 6° per kilometer which is lower than one can expect without invoking the pressure effect.

We wish to thank Walter M. Elsasser for interesting discussions and valuable suggestions concerning this paper.

APPENDIX A

Exchange of Radiation with Earth's Surface

In order to calculate the heat gained by a layer in the stratosphere from the earth's surface, we assume a model isothermal atmosphere (where the black-body intensity is I_b) extending from $u = 0$ to $u = u_0$, u_0 being at the earth's surface. At $u = u_0$ the atmosphere is bounded by a black body at a different temperature, radiating with the black-body intensity I_1. This model corresponds to a computation of the fourth and fifth terms and a neglect of the sixth term of equation (3).

The heat exchange with the lower layers for this model is

$$dR = -k\,(I_1 - I_b) \exp\left(-\int_u^{u_0} k \sec\theta\, du'\right) du\, d\Omega\, d\nu. \tag{A1}$$

The heat exchange is considered positive when radiation is lost from the layer. We use the same assumptions as in the derivation of equation (18). By evaluating the integral in equation (A1), the heat exchange can be written as

$$dR = -(I_1 - I_b)\cos\theta \frac{d}{du}\left[\frac{(\nu-\nu_0)^2 + a^2\beta^2 c^{-2}u^2}{(\nu-\nu_0)^2 + a^2\beta^2 c^{-2}u_0^2}\right]^{\gamma} du\, d\Omega\, d\nu . \tag{A2}$$

Integrating over all frequencies, we obtain

$$dR = 2a\beta c^{-1}(I_1 - I_b)(F_1 - 2\gamma u_0^2 u^{-2}F_2)\cos\theta\, du\, d\Omega , \tag{A3}$$

where

$$F_1 = \int_0^\infty \left[1 - \left(\frac{x^2+1}{x^2 + u_0^2u^{-2}}\right)^{\gamma}\right] dx ,$$

$$F_2 = \int_0^\infty \frac{(x^2+1)^{\gamma}}{(x^2 + u_0^2u^{-2})^{\gamma+1}}\, dx .$$

Assuming that $\gamma \gg 1$, these integrals can be evaluated by expanding in inverse powers of γ. The integrals become especially simple if we also assume that $ln(u_0^2u^{-2}) \gg \gamma^{-1}$. This implies that the equations given below are not valid very near the boundary $u = u_0$. This restriction is of no consequence for our purposes, as the lowest layers of the stratosphere are very far from the earth's surface, according to this condition.

Using the same procedures as those used in the derivation of equation (18), after integrating over the hemisphere, we find, for the total exchange of radiation for the entire band with the earth's surface,

$$dR = -\frac{4\pi}{3} 2^{1/2} N (I_1 - I_b)\left(\frac{Sa\beta}{c}\right)^{1/2} \rho\, (\rho_0^2 - \rho^2)^{-1/2}\rho\, dz , \tag{A4}$$

where ρ is the density at the height z and ρ_0 is the density at $u = u_0$, the position of the black body at a different temperature.

Integrating over the entire stratosphere, we find that the total heat exchanged with the surface is

$$R = -\frac{4\pi}{3} 2^{1/2} N (I_1 - I_b)\frac{Sac}{\beta}\left[\rho_0 - (\rho_0^2 - \rho_1^2)^{1/2}\right] , \tag{A5}$$

where ρ_1 is the density at the tropopause.

APPENDIX B

Radiation Loss from the Wings of the 50 μ H_2O Band

For the H_2O band in the region from 15 to 50 μ the relative importance of line absorption and absorption from the wings of some very strong lines near 50 μ is not known. In this section we assume that the absorption is primarily from the wings. This assumption gives results in conflict with present experimental evidence.

The radiation from the wings can be calculated by a method similar to the one used for the 15 μ CO_2 band. To a first approximation the absorption coefficient in the wings is given by the equation

$$k(\nu) = \frac{Sa}{\pi(\nu-\nu_0)^2} , \tag{B1}$$

which gives the same absorption as though a single very intense line existed at the center frequency of the band.

In order to calculate the radiation loss from the short wave-length wing of the water band, we make the same six assumptions as in the 15 μ CO_2 calculation described above. However, equation (B1) is used for the absorption coefficient instead of equation (1). Instead of integrating over the entire wave-number range, the integration is performed here only between ν_A and ν_B, two wave numbers in the region of continuous absorption.

The radiation emitted to the cosmic cold from a layer of optical thickness du in the solid angle $d\Omega$ is

$$dR = \pi^{1/2} I_b \beta \delta \cos^{1/2}\theta \left\{ \operatorname{erf}\left(\frac{\delta \rho \sec^{1/2}\theta}{\nu_A - \nu_0} \right) - \operatorname{erf}\left(\frac{\delta \rho \sec^{1/2}\theta}{\nu_B - \nu_0} \right) \right\} \rho d z d\Omega , \tag{B2}$$

where

$$\delta^2 = \frac{S a c}{2\pi\beta}, \qquad \operatorname{erf} x = 2\pi^{-1/2} \int_0^x \exp(-x^2)\, dx ,$$

and ρ is the density of the atmosphere at the height z.

Integrating this equation from height z to the top of the atmosphere, we obtain, for the total loss of energy to the cosmic cold from the frequency interval between ν_A and ν_B in the solid angle $d\Omega$,

$$\begin{aligned} \frac{dR}{d\Omega} = \pi^{1/2} I_b \rho \delta \cos^{1/2}\theta & \left\{ \operatorname{erf}\left(\frac{\delta \rho \sec^{1/2}\theta}{\nu_A - \nu_0} \right) - \operatorname{erf}\left(\frac{\delta \rho \sec^{1/2}\theta}{\nu_B - \nu_0} \right) \right\} \\ & - I_b (\nu_A - \nu_0) \cos\theta \left\{ 1 - \exp\left[- \frac{\delta^2 \rho^2 \sec\theta}{(\nu_A - \nu_0)^2} \right] \right\} \\ & - I_b (\nu_B - \nu_0) \cos\theta \left\{ 1 - \exp\left[- \frac{\delta^2 \rho^2 \sec\theta}{(\nu_B - \nu_0)^2} \right] \right\} . \end{aligned} \tag{B3}$$

If the arguments of the error integrals are small, the total radiation loss in the hemisphere is approximately

$$R = 4\pi I_b \rho^2 \delta^2 \left[(\nu_A - \nu_0)^{-1} - (\nu_B - \nu_0)^{-1} \right] . \tag{B4}$$

These results show that the radiation loss from a layer of thickness du from the wings of the water band depends on the height of the layer in the atmosphere (compare with eq. [15]). Using the values of the H_2O constants derived by Elsasser,[8] we compute that the stratosphere should be transparent to incident sunlight below 45 μ. This result conflicts with the experimental results in Figure 2. Either the previously determined constants for the H_2O band are greatly in error, or the absorption of H_2O is predominately a line absorption below 45 μ. Laboratory experiments to decide this point are now in progress.

[8] Walter M. Elsasser, *Heat Transfer by Infrared Radiation in the Atmosphere* (Cambridge: Harvard University Press, 1942), p. 55.

THE THEORY OF THE FLUCTUATIONS IN BRIGHTNESS OF THE MILKY WAY. I

S. CHANDRASEKHAR AND G. MÜNCH
Yerkes Observatory
Received July 11, 1950

ABSTRACT

In this paper the following statistical problem is considered. Let stars and interstellar clouds occur with a uniform distribution. Let the system extend to a linear distance L in the direction of a line of sight. Let a cloud reduce the intensity of the light of the stars immediately behind it by a factor q. Let the occurrence of clouds with a transparency factor q be governed by a frequency function $\psi(q)$. Given all this, it is required to find the probability distribution, $g(I, L)$, of the observed brightness, I. From a consideration of this problem it is shown that the following integral equation governs the distribution of brightness:

$$g(u, \xi) + \frac{\partial g}{\partial u} + \frac{\partial g}{\partial \xi} = \int_0^1 g\left(\frac{u}{q}, \xi\right)\psi(q)\frac{dq}{q},$$

where u is the observed brightness measured in suitable units and ξ is the average number of clouds in the direction of the line of sight. It is further shown that the foregoing integral equation enables us to obtain explicit formulae for all the moments of g as functions of ξ and the moments of $\psi(q)$. As an illustration of the use of these general formulae for the moments, an example investigated by Markarian has been reconsidered in an attempt to derive the mean and mean-square deviation of the optical thicknesses of the interstellar clouds.

1. *Introduction.*—The fact, now generally recognized, that interstellar matter occurs in the form of clouds and that the average number of such clouds intersected by a line of sight is of the order of 5 per kiloparsec requires a reorientation of the problems and objectives of stellar statistics. That such a reorientation is needed is brought out most clearly by the definiteness and the precision of the conclusions reached by Ambarzumian and his collaborators in three relatively brief investigations,[1] in which the cloud structure of interstellar matter is explicitly introduced as an essential element of the problem. Thus, in the investigation by Ambarzumian and Gordeladse, in which the observed association of emission and reflection nebulae is quantitatively accounted for on the hypothesis of a random distribution of stars and interstellar clouds by considering the volumes of space illuminated by stars of various spectral types, estimates are obtained for the average number of clouds per unit volume ($\sim 1.2 \times 10^{-4}$ per cubic parsec) and the average number of clouds intersected by a straight line (5–7 per kiloparsec). Similarly, from a simple analysis of the statistics of extragalactic nebulae, Ambarzumian deduced that the photographic absorption per cloud is of the order of 0.2 mag.; this, combined with the earlier estimate of the number of clouds in a line of sight, leads to a photographic extinction coefficient of 1.0–1.5 mag. per kiloparsec, which is in general agreement with other determinations of this quantity. The far-reaching nature of these conclusions—they were revolutionary at the time that they were drawn—should convince one that stellar statistics will gain enormously by making the distribution and the properties of interstellar clouds more immediate objectives of the investigation than has been customary so far. For example, the known fluctuations in the brightness of the Milky Way can be interpreted most readily in terms of the fluctuations in the numbers of the absorbing clouds in the line of sight; for, while other factors doubtless contribute to the observed fluctuations, these must be secondary to the effect of the fluctuations in the numbers of

[1] V. A. Ambarzumian and S. G. Gordeladse, *Bull. Abastumani Obs.*, No. 2, p. 37, 1938; V. A. Ambarzumian, *Bull. Abastumani Obs.*, No. 4, p. 17, 1940; and B. E. Markarian, *Contr. Burakan Obs. Acad. Sci. Armenian S.S.R.*, No. 1, 1946.

clouds, since so few of these are generally involved. Indeed, in a short note published in 1944, Ambarzumian[2] formulated the following problem which he considered basic for such an analysis:

Let stars and absorbing clouds occur with a uniform distribution in a plane of infinite extent. Further, let a cloud reduce the intensity of the light of the stars immediately behind it by a factor q. Let the occurrence of clouds with a "transparency" q be governed by a frequency function $\psi(q)$. What is, then, the probability distribution of the observed brightness?

Ambarzumian derived an integral equation for the required probability distribution and showed how its first and second moments can be expressed quite simply in terms of $\bar{q}$ and $\overline{q^2}$. However, when Markarian[1] came to applying this theory to observations, he found that Ambarzumian's assumption of the infinite extent of the system in the direction of the line of sight was too restrictive and that the problem must be considered for the case in which the average number of clouds in the line of sight is finite. The need for this generalization is apparent when we remember that the average number of clouds in the direction of galactic latitude β is n cosec β, where n is the corresponding number in the direction of the galactic pole; thus in our own galaxy $n \sim 3$ and n cosec $\beta \sim 10$ for $\beta = 20^\circ$. Moreover, this dependence of the average number of clouds on the galactic latitude will provide a valuable check on the analysis.

Markarian did not derive the integral equation governing the distribution of brightness for the more general problem; but he did obtain explicit expressions for the first and the second moments for the case in which all the clouds are equally transparent. In this paper we shall derive the general integral equation governing the distribution of brightness and show how all its moments can be found. And we shall illustrate the use of these general relations for the moments by an example.

2. *The basic integral equation.*—Let I denote the observed brightness and L the distance of the observer to the limits of the system in the direction of the line of sight. Then

$$I = \int_0^L \prod_{i=1}^{n(s)} q_i \eta \, ds \,, \tag{1}$$

where η is the emission per unit volume by the stars assumed to be uniformly distributed, $n(s)$ is the number of clouds in the distance interval $(0, s)$ in the line of sight and is a chance variable, and $q_i\,[i = 1, 2, \ldots, n(s)]$ is the factor by which the ith cloud cuts down the intensity of the light from the stars immediately behind it. As we have already stated in § 1, we shall assume that the q's occur with a known frequency, $\psi(q)$.

If ν is the average number of clouds per unit distance, then $n(s)$ will be governed by the Poisson distribution,

$$e^{-\nu s} \frac{(\nu s)^n}{n!} \qquad (n = 0, 1, \ldots) \,, \tag{2}$$

having the variance νs.

The problem is to determine the probability distribution of I. It is convenient to reformulate this problem in dimensionless variables. For this purpose we shall let

$$u = I \frac{\nu}{\eta} \qquad \text{and} \qquad \tau = \nu s \,. \tag{3}$$

Then

$$u = \int_0^\xi \prod_{i=1}^{n(\tau)} q_i \, d\tau \,, \tag{4}$$

where

$$\xi = \nu L \tag{5}$$

[2] *C.R. (Doklady) Acad. Sci. URSS*, **14**, 223, 1944.

is the average number of clouds to be expected in the distance L. Also, according to formula (2), the occurrence of a particular number of clouds, n, in the interval $(0, r)$ will be governed by the Poisson distribution,

$$e^{-r}\frac{r^n}{n!} \qquad (n = 0, 1, \ldots) . \tag{6}$$

Let $g(u, \xi)$ denote the frequency distribution of u for a given ξ. Since the q_i's are all less than, or equal to, 1, it follows from the definition of u as the integral (4) that u *can never exceed* ξ. Hence

$$g(u, \xi) = 0 \qquad \text{for} \qquad u > \xi . \tag{7}$$

In addition to $g(u, \xi)$, it is convenient to define the probability that u exceeds a specified value. Let

$$f(u, \xi) = \int_u^\xi g(u, \xi)\, du \tag{8}$$

denote this probability. An integral equation governing $f(u, \xi)$ can be derived in the following manner:

By definition

$$f(u, \xi) = \text{Probability that} \int_0^\xi \prod_{i=1}^{n(r)} q_i\, dr \geqslant u . \tag{9}$$

Equivalently, we may also write

$$f(u, \xi) = \text{Probability that} \left\{ \int_0^a \prod_{i=1}^{n(r)} q_i\, dr + \prod_{j=1}^{n(a)} q_j \int_a^\xi \prod_{i=1}^{n(r)-n(a)} q_i\, dr \right\} \geqslant u , \tag{10}$$

where a is an arbitrary positive constant $\leqslant \xi$. Replacing $r - a$ by r in the second integral on the right-hand side, we have

$$f(u, \xi) = \text{Probability that} \left\{ \int_0^a \prod_{i=1}^{n(r)} q_i\, dr + \prod_{j=1}^{n(a)} q_j \int_0^{\xi-a} \prod_{i=1}^{n(r)} q_i\, dr \right\} \geqslant u . \tag{11}$$

Now let $a \ll 1$. Then up to $O(a^2)$, we have only two possibilities: either there is no cloud in the interval $(0, a)$, or there is just exactly one cloud. The probabilities of these two occurrences—again, up to $O(a^2)$—are $1 - a$ and a, respectively. Hence

$$\begin{aligned} &\prod_{i=1}^{n(a)} q_i = 1 \text{ with probability } 1 - a , \\ &\qquad \geqslant q \text{ and } \leqslant q + dq \text{ with probability } a\psi(q)\, dq . \end{aligned} \tag{12}$$

We may, therefore, rewrite equation (11) in the form

$$\begin{aligned} f(u, \xi) = a \int_0^1 dq\, \psi(q) \times \text{probability that} \left\{ \theta a + q \int_0^{\xi-a} \prod_{i=1}^{n(r)} q_i\, dr \right\} \geqslant u \\ + (1 - a) \times \text{probability that} \left\{ a + \int_0^{\xi-a} \prod_{i=1}^{n(r)} q_i\, dr \right\} \geqslant u + O(a^2) , \end{aligned} \tag{13}$$

where $\theta \leqslant 1$ is some positive constant. Since we are neglecting all quantities of $O(a^2)$ and

higher, it is clearly sufficient to evaluate the integral in equation (13) which occurs with the factor α to zero order in α. Thus

$$f(u,\xi) = \alpha\int_0^1 dq\psi(q) \times \text{probability that}\left\{\int_0^{\xi}\prod_{i=1}^{n(r)} q_i\,dr\right\} \geqslant \frac{u}{q} + (1-\alpha) \times \text{probability that}\left\{\int_0^{\xi-\alpha}\prod_{i=1}^{n(r)} q_i\,dr\right\} \geqslant u-\alpha+O(\alpha^2); \tag{14}$$

or, remembering the definition of $f(u, \xi)$, we have

$$f(u,\xi) = \alpha\int_0^1 dq\psi(q)\, f\left(\frac{u}{q},\xi\right) + (1-\alpha)\, f(u-\alpha,\xi-\alpha) + O(\alpha^2). \tag{15}$$

Hence

$$f(u,\xi) = \alpha\int_0^1 dq\psi(q)\, f\left(\frac{u}{q},\xi\right) + f(u,\xi) - \alpha f(u,\xi) - \alpha\frac{\partial f}{\partial u} - \alpha\frac{\partial f}{\partial \xi} + O(\alpha^2). \tag{16}$$

The function $f(u, \xi)$ must therefore satisfy the integral equation,

$$f + \frac{\partial f}{\partial u} + \frac{\partial f}{\partial \xi} = \int_0^1 \psi(q)\, f\left(\frac{u}{q},\xi\right) dq. \tag{17}$$

Now, differentiating this equation with respect to u, we obtain the integral equation governing $g(u, \xi)$,

$$g(u,\xi) + \frac{\partial g}{\partial u} + \frac{\partial g}{\partial \xi} = \int_0^1 \psi(q)\, g\left(\frac{u}{q},\xi\right)\frac{dq}{q}. \tag{18}$$

We have already pointed out that u cannot take values *exceeding* ξ. But it can take the value ξ itself with exactly the probability $e^{-\xi}$, since this is the probability that no cloud will occur in the interval $(0, \xi)$. The distribution of u has therefore a delta function, $\delta(u - \xi)$, at $u = \xi$ with an "amplitude" $e^{-\xi}$. Therefore, writing

$$g(u,\xi) = \phi(u,\xi) + e^{-\xi}\delta(u-\xi),$$

we find that the differential equation for ϕ is

$$\phi(u,\xi) + \frac{\partial\phi}{\partial u} + \frac{\partial\phi}{\partial\xi} = \psi\left(\frac{u}{\xi}\right)\frac{e^{-\xi}}{\xi} + \int_{u/\xi}^1 \psi(q)\,\phi\left(\frac{u}{q},\xi\right)\frac{dq}{q}.$$

In deriving this equation the assumption has been made that since

$$\left(1 + \frac{\partial}{\partial u} + \frac{\partial}{\partial\xi}\right) e^{-\xi} \times \text{a function of } (u-\xi) \equiv 0,$$

the same is also true of $e^{-\xi}\delta(u - \xi)$.

For the case in which the system extends to infinity in the direction of the line of sight, equation (18) reduces to the one given by Ambarzumian,[2] namely,

$$g(u) + \frac{dg}{du} = \int_0^1 \psi(q)\, g\left(\frac{u}{q}\right)\frac{dq}{q}. \tag{19}$$

Equation (18) is the basic equation of the problem.

3. ***The moments of the distribution function*** $g(u, \xi)$.—We shall now show how the integral equation (18) enables us to determine all the moments,

$$\mu_n = \int_0^\xi g(u, \xi)\, u^n du \qquad (n = 0, 1, \ldots), \tag{20}$$

of the distribution function $g(u, \xi)$. But first we may note that, by definition,

$$\mu_0 = \int_0^\xi g(u, \xi)\, du \equiv 1; \tag{21}$$

all the other moments will, however, be functions of ξ.

Now, multiplying equation (18) by u^n and integrating over the range of u, we obtain

$$\mu_n + \int_0^\xi \frac{\partial g}{\partial u} u^n du + \frac{d\mu_n}{d\xi} = \int_0^1 dq\, q^n \psi(q) \int_0^\xi \frac{du}{q} \left(\frac{u}{q}\right)^n g\left(\frac{u}{q}, \xi\right). \tag{22}$$

An integration by parts reduces the integral on the left-hand side to $-n\mu_{n-1}$ if use is made of equation (7). Also, the integral on the right-hand side can be reduced in the following manner:

$$\begin{aligned} &\int_0^1 dq\, q^n \psi(q) \int_0^\xi \frac{du}{q} \left(\frac{u}{q}\right)^n g\left(\frac{u}{q}, \xi\right) \\ &\qquad = \int_0^1 dq\, q^n \psi(q) \int_0^{\xi/q} dx\, x^n g(x, \xi) \qquad (23) \\ &\qquad = \int_0^1 dq\, q^n \psi(q) \int_0^\xi dx\, x^n g(x, \xi) = \mu_n \int_0^1 dq\, q^n \psi(q). \end{aligned}$$

In the foregoing reductions use has again been made of the fact that $g(u, \xi) = 0$ for $u > \xi$. Thus equation (22) becomes

$$\frac{d\mu_n}{d\xi} + (1 - q_n)\, \mu_n = n\mu_{n-1} \qquad (n = 0, 1, \ldots), \tag{24}$$

where, for the sake of brevity, we have written

$$q_n = \overline{q^n} = \int_0^1 dq\, q^n \psi(q). \tag{25}$$

It may be noticed here that, by writing

$$\mu_n = \int_0^\xi \phi(u, \xi)\, u^n du + \xi^n e^{-\xi} = u_n + \xi^n e^{-\xi}$$

in equation (24), we find that the equation satisfied by u_n is

$$\frac{du_n}{d\xi} + (1 - q_n)\, u_n = q_n \xi^n e^{-\xi} + n u_{n-1}.$$

But this same differential equation also follows directly from the equation satisfied by ϕ.

It is evident that all the moments μ_n must vanish at $\xi = 0$. On the other hand, from equation (22) for $n = 2$, namely,

$$\frac{d\mu_2}{d\xi} + (1 - q_2)\, \mu_2 = 2\mu_1, \tag{26}$$

we conclude that $d\mu_2/d\xi$ also vanishes at $\xi = 0$. And by induction it follows quite generally from equation (24) that μ_n *and its first* $(n-1)$ *derivatives must vanish at* $\xi = 0$. Also, the μ_n's must be bounded for $\xi \to \infty$. As we shall see presently, these boundary conditions suffice to solve the system of equations (24) uniquely.

By successive applications of equation (24) for $n = 1, 2$, etc., we obtain

$$\left[\prod_{j=1}^{n}\left(\frac{d}{d\xi}+\alpha_j\right)\right]\mu_n = n!\,, \tag{27}$$

where

$$\alpha_j = 1 - q_j\,. \tag{28}$$

The solution of equation (27) which satisfies the boundary condition at $\xi = \infty$ is

$$\mu_n = \sum_{k=1}^{n} A_k e^{-\alpha_k \xi} + \frac{n!}{\prod_{j=1}^{n}\alpha_j}\,, \tag{29}$$

where the A_k's$(k = 1, \ldots, n)$ are n constants of integration.

The boundary conditions,

$$\mu_n = 0 \qquad \text{and} \qquad \frac{d^j\mu_n}{d\xi^j} = 0 \qquad (j = 1, \ldots, n-1)\,, \tag{30}$$

now require that

$$\sum_{k=1}^{n} A_k = -\frac{n!}{\prod_{j=1}^{n}\alpha_j}$$

and (31)

$$\sum_{k=1}^{n} A_k \alpha_k^j = 0 \qquad (j = 1, \ldots, n-1)\,.$$

The matrix of the system of equations (30) is seen to be the Vandermondie matrix;[3] its reciprocal is the matrix[4]

$$\left|\frac{S_{n-l-1,\,r}}{\prod_{j\neq r}^{(1,\,n)}(\alpha_r - \alpha_j)}\right|\,, \tag{32}$$

in which the $S_{n-l-1,\,r}$'s $(l = 0, 1, \ldots, n-1;\ r = 1, \ldots, n)$ are the independent symmetric functions in the $(n-1)$ variables $(\alpha_1, \ldots, \alpha_{r-1}; \alpha_{r+1}, \ldots, \alpha_n)$,

$$S_{0,\,r} = 1\,; \qquad S_{1,\,r} = -\sum_{j\neq r}^{(1,\,n)}\alpha_r\,; \ \ldots\,; \qquad S_{n-1,\,r} = (-1)^n\prod_{j\neq r}^{(1,\,n)}\alpha_j\,. \tag{33}$$

The constants A_k are therefore given by

$$A_k = -\frac{S_{n-1,\,k}}{\prod_{j\neq k}^{(1,\,n)}(\alpha_k - \alpha_j)}\,\frac{n!}{\prod_{j=1}^{n}\alpha_j} = \frac{(-1)^n n!}{\alpha_k\prod_{j\neq k}^{(1,\,n)}(\alpha_k - \alpha_j)} \qquad (k = 1, \ldots, n)\,. \tag{34}$$

[3] Cf. O. Perron, *Algebra* (Leipzig: De Gruyter, 1932), 1, No. 22, 92–94.

[4] Cf. S. Chandrasekhar, *Ap. J.*, **101**, 328, 1945, esp. eqs. (75) and (81).

Reverting to the variables $1 - q_j$ (eq. [28]), we have

$$A_k = \frac{n!}{\prod_{j\neq k}^{(0,\,n)} (q_k - q_j)} \qquad (k = 1, \ldots, n) . \tag{35}$$

Extending definition (35) also to $k = 0$, we can write the solution for μ_n in the form

$$\mu_n = n! \sum_{k=0}^{n} \frac{e^{-(1-q_k)t}}{\prod_{j\neq k}^{(0,\,n)} (q_k - q_j)} \qquad (n = 1, \ldots) . \tag{36}$$

In particular, for $n = 1$ and 2 we have

$$\mu_1 = \frac{1}{1-q_1}\left[1 - e^{-(1-q_1)t}\right]$$

and

$$\mu_2 = \frac{2}{(1-q_1)(1-q_2)} + \frac{2\,e^{-(1-q_1)t}}{(q_1-1)(q_1-q_2)} + \frac{2\,e^{-(1-q_2)t}}{(q_2-1)(q_2-q_1)} . \tag{37}$$

If all the clouds are characterized by the same value of q, then

$$q_j = q^j , \tag{38}$$

and equations (37) reduce to the ones given by Markarian.[5]

4. *A direct proof of the relations satisfied by the moments.*—It is of interest to verify that the relations between the moments of g obtained in § 3 and, in particular, the differential equation (eq. [24]) governing them are deducible directly from the definition of u as the integral (4). For this purpose we first establish the following lemma:

Lemma.—Let $f(x_1, \ldots, x_n)$ be a symmetrical function in the n variables $x_1, \ldots, x_n$. Then

$$\begin{aligned} I_n &= \int_b^a dx_n \int_b^a dx_{n-1} \int_b^a dx_{n-2} \cdots \int_b^a dx_1 f(x_1, \ldots, x_n) \\ &= n! \int_b^a dx_n \int_{x_n}^a dx_{n-1} \int_{x_{n-1}}^a dx_{n-2} \cdots \int_{x_2}^a dx_1 f(x_1, \ldots, x_n) . \end{aligned} \tag{39}$$

Proof.—First, we verify that the lemma is true for two variables; this is very readily done. Next we show that, on the assumption that the lemma is true for all multiple integrals of $(n-1)$ and lower folds, the truth of the lemma for n-fold integrals can be deduced. The general truth of the lemma would then follow by induction.

Considering, then, the n-fold integral I_n and transforming the $(n-1)$-fold integral over $x_{n-1}, x_{n-2}, \ldots, x_1$ in accordance with the lemma, we have

$$I_n = (n-1)! \int_b^a dx_n \int_b^a dx_{n-1} \int_{x_{n-1}}^a dx_{n-2} \cdots \int_{x_2}^a dx_1 f(x_1, \ldots, x_n) . \tag{40}$$

Splitting the range of integration over x_{n-1} from a to x_n and x_n to b, we have

$$I_n = (n-1)! \int_b^a dx_n \int_{x_n}^a dx_{n-1} \int_{x_{n-1}}^a dx_{n-2} \cdots \int_{x_2}^a dx_1 f(x_1, \ldots, x_n) + J , \tag{41}$$

[5] *Op. cit.*, eqs. (10) and (13).

where

$$J = (n-1)!\int_b^a dx_n \int_b^{x_n} dx_{n-1} \int_{x_{n-1}}^a dx_{n-2} \cdots \int_{x_2}^a dx_1 f(x_1, \ldots, x_n). \tag{42}$$

Now, inverting the order of the integration over x_n and x_{n-1} in J and using the symmetry of $f(x_1, \ldots, x_n)$ in x_{n-1} and x_n, we have

$$\begin{aligned} J &= (n-1)!\int_b^a dx_{n-1} \int_{x_{n-1}}^a dx_n \int_{x_{n-1}}^a dx_{n-2} \cdots \int_{x_2}^a dx_1 f(x_1, \ldots, x_n) \\ &= (n-1)!\int_b^a dx_n \int_{x_n}^a dx_{n-1} \int_{x_n}^a dx_{n-2} \int_{x_{n-2}}^a dx_{n-3} \cdots \int_{x_2}^a dx_1 f(x_1, \ldots, x_n). \end{aligned} \tag{43}$$

The $(n-2)$-fold integral over $x_{n-2}, x_{n-3}, \ldots, x_1$ in this last expression for J can be transformed in accordance with the converse form of the lemma for $(n-2)$ variables and leads to

$$J = (n-1)\int_b^a dx_n \int_{x_n}^a dx_{n-1} \int_{x_n}^a dx_{n-2} \int_{x_n}^a dx_{n-3} \cdots \int_{x_n}^a dx_1 f(x_1, \ldots, x_n). \tag{44}$$

By a further application of the lemma for the $(n-1)$ variables $x_{n-1}, x_{n-2}, \ldots, x_1$, we obtain

$$J = (n-1)(n-1)!\int_b^a dx_n \int_{x_n}^a dx_{n-1} \int_{x_{n-1}}^a dx_{n-2} \cdots \int_{x_2}^a dx_1 f(x_1, \ldots, x_n). \tag{45}$$

With J given by equation (45), equation (41) becomes

$$I_n = n!\int_b^a dx_n \int_{x_n}^a dx_{n-1} \int_{x_{n-1}}^a dx_{n-2} \cdots \int_{x_2}^a dx_1 f(x_1, \ldots, x_n); \tag{46}$$

and this verifies the lemma for n variables. The general truth of the lemma therefore follows by induction.

An immediate corollary of the lemma is

$$I_n = n\int_b^a dx_n \int_{x_n}^a dx_{n-1} \int_{x_n}^a dx_{n-2} \cdots \int_{x_n}^a dx_1 f(x_1, \ldots, x_n). \tag{47}$$

This alternative expression for I_n follows from an application of the lemma in the converse form to the $(n-1)$-fold integral over $x_{n-1}, x_{n-2}, \ldots, x_1$ in equation (46).

Returning to the problem of deriving the differential equation (24) connecting the moments of g, we first observe that, by definition,

$$\mu_m = \left[\int_0^\xi \prod_{i=1}^{n(r)} q_i \, dr\right]^m_{\text{average}}. \tag{48}$$

Alternatively, we can write

$$\mu_m = \int_0^\xi dr_m \int_0^\xi dr_{m-1} \int_0^\xi dr_{m-2} \cdots \int_0^\xi dr_1 \left\{\prod_{j=1}^{m} \prod_{i=1}^{n(r_j)} q_i\right\}_{\text{average}}. \tag{49}$$

The integrand of this m-fold integral is clearly a symmetrical function of the variables.

Accordingly, using the lemma in the form (47), we can rewrite the foregoing expression for μ_m in the form

$$\mu_m = m\int_0^\xi d\tau_m \int_{\tau_m}^\xi d\tau_{m-1}\int_{\tau_m}^\xi d\tau_{m-2}\cdots\int_{\tau_m}^\xi d\tau_1 \Big\{\prod_{j=1}^{m}\prod_{i=1}^{n(\tau_j)} q_i\Big\}_{\text{average}} . \tag{50}$$

With the integration over the variables carried out in this fashion,

$$\tau_j \geqslant \tau_m \qquad \text{for all} \qquad j \leqslant m-1 . \tag{51}$$

Under these circumstances

$$n(\tau_j) - n(\tau_m) = n(\tau_j - \tau_m) , \tag{52}$$

and

$$\prod_{j=1}^{m}\prod_{i=1}^{n(\tau_j)} q_i = \Big\{\prod_{i=1}^{n(\tau_m)} q_i^m\Big\}\Big\{\prod_{j=1}^{m-1}\prod_{i=1}^{n(\tau_j-\tau_m)} q_i\Big\} . \tag{53}$$

In view of the inequality (51), it is evident that the occurrence of clouds in the interval $(0, \tau_m)$ is uncorrelated with the occurrence of clouds in any of the intervals $\tau_j - \tau_m$ $(j = m-1, \ldots, 1)$. Hence

$$\Big\{\prod_{j=1}^{m}\prod_{i=1}^{n(\tau_j)} q_i\Big\}_{\text{average}} = \Big\{\prod_{i=1}^{n(\tau_m)} q_i^m\Big\}_{\text{average}} \times \Big\{\prod_{j=1}^{m-1}\prod_{i=1}^{n(\tau_j-\tau_m)} q_i\Big\}_{\text{average}} . \tag{54}$$

Using this result in equation (50), we have

$$\mu_m = m\int_0^\xi d\tau_m \Big\{\prod_{i=1}^{n(\tau_m)} q_i^m\Big\}_{\text{average}} \times \int_{\tau_m}^\xi d\tau_{m-1}\int_{\tau_m}^\xi d\tau_{m-2}\cdots\int_{\tau_m}^\xi d\tau_1 \times \Big\{\prod_{j=1}^{m-1}\prod_{i=1}^{n(\tau_j-\tau_m)} q_i\Big\}_{\text{average}} . \tag{55}$$

Now, writing τ_j in place of $\tau_j - \tau_m (j = m-1, \ldots, 1)$ in equation (55), we have

$$\mu_m = m\int_0^\xi d\tau \Big\{\prod_{i=1}^{n(\tau)} q_i^m\Big\}_{\text{average}} \times \int_0^{\xi-\tau} d\tau_{m-1}\int_0^{\xi-\tau} d\tau_{m-2}\cdots\int_0^{\xi-\tau} d\tau_1 \times \Big\{\prod_{j=1}^{m-1}\prod_{i=1}^{n(\tau_j)} q_i\Big\}_{\text{average}} , \tag{56}$$

where, for brevity, we have suppressed the subscript m in τ_m. The $(m-1)$-fold integral in equation (56) is clearly $\mu_{m-1}(\xi - \tau)$. Accordingly, we may rewrite equation (56) in the form

$$\mu_m = m\int_0^\xi d\tau \Big\{\prod_{i=1}^{n(\tau)} q_i^m\Big\}_{\text{average}} \mu_{m-1}(\xi - \tau) . \tag{57}$$

On the other hand (cf. eqs. [6] and [25]),

$$\left\{\prod_{i=1}^{n(r)} q_i^m\right\}_{\text{average}} = \sum_{n=0}^{\infty} \frac{e^{-r} r^n}{n!} \prod_{i=1}^{n} \int_0^1 dq_i q_i^m \psi(q_i)$$

$$= \sum_{n=0}^{\infty} e^{-r} \frac{(r q_m)^n}{n!} = e^{-r(1-q_m)}. \tag{58}$$

Hence

$$\mu_m = m \int_0^{\xi} dr\, e^{-r(1-q_m)} \mu_{m-1}(\xi - r). \tag{59}$$

But this is the integrated form of equation (24) when the boundary condition $\mu_m = 0$ at $\xi = 0$ is also satisfied. The equations and boundary conditions from which solution (36) for the moments was derived in § 3 have now been obtained directly from the definition of u.

5. *An application of the formulae for the moments μ_m to derive certain statistical properties of the interstellar clouds.*—As an illustration of the application of the formulae for the moments derived in § 3, we shall reconsider an example investigated by Markarian,[1] on the assumption that all the interstellar clouds are equally transparent.

Markarian's example is based principally on van Rhijn's tabulation of the counts[6] of the number of stars $N_m(\beta, \lambda)$, per square degree, brighter than a given apparent magnitude m, and in a region of the sky centered at galactic latitude β and galactic longitude λ. In terms of these numbers[7] Markarian evaluated the quantity

$$I(\beta, \lambda) = \sum_m \{ N_{m+1}(\beta, \lambda) - N_m(\beta, \lambda) \} \times 10^{-0.4m}, \tag{60}$$

as a function of β and λ. This quantity, $I(\beta, \lambda)$, is clearly a measure of the brightness of the Milky Way in the region considered. It is, therefore, comparable, apart from a constant of proportionality, to I as we have defined it in equation (1).

In a detailed investigation it will be necessary to compare the observed fluctuations of the quantity (60) from the mean with the theoretical distributions derived on the basis of the integral equation (18). However, in a first attempt, it may suffice to restrict ourselves to the dispersion of the brightness about the mean.

Since we may expect the average number of absorbing clouds in the direction of galactic latitude β to vary with β as cosec β, it is clear that, in determining the dispersion of $I(\beta, \lambda)$ about the mean, we must treat the regions with different β's, separately. Thus, denoting the dispersion in the brightness of the Milky Way at galactic latitude β as $\delta^2(\beta)$, we have

$$\delta^2(\beta) = \frac{\text{Mean}\{ I^2(\beta, \lambda) \}}{[\text{Mean}\{ I(\beta, \lambda) \}]^2} - 1, \tag{61}$$

where, in taking the means, β is kept constant.

In the investigation we have quoted, Markarian has derived values for the dispersion $\delta^2(\beta)$, according to equation (61) for those values of β for which van Rhijn's (Groups I–IV) and Baker and Kiefer's (Groups V–VII) tables permit a determination. His final results are summarized in Table 1.

Now, on the model of the distribution of stars and clouds adopted in this paper (§ 1), the value of $\delta^2(\beta)$ should be compared with the theoretical quantity,

$$\delta^2(\xi) = \frac{\mu_2}{\mu_1^2} - 1. \tag{62}$$

[6] *Groningen Pub.*, No. 43, 1924. Markarian has also used the data given in R. H. Baker and L. Kiefer, *Ap. J.*, **94**, 482, 1941.

[7] Since the areas actually used in van Rhijn's tabulation extend over an appreciable range of β, Markarian had to reduce the observed numbers to a mean latitude β by applying a correction based on the observed mean variation of $N_m(\beta, \lambda)$ with β.

With μ_1 and μ_2 given by equations (37), we have

$$\delta^2(\xi) = \frac{2(1-q_1)}{(1-q_2)(q_1-q_2)} \frac{(1-q_2)[1-e^{-(1-q_1)\xi}] - (1-q_1)[1-e^{-(1-q_2)\xi}]}{[1-e^{-(1-q_1)\xi}]^2} - 1, \quad (63)$$

where it may be recalled that ξ is the average number of clouds in the direction of the line of sight and q_1 and q_2 are the mean and the mean square of the transparency factor q of the clouds:

$$q_1 = \int_0^1 q\Psi(q)\,dq \quad \text{and} \quad q_2 = \int_0^1 q^2\Psi(q)\,dq. \quad (64)$$

While q_1 and q_2 occur as two independent parameters in equation (63), it is evident that,

TABLE 1

RESULTS OF MARKARIAN'S ANALYSIS OF $N_m(\beta, \lambda)$

	Group						
	I	II	III	IV	V	VI	VII
β	0°	±10°	±30°	±40°	−10°	±10°	0°
λ	100°	100°	100°	100°	160°	130°	130°
No. of regions used	11	12	10	11	10	9	11
$\delta^2(\beta)$	0.092	0.075	0.030	0.020	0.082	0.100	0.126

by virtue of definitions (64), our freedom in assigning values to q_2 for a given q_1 is strictly limited; for the inequality

$$q_1^2 \leqslant q_2 < q_1 \quad (65)$$

is a consequence of the definitions of these quantities only. And, moreover, the equality between q_1^2 and q_2 can occur only when all the clouds are equally transparent with a factor q_1. It may also be noted in this connection that, according to equation (63),

$$\delta^2(\xi) \to \frac{(1-q_1)(q_1-q_2)}{1-q_2} \quad \text{as} \quad \xi \to \infty \quad (66)$$

and

$$\delta^2(\xi) \to 0 \quad \text{as} \quad \xi \to 0.$$

For a comparison of the observed values of $\delta^2(\beta)$ with the theoretical predictions based on equation (63), we require a knowledge of the three parameters, ξ, q_1, and q_2, which the theoretical expression for $\delta^2(\xi)$ involves. However, of the three parameters, ξ and q_1 are not independent if we make use of the results of the counts of extragalactic nebulae.[8] According to these latter counts, the mean photographic absorption, $\Delta m(\beta)$, in the direction of galactic latitude β is given by

$$\Delta m(\beta) = 0^m.25 \operatorname{cosec} \beta. \quad (67)$$

If τ is the mean absorption, in magnitudes, per cloud, the number of clouds to be expected, on the average, in the direction β is

$$\xi = \frac{0^m.25\,|\operatorname{cosec}\beta|}{\tau}. \quad (68)$$

[8] E. P. Hubble, *Ap. J.*, **79**, 8, 1934.

But, by definition, τ is related to $\bar{q} = q_1$ by the equation

$$\tau = -2.5 \log q_1 . \tag{69}$$

Hence

$$\xi(\beta) = -0.1 \frac{|\operatorname{cosec} \beta|}{\log q_1} . \tag{70}$$

Consequently, for any assigned value of q_1, we can determine the average number of clouds in the direction β. Values of ξ derived in this fashion for three assigned values of q_1 (0.75, 0.80, and 0.85) are listed in Table 2.

TABLE 2

AVERAGE NUMBER OF CLOUDS IN DIRECTION OF GALACTIC LATITUDE β FOR THREE ASSIGNED VALUES OF q_1

q_1	τ (MAG.)	ξ			
		$\beta = 0°$	$\beta = \pm 10°$	$\beta = \pm 30°$	$\beta = \pm 40°$
0.75	0.31	∞	4.61	1.60	1.24
.80	.24	∞	5.94	2.06	1.61
0.85	0.18	∞	8.15	2.83	2.20

In interpreting his deduced values of $\delta^2(\beta)$, Markarian made the assumption that all the clouds are equally transparent. On this assumption, $q_2 = q_1^2$, and $\delta^2(\beta)$ becomes determinate when q_1 is given. However, the expression for $\delta^2(\xi)$, which allows for an arbitrary distribution of q, involves the additional parameter q_2. Accordingly, using equation (63), we have computed $\delta^2(\xi)$ for various values of q_2 and for $q_1 = 0.75$, 0.80, and 0.85, respectively. The results of the calculation are illustrated in the form of curves in Figure 1, *a* ($q_1 = 0.75$), *b* ($q_1 = 0.80$), and *c* ($q_1 = 0.85$).

To appreciate what latitude we have for changing q_2 for a given q_1 and what a difference in q_2 from q_1^2 means in terms of the distribution of q, we may note that, for the frequency function,

$$\psi(q) = (n+1) q^n \qquad (0 \leqslant q \leqslant 1) , \tag{71}$$

$$q_1 = \frac{n+1}{n+2} , \qquad q_2 = \frac{n+1}{n+3} , \qquad \text{and} \qquad \frac{q_2}{q_1^2} - 1 = \frac{1}{(n+3)(n+1)} . \tag{72}$$

In particular, for $n = 5$,

$$q_1 = 0.857 , \qquad q_1^2 = 0.735 , \qquad q_2 = 0.75 , \qquad \text{and} \qquad \frac{q_2}{q_1^2} - 1 = 0.021 . \tag{73}$$

Accordingly, for $q_1 = 0.85$, a change of q_2 from $(0.85)^2 = 0.7225$ to 0.7325 is by no means an unduly large change. Bearing this in mind, we conclude from an examination of the curves in Figure 1 that the predicted variation of $\delta^2(\xi)$ for a given q_1 depends rather sensitively on q_2; indeed, it would appear that relatively slight changes in q_2 (keeping q_1 fixed) affect $\delta^2(\xi)$ almost as much as quite appreciable changes in q_1 (keeping $q_2 = q_1^2$). This is a somewhat unexpected result disclosed by the present analysis.

In Figure 1, *a*, *b*, and *c* we have plotted the observed values of $\delta^2(\beta)$ against the ξ's appropriate for the values of q_1 to which each of the figures refers (cf. Table 2). It is seen that, with the present data, we cannot distinguish in a unique manner the different effects of q_1 and q_2. However, it does appear that

$$q_1 = 0.85 \qquad \text{and} \qquad q_2 = 0.7325 \tag{74}$$

give the best fit with the observations. It is of interest to recall in this connection that, on the balance of all the evidence available, Markarian favored[9] the acceptance of a value of $q_1 = 0.85$, though the agreement of his observed points with the curve $q_1 = 0.75$ and $q_2 = q_1^2 = 0.5625$ is definitely better than with the curve $q_1 = 0.85$ and $q_2 = q_1^2 = 0.7225$ (cf. Fig. 1, *a* and *c*).

While the values derived for q_1 and q_2 (eq. [74]) are uncertain, it is nevertheless of some interest to observe that these values correspond to a root-mean-square deviation of 0.1 in q. A variation in q of this amount (i.e., ± 0.1) about the mean value $q_1 = 0.85$ corresponds to a variation in the true optical thicknesses of interstellar clouds in the range

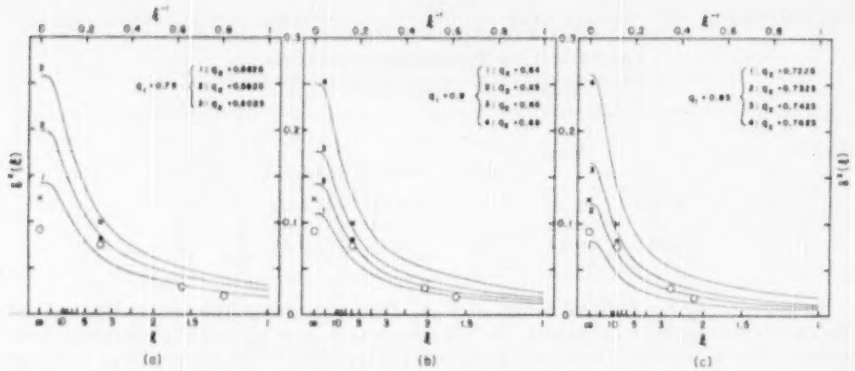

FIG. 1.—The transparency factor q of the interstellar clouds as derived from the observed dispersion in the brightness of the Milky Way at various galactic latitudes. The curves represent the predicted variation of the dispersion $\delta^2(\xi)$ with the average number of absorbing clouds, ξ, in the line of sight for various values of the mean (q_1) and mean square (q_2) of the transparency factor of the clouds. The different sets of curves are for different values of q_1 (0.75 in *a*; 0.80 in *b*; and 0.85 in *c*), the parameter distinguishing the curves in each set being q_2. The lowest curve in each is for the case in which all the clouds are equally transparent and $q_2 = q_1^2$.

The dispersion of the observed brightness of the Milky Way, $\delta^2(\beta)$, at various galactic latitudes can be represented as a variation with ξ if a value of q_1 is assumed (cf. eq. [70]). The values of $\delta^2(\beta)$ deduced by Markarian are plotted in the figure against the ξ's appropriate for each figure (cf. Table 2). The crosses, the open circles, and the solid dots refer to the regions centered at $\lambda = 130°$, $\lambda = 100°$, and $\lambda = 160°$, respectively.

0.29 and 0.05; a variation in the absorptive power of clouds of this amount is entirely reasonable.

Again, if we assume that the average photographic extinction coefficient is 2 mag. per kiloparsec,[10] then we shall need an average of 10–11 clouds per kiloparsec. This estimate is not necessarily in discord with the usual estimate[11] of 7 clouds per kiloparsec; for it may be estimated that a dispersion of 0.1 in q means that about three-fourths of all the clouds (i.e., 7 or 8 in the present instance) will have values in the range 0.75–0.95 and it is possible that the few dense clouds, recognized as such, are not included in the general survey. In any case the present rediscussion of Markarian's example would seem to indicate that a great deal of information concerning the interstellar clouds can be derived by an extension of the basic observational material and their discussion along the lines of this paper.

[9] This value of q_1 is also favored by L. Spitzer, *Ap. J.*, **108**, 276, 1948, esp. p. 278.

[10] H. van de Hulst, *Rech. Astr. Obs. Utrecht*, Vol. **11**, Part II, 1949.

[11] Cf. Spitzer, *op. cit.*; and B. Strömgren, *Ap. J.*, **108**, 242, 1948.

THE THEORY OF THE FLUCTUATIONS IN BRIGHTNESS OF THE MILKY WAY. II

S. CHANDRASEKHAR AND G. MÜNCH
Yerkes Observatory
Received July 11, 1950

ABSTRACT

In this paper the integral equation governing the fluctuations in brightness of the Milky Way is considered for the case in which the system extends to infinity in the direction of the line of sight. The equation is explicitly solved for the two cases in which all the clouds are equally transparent and when the frequency of occurrence of clouds with a transparency factor q is $(n+1)q^n$. The derived distributions of brightness are illustrated.

1. *Introduction.*—In the preceding paper[1] we derived a general integral equation governing the fluctuations in brightness of the Milky Way resulting from the varying number of absorbing clouds in the line of sight; and we showed how the moments of all orders of the distribution of brightness can be expressed explicitly in terms of the average number of clouds to be expected in the line of sight and the moments of the function giving the frequency of occurrence of clouds with a transparency factor q. While the illustrative example given in Paper I shows that the analysis of the observational material can be carried quite far with the aid of the moment relations only, it is clear that it will be useful to have explicit solutions of the basic integral equation (I, eq. [18]) at least for certain special forms of the frequency function $\psi(q)$ of q. As a preliminary to a general attack on this problem, we shall consider in this paper methods of solving the integral equation for the simpler case in which the system extends to infinity in the direction of the line of sight. In this latter case the equation to be considered is (cf. I, eq. [19])

$$g(u) + \frac{dg}{du} = \int_0^1 \frac{dq}{q}\, g\left(\frac{u}{q}\right) \psi(q)\,. \tag{1}$$

Regarding the solution of this equation, we know that its moments are given by

$$\mu_n = \frac{n!}{\prod_{j=1}^{n} (1 - q_j)}, \qquad q_j = \int_0^1 q^j \psi(q)\, dq\,. \tag{2}$$

This expression for μ_n is obtained by letting $\xi \to \infty$ in the solution given by Paper I, equation (36).

In this paper we shall restrict ourselves to two special forms of $\psi(q)$: the case in which all the clouds are equally transparent and the case in which $\psi(q) = (n+1)q^n$. It will appear that in both these cases equation (1) can be solved explicitly.

2. *The solution for the case in which all the clouds are equally transparent.*—Let q be the constant factor by which a cloud reduces the intensity of the light of the stars immediately behind it. In this case the equation governing $g(u)$ is

$$g(u) + \frac{dg}{du} = \frac{1}{q}\, g\left(\frac{u}{q}\right); \tag{3}$$

[1] See p. 380 of this issue; hereafter this paper will be referred to as "Paper I."

and its moments are given by

$$\mu_n = \frac{n!}{\prod_{j=1}^{n}(1-q^j)}. \tag{4}$$

The form of equation (3) suggests that we seek a solution as a Dirichlet series in the form

$$g(u) = \sum_{k=0}^{\infty} A_k e^{-u/q^k}, \tag{5}$$

where the A_k's are certain constants unspecified for the present. Substituting the foregoing form for g in equation (3) and equating the coefficients of the terms having the same exponential factor, we find

$$A_k\left(1-\frac{1}{q^k}\right) = \frac{A_{k-1}}{q} \qquad (k = 1, \ldots). \tag{6}$$

By repeated applications of the recurrence relation (6), we can express all the coefficients $A_k (k \geqslant 1)$ in terms of A_0. Thus

$$A_k = A_0 \frac{(-1)^k}{q^k} \prod_{j=1}^{k} \frac{q^j}{1-q^j} \qquad (k = 1, \ldots). \tag{7}$$

The constant A_0 itself is left arbitrary.

With the constants A_k given by equation (7), the solution for $g(u)$ takes the form

$$g(u) = A_0 \sum_{k=0}^{\infty} \frac{(-1)^k}{q^k} \prod_{j=1}^{k} \frac{q^j}{1-q^j} e^{-u/q^k}. \tag{8}$$

The constant A_0 in solution (8) can be determined by evaluating the moments of the solution and comparing them with equation (4). For $g(u)$ given by equation (8),

$$\mu_n = A_0 \sum_{k=0}^{\infty} \frac{(-1)^k}{q^k} \prod_{j=1}^{k} \frac{q^j}{1-q^j} \int_0^{\infty} e^{-u/q^k} u^n du, \tag{9}$$

or

$$\mu_n = n! A_0 \sum_{k=0}^{\infty} (-1)^k \prod_{j=1}^{k} \frac{q^{j+n}}{1-q^j}. \tag{10}$$

The infinite sum which occurs on the right-hand side of equation (10) can be expressed as an infinite product by using the identity

$$\prod_{j=1}^{\infty}(1-xq^{n+j}) = \sum_{k=0}^{\infty}(-1)^k x^k \prod_{j=1}^{k} \frac{q^{j+n}}{1-q^j}. \tag{11}$$[2]

This identity can be established by considering the function

$$\phi(x) = \prod_{j=1}^{\infty}(1-xq^{n+j}) \qquad (q<1), \tag{12}$$

[2] Identities similar to this one will be found in G. H. Hardy and E. M. Wright, *An Introduction to the Theory of Numbers* (Oxford: Clarendon Press, 1945), p. 275.

which satisfies the functional equation,

$$\phi(x) = (1 - xq^{n+1})\,\phi(xq). \tag{13}$$

Thus, expanding both sides of equation (13) by Taylor's series, we have

$$\sum_{k=0}^{\infty} \phi^{(k)}(0)\,\frac{x^k}{k!} = (1 - xq^{n+1}) \sum_{k=0}^{\infty} \phi^{(k)}(0)\,\frac{(xq)^k}{k!}, \tag{14}$$

where $\phi^{(k)}(0)$ denotes the value of the kth derivative of $\phi(x)$ at $x=0$. Comparing the coefficients of x^k on either side of equation (14), we obtain the recurrence relation,

$$(1 - q^k)\,\phi^{(k)}(0) = -kq^{k+n}\phi^{(k-1)}(0) \qquad (k = 1, \ldots). \tag{15}$$

By repeated applications of this relation and remembering that $\phi(0) = 1$, we find that

$$\phi^{(k)}(0) = (-1)^k k! \prod_{j=1}^{k} \frac{q^{j+n}}{1 - q^j} \qquad (k = 1, \ldots). \tag{16}$$

Hence

$$\begin{aligned} \phi(x) &= \sum_{k=0}^{\infty} \phi^{(k)}(0)\,\frac{x^k}{k!} \\ &= \sum_{k=0}^{\infty} (-1)^k x^k \prod_{j=1}^{k} \frac{q^{j+n}}{1 - q^j}. \end{aligned} \tag{17}$$

This is the required identity.

Setting $x = 1$ in the identity we have just established, we have

$$\prod_{j=1}^{\infty} (1 - q^{n+j}) = \sum_{k=0}^{\infty} (-1)^k \prod_{j=1}^{k} \frac{q^{j+n}}{1 - q^j}. \tag{18}$$

The quantity on the right-hand side of this equation is the same as that which occurs in equation (10). Hence

$$\mu_n = n!\,A_0 \prod_{j=1}^{\infty} (1 - q^{j+n}) = n!\,A_0 \prod_{j=n+1}^{\infty} (1 - q^j). \tag{19}$$

Comparing this expression for μ_n with that given by equation (4), we observe that, for agreement, we must choose

$$A_0 = \frac{1}{\prod_{j=1}^{\infty} (1 - q^j)}. \tag{20}$$

The fact that the value of A_0 determined in this fashion is independent of the order of the moment μ_n which we have chosen to compare provides the verification that the assumed form of the solution leads to the correct one.

With A_0 given by equation (20), the complete solution for $g(u)$ takes the form

$$g(u) = \frac{1}{\prod_{j=1}^{\infty} (1 - q^j)} \sum_{k=0}^{\infty} (-1)^k \frac{e^{-u/q^k}}{q^k} \prod_{j=1}^{k} \frac{q^j}{1 - q^j}. \tag{21}$$

The solution represented by series (21) is fairly rapidly convergent; though, for q approaching unity, larger and larger numbers of terms in the series must be included in an accurate numerical evaluation of $g(u)$.

Solutions for $g(u)$ for various values of q computed in accordance with equation (21) are given in Table 1; they are further illustrated in Figure 1.

TABLE 1

THE FUNCTION $g(u)$ FOR VARIOUS VALUES OF q

u	$g(u)$			u	$g(u)$		
	$q=0.5$	$q=0.6$	$q=0.7$		$q=0.75$	$q=0.80$	$q=0.85$
0.00	0	0	0	0.0	0	0	0
0.25	0.0220	0.0008	.....	0.5	0.0002	.....	.....
0.50	.1526	.0260	0.0005	1.0	.0038	0.0001	.....
0.75	.3163	.1072	.0098	1.5	.0437	.0030	.....
1.00	.4207	.2168	.0323	2.0	.1323	.0238	.....
1.25	.4547	.3124	.0838	2.5	.2308	.0767	0.0059
1.50	.4395	.3718	.1469	3.0	.2891	.1511	.0202
1.75	.3944	.3934	.2126	3.5	.2955	.2186	.0444
2.00	.3416	.3857	.2711	4.0	.2640	.2573	.0888
2.25	.2887	.3570	.3009	4.5	.2250	.2617	.1403
2.50	.2378	.3184	.3289	5.0	.1638	.2395	.1864
2.75	.1930	.2760	.3296	5.5	.1206	.2025	.2163
3.00	.1552	.2341	.3168	6.0	.0831	.1611	.2258
3.50	.0982	.1608	.2654	6.5	.0565	.1222	.2166
4.00	.0611	.1060	.2031	7.0	.0376	.0893	.1942
4.50	.0376	.0679	.1463	7.5	.0246	.0633	.1648
5.00	.0230	.0429	.1009	8.0	.0159	.0438	.1335
5.50	.0137	.0267	.0675	8.5	.0101	.0297	.1042
6.00	.0085	.0165	.0442	9.0	.0064	.0198	.0787
6.50	.0050	.0102	.0284	9.5	.0040	.0130	.0580
7.00	.0031	.0062	.0180	10.0	.0025	.0085	.0416
7.50	.0019	.0039	.0113	10.5	.0016	.0054	.0293
8.00	.0012	.0024	.0071	11.0	.0010	.0035	.0203
8.50	.0007	.0014	.0044	11.5	.0006	.0022	.0138
9.00	0.0004	0.0008	0.0027	12.0	0.0004	0.0014	0.0093

3. *The solution for the case* $\psi(q) = (n+1)q^n$.—Considering equation (1) quite generally and applying to it a Laplace transformation, we obtain

$$(s+1)G(s) = \int_0^1 dq\,\psi(q) \int_0^\infty \frac{du}{q}\, g\left(\frac{u}{q}\right) e^{-su}, \tag{22}$$

where

$$G(s) = \int_0^\infty g(u)\, e^{-su} du \tag{23}$$

denotes the Laplace transform of $g(u)$. The quantity on the right-hand side of equation (22) can also be expressed in terms of $G(s)$; for

$$\int_0^\infty \frac{du}{q}\, g\left(\frac{u}{q}\right) e^{-su} = \int_0^\infty dx\, g(x)\, e^{-sqx} = G(sq). \tag{24}$$

Equation (22) can therefore be written in the form

$$(s+1)G(s) = \int_0^1 dq\psi(q)G(sq). \tag{25}$$[3]

Solutions of this equation must be sought which satisfy the boundary condition,

$$G(0) = \int_0^\infty g(u)\,du = 1. \tag{26}$$

For the case

$$\psi(q) = (n+1)\,q^n, \tag{27}$$

equation (25) becomes

$$(s+1)G(s) = (n+1)\int_0^1 G(sq)\,q^n dq. \tag{28}$$

Letting $x = sq$ as the variable of integration on the right-hand side, we have

$$(s+1)G(s) = \frac{n+1}{s^{n+1}}\int_0^s G(x)\,x^n dx. \tag{29}$$

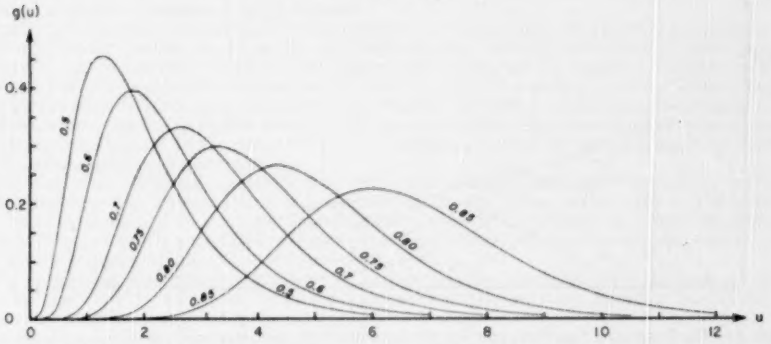

FIG. 1.—The frequency functions $g(u)$ for the case in which all the clouds are equally transparent. The different curves are labeled by the values of q to which they refer.

From this equation we derive

$$\frac{d}{ds}[s^{n+1}(s+1)G(s)] = (n+1)\,s^n G(s). \tag{30}$$

[3] For the case in which q takes only one discrete value, eq. (25) reduces to

$$(s+1)G(s) = G(sq).$$

The solution of this equation satisfying the boundary condition (26) is clearly

$$G(s) = \frac{1}{\prod_{n=0}^{\infty}(1+sq^n)}.$$

The inverse Laplace transform of $G(s)$ given by the foregoing equation can be found in accordance with the standard formula,

$$g(u) = \frac{1}{2\pi i}\int_{-i\infty}^{i\infty} e^{isu}\prod_{n=0}^{\infty}(1+sq^n)^{-1}.$$

The complex integral on the right-hand side can be evaluated by the method of residues and leads to the same solution as the one we derived by more elementary methods in § 2.

On further reduction, equation (30) becomes

$$(n+2)G(s) + (s+1)\frac{dG}{ds} = 0. \tag{31}$$

The solution of this equation satisfying the boundary condition (26) is

$$G(s) = \frac{1}{(s+1)^{n+2}}. \tag{32}$$

The inverse Laplace transform of this elementary function is known, and we have

$$g(u) = \frac{1}{\Gamma(n+2)} e^{-u} u^{n+1}. \tag{33}$$

This function is properly normalized, and it can be verified that the moments of equation (33) are in agreement with those predicted by equation (2).

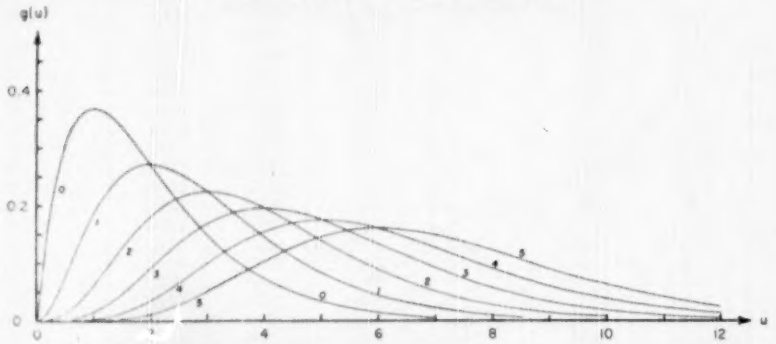

FIG. 2.—The frequency functions $g(u)$ for the case in which the occurrence of clouds with the transparency factor q is governed by $(n+1)\,q^n$. The different curves are labeled by the values of n to which they refer.

The family of frequency functions represented by equation (33) is illustrated in Figure 2. We notice the general similarity of the functions illustrated in Figures 1 and 2. However, in comparing the two sets of curves, it should be noted that, for the frequency function (27),

$$q_1 = \bar{q} = \frac{n+1}{n+2} \quad \text{and} \quad q_2 = \overline{q^2} = \frac{n+1}{n+3}. \tag{34}$$

Accordingly, the functions for the larger values of n should be compared with those for q approaching unity when q occurs with only one given value. And, when we make such a comparison, we observe that there are certain differences between the two sets of curves, which we may trace to the occurrence of clouds with varying absorptive power. Thus, comparing curves which correspond to the same mean value of q (for example, the curve for $q = 0.85$ in Fig. 1 and the curve for $n = 5$, $q_1 = 0.857$, in Fig. 2), we may conclude that the effect of a dispersion in q is to make the frequency function broader with excess both for large and for small values of u.

ON THE DOPPLER BROADENING OF ABSORPTION LINES BY TURBULENCE AND BY MULTIPLE INTERSTELLAR CLOUDS

SU-SHU HUANG
Yerkes Observatory
Received August 10, 1950

ABSTRACT

The influence of turbulence on an absorption line is studied in a way similar to that customarily used in treating the influence of thermal motions on the line. A mean line-absorption coefficient for the turbulent absorbing gas is first calculated on the assumption of various distribution functions for eddy velocities. Mathematically, all these cases lead to series expansions in terms of the same functions with different numerical coefficients. As in the case in which there is no turbulence, the mean line-absorption coefficient in a turbulent gas can be separated into two parts: one referring to the core of a line and the other to the wings. It is shown that the effect of turbulence in the wings is negligible; the damping part of the curve of growth is therefore unchanged by its presence.

Following a general treatment of the effects of turbulence, line profiles and curves of growth have been computed both for the case of a δ-function distribution of eddy velocities (which is equivalent to a step-function distribution of velocities in the line of sight) and for the case of a Gaussian distribution of eddy velocities. Both kinds of profiles and curves of growth are plotted in units of the pure thermal Doppler width for the same values of mean-square eddy velocities. In the case of the Gaussian distribution of eddy velocities, we can obtain line profiles and curves of growth from the original profiles and curves of growth by a mere change of scale. In the case of the δ-function distribution, the calculation can also be simplified, and the series expansion is not required.

The result of the numerical computation shows that a weak line that has been broadened by turbulence is much shallower than a strong line. It is also found that the flat portion of the curve of growth derived from the δ-function distribution is much lower than that derived from the Gaussian distribution. Thus it is concluded that, unless the real distribution function of eddy velocities is known, the value of the turbulent velocity derived from the curve of growth is uncertain.

The broadening of an absorption line by multiple interstellar clouds occurs in the same manner as does the broadening by turbulence; hence the line profiles and the curves of growth of interstellar lines are given directly by the present method.

I. INTRODUCTION

Since the discovery of turbulence in the atmospheres of supergiant stars by O. Struve and C. T. Elvey,[1] a number of investigations[2] has been carried out in this field. And more recently in explaining the spectrum of δ Canis Majoris, Unsöld and Struve[3] have called attention to the importance of the role played by macroscopic turbulence in the formation of absorption lines in stellar atmospheres, and they expressed it in terms of a broadening function of Gaussian form superimposed on an initial line contour.

In this paper we shall consider this problem from a somewhat different point of view. In contrast to Unsöld and Struve, who attacked the problem of the line profile formed in a stellar atmosphere directly, by introducing a broadening function, we shall consider, quite generally, the manner in which we may expect the line-absorption coefficient to be influenced by turbulence. The difference between these two approaches will be made apparent, and in the next paper[4] we shall combine these two kinds of broadening to explain the conflicting data on turbulence in stellar atmospheres.

[1] O. Struve, *Proc. Nat. Acad. Sci. Washington*, **18**, 585, 1932; *Ap. J.*, **79**, 409, 1934.

[2] E.g., O. Struve, *Ap. J.*, **104**, 138, 1946; H. R. Steel, *Ap. J.*, **102**, 43, 429, 1945; L. Goldberg, *Ap. J.*, **89**, 623, 1939; J. L. Greenstein, *Ap. J.*, **95**, 161, 1942; K. O. Wright, *J.R.A.S. Canada*, **40**, 183, 1946, and **41**, 49, 1947; R. B. King and K. O. Wright, *Ap. J.*, **106**, 224, 1947; and K. O. Wright, *Pub. Dom. Ap. Obs. Victoria*, Vol. **8**, No. 1, 1948.

[3] *Ap. J.*, **110**, 455, 1949.

[4] *Ap. J.*, **112**, 418, 1950; hereafter cited as "Paper II."

The plan of this paper is as follows: first, the line-absorption coefficient for various cases of the turbulent velocity distribution is calculated. Then, for the ideal case in which the spectral lines are formed in an absorbing tube, both the line profiles and the curve of growth are computed and drawn. It will appear that the manner of our treatment of broadening by turbulence can be directly applied also to the case of the broadening of interstellar lines by multiple clouds.

II. GENERAL DISCUSSION ON THE LINE ABSORPTION DUE TO THE DOPPLER EFFECT

There are two ways in which the Doppler effect can influence a spectral line. One is that in which the various parts of an absorbing gas act independently, without any interference. An example of this is provided by the effect of stellar rotation on the spectral line. The characteristic feature of this and similar examples is that the absorbing medium moves as a whole relative to the source of radiation (photosphere) or observer. Thus, in passing through the reversing layer, continuous radiation from the photosphere is absorbed by a layer of gas with uniform velocity (apart from thermal motion) and will never be absorbed again by another part of gas with a different velocity. The mean line-absorption coefficient, therefore, does not change; in consequence, the line becomes broadened, but its equivalent width remains unchanged. Hence in this case the profile of every spectral line is completely and uniquely defined by a single broadening function (normalized to unity) and by its original contour.

On the other hand, if between the source of radiation and the observer there is an absorbing medium with a nonuniform motion, the beam of light coming from the source can be absorbed once, twice, etc., by atoms having different velocities. The mean line-absorption coefficient will therefore be changed by the Doppler effect. An example of such a case is provided by thermal broadening; and, as is well known, thermal motion not only broadens a line but also augments its equivalent width. In this case the relation between the final line contour and the original one is no longer uniquely determined by a single broadening function but depends on the number of absorbing atoms as well.

The difference between the two types of Doppler broadening which we have described arises from the uniformity or otherwise of the relative motion of the absorbing medium with respect to the source and the observer. And we may ask to which of the two types broadening by turbulence belongs. Both views have been advanced regarding the nature of turbulent broadening; each will be true in certain limiting cases. If the smallest turbulent eddy present has a linear dimension greater than the depth of the reversing layer, the resulting broadening will behave exactly like broadening by rotation. (We shall call this the "first limiting case of broadening by turbulence.") On the other hand, if the linear dimension of the largest eddy is smaller than the depth of the reversing layer, the turbulent motion will have the same effect on the absorption lines as thermal motion has. (We shall call this the "second limiting case of turbulent broadening.") In practice, both these effects will be simultaneously present. Unsöld and Struve, by assuming macroscopic turbulence on a very large scale, solved the problem of the first limiting case of turbulence in stellar atmospheres. They used a broadening function of Gaussian form; this has recently been verified by measurements of the big eddies on the solar surface by R. S. Richardson and M. Schwarzschild.[6] As we have stated, this limiting case has no effect on the equivalent width and hence will not change the curve of growth. The idea of the second limiting case has been widely used since the time when turbulence in stellar atmospheres was first discovered.

As the first limiting case has been fully worked out, in this paper we shall examine in detail the second limiting case, and, combining the results of the two cases, we can visualize the intermediate case. Thus the results on the curve of growth derived for the second limiting case will be directly applicable to the intermediate case, while the line

[6] *Ap. J.*, **111**, 351, 1950.

profile derived from the second limiting case should be further broadened by a broadening function characterizing the first limiting case. How much this broadening function will affect the line profile depends on the relative importance of eddies with sizes larger than the thickness of the reversing layer, compared with that of smaller ones.

Now consider the interstellar lines produced by multiple clouds. As the peculiar velocities of the clouds are different from one another, the effect on the line absorption will be to disperse the thermal velocities relative to the observer. Hence a mean line-absorption coefficient can be introduced to calculate both the profile and the equivalent width of an interstellar line, provided that the mean value is taken with respect both to the thermal distribution inside a cloud and to the relative velocity distribution of the clouds themselves. Thus we see that both turbulence and the multiple nature of interstellar clouds can be treated in the same way; i.e., the effect of both is to redistribute the velocities and thus to change the shape of the mean atomic line-absorption coefficient. It is therefore necessary for us to consider, first, the distribution of the eddy velocities in a turbulent fluid and the residual velocities of clouds in interstellar space.

III. THE VELOCITY DISTRIBUTION OF THE EDDIES

In the subsequent discussion we shall restrict ourselves to eddies with a linear dimension less than the thickness of the reversing layer. This is equivalent to assuming that the eddies with sizes greater than the thickness of the reversing layer have negligible velocities. Now the convection zone under the atmosphere supplies energy to the eddies of sizes comparable to the thickness of the atmosphere; and, according to current ideas, we may expect that a hierarchy of eddies with smaller and smaller sizes will be formed inside these larger eddies. The energy supplied to the large eddies by the thermal instability will flow down the hierarchy of the intermediate eddies and will finally be dissipated by the small eddies by viscosity. Mathematically, this hierarchy of eddies can be represented by a spectrum of turbulence. For a general review of these ideas we may refer to S. Chandrasekhar's Russell Lecture.[6] In the equilibrium region (i.e., the so-called "Kolmogoroff region"), where the eddies principally transfer energy to smaller eddies and where the statistical theory of turbulence holds, the spectrum of turbulence follows a power law. This suggests at once the possibility of computing the distribution of velocities ξ_k among the eddies with different sizes, $1/k$. Thus let $p(k)dk$ be the probability of finding an eddy with a wave number between k and $k + dk$. We have, by the definition of the spectrum function $F(k)$, the following equation:

$$F(k)\,dk = \tfrac{1}{2}\xi_k^2 p(k)\,dk\,. \tag{1}$$

If, as we have mentioned earlier,

$$F(k) = k^{-n}\,, \tag{2}$$

from equation (1) it follows that

$$p(k)\,dk = \frac{dk}{k}\,. \tag{3}$$

In order to express this result in terms of the velocity, we shall let $P(\xi_k)$ be the probability that an eddy with a mean velocity between ξ_k and $\xi_k + d\xi_k$ occurs. Then the relation

$$p(k)\,dk = P(\xi_k)\,d\xi_k \tag{4}$$

leads directly to the normalized distribution function,

$$P(\xi_k) = \frac{1}{\xi_k \log\,(\xi_0/\xi_a)}\,, \tag{5}$$

[6] *Ap. J.*, **110**, 329, 1949.

where ξ_0 and ξ_s represent the upper and the lower cutoff limits, respectively.

At this point we shall make an estimate of the size of the eddies which are present in stellar atmospheres. From Chandrasekhar's recent work[7] we know that

$$\frac{k_s}{k_0} = 0.2R^{3/4}, \tag{6}$$

where k_s and k_0 are the cutoff wave numbers at the upper and the lower limits of the Kolmogoroff spectrum. When the equilibrium spectrum prevails, we have

$$\frac{k_s}{k_0} = \left(\frac{\xi_0}{\xi_s}\right)^3. \tag{7}$$

Also the Reynolds number R is given by

$$R = \frac{\rho l v}{\mu}. \tag{8}$$

Here ρ is the density, l the linear dimension of the system, v the velocity, and μ the coefficient of viscosity. The velocity v may represent the differential rotation, the convective motion due to various causes, or whatever motion originates the turbulence. To see the order of magnitude of R in stellar atmospheres, we shall use the well-known formula for μ, given by the kinetic theory of gases, namely,

$$\mu = \tfrac{1}{3}\rho\lambda\bar{v}_t, \tag{9}$$

where the mean free path λ can be expressed in terms of the diameter σ of particles and the number n of particles per unit volume, in the form

$$\lambda = \frac{1}{n\pi\sigma^2\sqrt{2}},$$

and $\bar{v}_t$ represents the mean thermal velocity. It follows from equations (8) and (9) that

$$R = \frac{3lv}{\lambda\bar{v}_t}.$$

As l/λ does not vary greatly from a supergiant star to a star of the main sequence, the Reynolds number in stellar atmospheres depends mainly on the relative magnitude of the turbulent velocity and the thermal velocity. Using solar values ($n = 10^{16}/\text{cm}^3$, $l = 10^7$ cm, $\sigma = 10^{-8}$ cm) for computing $3l/\lambda$, we have

$$R = 10^8\frac{v}{\bar{v}_t}.$$

Hence from equation (6) the size of the smallest eddy l_s is given by

$$l_s = \frac{1}{k_s} = \frac{5}{R^{3/4}k_0} = 5\times 10^{-4}l\left(\frac{\bar{v}_t}{v}\right)^{3/4}. \tag{10}$$

Unfortunately, the velocity distribution which will actually show up in the absorption line will not be so simple as that given in equation (5). As the big eddies[8] with their relatively higher velocities carry the smaller ones with them, they are the most effective

[7] *Proc. R. Soc. London*, *A*, **200**, 20, 1949.

[8] Here and elsewhere in the present paper by "big eddies" we mean an eddy which has a linear dimension of the same order of magnitude as, but smaller than, the thickness of the reversing layer.

as far as the Doppler broadening is concerned. The velocity of the smaller eddies appears only as a fluctuation about the mean velocity of the big eddies. But we have no information about the behavior of the big eddies (with sizes larger than $1/k_0$). The statistical theory of turbulence which has been successfully worked out for the equilibrium region in the turbulent spectrum fails to treat the big eddies. In fact, the spectrum of the big eddies depends so much on the boundary conditions and the manner in which the energy is supplied that a *general* theory of the big eddies cannot be given. Only after we know completely the mechanism of the creation of turbulence in stellar atmospheres can we develop a theory of the big eddies for each individual set of boundary conditions. That these conditions are deciding factors for the eddies that we actually observe may be seen also from the fact that the turbulence in the solar atmosphere is observed to have a nonisotropic nature.[9] All that we can do now is to guess physically the plausible distributions that the velocities of the big eddies may have. From among all simple distributions, we shall choose the δ-function and the Gaussian function as examples for computation. As we shall see later that a δ-function distribution of space velocities is equivalent to a step-function distribution in velocities in the line of sight, this distribution has an abrupt cutoff at a certain velocity. The Gaussian function, on the other hand, gives velocities extending to infinity. The actual distribution is likely to be intermediate between these two. A comparison of our results with the observed data would therefore give us some general information about the turbulence in stellar atmospheres.

In what follows we shall begin with a general consideration of Doppler broadening by turbulence, without limiting ourselves to these two special distributions. Then after the general treatment we shall discuss these special distributions individually.

IV. THE PROBABILITY DISTRIBUTION OF VELOCITIES IN THE LINE OF SIGHT

The distribution function $P(\xi)d\xi$ as defined in Section III applies to the magnitude of the velocity ξ only. As these velocities are orientated at random, we have first to derive the probability distribution of the velocity component in the line of sight (say, the X-direction) before we can average the line-absorption coefficient. Let θ be the angle that the velocity vector makes with the X-axis; then

$$\xi_x = \xi \cos\theta . \tag{11}$$

The probability distribution $f(\xi_x)d\xi_x$ of ξ_x is given by

$$f(\xi_x)\, d\xi_x = \tfrac{1}{2}\int P(\xi) \sin\theta d\xi d\theta ; \tag{12}$$

this follows directly from the standard method of transforming the probability function from one physical variable into another related variable. We may write equation (12) simply as

$$f(\xi_x) = \tfrac{1}{2}\int P(\xi)\frac{d\xi}{\xi}. \tag{13}$$

The calculation of $f(\xi_x)$ according to equation (13) for a given $P(\xi)$ is straightforward. A list of various possibilities is given in Table 1. In this table c_n and b_n simply represent normalizing factors, thus

$$c_n = \frac{n-1}{\xi_s^{-n+1} - \xi_0^{-n+1}} \qquad (n \neq 1),$$

$$c_1 = \frac{1}{\log(\xi_0/\xi_s)},$$

[9] For detailed discussion see Sec. IV of Paper II.

and

$$b_n = \frac{n+1}{\xi_0^{n+1}}.$$

For the constant distribution, the resulting expression for $f(\xi_z)$ includes a term in log ξ_z; however, this function is integrable in spite of its singularity at $\xi_z = 0$.

TABLE 1

PROBABILITY DISTRIBUTION OF VELOCITY COMPONENT

Distribution Function	$P(\xi)$	Range of ξ	$f(\xi_z)$	Range of ξ_z
δ-Function	$\delta(\xi-\xi_0)$	ξ_0	$1/2\xi_0$	$\lvert\xi_z\rvert \leqslant \xi_0$
Gaussian function	$(4j^3/\sqrt{\pi})\xi^2 e^{-j^2\xi^2}$	$0\to\infty$	$(j/\sqrt{\pi})e^{-j^2\xi_z^2}$	$\lvert\xi_z\rvert \leqslant \infty$
Inverse ξ^n $(n<0)$	c_n/ξ^n	$\xi_z\to\xi_0$	$(c_n/2n)[(1/\xi_z^n)-(1/\xi_0^n)]$	$\lvert\xi_z\rvert \leqslant \xi_0$
			$(c_n/2n)[(1/\lvert\xi_z\rvert^n)-(1/\xi_0^n)]$	$\xi_0 \geqslant \lvert\xi_z\rvert \geqslant \xi_s$
Constant	$1/\xi_0$	$0\to\xi_0$	$(1/2\xi_0)\log(\xi_0/\lvert\xi_z\rvert)$	$\lvert\xi_z\rvert \leqslant \xi_0$
ξ^n $(n>0)$	$b_n\xi^n$	$0\to\xi_0$	$(b_n/2n)(\xi_0^n-\lvert\xi_z\rvert^n)$	$\lvert\xi_z\rvert \leqslant \xi_0$

V. THE VELOCITY FLUCTUATIONS OF BIG EDDIES CAUSED BY THE PRESENCE OF SMALL EDDIES

As mentioned earlier, the velocity of the smaller eddies appears as a sort of fluctuation about the mean value of the velocity of the big eddies. If the distribution function of big-eddy velocities may be fairly represented by one of the functions listed in Table 1, the true distribution of turbulent velocities as observed would be the result of a superposition of fluctuations over this function. This is a complicated problem and cannot easily be solved. But on the assumption that the fluctuations behave as a Gaussian error function, the calculation will be much simplified. This is possible because we can then absorb this fluctuation into the thermal motion on account of the additive property of Gaussian functions. Thus, if we let ξ_2 be the final turbulent velocity in the line of sight (i.e., the velocity of big eddy plus the velocity of fluctuation), its probability distribution will be given by

$$W_2(\xi_2)\,d\xi_2 = d\xi_2 \int_{-\xi_0}^{\xi_0} \frac{j_2}{\sqrt{\pi}} f(\xi_z)\, e^{-j_2^2(\xi_2-\xi_z)^2} d\xi_z. \tag{14}$$

The constant j_2 may be a function of k, but, for simplicity, we shall take it as a constant in the subsequent calculation.

The probability distribution, $W_1(\xi_1)d\xi_1$, of the thermal velocity component in the line of sight, ξ_1, is well known:

$$W_1(\xi_1)\,d\xi_1 = \frac{j_1}{\sqrt{\pi}} e^{-j_1^2\xi_1^2} d\xi_1, \tag{15}$$

where

$$\overline{\xi_1^2} = \frac{1}{2j_1^2}, \qquad \overline{|\xi_1|} = \frac{1}{j_1\sqrt{\pi}}.$$

The mean-square velocity of turbulent motion is given by

$$\overline{\xi_2^2} = \frac{1}{2j_2^2} + \overline{\xi_s^2},$$

where

$$\overline{\xi_x^2} = \int_{-\xi_0}^{\xi_0} \xi_x^2 f(\xi_x)\, d\xi_x .$$

Before starting to compute the line-absorption coefficient, it is convenient to transform, first, an integral of the form

$$I_\varphi = \int\int_{-\infty}^{\infty} W_1(\xi_1)\, W_2(\xi_2)\, \varphi(\xi_1 + \xi_2)\, d\xi_1 d\xi_2 , \tag{16}$$

where φ is a function of $\xi_1 + \xi_2$ only, while $W_1(\xi_1)$ and $W_2(\xi_2)$ are given by equations (15) and (14), respectively.

Introducing

$$\xi = \xi_1 + \xi_2 - \xi_x , \tag{17}$$

we can easily transform the integration over ξ_1 and ξ_2 to one over ξ and ξ_1. Then the integration over ξ_1 can be easily effected. If we write

$$\frac{1}{j^2} = \frac{1}{j_1^2} + \frac{1}{j_2^2} , \tag{18}$$

the final result is

$$I_\varphi = \frac{j}{\sqrt{\pi}} \int_{-\xi_0}^{\xi_0} f(\xi_x)\, d\xi_x \int_{-\infty}^{\infty} \varphi(\xi + \xi_x)\, e^{-j^2\xi^2} d\xi . \tag{19}$$

This is the form which will be used later on.

VI. GENERAL CONSIDERATIONS ON THE LINE-ABSORPTION COEFFICIENT

The line-absorption coefficient $k(\nu)$ of an atom at frequency ν is given by

$$k(\nu) = \frac{\pi e^2}{mc} f \frac{2\gamma}{4\pi^2 (\nu - \nu_0)^2 + \gamma^2} , \tag{20}$$

where the various symbols have their usual meanings.[10] Owing to the Doppler effect, an atom moving with a radial velocity $\xi_1 + \xi_2$ gives rise to an absorption line which is shifted by an amount $\nu_0(\xi_1 + \xi_2)/c$ from its position ν_0 at rest. Averaging over all possible velocities of ξ_1 and ξ_2, we have the final expression for the line-absorption coefficient,

$$k(\nu) = \int\int_{-\infty}^{\infty} W_1(\xi_1)\, W_2(\xi_2)\, k\left[\nu - \frac{\nu_0}{c}(\xi_1 + \xi_2)\right] d\xi_1 d\xi_2 , \tag{21}$$

which is evidently of the form given by equation (16). Thus it follows from equation (19) that

$$k(\nu) = \frac{j}{\sqrt{\pi}} \int_{-\xi_0}^{\xi_0} f(\xi_x)\, d\xi_x \int_{-\infty}^{\infty} k\left[\nu - \frac{\nu_0}{c}(\xi + \xi_x)\right] e^{-j^2\xi^2} d\xi . \tag{22}$$

In the usual manner we shall let

$$\frac{\nu_0 \xi}{c} = \Delta\nu_1 , \qquad \frac{\nu_0 \xi_x}{c} = \Delta\nu_2 , \qquad \text{and} \qquad \frac{\nu}{cj} = \Delta\nu_D . \tag{23}$$

[10] For detailed discussion see A. Unsöld, *Physik der Sternatmosphären* (Berlin: J. Springer, 1938). Note also that the γ used here is half the value of the same quantity defined there.

Now, writing

$$y = \frac{\Delta\nu_1}{\Delta\nu_D} = j\xi\,, \qquad z = \frac{\Delta\nu_2}{\Delta\nu_D} = j\xi_z\,, \qquad \nu - \nu_0 = v\Delta\nu_D\,, \qquad \text{and} \qquad a = \frac{\gamma}{2\pi\nu_D}\,, \tag{24}$$

we can rewrite equation (22) in the following form:

$$k(v) = k_0 \frac{a}{\pi} \int_{-z_0}^{z_0} f\left(\frac{z}{j}\right) d\left(\frac{z}{j}\right) \int_{-\infty}^{\infty} \frac{e^{-y^2} dy}{(v - y - z)^2 + a^2}\,, \tag{25}$$

where

$$k_0 = \frac{\sqrt{\pi}\, e^2}{mc} f \frac{1}{\Delta\nu_D} \qquad \text{and} \qquad z_0 = j\xi_0\,. \tag{26}$$

Measuring all velocities in units of $1/j$ and transforming the integral over y in the usual manner,[11] we can express $k(v)$ in the form

$$k(v) = \frac{k_0}{\sqrt{\pi}} \int_0^{\infty} dx\, e^{-(x^2/4 + ax)} \int_{-z_0}^{z_0} f(z) \cos[(v - z)x]\, dz\,. \tag{27}$$

The problem now reduces to the evaluation of this integral for the various distributions $f(z)$ given in Table 1.

For any function $f(z)$ we have

$$\int_{-z_0}^{z_0} f(z) \cos[(v - z)x]\, dz = \cos vx \sum_{n=0}^{\infty} (-1)^n A_{2n} x^{2n}\,, \tag{28}$$

with $A_0 = 1$ in all cases. In Table 2 we list the expansion coefficients A_{2n} for some ex-

TABLE 2

EXPANSION COEFFICIENTS A_{2n} FOR VARIOUS SIMPLE DISTRIBUTION FUNCTIONS
($A_0 = 1$ in All Cases)

Name	A_{2n} $(n \geq 1)$
δ-Function	$\dfrac{z_0^{2n}}{(2n+1)!}$
Inverse ξ^n $\quad n = 1$	$\dfrac{1}{\log(z_0/z_a)} \dfrac{z_0^{2n} - z_a^{2n}}{2n(2n+1)!}$
Inverse ξ^n $\quad n = 2$	$\dfrac{z_0 z_a}{(z_0 - z_a)} \dfrac{z_0^{2n-1} - z_a^{2n-1}}{(2n-1)(2n+1)!}$
Constant	$\dfrac{z_0^{2n}}{(2n+1)(2n+1)!}$
ξ^n $\quad n = 1$	$\dfrac{2 z_0^{2n}}{(2n+2)!}$
ξ^n $\quad n = 2$	$\dfrac{3 z_0^{2n}}{(2n+3)(2n+1)!}$

amples of the distribution functions $f(z)$.

[11] F. Reiche, *Verh. Deutschen phys. Gesellsch.*, **15**, 3, 1913; also see Unsöld, *op. cit.*, p. 161.

In Table 2 we have not listed A_{2n} for the case of a Gaussian distribution because, if the turbulent velocity is distributed in a pure Gaussian form, equation (14) will simply become

$$W_2(\xi_2) = \frac{j_z}{\sqrt{\pi}} e^{-j_z^2 \xi_2^2}. \tag{29}$$

Introducing

$$H_{2n}(v, a) = \frac{1}{\sqrt{\pi}} \int_0^\infty e^{-(x^2/4 + ax)} x^{2n} \cos(vx)\, dx$$

$$= \frac{2^{2n+1}}{\sqrt{\pi}} \int_0^\infty e^{-t^2 - 2at} t^{2n} \cos(2vt)\, dt \tag{30}$$

and using equation (28), we may write equation (27) in the following form:

$$k(v) = k_0 \sum_{n=0}^{\infty} (-1)^n A_{2n} H_{2n}(v, a). \tag{31}$$

Restricting ourselves to the case of small damping (which is usually the case in stellar atmospheres and is always so in the interstellar gas), we have

$$H_{2n}(v, a) = \frac{2^{2n+1}}{\sqrt{\pi}} [k_{2n}(v) - 2aK_{2n+1}(v)] + O(a^2), \tag{32}$$

where

$$K_m(v) \equiv \int_0^\infty e^{-t^2} t^m \cos(2vt)\, dt. \tag{33}$$

Further, let

$$F_m(v) \equiv \int_0^\infty e^{-t^2} t^m \sin(2vt)\, dt. \tag{34}$$

We have,

$$K_0(v) = \int_0^\infty e^{-t^2} \cos(2vt)\, dt = \tfrac{1}{2}\sqrt{\pi}\, e^{-v^2} \tag{35}$$

and

$$F_0(v) = \int_0^\infty e^{-t^2} \sin(2vt)\, dt = e^{-v^2} \int_0^v e^{x^2} dx. \tag{36}$$

The function $F_0(v)$ has been tabulated by W. L. Miller and A. R. Gordon[12] and can be found in any standard book in this field.[13] [It is usually denoted by $F(v)$.] And for $m \geqq 2$ we have the following recurrence formulae:

$$K_m(v) = \tfrac{1}{2}[(m-1) K_{m-2}(v) - 2v F_{m-1}(v)] \tag{37}$$

and

$$F_m(v) = \tfrac{1}{2}[(m-1) F_{m-2}(v) + 2v K_{m-1}(v)]. \tag{38}$$

A few of both functions $K_m(v)$ and $F_m(v)$ are listed in Table 3.

In terms of the K's, equation (31) can be written in the form

$$k(v) = k_0 (X - 2aY), \tag{39}$$

[12] *J. Phys. Chem.*, **35**, 2878, 1931.

[13] E.g., A. C. G. Mitchell and M. W. Zemansky, *Resonance Radiation and Excited Atoms* (Cambridge: At the University Press, 1934).

where

$$X(v) = \frac{2^{2n+1}}{\sqrt{\pi}} \sum_{n=0}^{\infty} (-1)^n A_{2n} K_{2n}(v), \tag{40}$$

$$Y(v) = \frac{2^{2n+1}}{\sqrt{\pi}} \sum_{n=0}^{\infty} (-1)^n A_{2n} K_{2n+1}(v). \tag{41}$$

Like $H_0(v, a)$, which gives the variation of the line-absorption coefficient without the inclusion of the effect of turbulence, each $H_{2n}(v, a)$ as given by equation (32) consists of two terms. The first term is dominant for small values of v, while the other, which represents the damping effect, becomes more and more important as v increases. We shall first investigate the damping term.

TABLE 3

FIRST FEW FUNCTIONS $K_m(v)$ AND $F_m(v)$

m	$K_m(v)$	$F_m(v)$
1	$\frac{1}{2} - vF_0$	$\frac{1}{2}\sqrt{\pi}ve^{-v^2}$
2	$\frac{1}{2}\sqrt{\pi}(1-2v^2)e^{-v^2}$	$\frac{1}{2}[v+(1-2v^2)F_0]$
3	$\frac{1}{4}[(1-v^2)-(3v-2v^3)F_0]$	$\frac{1}{4}\sqrt{\pi}(3v-2v^3)e^{-v^2}$
4	$\frac{1}{4}\sqrt{\pi}(3-12v^2+4v^4)e^{-v^2}$	$\frac{1}{4}[(5v-2v^3)+(3-12v^2+4v^4)F_0]$
5	$\frac{1}{8}[(4-9v^2+2v^4)-(15v-20v^3+4v^5)F_0]$	$\frac{1}{8}\sqrt{\pi}(15v-20v^3+4v^5)e^{-v^2}$

It is well known that $K_1(v)$ behaves like $1/v^2$ as $v \to \infty$. We shall now show that $K_2(v) \sim 1/v^4$. This can be seen when we substitute the expansion

$$F_0(v) = \frac{1}{2v} + \frac{1}{4v^3} + \frac{3}{8v^5} + \frac{15}{16v^7} + \ldots \tag{42}$$

for $F_0(v)$ in $K_2(v)$ as given in Table 3. In general, we can show that $K_{2n+1}(v)$ behaves like $1/v^{2(n+1)}$ as v becomes sufficiently great.

Writing

$$f \equiv K_{2n+1}(v) \qquad \text{and} \qquad g \equiv F_{2n}(v) \tag{43}$$

and differentiating with respect to v, we obtain

$$\frac{df}{dv} + (2n+1)\, g + 2vf = 0 \tag{44}$$

and

$$\frac{dg}{dv} = 2f; \tag{45}$$

or, eliminating g, we have

$$\frac{d^2 f}{dv^2} + 2v\frac{df}{dv} + 4(n+1)\, f = 0. \tag{46}$$

From these equations it follows that, as $v \to \infty$, f has an expansion of the form

$$f = \sum_{m=1}^{\infty} a_m v^{-2(n+m)}, \tag{47}$$

where the coefficients a_m satisfy the recurrence relation

$$\frac{a_{m+1}}{a_m} = \frac{(n+m)\ (2n+2m+1)}{2m}. \tag{48}$$

Hence

$$f = a_1 [\, v^{-2(n+1)} + \tfrac{1}{2}\,(n+1)\ (2n+3)\ e^{-2(n+2)} + \ldots], \tag{49}$$

and

$$g = -\frac{2a_1}{(2n+1)} [\, v^{-(2n+1)} + \ldots]. \tag{50}$$

These equations complete the verification.

For K_{2n} and F_{2n-1} such expansions become impossible because we cannot put an even function of v in terms of odd powers of v and an odd function in terms of even powers.

We have thus proved that the contribution of the higher terms to the damping part $V(v)$ of the line-absorption coefficient given by equation (39) is not important; or, in other words, the existence of turbulence does not affect the form of $k(v)$ as v becomes great. Hence the damping wing of a line profile and the damping branch of the curve of growth are not appreciably affected by the presence of turbulence. This point simplifies our subsequent calculation and also any later theory that may be concerned with the influence of turbulence on the absorption lines.

VII. THE LINE-ABSORPTION COEFFICIENT FOR SOME SPECIAL VELOCITY DISTRIBUTIONS

For actual computation, the series expansion for the line-absorption coefficient developed in the last section converges very slowly, especially for the case in which the turbulent velocity is much higher than the thermal motion. Fortunately, for some special velocity-distribution functions there are special solutions which are very simple to use for purposes of computation. It should first be noted that $H_0(v, a)$ as defined in equation (32) for $n = 0$ can be written in the following form:

$$H_0(v, a) = \frac{a}{\pi} \int_{-\infty}^{\infty} \frac{e^{-y^2} dy}{(v-y)^2 + a^2}. \tag{51}$$

For small a we have, as a first approximation,

$$H_0(v, a) = e^{-v^2} - \frac{2a}{\sqrt{\pi}} [1 - 2v F_0(v)]. \tag{52}$$

Hence we can write equation (25) as

$$k(v) = k_0 \int_{-z_0}^{z_0} f(z) \left[e^{-(v-z)^2} - \frac{2a}{\sqrt{\pi}} \{1 - 2(v-z) F_0(v-z)\} \right] dz. \tag{53}$$

It is this equation that we shall use for the actual computations later on. If, furthermore, we are interested in the Doppler core only, then

$$k(v) = k_0 \int_{-z_0}^{z_0} f(z)\, e^{-(v-z)^2} dz. \tag{54}$$

For some simple forms of $f(z)$, $k(v)$ can be put into the form of an error function, while, for some other functions, $k(v)$ can be numerically integrated quite easily.

We shall start by introducing the error function, $E_2(x)$,

$$E_2(x) = \frac{2}{\sqrt{\pi}} \int_0^x e^{-t^2} dt. \tag{55}$$

Then for

$$f(z) = \frac{1}{2z_0},$$

which corresponds to the δ-function distribution, we have, as a result of some direct transformations, the following expression for $k(v)$:

$$k(v) = \frac{k_0}{z_0}\left[\frac{\sqrt{\pi}}{4}\{E_2(v+z_0) - E_2(v-z_0)\} - \frac{a}{\sqrt{\pi}}\{F_0(v+z_0) - F_0(v-z_0)\}\right]. \quad (56)$$

As both $E_2(x)$ and $F_0(x)$ have been extensively tabulated, $k(v)$ can be calculated to the same degree of exactness and completeness for this case as for the case of pure thermal broadening.

In the case

$$f(z) = \frac{n+1}{2n z_0^{n+1}}(z_0^n - |z|^n),$$

which corresponds to the last column of Table 1, we have

$$k(v) = \frac{n+1}{2n z_0^{n+1}}[M_n(v) - 2aN_n(v)], \quad (57)$$

where

$$M_n(v) = z_0^n \int_{v-z_0}^{v+z_0} e^{-x^2} dx - \left[\int_0^{v+z_0} + (-1)^n \int_{v-z_0}^{v}\right] e^{-x^2}(x-v)^n dx \quad (58)$$

and

$$N_n(v) = \frac{2z_0^n}{\sqrt{\pi}} F_0(v+z_0)\,\delta_{n,\text{odd}} - \frac{n}{\sqrt{\pi}} \int_{v-z_0}^{v+z_0} (v-t)^{n-1} F_0(t)\,dt. \quad (59)$$

For integral values of n, $M_n(v)$ can easily be expressed as a sum of error functions, while $N_n(v)$ can be reduced to an integral of the type $\int_0^t F_0(t)dt$. The expressions for M_n in the cases $n = 1$ and $n = 2$ are given below:

$$M_1 = \tfrac{1}{2}[\sqrt{\pi}(v+z_0)E_2(v+z_0) + \sqrt{\pi}(v-z_0)E_2(v-z_0) - 4vE_2(v) + e^{-(v+z_0)^2} + e^{-(v-z_0)^2} - 2e^{-v^2}],$$

$$M_2 = \tfrac{1}{2}[\sqrt{\pi}(z_0^2 - v^2 - \tfrac{1}{2})\{E_2(v+z_0) - E_2(v-z_0)\} + (v+z_0)e^{-(v-z_0)^2} - (v-z_0)e^{-(v+z_0)^2}].$$

As the damping part of the absorption coefficient is not important in our present problem, the lengthy expressions for $N_n(v)$ will not be given here.

For other distributions it has not proved possible to put $k(v)$ into finite form, and numerical integration becomes necessary. Thus for the inverse ξ^n distribution we have, for the Doppler core,

$$k(v) = k_0 \frac{C_n}{2n}\left[\int_{z_s}^{z_0} z^{-m}\{e^{-(v+z)^2} + e^{-(v-z)^2}\}\,dz - \frac{\sqrt{\pi}}{2} z_0^{-m}\{E_2(v+z_0) - E_2(v-z_0)\} + \frac{\sqrt{\pi}}{2} z_s^{-m}\{E_2(v+z_s) - E_2(v-z_s)\}\right]. \quad (60)$$

Finally, we shall consider a Gaussian distribution of the turbulent velocities. As two Gaussian distributions (i.e., the thermal and the turbulent) combine to form another Gaussian distribution by only a change of scale, the total broadening due to both the turbulent and the thermal motions can be derived from the original pure thermal profile. In the formulae for the line-absorption coefficient, $\nu - \nu_0$ has been measured in units of $\Delta\nu_D = \nu_0/cj$ (see eq. [23]), which is the total Doppler width for both the thermal and the turbulent broadening. In order to compare the final results due to the various velocity-distribution functions, it is necessary to reduce all frequency shifts to the same units, i.e., the Doppler width for the pure thermal broadening $\Delta\nu_{D1}$, which will be defined as

$$\Delta\nu_{D1} = \frac{\nu_0}{c\, j_1}. \tag{61}$$

Let v_1 now denote $\nu - \nu_0$ measured in units of $\Delta\nu_{D1}$; then

$$\nu - \nu_0 = v_1 \Delta\nu_{D1} = v\Delta\nu_D,$$

or

$$v = a\, v_1, \qquad a = \frac{j}{j_1}. \tag{62}$$

In a similar way let a_1 be the damping constant measured in units of $\Delta\nu_{D1}$; thus

$$a = \frac{\gamma}{2\pi\Delta\nu_D} = a\frac{\gamma}{2\pi\Delta\nu_{D1}} = a\, a_1. \tag{63}$$

Finally, because k_0 involves as a factor the Doppler width (see eq. [26]), we shall have

$$k_0\,(\Delta\nu_D) = a\, k_0'\,(\Delta\nu_{D1}). \tag{64}$$

Here j (final), j_1 (thermal), and j_2 (turbulent) are related by equation (18). It is well known that, with a pure Gaussian distribution of velocities in the absorbing gas, the mean line-absorption coefficient is given by

$$k\,(v) = k_0 H_0\,(v,\ a), \tag{65}$$

if v is measured in terms of the total Doppler width, ν_0/cj. Thus, in terms of the new unit—the pure thermal Doppler width, ν_0/cj_1—we have

$$k\,(v_1) = k_0' a\, H_0\,(a\, v_1,\ a\, a_1). \tag{66}$$

Neglecting the damping term, the first approximation is

$$k\,(v_1) = k_0' a\, e^{-(av_1)^2}. \tag{67}$$

If the turbulent velocity distribution consists partly of a Gaussian distribution (fluctuation) and partly of another distribution (mean distribution of the big-eddy velocities), as suggested by equation (14), all results derived from equation (53) should be modified by substituting v_1, a_1, and k_0' for v, a, and k_0 according to equations (62), (63), and (64), respectively.

VIII. APPLICATION TO THE MULTIPLE INTERSTELLAR CLOUDS

In the investigation of the chemical abundances in interstellar space a curve of growth calculated under some assumption is always necessary for comparison with the observed data. The calculation of the curve of growth for the interstellar clouds is somewhat dif-

ferent from the similar calculation for a stellar atmosphere. On the one hand, the problem for interstellar space is somewhat simpler because the damping factor can always be neglected; on the other hand, it is somewhat more difficult because the different clouds moving with random velocities further broaden the line and increase its equivalent width. This difficulty is similar to that of the turbulence complicating the broadening of the absorption line in stellar atmospheres. B. Strömgren[14] first computed the curve of growth for two clouds with different radial velocities by averaging the line-absorption coefficient over the two clouds. On the other hand, L. Spitzer,[15] in deriving the equivalent width for the case of many clouds, averaged directly over the equivalent width itself. It is evident that the problem of broadening by multiple clouds is the same as that treated in the two previous sections of the present paper, because a distribution function $\varphi(\xi)$ of radial velocities of clouds simply takes the place of the distribution function $f(\xi)$ of the turbulent velocity. If inside each cloud there is, furthermore, turbulent motion, then the function $\varphi(\xi)$ takes care both of the residual velocity distribution of individual clouds and of the turbulent velocity distribution inside each cloud. Thus, setting $a = 0$ and replacing $f(\xi)$ by $\varphi(\xi)$ in the equations derived in the previous sections, all the results apply to $k(v)$ in the case of multiple interstellar clouds. In fact, Spitzer used a step-function for $\varphi(\xi)$ which is equivalent, as we have seen, to the δ-function distribution of the magnitude of the space velocity. The only difference between Spitzer's approach and ours lies in the fact that, while he averaged the equivalent width, we have introduced the mean line-absorption coefficient. Physically to average the equivalent width directly is more appropriate than to average the absorption coefficient, if we consider only the equivalent width but not the line profile. However, even in the simplified case considered by Spitzer, some approximations had to be introduced to carry out the calculation. As we shall presently see, the approximations introduced by Spitzer make his results equivalent to averaging the absorption coefficient.

Spitzer assumed a rectangular profile for the spectral line formed by each cloud and a rectangular shape of the velocity distribution of clouds. Thus, letting u denote the distance in angstrom units of a point in the spectrum from the center of the line λ_0, i.e.,

$$u = \lambda - \lambda_0,$$

we have, for the atomic line-absorption coefficient,

$$\begin{aligned} k(u) &= \text{Constant} = k_0, && |u| \leqslant F b_i, \\ &= 0 && |u| > F b_i; \end{aligned} \tag{68}$$

and, for the velocity distribution,

$$\begin{aligned} \varphi(\xi) &= \frac{1}{2\xi_0}, && |\xi| \leqslant \xi_0, \\ &= 0 && |\xi| > \xi_0. \end{aligned} \tag{69}$$

The mean line-absorption coefficient over all the clouds is therefore given by

$$\overline{k(u)} = \frac{1}{2\xi_0} \int_{-\xi_0}^{\xi_0} k\left(u - \frac{\lambda_0}{c}\xi\right) d\xi. \tag{70}$$

Introducing the new variable

$$y = u - \frac{\lambda_0 \xi}{c}$$

and putting

$$\lambda_0 \xi_0 = F b_i c,$$

[14] *Ap. J.*, **108**, 242, 1948. [15] *Ap. J.*, **108**, 276, 1948.

we can write equation (70) in the form

$$\overline{k(u)} = \frac{1}{2Fb_e}\int_{u-Fb_e}^{u+Fb_e} k(y)\,dy\,. \tag{71}$$

Here $k(y)$ is given by equation (68). Thus, for $|u| \leq Fb_e - Fb_i$ and $Fb_e > Fb_i$, the whole range of $k(y)$ which does not vanish lies inside the integration range. Therefore,

$$\overline{k(u)} = k_0\left(\frac{b_i}{b_e}\right), \qquad |u| \leqslant Fb_e - Fb_i\,. \tag{72}$$

If $|u| > Fb_e + Fb_i$, the nonvanishing part of $k(y)$ lies outside the limits of integration; hence

$$\overline{k(u)} = 0\,, \qquad |u| > Fb_e + Fb_i\,. \tag{73}$$

If $u < Fb_i - Fb_e$, the integration limits become $-Fb_i$ and $u + Fb_e$; if $u > Fb_e - Fb_i$, they are $u - Fb_e$ and Fb_i. Both cases lead to the same result, namely,

$$\overline{k(u)} = \frac{k_0}{2Fb_e}(Fb_e + Fb_i - |u|)\,. \tag{74}$$

The equivalent width D of the line formed by n clouds, each with N absorbing atoms, is simply

$$D = \int_{-\infty}^{\infty}(1 - \exp[-nN\overline{k(u)}])\,du\,. \tag{75}$$

Substituting $k(u)$ from equations (72)–(74) in equation (75), we obtain

$$D = 2Fb_e(1 - e^{-x})\left\{1 + \frac{b_i}{b_e}\psi(x)\right\}, \tag{76}$$

where

$$x = nNk_0\left(\frac{b_i}{b_e}\right) \quad \text{and} \quad \psi(x) = \frac{1 + e^{-x}}{1 - e^{-x}} - \frac{2}{x}.$$

This is the same result as that given by Spitzer.

A more general formula for D than that given by equation (76) can be derived by substituting

$$k(v) = k_0\int_{-z_0}^{z_0}\varphi(z)\,e^{-(v-z)^2}dz \tag{77}$$

in equation (75). Assuming a form of $\varphi(z)$, we can solve for $k(v)$ by equation (77) and thus obtain D. No other assumption is required in the present method. If $\varphi(z)$ has a rectangular shape, a better formula for $k(v)$ would be given by equation (56), with $a = 0$. We shall calculate some curves of growth for this case in the next section.

IX. THE IDEALIZED LINE PROFILE AND THE CURVE OF GROWTH

Once the atomic line-absorption coefficient has been computed, the line profile and the curve of growth can be calculated for any desired model. As an illustration we shall consider here only an idealized case in which the spectral line is produced in an absorbing tube. For the reason given in Section VII, the damping part of the absorption coefficient will be omitted in the following calculation.

Let N be the number of absorbing atoms per unit volume and l the length of tube; then we have, for the line profile,

$$A(v) = 1 - e^{-Nlk(v)}\,. \tag{78}$$

Here $k(v)$ is given by equation (53) or an equivalent formula. Writing

$$C = N l k_0' , \tag{79}$$

we have the curve of growth which relates the equivalent width D with C:

$$D(C) = \int_0^\infty A(v)\, dv . \tag{80}$$

If the turbulent velocity follows a Gaussian distribution, the line profile is given by (cf. eqs. [67] and [78])

$$A(v_1) = 1 - \exp[C a e^{-(a v_1)^2}] . \tag{81}$$

The curve of growth in the presence of turbulence, plotted in a log D − log C scale, is thus the same as the curve of growth derived for pure thermal broadening translated in both directions along the co-ordinate axes. This can be easily seen in the following way: From equations (80), (66), and (79) the equivalent width $D(C, a_1, \mathfrak{a})$ is given by

$$D(C, a_1, \mathfrak{a}) = \int_0^\infty [1 - e^{-C a H_0(a v_1,\ \mathfrak{a} a_1)}]\, d v_1 . \tag{82}$$

Let β represent the ratio of mean velocity of turbulence to that of the thermal motion, i.e., j_1/j_2 (hence β is a measure of the strength of turbulence); then $\beta = (1 - \mathfrak{a}^2)^{1/2}/\mathfrak{a}$ because of equations (18) and (62). Hence $\mathfrak{a} = 1$ corresponds to the case in which there exists no turbulence. Thus it follows directly from equation (82) that

$$D(C, a_1, \mathfrak{a}) = \frac{1}{\mathfrak{a}} D(\mathfrak{a} C, \mathfrak{a} a_1, 1) , \tag{83}$$

which proves our statement.

Equation (83) also shows the usual way of determining the turbulent velocity from the flat portion of the curve of growth, because the difference between the ordinate of the two curves of growth at the flat portion is log (j_1/j).

Next we shall consider the case of a pure δ-function distribution of the turbulent velocity without any fluctuations, i.e., $j = j_1$ in equation (22); hence $k_0 = k_0'$. It follows from equations (78) and (56) that the line profile is given by

$$A(v) = 1 - \exp\left[-\frac{\sqrt{\pi}}{4} \frac{C}{z_0} \{ E_2(v + z_0) - E_2(v - z_0) \} \right] . \tag{84}$$

Here z_0, like β in the previous case, is a measure of the strength of turbulence. The method of comparing the parameter β of the one case with the parameter z_0 of the other case will be treated later.

For the equivalent width based upon the line profile (84), no such simple property as that represented by equation (83) for the Gaussian distribution exists. Hence we have to compute the curves of growth for the various values of z_0 separately. However, since to a sufficient accuracy

$$|E_2(x)| \simeq 1, \qquad |x| \geqq 3 , \tag{85}$$

the curve of growth for values of $z_0 \geqq 3$ can be readily computed. Splitting the integration into two parts and introducing the approximation given by equation (85), we have

$$D(C, z_0) = (z_0 - x_0)\, [1 - e^{-C\sqrt{\pi}/2 z_0}] + F(C, z_0) , \tag{86}$$

where

$$F(C, z_0) = \int_{-x_0}^{x_0} \left[1 - \exp\left\{ -\frac{\sqrt{\pi}}{4} \frac{C}{z_0} [1 - E_2(v)] \right\} \right] d v . \tag{87}$$

Let

$$z_0 = n x_0 \qquad (n \geqq 1) \ ;$$

then

$$D(C, n x_0) = (n-1)\, x_0 \{1 - e^{-C\sqrt{\pi}/2x_0}\} + F\left(\frac{C}{n}, x_0\right) \tag{88}$$

$$= (n-1)\, x_0 \{1 - e^{-C\sqrt{\pi}/2x_0}\} + D\left(\frac{C}{n}, x_0\right).$$

Hence we can derive $D(C, nx_0)$ from $D(C, x_0)$, provided that $n \geqq 1$.

For other distributions, numerical integration is always necessary. In any case the series expansion for the equivalent width D begins with a linear term in C; hence, for small values of C, the linear relationship between the equivalent width and the number of absorbing atoms always holds, no matter whether there is turbulence or not.

X. ILLUSTRATIONS AND CONCLUDING REMARKS

We have introduced into the Gaussian distribution of turbulent velocity a parameter β as a measure of the strength of turbulence compared with the thermal motion, while another parameter, z_0, is introduced into the other cases. In order to compare the results of the different distributions, it is necessary to measure the strength of turbulence in the same scale. In the following discussion we shall limit ourselves to the comparison of the parameter of the δ-function distribution with the parameter of the Gaussian distribution. For the other distributions there will be similar relations.

In comparing the results derived on the δ-function distribution and the Gaussian distribution, we shall suppose that the mean-square velocities are the same for the two distributions:

$$\overline{\xi_\delta^2} = \overline{\xi_g^2} \qquad \text{or} \qquad \beta = \left(\frac{2}{3}\right)^{\frac{1}{2}} z_0 . \tag{89}$$

The computation of line profiles for the two distributions (the δ-function and the Gaussian) according to equations (84) and (81) have been carried out, and the results are illustrated in Figure 1. With a definite value of the number of absorbing atoms, C, each curve shows how the line profile broadens for the two velocity distributions as the strength of turbulence z_0 increases. The heavy line in each curve represents the undisturbed line profile of pure thermal broadening. The full line gives the profile derived from the Gaussian distribution, while the dotted line shows that derived from the δ-function distribution with the same strength of turbulence. Detailed explanations are given at the end of the figure. As we have said, the actual distribution of turbulent velocities is likely to be intermediate between the two cases illustrated.

From an examination of the figure it is apparent that a weak line broadened by turbulence looks much shallower than a strong line. This phenomenon was, in fact, observed by Struve in the spectrum of δ Canis Majoris, a star which is known to have a turbulent atmosphere. Of course, for δ Canis Majoris the other kind of turbulent broadening by the eddies greater than the thickness of the reversing layer has to be considered before any real conclusion can be drawn.

We have plotted the curves of growth for both distributions in Figure 2. The distinction between the heavy, the full, and the dotted lines is the same as in Figure 1. It is found that the flat portion of the curve of growth derived from the δ-function distribution is much below that of the curve of growth derived from the Gaussian distribution with the same mean-square eddy velocity. In practice the mean-square turbulent velocity is usually evaluated from the flat portion of the curve of growth; if the observed curve of growth is compared with that derived from the δ-function distribution, then the mean-square turbulent velocity derived would be much greater than if the observed curve had been compared with the curve of growth derived from the Gaussian distribution.

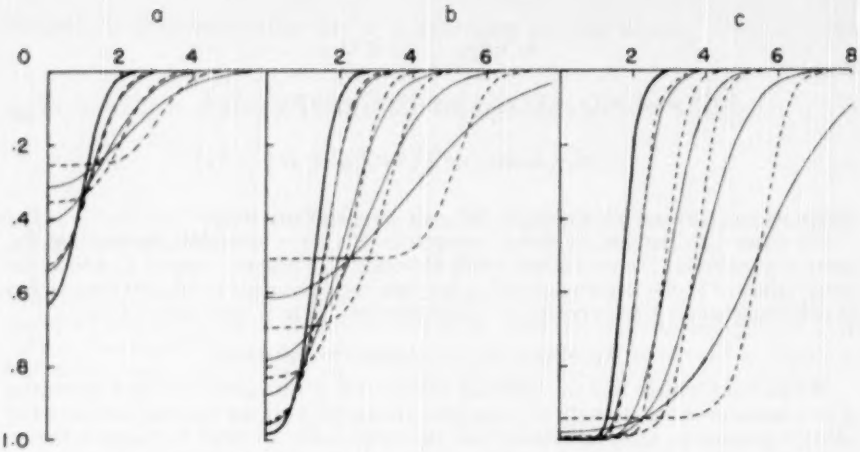

FIG. 1.—The change of line contours with increasing turbulence. Each figure represents the contours with a constant number of absorbing atoms, C, as turbulence increases. The heavy line in each figure represents the undisturbed line profile for pure thermal broadening. The full lines represent the profiles derived from the Gaussian distribution of eddy velocities, while the dotted lines represent the profile derived from the δ-function distribution of the eddy velocities with the same values of z_0, which measures the strength of turbulence compared with the thermal motion (cf. eq. [89]). All curves are plotted in units of the pure thermal Doppler width. *a*, $C = 1$, $z_0 = 1, 2, 3$; *b*, $C = 4$, $z_0 = 1, 2, 3, 5$; and *c*, $C = 16$, $z_0 = 1, 2, 3, 5$.

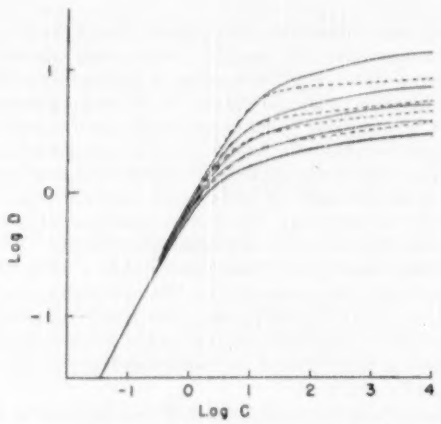

FIG. 2.—The change of curves of growth with turbulence. The heavy lines represent the curves of growth for the case in which no turbulence is present. The full-line curves show the change of the curves of growth with turbulence if the distribution of eddy velocities is Gaussian; the dotted-line curves show the same phenomena if the distribution is a δ-function. The strengths of turbulence, z_0, for these four pairs of curves are $z_0 = 1, 2, 3$, and 5, respectively.

Thus it is seen that, if the turbulent velocity distribution is not known exactly, the mean-square turbulent velocity, as determined by the curve-of-growth method, is uncertain. Moreover, it is very difficult to say anything about the turbulent velocity distribution from the observed curve of growth because the change of shape of the curve of growth from one distribution to another is too slight to be noticed in the observed curve of growth, which usually consists of a number of scattered points. Hence a study of the line profile would be more important in understanding the turbulence in stellar atmospheres. For example, we have seen that the shapes of the line contours caused by the δ-function and by the Gaussian distribution of turbulent velocities are so different that they can be distinguished from one another if the turbulent velocity is greater than the thermal velocity. Another point we may notice is that lines formed in different layers may be broadened in different ways by the turbulence. In other words, the effect of the distribution of turbulent velocities may be different for different lines. If that is the case, the line-absorption coefficient is not only a function of wave length but also a function of the depth.

During the present investigation I have received kind encouragement and valuable advice from both Professor S. Chandrasekhar and Professor O. Struve, and I wish to express my sincere thanks to them.

ON TURBULENCE IN THE ATMOSPHERES OF THE SUN AND THE STARS

SU-SHU HUANG
Yerkes Observatory
Received August 10, 1950

ABSTRACT

The effect of turbulence in a stellar atmosphere on absorption lines formed in it is shown to consist of two parts. Which part a particular eddy contributes to depends on its relative size in comparison with the thickness of the reversing layer. The large eddies broaden the absorption lines without increasing their equivalent widths, while the small ones both broaden the lines and increase their equivalent widths. By using these ideas, an interpretation of the observed data on turbulence in stellar atmospheres is suggested. Thus the most important thing determining the nature of broadening of absorption lines by turbulence is the size of the fastest-moving eddies. As the linear dimension of the fastest-moving eddies can be greater or smaller than, or equal to, the thickness of the reversing layer, it is quite natural not only that the values of turbulent velocity derived from the curve of growth and from the line profiles should disagree in most cases but also that the difference between these values should vary from one star to another.

Finally, the turbulent spectrum in the solar atmosphere is considered, and a curve relating the velocity and the size of turbulent elements in the solar atmosphere is plotted as a result of the present analysis of the observed data. This curve modifies the one given recently by Richardson and Schwarzschild.

I. METHODS OF OBSERVING TURBULENCE IN STELLAR ATMOSPHERES

As has been shown in the previous paper,[1] the effect of turbulence in a stellar atmosphere on absorption lines formed in it can be divided into two parts. The first is due to eddies with linear dimensions greater than the thickness of the reversing layer; we shall call these "the large eddies." The second is due to eddies with linear dimensions less than the thickness of the reversing layer; we shall call these "the small eddies." The large eddies broaden the absorption lines without increasing their equivalent widths. The small eddies both broaden the lines and increase their equivalent widths. The division of the eddies into large and small is made only for convenience because, by introducing this division, we can interpret more simply the different types of information relating to turbulence in the stellar atmospheres.

Before we analyze the relevant observational data, it may be useful to summarize the possible ways in which turbulence in stellar atmospheres can be inferred and what the observations really mean. Consider, first, the method of the curve of growth. Most investigations[2] on turbulence in stellar atmospheres have utilized this method. The turbulent velocity derived from the curve of growth is the most probable velocity (or as it is sometimes called, the "random velocity," which is $\sqrt{2}$ times the root-mean-square velocity) of the small eddies. We cannot observe the large eddies by this method.

The second method of observing turbulence is by an analysis of the line profiles; C. W. Allen's recent work on the solar line profiles is an example of this method.[3] A line is broadened both by the large eddies and by the small eddies, although they broaden the line in different manners.

The last method of observing the turbulence in stellar atmospheres is the direct one of

[1] "On the Doppler Broadening of Absorption Lines by Turbulence and by Multiple Interstellar Clouds," which we shall hereafter denote as "Paper I."

[2] See references in Paper I.

[3] *M.N.*, **109**, 343, 1949. Also P. ten Bruggencate, *Zs. f. Ap.*, **18**, 316, 1939; H. C. van de Hulst, *B.A.N.*, **10**, 79, 1946; and R. O. Redman, *M.N.*, **97**, 552, 1937.

R. S. Richardson and M. Schwarzschild,[4] by measuring the Doppler shift of the Fraunhofer lines produced by the individual solar granules. Since Richardson and Schwarzschild succeeded in measuring individual eddies with diameters of the order of 1500 km, it indicates that their results refer to the very large eddies.

II. THE PROPERTIES OF A LINE PROFILE BROADENED BY EDDIES OF ALL SIZES

In this section we shall investigate the form of an absorption line after it has been broadened both by the large eddies and by the small eddies. The broadening by the large eddies has been investigated by Unsöld and Struve,[5] who have shown that this type of broadening has the same features as instrumental broadening. The broadening by the small eddies has been studied in Paper I, in which we have seen that the line-absorption coefficient is changed by the existence of this kind of turbulence. Now we shall examine the general case in which both kinds of eddies are present.

Let the line depth in a line broadened simply by the small eddies be $A(v)$, where v is the frequency difference from the center of the line measured in units of the pure thermal Doppler width (see Sec. VII, Paper I).

Here we shall not limit ourselves to any model of the line formation; thus we may have

$$A(v) = 1 - e^{-Nlk(v)} \tag{1}$$

for the idealized case of pure absorption, or

$$A(v) = \frac{R_c Nlk(v)}{R_c + Nlk(v)}, \tag{2}$$

or any other approximate formula for the case of a stellar atmosphere.[6]

As there exists a hierarchy of small eddies in each large eddy, the final line profile can be obtained by applying a broadening function to the profile given by equation (1) or equation (2). Hence, using a broadening function of the Gaussian type,

$$B(v) = \frac{\gamma}{\sqrt{\pi}} e^{-\gamma^2 v^2}, \tag{3}$$

we have the following expression for the line profile $A'(v_1)$ broadened by both kinds of eddies:

$$A'(v_1) = \frac{\gamma}{\sqrt{\pi}} \int_{-\infty}^{\infty} e^{-\gamma^2 (v_1 - v)^2} A(v)\, dv. \tag{4}$$

The Gaussian form of the broadening function was first used by Unsöld and Struve and has later been verified by Richardson and Schwarzschild's measurement on the solar atmosphere. In equation (3) γ is related to the mean-square line width $\overline{v_l^2}$, which is due solely to the large eddies (i.e., the mean-square line width if the small eddies were not present at all); thus

$$\overline{v_l^2} = \frac{1}{2\gamma^2}. \tag{5}$$

Here $\overline{v_l^2}$ is a direct measure of the mean-square velocity of the large eddies. A simple relation follows from equation (4).

Consider the mean-square width of the final profile given by equation (4):

$$\overline{v_1^2} = \frac{\int_{-\infty}^{\infty} v_1^2 A'(v_1)\, dv_1}{\int_{-\infty}^{\infty} A'(v_1)\, dv_1} = \frac{\int_{-\infty}^{\infty} (v^2 + [1/2\gamma^2])\, A(v)\, dv}{\int_{-\infty}^{\infty} A(v)\, dv}. \tag{6}$$

[4] *Ap. J.*, **111**, 351, 1950. [5] *Ap. J.*, **110**, 455, 1949.

[6] See, e.g., A. Unsöld, *Physik der Sternatmosphären* (Berlin: J. Springer, 1938).

But

$$\frac{\int_{-\infty}^{\infty} v^2 A\,(v)\,dv}{\int_{-\infty}^{\infty} A\,(v)\,dv} = \overline{v_s^2}, \tag{7}$$

where $\overline{v_s^2}$ denotes the mean-square line width, which is due solely to the small eddies (i.e., the mean-square line width if the large eddies were not present at all), because $A(v)$ is the profile broadened purely by small eddies. Hence equation (6) reduces to

$$\overline{v_l^2} = \overline{v_s^2} + \overline{v_l^2}, \tag{8}$$

or, equivalently,

$$\overline{\xi^2} = \overline{\xi_s^2} + \overline{\xi_l^2}. \tag{9}$$

The mean-square velocity, $\overline{\xi^2}$, derived from the line profile is therefore equal to the sum of the mean-square velocities of the small eddies, $\overline{\xi_s^2}$, and the mean-square velocity of the large eddies, $\overline{\xi_l^2}$.

For the mean line widths we have

$$\overline{|v_l|} = \frac{\int_{-\infty}^{\infty}\left[e^{-\gamma^2 v^2} + 2\gamma v \int_0^{\gamma v} e^{-y^2} dy\right] A\,(v)\,dv}{2\gamma\sqrt{\pi}\int_0^{\infty} A\,(v)\,dv}. \tag{10}$$

If we consider only the Doppler core of a weak line, we may write

$$A\,(v) \simeq aC\,e^{-a^2 v^2}, \tag{11}$$

which reduces equation (10) to a simple form:

$$\overline{|v_l|} = \left(\frac{1}{\pi a^2} + \frac{1}{\pi\gamma^2}\right)^{1/2} = \left(\overline{|v_l|}^2 + \overline{|v_s|}^2\right)^{1/2}. \tag{12}$$

III. INTERPRETATION OF THE TURBULENCE IN STELLAR ATMOSPHERES

Most of the information on stellar turbulence has been derived from the curve of growth. However, more recently Struve has considered the line profile in studying turbulence in δ Canis Majoris.[7] He found that the turbulent velocity derived from the line profile is much greater than that determined from the curve of growth. This is not surprising, in view of present considerations. The random turbulent velocity derived from the curve of growth by H. R. Steel is 4.9 km/sec,[8] while Struve's estimate of this quantity from the line contours is 30 km/sec. From equation (9) we can readily find the most probable velocity of the large eddies to be 29.6 km/sec. Hence more than 98 per cent of the turbulent energy in the atmosphere of δ Canis Majoris exists in the form of large eddies.

That the large eddies are predominant in such supergiant stars as δ Canis Majoris, α Cygni, etc., must be due to the relatively small thickness of the reversing layer compared with the stellar radius. This can be understood more explicitly in terms of the spectrum of turbulence in the following way: The turbulent velocity is zero for the very large eddies and at first increases as the eddy size decreases. On the other hand, in the equilibrium region and in the dissipation region the turbulent velocity of an eddy de-

[7] *Ap. J.*, **104**, 138, 1946. [8] *Ap. J.*, **102**, 429, 1945.

creases as its size decreases until the turbulent velocity once more becomes zero, and in between there must be a maximum velocity, which represents physically the fastest-moving eddies. These eddies, owing to their high velocity, contribute most to the line broadening. Now, if the fastest-moving eddies have linear dimensions larger than the thickness of the reversing layer, the large eddies will be predominant in that atmosphere. On the other hand, if their size is smaller than the thickness of the reversing layer, the small eddies will be dominant. Hence a stellar atmosphere has most of its turbulent energy contained either in its large eddies or in its small eddies. Observationally, either the value of the turbulent velocity derived from the curve of growth will be comparable with that derived from the line contour, or the turbulent velocity derived from the curve of growth will be negligible, while the line contours show an appreciable turbulent broadening. Only when the size of the fastest-moving eddies is comparable with the thickness of the reversing layer will both kinds of eddies have equal strength. In that case the turbulent velocity derived from the line profile will be greater but still of the same order of magnitude as that derived from the curve of growth. Unfortunately, the turbulent velocity derived from the line profile is in most cases not available, so that a comparison which would furnish the most information about the nature of turbulence in stellar atmospheres is not possible. If, furthermore, the hierarchy of eddies in all supergiant stars follows the same pattern, the thickness of the reversing layer alone completely determines the nature of turbulent broadening.

Conversely, the relative thickness of the reversing layer can be found from the present considerations. Stars like δ Canis Majoris and α Cygni, in the spectra of which the lines are broadened predominantly by the large eddies, must have a thin reversing layer. On the other hand, stars which show a high turbulent velocity in the curve of growth must possess a thick reversing layer. For example, ϵ Aurigae has an extended atmosphere of about 10^8 km in thickness, and Struve[9] found by the curve-of-growth method a high turbulent velocity of 20 km/sec. The giant component of ζ Aurigae, which has the same extended atmosphere as ϵ Aurigae, must show, according to the present interpretation, a high turbulent velocity in the curve of growth. In fact, O. C. Wilson's determination[10] from the curve of growth shows the turbulent velocity to vary from 6.5 km/sec at a height of 2.4×10^6 km to 13 km/sec at a height of 22.4×10^6 km. Again, the star 17 Leporis, which shows a velocity of 67 km/sec,[9] owing to small eddies, must have an extended atmosphere, unless its turbulent spectrum follows a different law from that of the other stars. Thus the observed data on turbulence in stellar atmospheres can be understood, at least qualitatively, in terms of the hierarchy of eddies as introduced by Kolmogoroff.[11]

IV. THE SPECTRUM OF TURBULENCE IN THE SOLAR ATMOSPHERE

From the solar curve of growth the random turbulent velocity of the small eddies was found to be 0.9 km/sec by K. O. Wright,[12] 1.7 km/sec by J. L. Greenstein,[13] and 2.0 km/sec by A. K. Pierce and L. Goldberg.[14] We shall take the mean square of these three values, which is 2.6 (km/sec)^2. We take the mean square because it is the square of the velocity that is directly determined from the curve of growth. From the profiles of faint solar lines, Allen[3] found a random turbulent velocity of 2.79 km/sec at the limb and 1.74 km/sec at the center of the solar disk. The mean square of these two values is

[9] O. Struve and C. T. Elvey, *Ap. J.*, **79**, 409, 1934; *Astr. Symposium, Western Reserve Acad., Hudson, Ohio*, 1938; *Pop. Astr.*, **46**, 431, 497, 1938.

[10] *Pub. A.S.P.*, **53**, 228, 1941.

[11] S. Chandrasekhar, *Ap. J.*, **110**, 329, 1949; G. K. Batchelor, *Proc. Cambridge Phil. Soc.*, **43**, 533, 1947.

[12] *Ap. J.*, **99**, 249, 1944.

[13] *Ap. J.*, **107**, 151, 1948.

[14] *Quart. Progress Rept., University of Michigan, October, 1947.*

5.4 (km/sec)^2. According to Section II, this value shows the combined effect due to both the large eddies and the small eddies. The random turbulent velocity of the large eddies should therefore be 1.7 km/sec, as given by equation (9). This value is subject to some uncertainty due to the inconsistency of the data derived from the curve of growth as given by various authors. Richardson and Schwarzschild's measurement of the random turbulent velocity of eddies with 1500-km diameter is 0.37 km/sec. Thus we can see that the eddies with 1500-km diameter are not the most important ones (i.e., not the fastest ones) among the large eddies. It is therefore obvious that the most important contribution to the line broadening due to the large eddies must come from eddies with sizes smaller than 1500 km.

Next we shall consider the question of the spectrum of turbulence in the solar atmosphere. Richardson and Schwarzschild in their recent paper[4] made an attempt to draw a curve representing the spectrum of turbulence in the solar atmosphere. However, there are certain uncertainties in their method of drawing the curve; for, according to our deductions, the random turbulent velocity derived from the line profile shows only the combined effect of both the large and the small eddies. It is not an intrinsic quantity connected with the nature of the turbulence, nor does it represent the velocity of the fastest-moving eddies, as Richardson and Schwarzschild have assumed. Consequently, the position of the dotted line in their figure (Fig. 4 of the paper cited) would not seem to be correct. Moreover, we have no theory to predict where the Kolmogoroff region begins. If Allen's suggestion of the nonisotropic nature of turbulence in the solar atmosphere represents an intrinsic effect, it will be an open question as to how much of the theory of turbulence as heretofore developed for the isotropic case can be applied to the turbulence in the solar and stellar atmospheres.

Regarding the other two points in their diagram, we believe that the one determined by the Doppler shift of granules is definite, while the other is subject to a horizontal uncertainty. As the velocity determined by the curve-of-growth method is the random velocity of the small eddies, we cannot tell exactly what size of the representative eddy corresponds to this random velocity, unless we know the law of distribution of turbulent velocities of these small eddies. Of course, in any case it would not be very much different from the value that Richardson and Schwarzschild have assumed because the representative size must be smaller—but not too much smaller—than the thickness of the reversing layer.

At the present time it is too early to derive a rigorous turbulent spectrum for the solar atmosphere. A particular difficulty is that the turbulence may not be isotropic; for, owing to the difference of boundary conditions in different directions, it is more likely than not that the turbulence will be axisymmetric. Indeed, an early investigation of J. Evershed[15] has shown that the small Doppler shifts of the Fraunhofer lines of the solar atmosphere appear mostly at a distance from the center of the disk and rarely at the center. From this, Evershed concluded that the motion of gases which produces these shifts would be parallel to the solar surface. This conforms with Allen's conclusion. Thus, both from theoretical considerations and from the results of different observational methods, we should conclude that the turbulence in the solar atmosphere will not be isotropic. This conclusion complicates any theory that may concern turbulence in stellar atmospheres. Especially in our fundamental equation (4) we did not take into account the nonisotropic nature of the turbulence. However, as all the observed quantities are results of the integrated effect over all the disk of the sun (or of the star), equation (4) will still be true if we regard it as an average relation for three mutually perpendicular directions (one radial and two tangential).

Returning to the spectrum of turbulence in the solar atmosphere, we recall that the random velocity of the large eddies is 1.7 km/sec, while that of the small eddies is

[15] *M.N.*, **94**, 96, 1934.

1.6 km/sec. From this we conclude that the fastest-moving eddies must have linear dimensions comparable with the thickness of the reversing layer, say, 100 km. The mean velocity of eddies with that size will be very near to 1.7 km/sec. The eddies with 1500-km diameters have velocities of 0.37 km/sec, as determined by Richardson and Schwarzschild. Hence a part of the relation between the velocity and the diameter of turbulent elements (i.e., from diameter 1500 km to diameter 100 km) is approximately known. As the diameter decreases from 100 km, the random velocity must decrease very slowly to a representative point of the small eddies with velocity 1.6 km/sec. There will not be a Kolmogoroff region immediately after the maximum, because a certain readjustment is required before the equilibrium state is finally reached. The spectrum of turbulence in the solar atmosphere as given in Figure 1 is therefore only very tentative.

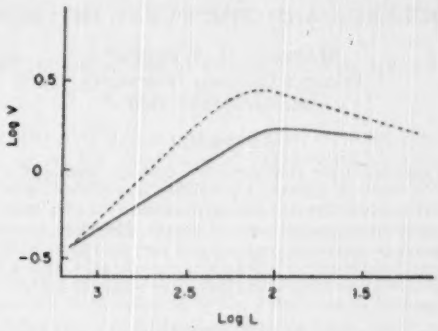

FIG. 1.—The spectrum of turbulence in solar atmospheres. The diameter of the eddy, L, is measured in kilometers, while the random turbulent velocity, V, is measured in kilometers per second. The full line is derived as a result of the present analysis, while the dotted line is reproduced here from Richardson and Schwarzschild's paper. The main difference between these two curves originates from the different interpretations of the turbulent velocity derived from the study of the line contours.

Finally, I should like to express my sincere thanks to Professor S. Chandrasekhar for his kind encouragement.

TURBULENCE AND THE CURVE OF GROWTH

MARSHAL H. WRUBEL*
Princeton University Observatory
Received July 10, 1950

ABSTRACT

Although eddies of all sizes affect the absorption-line contour, small eddies have greater effect upon the total absorption and the curve of growth. A weighting function $s(k)$ is derived for various circumstances of line formation. It is shown that all eddies of diameter smaller than two and a half times the scale height of the atmosphere appear in the curve of growth. Therefore, to explain the large differences observed in supergiant spectra between line contours and curves of growth, this theory requires a spectrum of turbulence with considerable energy in very long wave lengths. Such a spectrum may possibly be due to the effect which turbulence at deep layers may have upon the higher regions of the atmosphere in which the lines are formed.

I. INTRODUCTION

There are several major spectroscopic observations for which turbulence has been suggested as a possible explanation. Struve and Elvey[1] observed that curves of growth for certain supergiant stars indicate a dispersion in the velocity of the absorbing atoms by far too large to be thermal. These velocities were interpreted as due to turbulence. K. O. Wright[2] has shown that curves of growth for α Persei differ, depending upon whether they are plotted with neutral or with ionized atoms and with lines of high or low excitation potential. He found that the turbulent velocities are greater for ionized atoms and low-excitation lines. Struve[3] pointed out that there was some difficulty in correlating the curve of growth for δ Canis Majoris with high-dispersion line contours. The line-contour velocity was larger than that found from the curve of growth. This was also found in η Aquilae by Schwarzschild,[4] who suggested large-scale motions as the explanation. K. O. Wright and Miss van Dien[5] observed a similar effect in ϵ Aurigae and pointed out further that the turbulent velocities from line profiles showed no correlation with excitation potential, while those from the curve of growth did, as in α Persei.

The discrepancy between curve-of-growth and line-contour velocities may be explained qualitatively in the following manner. One may describe an absorption line as formed in a column of the atmosphere lying above a particular depth. Motions in the line of sight of one part of this column relative to another tend to increase the total absorption of the line in the same way as an increase in the temperature. However, motions of the column as a whole relative to neighboring columns of the atmosphere do not increase the absorption but change the contour of the line (as observed from the star as a whole) in the same way as a rotation of the atmosphere. Thus one would expect that only small-scale motions (or small "eddies") would influence the curve of growth, while eddies of all sizes influence the line contour.

Eddies are rather difficult to deal with in a physical theory. A more precise meaning

* National Research Council Post-doctoral Fellow, 1949–1950.

[1] *Ap. J.*, **79**, 409, 1934.

[2] *J.R.A.S. Canada*, **40**, 183, 1946; *Contr. Dom. Ap. Obs. Victoria*, No. 2, and *J.R.A.S. Canada*, **41**, 49, 1947; *Contr. Dom. Ap. Obs. Victoria*, No. 6.

[3] *Ap. J.*, **104**, 138, 1946.

[4] M. Schwarzschild, B. Schwarzschild, and W. S. Adams, *Ap. J.*, **108**, 225, 1948.

[5] *J.R.A.S. Canada*, **43**, 15, 1949.

is given to the quantities involved if one discusses turbulence as Heisenberg[6] has done in terms of the Fourier analysis of the velocity field. Then the diameter of an eddy may be identified with half the wave length λ of one of Heisenberg's velocity waves; or, if k is the wave number, defined as

$$k = \frac{2\pi}{\lambda}, \tag{1}$$

the diameter of an eddy is π/k. Consider a radial-velocity wave along the line of sight,

$$v_k = v_{0,k} \sin (k z - k \delta). \tag{2}$$

If the region in which the absorption line is formed is small compared with the wave length of the velocity wave, the dispersion of velocity within this region will be small, and the wave will have little effect on the curve of growth. However, there will be a motion of the column as a whole, and this wave will appear in the line profile. If the region of line formation is very much larger than λ, the dispersion of velocity within the region will be large, and eddies of this wave length will affect the curve of growth. Therefore, if each wave length can be considered separately, the dispersion of velocity in the line profile is an integral over all wave lengths in the spectrum of turbulence of the dispersion in each wave length. However, the dispersion of velocity in the curve of growth is an integral over all wave lengths of the dispersion in each wave length weighted by $s(k)$, where $s(k)$ varies from zero for very large wave lengths to 1 for very small wave lengths.

II. THEORY OF $s(k)$

The radiative-transfer problem for a turbulent atmosphere is formidable. Theoretically, it may be formulated in terms of the line-absorption coefficient for the nonturbulent atmosphere, but in this case there is no stratification in layers or shells, and the maximum of the absorption coefficient at each depth is displaced from the center of the nonturbulent line according to the turbulent velocity at that point at that time. Further, the absorption processes depend upon the instantaneous velocity field, but all that existing theories of turbulence can give are some statistical attributes of the velocity field. However, it is not unreasonable to assume that valid approximations can be made which will yield more useful results than have the qualitative arguments employed thus far.

The assumption is made throughout this paper that the turbulent velocities follow a Maxwellian distribution. Further, the form of the atomic absorption coefficient is ignored, and it is assumed that the dispersion of velocity as measured from the curve of growth is the dispersion of radial velocity in the line-forming region. In the Heisenberg theory the amplitude of each velocity wave is time-dependent; its time average, however, is constant. In the approximation of this paper the time-dependent amplitude is replaced by its time average. The average over the different configurations of the system becomes an average over the phases of the waves relative to some fixed point. Since we assume no correlation between phases for waves of different k, all cross-products vanish; thus each wave length may be treated separately, and a unique $s(k)$ assigned. (This would not seem to be the case in a more exact formulation of the problem.)

To demonstrate the procedure for deriving $s(k)$, let us consider the simple case of an absorption line completely formed in a finite layer of the atmosphere. Further, let us assume no continuous absorption, so that every depth of this layer is equally effective.

The radial-velocity field within this transparent layer is expressible as a series of terms of the form given in equation (2), z measured outward. The average velocity in this layer is therefore a sum of terms of the form

$$\bar{v}_k = -(2/kH)\, v_{0,k} \sin k\delta \sin (kH/2), \tag{3}$$

[6] *Zs. f. Phys.*, **124**, 628, 1948. The main points of this theory may also be found in the third Henry Norris Russell Lecture (S. Chandrasekhar, *Ap. J.*, **110**, 329, 1949).

where $z = 0$ at the center of the layer and H is its thickness. The dispersion of velocity will therefore contain cross-terms, as well as terms of the form

$$\overline{(v_k - \bar{v}_k)^2} = \frac{v_{0,k}^2}{H}\left[\frac{H}{2} - \frac{1}{2k}\cos 2k\delta \sin kH - \frac{4}{k^2H}\sin^2 k\delta \sin^2(kH/2)\right]. \quad (4)$$

However, this expression must be averaged over all possible phases, δ, from 0 to $2\pi/k$, corresponding to the fact that all phases are equally probable at the center of the layer. It is at this point that the cross-products vanish if there is no correlation between phases for different wave lengths. The resulting dispersion due to wave k is

$$V_k^2 = \overline{(v_k - \bar{v}_k)^2} = \tfrac{1}{2} v_{0,k}^2 [1 - (2/kH)^2 \sin^2(kH/2)]. \quad (5)$$

We may now identify the expression in brackets with the weighting function $s(k)$ that we have been seeking. It is immediately seen that it tends to zero for infinite wave lengths (zero k) and becomes 1 for the first time if $H = \lambda$; thus,

$$s(k) = 1 - (2/kH)^2 \sin^2(kH/2). \quad (6)$$

Strictly speaking, s is a function of the dimensionless product $kH/2$. Finally, the dispersion observed in the curve of growth is the sum

$$\sum_k V_k^2 = \frac{1}{2}\sum_k v_{0,k}^2 s(k). \quad (7)$$

Although this simple problem demonstrates the method of deriving $s(k)$, we must improve our model of line formation before we can deduce any results from the method. First of all, every depth in the atmosphere does not contribute equally to the line. Actually, the contribution of every point in the line-forming column is cut down by the absorption above it. Further, we ought to take into account the variation with depth of the number of atoms producing the absorption line. Thus in a more general case the averages with depth become weighted averages, the nature of the weighting function varying with the model of line formation under discussion.

Treating each wave length separately, let us again consider equation (2), where $v_{0,k}$ may actually be a function of depth. Suppose that the contribution of the velocity at each depth to the observed absorption is given the weight W; then

$$\bar{v}_k = \frac{1}{\overline{W}}\int_{-\infty}^{+\infty} W v_{0,k} \sin(kz - k\delta)\, dz, \quad (8)$$

where

$$\overline{W} = \int_{-\infty}^{+\infty} W dz. \quad (9)$$

Then

$$\overline{(v_k - \bar{v}_k)^2} = \frac{1}{\overline{W}}\left[\int_{-\infty}^{+\infty} W v_{0,k}^2 \sin^2(kz - k\delta)\, dz\right] - \bar{v}_k^2; \quad (10)$$

and the final average over δ gives

$$\overline{(v_k - \bar{v}_k)^2} = \frac{1}{2\overline{W}}\int_{-\infty}^{+\infty} W v_{0,k}^2 dz - \frac{1}{2\overline{W}^2}\left\{\left[\int_{-\infty}^{+\infty} W v_{0,k} \sin kz\, dz\right]^2 + \left[\int_{-\infty}^{+\infty} W v_{0,k} \cos kz\, dz\right]^2\right\}, \quad (11)$$

which may be written as

$$V^2 = \overline{(v_k - \bar{v}_k)^2} = \tfrac{1}{2}\{\overline{v_{0,k}^2} - [\overline{v_{0,k}\sin kz}^2 + \overline{v_{0,k}\cos kz}^2]\}$$
$$= \tfrac{1}{2}\{\overline{v_{0,k}^2} - \mathrm{Mod}^2[\overline{v_{0,k}e^{ikz}}]\}. \tag{12}$$

As a reasonable weighting function we choose

$$W = N\alpha B(T)\, e^{-\tau}, \tag{13}$$

where N is the number of atoms per cubic centimeter, α is the atomic line-absorption coefficient, $B(T)$ is the Planck function, and τ is the optical depth in the continuum. A similar weighting function is involved in the integration of the source function for pure absorption. In the following, $B(T)$ will be treated as a constant and can be eliminated. The integrations over z may be replaced by integrations over τ, since

$$d\tau = -\kappa\rho\, dz, \tag{14}$$

where κ is the continuous absorption coefficient and ρ is the density. The weight now becomes $\eta\exp(-\tau)$, where η is the ratio of the line absorption to the continuous absorption (per gram), and all integrations are from $\tau = 0$ to $\tau = \infty$.

At this point it is convenient to introduce a scale-height law of the density gradient

$$\rho = \rho_0 e^{-z/H}. \tag{15}$$

One would perhaps not expect regions greater than one scale height in diameter to behave as units; or, in this context, eddies greater in diameter than one scale height are probably infrequent. Further, if one assumes that

$$\kappa = \beta\rho = \beta\rho_0 e^{-z/H}, \tag{16}$$

then

$$z = \tfrac{1}{2}H\log(C/\tau), \tag{17}$$

where

$$C = \tfrac{1}{2}\beta\rho_0^2 H. \tag{18}$$

The quantity in equation (12) of which we want the square of the modulus is now

$$\frac{1}{W}\int_0^\infty \eta\, e^{-\tau} v_{0,k}\, e^{i(kH/2)\log(C/\tau)}\, d\tau, \tag{19}$$

which reduces to

$$C^{ikH/2}\frac{1}{W}\int_0^\infty \eta\, e^{-\tau} v_{0,k}\tau^{-ikH/2}\, d\tau. \tag{20}$$

Since

$$\mathrm{Mod}^2 C^{ikH/2} = 1 \tag{21}$$

and the sign of the modulus is unchanged by replacing $-i$ by $+i$, we finally get

$$V_k^2 = \tfrac{1}{2}\left\{\overline{v_{0,k}^2} - \mathrm{Mod}^2\left[\frac{1}{W}\int_0^\infty v_{0,k}\eta\, e^{-\tau}\tau^{ikH/2}\, d\tau\right]\right\}, \tag{22}$$

which is the form we shall use in the following discussion.

III. CALCULATION OF $s(k)$

We shall consider two limiting cases for the behavior of $v_{0,k}$ with depth. First we shall assume that $v_{0,k}$ is constant; then we shall assume that it varies so that the product of

the density and the square of the amplitude is constant. For each of these cases we shall consider three variations of η with depth. First we shall take η constant; then we shall allow η to vary as it would for low-excitation lines of neutral and ionized iron in the sun's atmosphere.

When η is constant,

$$\overline{W} = \eta \int_0^\infty e^{-\tau} d\tau = \eta \,. \tag{23}$$

This cancels the η in the numerator of equation (22). If, further, $v_{0,k}$ is constant,

$$V_k^2 = \tfrac{1}{2} v_{0,k}^2 \left[1 - \mathrm{Mod}^2 \int_0^\infty e^{-\tau} \tau^{ikH/2} d\tau \right]; \tag{24}$$

and we identify the quantity in brackets with $s(k)$. The integral on the right-hand side is $\Gamma(1 + ikH/2)$, of which the modulus can be written in terms of the hyperbolic sine. Thus we have

$$s(k) = 1 - [(\tfrac{1}{2}\pi kH) / \sinh(\tfrac{1}{2}\pi kH)] \,. \tag{25}$$

Values of $s(k)$ are given in Table 1 and plotted in Figure 1. It is interesting to note that

TABLE 1

THE FUNCTION $s(k)$ FOR TWO MODEL DISTRIBUTIONS

kH/π	$kH/2$	$s(k)$					
		$v_{0,k}$ = Const.			$\rho v_{0,k}^2$ = Const.		
		η Const.	*Fe* I	*Fe* II	η Const.	*Fe* I	*Fe* II
0.0	0	0	0	0	0.153	0.162	0.203
0.1	0.157	0.039	0.047	0.057	0.202	0.215	0.257
0.2	0.314	0.142	0.169	0.200	0.324	0.350	0.413
0.3	0.471	0.288	0.328	0.389	0.486	0.510	0.589
0.4	0.628	0.428	0.490	0.578	0.628	0.650	0.740
0.5	0.785	0.578	0.640	0.730	0.740	0.768	0.845
0.6	0.942	0.692	0.760	0.847	0.822	0.848	0.911
0.7	1.100	0.782	0.843	0.918	0.881	0.901	0.950
0.8	1.256	0.848	0.901	0.954	0.921	0.936	0.967
0.9	1.414	0.895	0.940	0.970	0.950	0.960	0.978
1.0	1.571	0.928	0.968	0.980	0.969	0.977	0.980
1.1	1.728	0.952	0.980	0.985	0.979	0.986	0.986
1.2	1.885	0.980	0.990	0.990	0.984	0.990	0.990
1.3	2.042	1.000	1.000	1.000	1.000	1.000	1.000

this expression for $s(k)$ remains unchanged if the weighting function is $\eta \exp(-a\tau)$ where a is a constant, since this introduces only a term of modulus unity.

The variation of η with depth was found in a crude way as follows. With the temperature distribution of Münch's model solar atmosphere,[7] the number of absorbing atoms per gram was computed at each depth, and the line-absorption coefficient was assumed to be directly proportional to this. Dividing by $\bar{\kappa}$ as given in Münch's tables, we get the relative variation of η with depth.

Examining equation (22) for $v_{0,k}$ = Constant, one notices that the integral whose

[7] *Ap. J.*, **106**, 217, 1947.

modulus is to be taken will become a series of Γ-functions if η is expressed as the product of a polynomial in τ and an exponential, thus:

$$\eta = (a + b\tau + c\tau^2)\, e^{-(\gamma-1)\tau}. \tag{26}$$

Further, since only the real parts of these Γ-functions will differ and since each will differ by unity from the preceding one, the usual recursion formula for these functions may be used to reduce all to one Γ-function. This is just $\Gamma(1+ ikH/2)$, which has already appeared in equation (25). If η is expressed by equation (26), we finally find

$$1 - s(k) = \frac{[1 + (b/a\gamma) + (c/a\gamma^2)(2 - [k^2H^2/4])]^2 + [(b/2a\gamma) + (3c/a\gamma^2)]^2[kH/2]^2}{(1 + [b/a\gamma] + [2c/a\gamma^2])^2} \times \mathrm{Mod}^2\, \Gamma(1 + ikH/2). \tag{27}$$

For lines of 1-volt excitation potential, fairly good representation of the run of η is found by fitting a curve of the form given in equation (26) at $\tau = 0.01, 0.5$, and 1.0. For *Fe* I, $(\gamma - 1) = 4$; *Fe* II, $(\gamma - 1) = 4.2$, give best results. The values of the resulting coefficients are given in Table 2. Corresponding values for $s(k)$ are given in Table 1 and plotted in Figure 1. They show that the weight given long wave lengths is somewhat

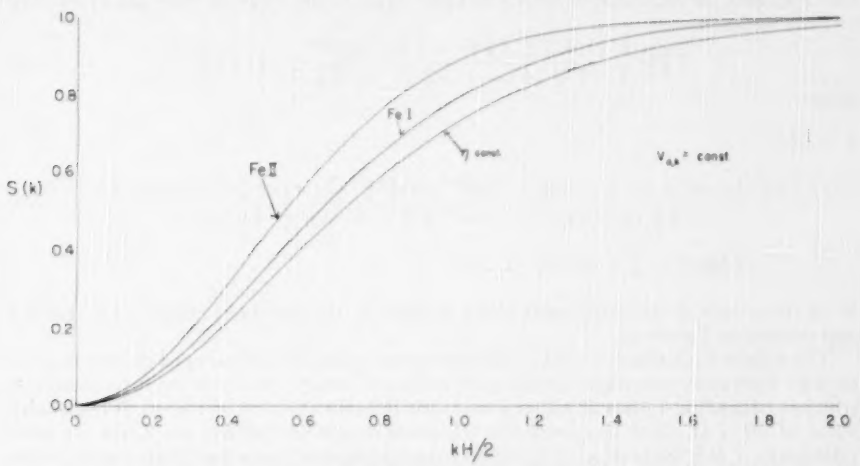

FIG. 1.—The weighting function $s(k)$ for $v_{0,b}$ = Constant and η' variation as indicated

TABLE 2

ADOPTED COEFFICIENTS FOR THE EVALUATION OF $s(k)$

Coefficient	*Fe* I	*Fe* II
γ	+ 5	+ 5.2
a	+ 6.74	+ 3.46
b	−13.91	−16.90
c	+18.07	+38.73

greater than for the case η = Constant; however, in general, the curves change very little.

We consider now the case of turbulence increasing with height in such a way that

$$\rho \bar{v}^2_{0,\,k} = G_k \,. \tag{28}$$

Using equation (15), we find

$$\bar{v}^2_{0,\,k} = G_k \rho_0^{-1} e^{+z/H} \,. \tag{29}$$

With z given in equation (17), we can derive an expression for V_k^2 from equation (12). If we identify as $s(k)$ that factor of V_k^2 which tends to 1 for waves of infinitely small wave length, we get

$$V_k^2 = \tfrac{1}{2} G_k C^{1/2} \rho_0^{-1} \Gamma(\tfrac{1}{2})\, s(k) \,, \tag{30}$$

where

$$s(k) = 1 - \mathrm{Mod}^2\, \Gamma(\tfrac{3}{4} + \tfrac{1}{2} ikH) / \Gamma(\tfrac{1}{2}) \,. \tag{31}$$

In this case, even waves of infinite wave length have a finite contribution. Equation (31) is tabulated in Table 1 and plotted in Figure 2. (By changing the weight to $\eta \exp(-a\tau)$, we introduce a factor $a^{1/2}$ in equation [30].)

Arguments similar to those given above for η of the form given in equation (26) show that $s(k)$ may be expressed in terms of $\Gamma(\frac{3}{4} + ikH/2)$ and $\Gamma(\frac{1}{2})$ for the case of varying η. Thus we have

$$V_k^2 = \frac{1}{2} \frac{(1 + [b/2a\gamma] + \frac{3}{4}[c/a\gamma^2])}{(1 + [b/a\gamma] + 2[c/a\gamma^2])} \Gamma(\tfrac{1}{2})\, s(k) \,, \tag{32}$$

where

$$1 - s(k) = \frac{[1 + \frac{3}{4}(b/a\gamma) + (c/a\gamma^2)(\frac{21}{16} - [k^2H^2/4])]^2 + [(b/a\gamma) + \frac{5}{4}(c/a\gamma^2)]^2 [kH/2]^2}{[1 + (b/2a\gamma) + \frac{3}{4}(c/a\gamma^2)][1 + (b/a\gamma) + (2c/a\gamma^2)]} \times \mathrm{Mod}^2\, \Gamma(\tfrac{3}{4} + \tfrac{1}{2} ikH) / \Gamma(\tfrac{1}{2}) \,. \tag{33}$$

With the values of the coefficients given in Table 2, $s(k)$ has been tabulated in Table 1 and plotted in Figure 2.

The weight with which eddies of different sizes appear in the curve of growth is given by $s(k)$. However, one might choose to describe the result crudely in the form of an $s(k)$ which is either 0 or 1; that is, either a wave has full effect or no effect at all. A reasonable value of $kH/2$ at which to choose the transition would be that one for which the computed $s(k) = 0.5$. Inspection of the accompanying figures shows that these points lie between $kH/2 = 0.4$ and $kH/2 = 0.7$. Let us see what a transition at $kH/2 = 0.6$ would mean. Since the diameter, D, of an eddy is π/k,

$$\frac{\pi H}{2D} = 0.6 \,. \tag{34}$$

Thus the critical eddy is about two and a half times the scale height in diameter. This is a somewhat surprising result. It means that only eddies larger than two and a half times the scale height contribute to the profile alone and not to the curve of growth. Thus, to explain observed differences between profiles and curves of growth, one must suppose that a great deal of energy lies in very large eddies, in contrast to what one would expect. This crude analysis is confirmed in the detailed application of the computed values of $s(k)$ to a specific spectrum of turbulence as given below.

IV. APPLICATION TO ASSUMED SPECTRUM

The distribution of energy among eddies of various wave numbers is given by the spectrum of turbulence, $F(k)$. Thus $\rho F(k)dk$ is the energy per unit volume between wave numbers k and $k + dk$. We now assume a three-dimensional spectrum. Since we are concerned only with radial velocities and wave lengths measured in the z-direction, this must be transformed to the one-dimensional spectrum, $F_z(k_z)$. The transformation is given in Heisenberg's paper as

$$F_z(k_z) = \int_{k_z}^{\infty} \frac{F(k)}{k^3}(k^2 - k_z^2)\,dk. \tag{35}$$

Now the quantity R, in which

$$R = \frac{\int_0^{\infty} s(k_z) F_z(k_z)\,dz}{\int_0^{\infty} F_z(k_z)\,dz}, \tag{36}$$

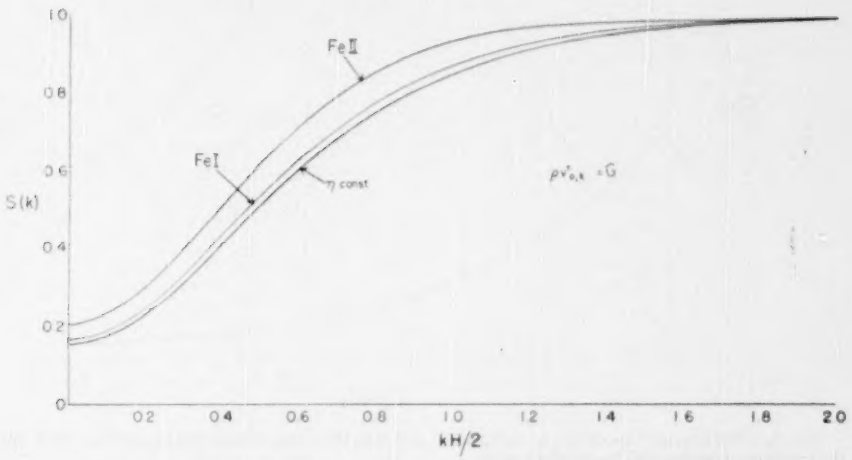

FIG. 2.—The weighting function $s(k)$ for $\rho v^2_{0,k} = G_k$ and η variation as indicated

gives the square of the ratio of the velocity measured in the curve of growth to the velocity measured in the line contour.

The spectrum we shall discuss is given in Figure 3. The thin line represents the three-dimensional spectrum; the thick line its one-dimensional transformation. The form of the spectrum was selected in keeping with the following assumptions: a linear region for small k, a broad maximum in the neighborhood of eddies of diameter equal to the scale height, and a Kolmogoroff region, $F(k)$, proportional to $k^{-5/2}$ for large k. The linear region illustrated here starts at the origin. However, a linear region starting at $kH/\pi = 0.5$ corresponding to eddies of diameter twice the scale height, and no linear region at all were also considered with only slightly different results. The ratio given in equation (36) was computed for the spectrum illustrated, and all $s(k)$'s were computed from Figures 1 and 2. Values of this ratio are given in Table 3 for all cases. The greatest difference between curve-of-growth and line-contour velocities is found when η and $v_{0,k}$ are constant. Since the ratio of the squares of the velocities is 71 per cent, the ratio of the velocities

themselves is 84 per cent. Thus the velocities determined by the two methods would be almost indistinguishable observationally.

How, then, can one explain the large differences observed in supergiants by using the values of $s(k)$ computed above? Only by increasing the energy in large wave lengths where $s(k)$ is small. This means that the usual assumption that eddies much larger than the scale height are rare must be revised. Indeed, it seems reasonable that turbulence at deep layers where the temperature is greater and the corresponding scale height larger can set the upper regions in motion. Thus, although one might still expect a maximum in the turbulence spectrum at the scale height of the line-forming region, a secondary maximum may also exist at long wave lengths corresponding to the scale height of a much deeper turbulent region. Using the data of Richardson and Schwarzschild,[8] Frenkiel[9] has discovered a small maximum at small k in the sun's turbulence. If the maximum were to dominate in the case of supergiants, large differences between curves of growth and contours would be expected.

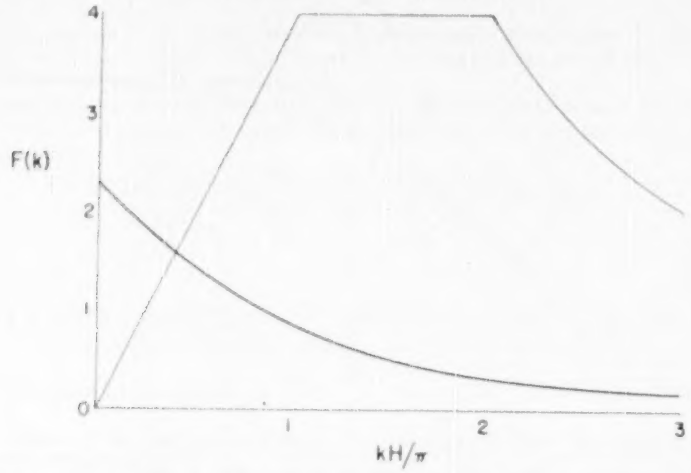

FIG. 3.—The assumed spectrum of turbulence: *thin line*, the three-dimensional spectrum; *thick line*, the spectrum transformed to one dimension.

TABLE 3

EFFECT OF TURBULENCE ON LINE PROFILES AND CURVE OF GROWTH

R (IN PER CENT) = σ^2 CURVE OF GROWTH/v^2 LINE PROFILE		
η	v_0, h = Const.	$\beta v_0^2, h = G$
η Const.	71	79
Fe I	74	80
Fe II	76	82

[8] *Ap. J.*, 111, 351, 1950.

[9] The author wishes to thank Dr. Frenkiel for permission to mention his results in advance of publication.

It would be of interest to compare the curves of growth for *Fe* I and *Fe* II. Since the values for $s(k)$ differ so little in these cases, little difference would be expected unless the spectrum of turbulence varies rapidly in the long-wave-length region. This might be the case if there is a steep maximum at small k, as suggested above.

Although this analysis is approximate in many ways, it does not seem likely that refinement of the theory will eliminate the requirement of more energy than has previously been suspected in large eddies.

In conclusion I wish to express my thanks to Dr. Martin Schwarzschild for constant encouragement and advice and to Dr. Lyman Spitzer, Jr., and Dr. Bengt Strömgren for many stimulating discussions. I am further grateful to the National Research Council for the Fellowship which has sponsored my research during the past year.

THE APSIDAL MOTION OF GIANT BINARY STARS

LLOYD MOTZ
Rutherfurd Observatory, Columbia University
Received June 28, 1950

ABSTRACT

The apsidal motion of giant binary stars built on two different models is investigated. In the first model an intermediate isothermal zone between the convective core and the radiative envelope is assumed. The internal data for this model are taken from case 4 of the Richardson-Schwarzschild noise-zone model as applied to a star of 10 solar masses with $R/R_\odot$ equal to 58.9. The second-order apsidal-motion coefficient for this case is equal to 0.003059, which gives a value of 3.7 for the effective polytropic index. This agrees well with the apsidal motion as measured by Wood for the F2 giant TX UMa.

In the second model a difference in chemical composition between the radiative envelope and the interior is assumed, with the convective core and the intermediate zone having the same chemical composition. The internal data for a star of 10 solar masses and $R/R_\odot$ equal to 66, as given by Hen and Schwarzschild in case 15, are used. This model leads to an effective index of 4.01.

I. INTRODUCTION

Within the last few years various attempts have been made to bring the theory of the internal constitution of the red giant stars into conformity with the carbon-cycle theory of energy generation.[1] Although the models that have been developed are not satisfactory for the extreme red giants, they appear to represent the intermediate cases fairly well. In view of this, one may hope that the extreme red giants may ultimately be described by some variation of such models rather than by models of a radically different kind. For this reason it is important to determine how well the internal density and mass distributions obtained for these models agree with what one would expect from the observations of the apsidal motions of giant binary stars. It has already been shown[2] that the apsidal motion of a binary stellar system is quite sensitive to a change in the effective polytropic indices of the component stars. For this reason it is possible to use the observational information obtained from the apsidal motion to determine the effective index. A comparison of this observational result with the effective index derived from an integration of the apsidal-motion equations for a particular model can then be used to check the internal structure of the model.

In the present paper a comparison is made between the observed apsidal motion of a single giant binary and that obtained for two different models described by Richardson and Schwarzschild.[1] The only case of a giant binary star for which fairly reliable apsidal-motion data are known appears to be TX UMa, which has been analyzed by Wood.[3] This is a giant star of spectral type F2, for which the apsidal motion indicates an effective polytropic index of 3.7.

The two models which are discussed in this paper are the case 4 noise-zone model of Richardson and Schwarzschild and the case 15 chemical inhomogeneous model of Hen and Schwarzschild. These two models are quite similar in their general characteristics, corresponding to giants of 10 solar masses with central temperatures of 30,000,000° and with radii equal approximately to $60R_\odot$.

Although the noise-zone model can have no counterpart in nature because it contra-

[1] R. S. Richardson and M. Schwarzschild, *Ap. J.*, **108**, 373, 1948; Li Hen and M. Schwarzschild, *M.N.*, **109**, 631, 1949. The author is grateful to Dr. Hen and Dr. Schwarzschild for allowing him to study their manuscript before publication.

[2] L. Motz, *Ap. J.*, **94**, 253, 1941; G. Keller, *Ap. J.*, **108**, 347, 1948.

[3] *Contr. Princeton U. Obs.*, **21**, 22, 1946.

dicts the second law of thermodynamics,[4] it is nevertheless useful to investigate its apsidal-motion properties because of its intermediate isothermal zone. The transition from a degenerate core (which cannot be excluded in giant stars) to the nondegenerate radiative envelope of a star may occur through an extensive isothermal zone, as described by Chandrasekhar.[5]

In the following sections the equations for the apsidal motion of triple-zone stars are developed and integrated numerically for the cases mentioned above.

II. THE DIFFERENTIAL EQUATIONS OF THE APSIDAL MOTION

If r is the mean distance of a surface of constant density ρ from the center of a binary component and r' is the actual distance of a point on the distorted surface from the center of the star, then, according to T. E. Sterne,[6] the distortion of the surface of constant density in this star generated by the other component is described by the series

$$r' = r[1 + Y_2(r, \theta) + \ldots],$$

where θ is the angle between r and a line joining the centers of the two stars. If we consider the deformation up to the first power only, the radial dependence of Y_2 is described by the differential equation,

$$\frac{\partial^2 Y_2}{\partial r^2} - \frac{6}{r^2} Y_2 + \frac{6\rho}{S(r)}\left[r^2 \frac{\partial Y_2}{\partial r} + r Y_2 \right] = 0, \tag{1}$$

where

$$S(r) = 3\int_0^r \rho \xi^2 d\xi .$$

Sterne has shown that the rate of advance (frequency), ω, of the apsidal motion is proportional to some function k_2 of the logarithmic derivative of the deformation coefficient Y_2 at the outer surface of the star. Indeed, we have

$$\frac{\omega}{\nu} = k_{2,1}\frac{a_1^5}{A^5}\left\{\frac{m_2}{m_1}[15 f_2(e) + g_2(e)] + g_2(e)\right\}$$

$$+ k_{2,2}\frac{a_2^5}{A^5}\left\{\frac{m_1}{m_2}[15 f_2(e) + g_2(e)] + g_2(e)\right\}.$$

Here ν is the frequency of orbital revolution in the same units as ω; $k_{2,1}$ is the value of k for the first component; $k_{2,2}$ is the value of k for the second component; m_1 and m_2 are the masses of the two stars; A is the semi-major axis of the orbit; a_1 and a_2 are the radii of the two stars in the same units as A; and e is the orbital eccentricity. $f_2(e)$ and $g_2(e)$ are the following rational functions of e:

$$f_2(e) = (1 - e^2)^{-5}(1 + 1.5e^2 + 0.125e^4),$$

$$g_2(e) = (1 - e^2)^{-2}.$$

The quantity k_2 has to be evaluated in terms of Y_2 and its derivative at the surface of the star:

$$k_2 = \frac{3 - \eta_2(a)}{4 + 2\eta_2(a)}, \tag{2}$$

[4] T. Gold, *M.N.*, **109**, 115, 1949.

[5] *Introduction to the Study of Stellar Structure* (Chicago: University of Chicago Press, 1939), pp. 447–449.

[6] *M.N.*, **99**, 455, 1939.

where

$$\eta_2(a) = \left[\frac{r}{Y_2}\frac{\partial Y_2}{\partial r}\right]_{r=a}. \tag{3}$$

From equations (2) and (3) we see that, to evaluate k, we must obtain a solution of equation (1) which is finite at the center of the star and find its logarithmic derivative at the surface. From equation (3) we see that for our purpose the necessary solution need be specified only to within a multiplicative constant, the value of which in any particular case is determined by the external boundary conditions.

III. THE EQUATIONS FOR THE NOISE-ZONE MODEL

In order to avoid the difficulties associated with the low central temperatures for giant stellar models based on the classical equilibrium conditions, R. S. Richardson and M. Schwarzschild[1] have investigated a nonclassical model comprising three zones. In this model it is assumed that the turbulence in the convective core of a giant star emits acoustical waves of such strength that the entire energy flux is carried solely by noise through the layers surrounding the core. These layers would thus constitute an isothermal zone lying between the convective core and the radiative envelope of the star.

To obtain the deformation coefficients for this case, we must integrate equation (1) through each of the three zones successively, applying the appropriate boundary conditions at each interface.

In the convective core it is convenient to introduce the new dependent variable,

$$F = YS, \tag{4}$$

which satisfies the equation

$$\frac{d^2F}{dr^2} - \left[\frac{6}{r^2} + 3\frac{d\rho}{dr}\frac{r^2}{S}\right]F = 0. \tag{5}$$

In addition, we introduce the polytropic variables θ and ξ and the polytropic index $n = 1.5$, where

$$r = a\xi, \qquad p = p_c\theta^{2.5}, \qquad a = t_c p_c^{-1/2}(2.5)^{1/2}R, \tag{6}$$

and the subscript c refers to the central values. In equations (6) we have introduced the dimensionless variables p and t as defined by Schwarzschild:

$$P = p\frac{GM^2}{4\pi R^4}, \qquad T = t\frac{\mu H}{k}\frac{GM}{R}, \qquad M_r = qM, \qquad r = xR. \tag{7}$$

We may note, in addition, that

$$x = t_c\rho_c^{-1/2}(2.5)^{1/2}\xi, \qquad \rho = \rho_c\theta^{1.5} = \frac{p_c}{3t_c}\bar{\rho}\theta^{1.5}. \tag{8}$$

Here $\bar{\rho}$ is the average density of the star. We shall also make use of the homology invariant quantities,

$$U = \xi\theta^{3/2}\left(-\frac{d\theta}{d\xi}\right)^{-1}, \qquad V = -2.5\frac{\xi}{\theta}\frac{d\theta}{d\xi}, \qquad UV = \tfrac{5}{2}\xi^2\theta^{1/2}. \tag{9}$$

If we use the above relations, we obtain, in the convective core, the equation

$$\frac{d^2F}{d\xi^2} - \left(\frac{6}{\xi^2} - \tfrac{3}{2}\theta^{1/2}\right)F = 0. \tag{10}$$

A slightly different form of this equation can be obtained by using the quantities in equation (9):

$$\frac{d^2F}{d\xi^2}-\frac{3}{\xi^2}(2-\tfrac{1}{5}UV)F=0. \tag{11}$$

To avoid numerical integration in the core, we use a series solution obtained previously[2] which is valid in the neighborhood of the center of the star. To insure the necessary accuracy out to the interface of the core, ten terms of the series are used:

$$\begin{aligned}F=\xi^2[1&-0.10714286\xi^2+7.936508\times10^{-3}\xi^4\\&-4.4642857\times10^{-4}\xi^6+2.193986\times10^{-5}\xi^8\\&-9.61609\times10^{-7}\xi^{10}+3.93739\times10^{-8}\xi^{12}\\&-1.5083\times10^{-9}\xi^{14}+5.565\times10^{-11}\xi^{16}\\&-1.97\times10^{-12}\xi^{18}+6.3\times10^{-14}\xi^{20}+\ldots]\end{aligned} \tag{12}$$

and

$$\frac{dF}{d\xi}=\xi^2[3-0.53571429\xi^2+5.5555556\times10^{-2}\xi^4-\ldots]. \tag{13}$$

For case 4 of the noise-zone model as given by Richardson and Schwarzschild, the value of ξ at the core-zone interface is $\xi_1=2$. For the value of F and its derivative at this interface we obtain

$$F(2)=5.3969036,\qquad \left(\frac{dF}{d\xi}\right)_{\xi=2}=6.1597184. \tag{14}$$

To pursue the integration further, we require the correct form of equation (1) in the isothermal zone. If we follow Richardson and Schwarzschild and use the isothermal variables χ and ψ, defined by

$$r=l_1p_1^{-1/2}\frac{R}{\chi}\qquad\text{or}\qquad x=\frac{l_1p_1^{-1/2}}{\chi} \tag{15}$$

and

$$U=e^{-\psi}\left(-\frac{d\psi}{d\chi}\right)^{-1}\chi^{-3},\qquad V=-\chi\frac{d\psi}{d\chi},\qquad UV=\chi^{-2}e^{-\psi}, \tag{16}$$

then it is convenient to introduce the new dependent variable,

$$\tilde{\vartheta}=Y\chi S. \tag{17}$$

In terms of these new variables, our differential equation becomes

$$\frac{d^2\tilde{\vartheta}}{d\chi^2}-\chi^{-2}(6-\chi^{-2}e^{-\psi})\,\tilde{\vartheta}=0. \tag{18}$$

If we make use of the last of equations (16) and the equation

$$\frac{d^2\psi}{d\chi^2}=\chi^{-4}e^{-\psi}, \tag{19}$$

we obtain two slightly different forms for our equation:

$$\frac{d^2\tilde{\vartheta}}{d\chi^2}-\chi^{-2}(6-UV)\,\tilde{\vartheta}=0,\qquad \frac{d^2\tilde{\vartheta}}{d\chi^2}-\left(6\chi^{-2}-\frac{d^2\psi}{d\chi^2}\right)\tilde{\vartheta}=0. \tag{20}$$

In order to integrate this equation numerically through the isothermal zone, we require two values of $\mathfrak{F}$ in the neighborhood of the interface. These we obtain by using a power-series solution for $\mathfrak{F}$ that is valid in the neighborhood of the interface at $\chi = 0.37683$ and then applying the boundary conditions at that point.

If we start from the second of equations (20), we can obtain the required power-series solution by deriving a recurrence formula for the differential coefficients of $\mathfrak{F}$. Thus

$$\frac{d^n\mathfrak{F}}{d\chi^n} = \sum_{i=0}^{n-2} (-1)^i \binom{n-2}{i} \left[6\chi^{-(i+2)}\,(i+1)\,! + (-1)^{i+1} \frac{d^{i+2}\psi}{d\chi^{i+2}} \right] \frac{d^{n-2-i}\mathfrak{F}}{d\chi^{n-2-i}}. \tag{21}$$

The differential coefficients $d^{i+2}\psi/d\chi^{i+2}$ can be found from equation (19) with the aid of the recurrence formula,

$$\frac{d^n\psi}{d\chi^n} = \sum_{i=0}^{n-3} (-1)^{(i+1)} \binom{n-3}{i} \left[\frac{4i!}{\chi^{i+1}} + (-1)^i \frac{d^{i+1}\psi}{d\chi^{i+1}} \right] \frac{d^{n-1-i}\psi}{d\chi^{n-1-i}}. \tag{22}$$

We can now write down the expansion for $\mathfrak{F}$ in terms of the coefficients (21) evaluated at the point 0.37683 thus:

$$\begin{aligned} \mathfrak{F} &= A + B(\chi - 0.37683) + \frac{1}{2}\left(\frac{d^2\mathfrak{F}}{d\chi^2}\right)_{0.37683} (\chi - 0.37683)^2 + \dots \\ &= A + B(\chi - 0.37683) - 3.669750A\,(\chi - 0.37683)^2 \\ &\qquad - [32.088603A + 1.2232501B](\chi - 0.37683)^3 \\ &\qquad + [120.0576A - 16.04405B](\chi - 0.37683)^4 - \dots . \end{aligned} \tag{23}$$

To evaluate the constants A and B, we apply the boundary conditions at the interface, which state that F and its first derivative must be continuous across the interface. In terms of the core and zone variables these boundary conditions assume the form

$$\chi_1 F(\xi_1) = \mathfrak{F}(\chi_1), \qquad \left(\frac{d\mathfrak{F}}{d\chi}\right)_1 = F(\xi_1) - \xi_1 \left(\frac{dF}{d\xi}\right)_1, \tag{24}$$

where the subscript 1 refers to the interface values of the quantities.

From the first condition we obtain

$$\mathfrak{F}(\chi_1) = A = \chi_1 F(\xi_1) = 2.033715\,;$$

and, from the second,

$$\left(\frac{d\mathfrak{F}}{d\chi}\right)_1 = B = F(\xi_1) - \xi_1 \left(\frac{dF}{d\xi}\right)_1 = -6.922533\,.$$

Thus

$$\begin{aligned} \mathfrak{F} &= 2.033715 - 6.922533t - 7.463594t^2 - 56.790072t^3 + \dots , \\ t &= (\chi - 0.37683)\,. \end{aligned} \tag{25}$$

From this expansion we can now evaluate $\mathfrak{F}$ at the two points $\chi = 0.375$ and $\chi = 0.370$; we obtain the values 2.046358 and 2.080663, respectively. With these two initial values we can now integrate the first form of equation (20) numerically through the noise zone, that is, from $\chi = 0.375$ to $\chi = 0.0913$. This integration can be carried out by means of the difference recurrence formulae of Feinstein and Schwarzschild,[7]

$$Z_{i+1} = Z_i B_i - Z_{i-1}, \qquad Z_i = \frac{12}{B_i + 10}\,\mathfrak{F}_i, \qquad B_i = 2 + \frac{\omega^2 b_i}{1 - (\omega^2 b_i/12)}. \tag{26}$$

[7] *Rev. Sci. Inst.*, **12**, 405, 1941.

Here ω is the step value, equal to 0.005 in this case, and b_i is the negative value of the coefficient of $\mathfrak{F}$ in the differential equation.

With the aid of equations (26), the value of $\mathfrak{F}$ at $\chi = 0.0913$, the point where the isothermal zone ends, is found to be equal to 14.179227.

From the table of $\mathfrak{F}$-values obtained from the integration, one finds that the value of the derivative of $\mathfrak{F}$ at $\chi = 0.0913$ is

$$\left(\frac{d\mathfrak{F}}{d\chi}\right)_{\chi=0.0913} = -274.8632.$$

In the remaining radiative portion of the star the differential equation in the form (5) is used, with the independent variable $x = r/R$ and with the additional relations,

$$\rho = \frac{p}{3t}\bar{\rho}, \qquad U = x^3 pt^{-1}q^{-1}, \qquad V = qt^{-1}x^{-1}. \tag{27}$$

Equation (5) becomes

$$\frac{d^2F}{dx^2} - x^{-2}\left(6 + 3x^4\bar{\rho}^{-1}q^{-1}\frac{d\rho}{dx}\right)F = 0$$

or

$$\frac{d^2F}{dx^2} - x^{-2}\left[6 + U(x-1)^{-1}\frac{d\log p}{d\log([1/x]-1)} - \frac{d\log t}{d\log([1/x]-1)}\right]F = 0. \tag{28}$$

To integrate this equation numerically through the radiative zone, from $x = 0.0175$ to the surface at $x = 1$, we again make use of formulae (26). To do this, we require two values of F in the neighborhood of the interface. We obtain these values by finding a power-series solution of equation (28) that is valid in the neighborhood of $x = 0.0175$. For this purpose it is necessary to express U, $d\log p/d\log([1/x]-1)$, and $d\log t/d\log([1/x]-1)$ as power series in $w = (x - 0.0175)$. This can be done with the aid of difference tables prepared from the Richardson-Schwarzschild integrations. We find

$$U = 0.3796 + 17.92396w - 168.05199w^2 - 6486.8633w^3 + \ldots,$$

$$\frac{d\log p}{d\log([1/x]-1)} = 2.3051 - 10.765579w + 1486.2609w^2 - 75460.4718w^3 + \ldots,$$

$$\frac{d\log t}{d\log([1/x]-1)} = 0.542603 - 0.3432605w + 262.3037w^2 - 16183.194w^3 + \ldots.$$

On using these expansions in equation (28), we find for F the solution

$$F = A + Bw + 8684.082Aw^2 + (2894.7148B - 346507.76A)w^3 + 276.955(116257.5A - 625.570B)w^4 + \ldots. \tag{29}$$

The constants A and B can now be found with the aid of the boundary conditions at the second interface (subscript 2),

$$\left(\frac{d\mathfrak{F}}{d\chi}\right)_{\chi=0.0913} = F(0.0175) - 0.0175\left(\frac{dF}{dx}\right)_{x=0.0175}$$

and

$$\chi_2 F(x_2) = \mathfrak{F}(\chi_2).$$

Thus

$$A = 155.3037, \quad \text{and} \quad B = 24580.969.$$

With these values for A and B, we can find two initial values for F from equation (29):

$$F(0.0175) = 155.3037\,, \quad \text{and} \quad F(0.0196) = 213.04639\,;$$

and with the aid of these we can integrate equation (28) numerically.

Since the Richardson-Schwarzschild data in the radiative zone are given in terms of the variable $z = \log_{10}(x^{-1} - 1)$, it is desirable to make the following substitutions:

$$x = (10^z + 1)^{-1} \quad \text{and} \quad F = 10^{z/2}(10^z + 1)^{-1} V\,. \tag{30}$$

The equation for V becomes

$$\frac{d^2V}{dz^2} - 5.30187\left\{0.25 + 10^z(10^z+1)^{-1} \times \left[\frac{6\times 10^z}{10^z+1} - U\left(\frac{d\log p}{d\log[(1/x)-1]} - \frac{d\log t}{d\log[(1/x)-1]}\right)\right]\right\} V = 0\,. \tag{31}$$

From the two initial values of F, two initial values of V can be found:

$$V = 1185.32319 \quad \text{for } z = 1.75\,, \qquad V = 1538.34319 \quad \text{for } z = 1.70\,.$$

The numerical integration is now performed with the aid of equation (26), where $\mathfrak{F}_i$ is replaced by V_i and b_i is the negative value of the coefficient of V in equation (31). The step-value ω is equal to 0.05, and the two initial values of Z are

$$Z_1 = 1178.2735\,, \quad \text{and} \quad Z_2 = 1529.3286\,.$$

The numerical work need not be carried out to the very edge of the star, since U vanishes for values of z smaller than -1.00. For regions of the star beyond this point the equation for F has the simple form

$$\frac{d^2F}{dx^2} - 6x^{-2}F = 0\,, \tag{32}$$

with the general solution,

$$F = C_1x^{-2} + C_2x^3\,, \tag{33}$$

where C_1 and C_2 are the constants of integration.

From equations (2) and (3) we see that the distortion at the surface of the star can be found as soon as the two constants C_1 and C_2 are evaluated. We have, in fact,

$$\eta(R) = \left[\frac{x}{F}\frac{\partial F}{\partial x} - \frac{x}{S}\frac{\partial S}{\partial x}\right]_{x=1} = \left(F^{-1}\frac{\partial F}{\partial x}\right)_{x=1}, \tag{34}$$

since $\partial S/\partial x$ is proportional to the density ρ, which vanishes at $x = 1$, the surface of the star. But

$$(F)_{x=1} = C_1 + C_2 \quad \text{and} \quad \left(\frac{\partial F}{\partial x}\right)_{x=1} = 3C_2 - 2C_1\,, \tag{35}$$

so that

$$\eta(R) = \frac{3C_2 - 2C_1}{C_1 + C_2}\,. \tag{36}$$

From the numerical integration of equation (31) we obtain the following results:

For $z = -0.90$ or $x = 0.888178$; $F = 4166994.6$;

For $z = -1.00$ or $x = 0.909091$: $F = 4465625.6$.

If we substitute these values in equation (33), we obtain

$$C_1 = 18092.15 \quad \text{and} \quad C_2 = 5914612.0 ;$$

and these, substituted in equation (36), give us

$$\eta (R) = 2.98475 . \tag{37}$$

From equation (2) we can now calculate the apsidal motion. We find for the coefficient k_2 the value 0.003059. We can now use this value to find the effective polytropic index of the model by comparing this result with the table of values calculated by S. Chandrasekhar[8] for a set of polytropic models. For the polytropic indices 1, 1.5, 2, 3, and 4 Chandrasekhar finds the following values for k_2: 0.25992, 0.1446, 0.0741, 0.0144, and 0.00134.

An accurate comparison of our value of k_2 with those given for the polytropes can best be made graphically by plotting the latter k's against the indices. When this is done, it is found that the noise-zone model corresponds to an effective index of 3.70.

IV. GIANT MODEL WITH CHEMICAL INHOMOGENEITIES

Hen and Schwarzschild[1] have investigated the internal structure of a series of giant model stars which contain a change in chemical composition in their radiative parts. Each of these models consists of three zones: a convective core; an intermediate radiative zone with the same chemical composition as the core; and a radiative envelope differing in composition from that of the core. The investigations of Hen and Schwarzschild have shown that, if these models are applied to stars with given mass and central temperature (30,000,000° K to insure the carbon cycle), it should be possible to obtain radii corresponding to giants of intermediate spectral class. In all, fifteen different models were integrated, but only the extreme case 15 approximates a late-type giant star. Since this model in its general characteristics is similar to the noise-zone model discussed in the previous sections of this paper, it was decided to investigate its apsidal motion also.

To obtain the distortion at the surface of the model under consideration, we can use the same solutions for the core and the radiative envelope as those developed in the first part of this paper. It is only in the intermediate radiative zone that we must use a solution different from that applicable to the isothermal zone. Since the internal data for this zone are given by Hen and Schwarzschild, it is possible to integrate numerically through this region.

Because the convective core is still to be described as a polytrope of index 1.5, equations (10) and (11) are still applicable, and we may therefore use the series solution (12) out to the boundary of the core. For this case the boundary occurs at $\xi_1 = 1.1204$, and we obtain

$$F(\xi_1) = 1.233689 \quad \text{and} \quad \left(\frac{dF}{d\xi}\right)_{\xi=\xi_1} = 3.022349 . \tag{38}$$

Since in the intermediate radiative zone we shall use the variables (7), our differential equation is essentially the same as equation (28). If we introduce U as defined by equation (27) into the first of equations (28), we obtain for the intermediate zone the equation

$$\frac{d^2F}{dx^2} - x^{-2}\left(6 + \frac{xU\,d\log\rho}{dx}\right)F = 0 ,$$

[8] *M.N.*, **93**, 451, 1933.

or

$$\frac{d^2F}{dx^2} - x^{-2}\left(6 + \frac{Ud\log\rho}{d\log x}\right)F = 0\,. \tag{39}$$

To integrate this equation numerically, we shall use the variables introduced by Hen and Schwarzschild,

$$\lambda = \log_{10}\frac{p}{p_0}, \qquad \tau = \log_{10}\frac{l}{l_0}, \qquad y = \log_{10}\frac{x}{x_0}, \tag{40}$$

where p_0, l_0, and x_0 are numerical constants, the values of which need not concern us here. Remembering the definition of ρ as given in equation (27), we obviously have, from equation (39), the equation

$$\frac{d^2F}{dx^2} - x^{-2}\left(6 + \frac{Ud[\lambda-\tau]}{dy}\right)F = 0$$

or

$$\frac{d^2F}{dy^2} - A^{-1}\frac{dF}{dy} - A\left(6 + \frac{Ud[\lambda-\tau]}{dy}\right)F = 0\,, \tag{41}$$

where $A = \log_e 10$.

For purposes of numerical integration it is desirable to eliminate the first-order derivative. We do this by means of the substitution

$$V = Fe^{-(y/2A)}\,,$$

which leads to the equation

$$\frac{d^2V}{dy^2} - A\left(6 + 0.25A^{-2} + \frac{Ud[\lambda-\tau]}{dy}\right)V = 0\,. \tag{42}$$

To integrate this equation numerically, we must first obtain two starting values in the neighborhood of the boundary of the core. We proceed as usual by finding a series solution of equation (42) that is valid at the boundary and then by applying the continuity conditions to this solution and the zone solution at the interface.

From difference tables prepared from the data of Hen and Schwarzschild we obtain the following expansions:

$$U = 2.631 - 1.667y - 6.667y^2\,, \qquad (\lambda - \tau) = 0.651770 - 0.6425y - 2.15y^2\,.$$

If we substitute these expansions in equation (42), we find the following series solution which is valid in the neighborhood of the first interface, $y_1 = 0$ and $x_1 = x_0 = 0.005$:

$$V = b_0 + b_1y + \tfrac{1}{2}a_0b_0y^2 + (\tfrac{1}{6})(a_1b_0 + a_0b_1)\,y^3 + (\tfrac{1}{12})(\tfrac{1}{2}a_0^2b_0 + a_1b_1 + a_2b_0)\,y^4 + (\tfrac{1}{20})(a_0b_3 + a_1b_2 + a_2b_1 + a_3b_0)\,y^5 + \ldots,$$

where b_0 and b_1 are constants that have to be determined by means of the boundary conditions, and the a's have the following values:

$$a_0 = 6A + 0.25A^{-2} - 1.69042A$$
$$= 9.970306\,,$$

$$a_1 = -28.51596\,, \qquad a_2 = 26.368336\,, \qquad a_3 = 66.010594\,.$$

The boundary conditions at the first interface are the following:

$$F(\xi_1) = F(x_1) \qquad \text{or} \qquad F(\xi_1) = V(0)$$
$$= b_0$$

and

$$A\left(\xi\frac{dF}{d\xi}\right)_{\xi=\xi_1}=\left(\tfrac{1}{2}VA^{-1}+\frac{dV}{dy}\right)_{y=0}$$

or

$$A\left(\xi\frac{dF}{d\xi}\right)_{\xi=\xi_1}=\tfrac{1}{2}b_0A^{-1}+b_1.$$

Combining these equations with equation (38), we finally obtain

$$V=1.233689+7.529195y+6.150128y^2+6.648092y^3-10.071104y^4+\ldots.$$

We can now obtain from this expansion two initial values of V to start the numerical integration through the intermediate radiative zone. These values are

$$V(0)=1.23369 \quad \text{and} \quad V(0.01)=1.309604.$$

The numerical integration of equation (42) now proceeds as usual with the aid of equation (26) from the first interface, at $y=0$, to the second interface, at $y=0.4388$ or $x_2=0.015$, in steps of 0.01.

From the results of this integration we can, with the aid of the boundary conditions at the second interface, determine the constants A and B in the expansion (29), which is valid in the neighborhood of this interface, although the expansion is in powers of $(x-0.0175)$ rather than of $(x-0.0150)$. We have included enough terms in equation (29) to insure the required accuracy.

If the subscript i refers to the intermediate zone and the subscript e to the envelope, then the boundary conditions at the second interface are

$$F_i(x_2)=F_e(x_2) \quad \text{and} \quad \left(\frac{dF_i}{dx}\right)_{x=x_2}=\left(\frac{dF_e}{dx}\right)_{x=x_2}.$$

From the numerical integration in the intermediate zone we obtain the values

$$V(0.4388)=5.977262 \quad \text{and} \quad \left(\frac{dV}{dy}\right)_{y=0.4388}=14.73153.$$

If we use these values of V and its derivative in the above boundary conditions, remembering the relationship between V and F_i, we obtain for A and B in equation (29) the values 8.447033 and 935.3533, respectively. If we substitute these numbers in equation (29), we can use that expansion to determine two initial values of F_e in the neighborhood of the interface,

$$F_e(0.0175)=8.447033, \qquad z_1=1.75,$$

$$F_e(0.0196)=10.73488, \qquad z_2=1.70.$$

Just as in the case of the noise-zone model, we can now use these initial values and formulae (26) to integrate equation (31) numerically through the envelope up to the point $z=-1.00$. Beyond that point we again use the result (33). Proceeding in this way, we obtain the following results:

$$C_1=1149.8075 \quad \text{and} \quad C_2=468500.06.$$

Substituting these values in equation (36), we obtain $\eta(R)=2.987759$, and, from this, $k_2=0.00123$.

If we compare this value of k with those found for polytropes, we see that the model of the star we are considering corresponds to an effective index of 4.01.

V. CONCLUSION

In order that the carbon cycle shall be adequate to account for the energy generation of giant stars, the central temperatures of these stars must be of the order of 30,000,000°. It is known that one can attain such temperatures and sufficiently large radii for the intermediate giant stars by adopting a three-zone model of the type considered in this paper. Schwarzschild and his collaborators have shown that the convective cores in such models are similar to those found in the main-sequence stars, so that one would expect the apsidal motion of binary stars built on such models to approximate that found for the main-sequence stars. This is borne out by the analysis in this paper, which shows that these models have effective indices lying between 3.7 and 4. This agrees with the observational evidence for the star TX UMa.

DIFFUSE REFLECTION BY PLANETARY ATMOSPHERES

HENRY G. HORAK
Yerkes Observatory
Received August 15, 1950

ABSTRACT

An attempt is made to interpret quantitatively the photometric observations which have been made of the planets by using the laws of diffuse reflection recently derived by Chandrasekhar. The basic problem is presented in Section I. Consider a planet at a particular phase. By assuming a certain law of reflection, we can compute the intensity at any point on the disk of the planet. The limb darkening readily follows; however, in order to compute the magnitude of the planet, it is necessary to perform an integration over the visible crescent. This can be accomplished by using an appropriate cubature formula. The problem then consists in finding a law of diffuse reflection which will "predict" the magnitude and limb-darkening observations of a planet. The laws of diffuse reflection are summarized in Section II. The geometry of the problem is discussed and certain necessary formulae derived in Sections III and IV. The observational data are briefly discussed in Section V. The results of the computations aregiven in the last section. The observations of Saturn can be represented by a semi-infinite atmosphere characterized by a forward-throwing type of phase function. This phase function has the form $0.985(1 + 0.9 \cos \Theta)$ for yellow light and $0.925(1 + 0.65 \cos \Theta)$ for blue light. The visual phase-curve is computed, and the Bond albedo is found to be 0.70.

The visual and photographic phase-curves of Venus can be represented by known laws of diffuse reflection for $\alpha < 130°$. At larger phase angles the planet is much too bright. Isotropic scattering with $\varpi_0 = 0.95$ appears to give the closest agreement in both the visual and the photographic cases. The limb darkening in yellow light can also be represented fairly well by isotropic scattering with $\varpi_0 = 0.95$. Polarization computations show that the polarization of the Venus atmosphere is not due to Rayleigh scattering.

I. INTRODUCTION

The object of this investigation is to interpret quantitatively the photometric observations which have been made of the planets. The main emphasis will be placed on Saturn and Venus.

At various phase angles (Fig. 1) the following quantities have been measured by observers: (1) the visual and photographic magnitudes, (2) the limb darkening in various colors, and (3) the polarization. In the case of the inferior planets, almost all phases can be observed, while for the superior planets the observable range in phase is considerably restricted, e.g., Saturn can be observed only for phase angles less than 6°.

In order to interpret the observations, it is necessary to solve the following theoretical problem: Given a plane-parallel, homogeneous, scattering atmosphere (finite or semi-infinite in depth) on which there is incident a parallel beam of natural light of flux density πF; let an individual scattering process be described in terms of the phase function $p(\cos \Theta) = \varpi_0 P(\cos \Theta)$, where ϖ_0 is the albedo for single scattering and $P(\cos \Theta)$ is the probability that the light is scattered at the angle Θ to the original direction. It is required to find the specific intensity I of the reflected radiation in any direction. Sometimes it might be necessary to suppose that the atmosphere is of finite optical thickness, at the base of which there is a ground or cloud layer which reflects, say, according to Lambert's law. If the plane polarization of the scattered light is taken into account, the problem is increased in complexity, and it is necessary to express the radiation field in terms of a vector whose components are the three Stokes's parameters,[1] I, Q, and U. The solution of the problem then consists in determining these three parameters for the light reflected in any direction.

Early attempts to solve this intricate problem were not very successful. Schoenberg

[1] S. Chandrasekhar, *Ap. J.*, **104**, 110–112, 1946.

and others[2] tried to obtain solutions by computing the contribution to the emergent radiation by light which had suffered one and two scattering processes, respectively, in the atmosphere. This leads to rather lengthy formulae of doubtful accuracy. The use of the equation of radiative transfer has proved to be a more fruitful approach. All the orders of scattering are automatically included in the formulation of this equation. Gerasimovič[3] used Eddington's approximation method to solve this equation for a phase function of the form $(1 + q \cos \Theta + p \cos^2 \Theta)/(1 + [p/3])$, where q and p are constants. While his results are quite inadequate (as the writer discovered while making computations for this paper), nevertheless he formulated the basic problem and drew attention to the need for better photometric observations. In recent years Chandrasekhar[4] has applied a new and powerful mathematical technique and succeeded in obtaining exact solutions of the equation of transfer for many forms of the phase function. These solutions lend themselves readily to numerical computation and hence are valuable for many applications.

Now consider a planet at a particular phase angle. The planet is assumed to be spherical in shape. At each point of the visible crescent we can imagine that there is located a plane-parallel atmosphere, scattering light according to a certain phase function. The angles of incidence and reflection and the azimuthal angles are readily determined from the geometry of the problem. The intensities of the light reflected to the earth at various points of the disk can then be computed. The limb darkening follows by expressing the intensities computed for points along the intensity equator[5] in terms of the intensity of one of the points; and, finally, the magnitude of the planet can be derived from an integration (by mechanical cubature) of the intensity over the visible crescent. In polarization computations it is necessary to calculate the three Stokes's parameters for each point. The degree of polarization and the inclination of the plane of polarization to the intensity equator for each point can then be immediately derived. An integration over the visible crescent then gives the degree of polarization of the emergent flux. Now, if we have chosen our law of reflection properly, our theoretical results should agree with the observations. In practice we must proceed by trial and error. This requires a considerable amount of computing.

There are certain limitations to this method which need to be mentioned. It is necessary to assume that a planet possesses a homogeneous atmosphere; otherwise it is not valid to compare our theoretical results with observations. Such an assumption should not lead to serious errors except possibly in the case of Jupiter, where the various bands differ in brightness by fairly large amounts.

There is a test for homogeneity which involves the use of the Helmholtz principle of reciprocity.[6] Minnaert[7] showed that the observations of limb darkening on Venus indicate either a nonhomogeneous atmosphere or systematic errors of measurement.

Another difficulty concerns variations of the planetary light with time. Becker[8] showed that, apart from the ordinary geometrical effects, the magnitude of Saturn undergoes a variation with amplitude $\sim$0.33 and with a variable period of 5–15 years. This emphasizes the necessity for *simultaneous* magnitude and limb-darkening measurements. Unfortunately, these are not available at the present time. Thus we shall have to assume that the visual-magnitude observations are consistent with the yellow-filter measures of limb darkening, and similarly for the photographic and blue-filter measures.

[2] *Handb. d. Ap.*, **2**, 38, 1932.

[3] *Pulkovo Obs. Bull.*, **15**, 1, 1937.

[4] Cf. *Radiative Transfer* (Oxford: Clarendon Press, 1950).

[5] The intensity equator is the intersection of the surface of the planet with the plane defined by the centers of the sun, planet, and earth.

[6] M. Minnaert, *Ap. J.*, **93**, 403, 1941; also cf. n. 4.

[7] *B.A.N.*, Vol. **10**, No. 367, 1946. [8] *A.N.*, **277**, 65, 1949.

II. THE LAWS OF DIFFUSE REFLECTION

The various laws of diffuse reflection are summarized in this section. The natural light of flux density πF is assumed incident on a plane-parallel atmosphere at an angle of incidence β and with an azimuthal angle φ_0. The emergent intensity in a direction ϑ to the normal and with azimuth φ is given by $I(0; \vartheta, \varphi)$. The following notation is used: $\mu_0 = \cos\beta$, $\mu = \cos\vartheta$, ϖ_0 = albedo for single scattering, $p(\cos\Theta)$ = phase function.

a) ISOTROPIC SCATTERING, $p(\cos\Theta) = \varpi_0$

The emergent intensity in the case of a semi-infinite atmosphere is given by

$$I(0; \mu) = \frac{\varpi_0 F}{4}\left(\frac{\mu_0}{\mu_0 + \mu}\right) H(\mu_0)\, H(\mu), \tag{1}$$

the H-functions of which are tabulated in *Radiative Transfer* (p. 125).

b) ASYMMETRIC PHASE FUNCTION, $p(\cos\Theta) = \varpi_0(1 + x\cos\Theta)$

For the case of a semi-infinite atmosphere

$$\begin{aligned} I(0; \mu, \varphi) = \frac{\varpi_0 F}{4}\frac{\mu_0}{\mu_0 + \mu}\{&\psi(\mu)\psi(\mu_0) - x\phi(\mu)\phi(\mu_0) \\ &+ x\,[(1-\mu^2)^{1/2}H^{(1)}(\mu)]\,[(1-\mu_0^2)^{1/2}H^{(1)}(\mu_0)]\cos(\varphi_0 - \varphi)\}, \end{aligned} \tag{2}$$

in which the necessary functions for $x = 1$ are tabulated in *Radiative Transfer* (pp. 141, 142). For $x = 0$ the phase function reduces to that for isotropic scattering. Solutions for values of x between 0 and 1 can be obtained by interpolation.

c) RAYLEIGH SCATTERING

For the case of a semi-infinite atmosphere,

$$\begin{aligned} I_l(0; \mu, \varphi) = \frac{3F}{32}\frac{\mu_0}{\mu_0 + \mu}\{&\psi(\mu)[\psi(\mu_0) + \chi(\mu_0)] + 2\phi(\mu)[\phi(\mu_0) + \zeta(\mu_0)] \\ &- 4\mu\mu_0(1-\mu^2)^{1/2}(1-\mu_0^2)^{1/2}H^{(1)}(\mu)\,H^{(1)}(\mu_0)\cos(\varphi_0 - \varphi) \\ &- \mu^2(1-\mu_0^2)\,H^{(2)}(\mu)\,H^{(2)}(\mu_0)\cos 2(\varphi_0 - \varphi)\}, \end{aligned} \tag{3}$$

$$\begin{aligned} I_r(0; \mu, \varphi) = \frac{3F}{32}\frac{\mu_0}{\mu_0 + \mu}\{&\chi(\mu)[\psi(\mu_0) + \chi(\mu_0)] + 2\zeta(\mu)[\phi(\mu_0) + \zeta(\mu_0)] \\ &+ (1-\mu_0^2)\,H^{(2)}(\mu)\,H^{(2)}(\mu_0)\cos 2(\varphi_0 - \varphi)\}, \end{aligned} \tag{4}$$

$$\begin{aligned} U(0; \mu, \varphi) = \frac{3F}{16}\frac{\mu_0}{\mu_0 + \mu}\{&2(1-\mu^2)^{1/2}(1-\mu_0^2)^{1/2}\mu_0 H^{(1)}(\mu)\,H^{(1)}(\mu_0)\sin(\varphi_0 - \varphi) \\ &+ \mu(1-\mu_0^2)\,H^{(2)}(\mu)\,H^{(2)}(\mu_0)\sin 2(\varphi_0 - \varphi)\}, \end{aligned} \tag{5}$$

where $I_l(0; \mu, \varphi)$ and $I_r(0; \mu, \varphi)$ are the intensities in the directions parallel and perpendicular, respectively, to the meridian plane containing the directions μ and φ. The necessary functions are tabulated in *Radiative Transfer* (p. 261). The quantities I_l and I_r are related to I and Q through the expressions $I_l + I_r = I$ and $I_l - I_r = Q$.

d) THE PLANETARY PROBLEM

In this case there is a finite Rayleigh-scattering atmosphere situated on top of a Lambert reflecting ground surface.

$$I_l(0;\mu,\varphi) = \frac{F}{8}\frac{\mu_0}{\mu_0+\mu}\{\tfrac{3}{4}[\psi(\mu)\psi(\mu_0)+2\phi(\mu)\phi(\mu_0)+\psi(\mu)\chi(\mu_0)+2\phi(\mu)\zeta(\mu_0)$$
$$-\xi(\mu)\xi(\mu_0)-2\eta(\mu)\eta(\mu_0)-\xi(\mu)\sigma(\mu_0)-2\eta(\mu)\theta(\mu_0)]$$
$$-3(1-\mu^2)^{1/2}(1-\mu_0^2)^{1/2}[X^{(1)}(\mu)X^{(1)}(\mu_0)-Y^{(1)}(\mu)Y^{(1)}(\mu_0)][\mu\mu_0\cos(\varphi_0-\varphi)] \quad (6)$$
$$-\tfrac{3}{4}[X^{(2)}(\mu)X^{(2)}(\mu_0)-Y^{(2)}(\mu)Y^{(2)}(\mu_0)][\mu^2(1-\mu_0^2)\cos 2(\varphi_0-\varphi)]\}$$
$$+\frac{F}{4}\frac{\lambda_0}{1-\lambda_0 s}\mu_0\{\gamma_l^{(1)}(\mu)\gamma_l^{(1)}(\mu_0)+\gamma_l^{(1)}(\mu)\gamma_r^{(1)}(\mu_0)\},$$

$$I_r(0;\mu,\varphi) = \frac{F}{8}\frac{\mu_0}{\mu_0+\mu}\{\tfrac{3}{4}[\chi(\mu)\psi(\mu_0)+2\zeta(\mu)\phi(\mu_0)+\chi(\mu)\chi(\mu_0)+2\zeta(\mu)\zeta(\mu_0)$$
$$-\sigma(\mu)\xi(\mu_0)-2\theta(\mu)\eta(\mu_0)-\sigma(\mu)\sigma(\mu_0)-2\theta(\mu)\theta(\mu_0)]$$
$$+\tfrac{3}{4}[X^{(2)}(\mu)X^{(2)}(\mu_0)-Y^{(2)}(\mu)Y^{(2)}(\mu_0)][(1-\mu_0^2)\cos 2(\varphi_0-\varphi)]\} \quad (7)$$
$$+\frac{F}{4}\frac{\lambda_0}{1-\lambda_0 s}\mu_0\{\gamma_r^{(1)}(\mu)\gamma_l^{(1)}(\mu_0)+\gamma_r^{(1)}(\mu)\gamma_r^{(1)}(\mu_0)\},$$

$$U(0;\mu,\varphi) = \frac{3F}{32}\frac{\mu_0}{\mu_0+\mu}\{(1-\mu^2)^{1/2}(1-\mu_0^2)^{1/2}[X^{(1)}(\mu)X^{(1)}(\mu_0)-Y^{(1)}(\mu)Y^{(1)}(\mu_0)]$$
$$\times[4\mu_0\sin(\varphi_0-\varphi)] \quad (8)$$
$$+[X^{(2)}(\mu)X^{(2)}(\mu_0)-Y^{(2)}(\mu)Y^{(2)}(\mu_0)][2\mu(1-\mu_0^2)\sin 2(\varphi_0-\varphi)]\},$$

where λ_0 is the Lambert albedo for the ground surface. The necessary functions have been computed[9] for various thicknesses of the finite layer.

III. THE GEOMETRY OF THE PROBLEM

Consider a planet illuminated by the sun. It is assumed that the sun is so distant that the light-rays received by the planet are parallel.

In Figure 1, S, E, and P represent, respectively, the centers of the sun, earth, and planet. The distances between sun and planet, sun and earth, and earth and planet are designated, respectively, by r, R, and Δ. The phase angle, α, is defined by the angle SPE.

Figure 2 shows the planet at a particular phase. In this figure O is the center of the planet, ρ the radius, OE the direction to the earth, OS the direction to the sun, and the great circle $CESG$ is the intensity equator with poles P and N, Q is any point on the planetary surface, and OQz defines the vertical at Q. Let a planetary co-ordinate system be assumed whose fundamental circles are the intensity equator and the meridian circle PEN. The co-ordinates are ζ (longitude) and η (co-latitude). For the point Q, $\zeta = EF$ and $\eta = PQ$.

The atmosphere at Q can be taken as plane-parallel. A rectangular co-ordinate system with axes x, y, and z can be set up at Q, so that the z-axis is in the radial direction. The x-axis is taken in the horizon plane, with its direction so chosen that the azimuthal angle, φ_0, for the incident ray from the sun to Q is zero.

[9] S. Chandrasekhar, unpublished. The formulae for this case are readily obtained from the development given by Chandrasekhar in *Radiative Transfer*, chap. x, pp. 270 ff.

The angles of incidence and reflection are determined by

$$\cos \beta = \mu_0 = \sin \eta \cos (\zeta - \alpha), \tag{9}$$

$$\cos \vartheta = \mu = \sin \eta \cos \zeta, \tag{10}$$

where β and ϑ are acute angles.

The azimuthal angle for the ray reflected to the earth is given by μ

$$\cos \varphi = \frac{\cos \vartheta \cos \beta - \cos \alpha}{\sin \vartheta \sin \beta}, \tag{11}$$

and

$$\sin \varphi = \frac{\sin \alpha \cos \eta}{\sin \vartheta \sin \beta}. \tag{12}$$

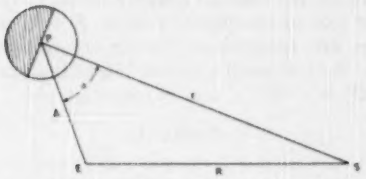

FIG. 1.—S represents the sun, E the earth, and P the planet. The phase angle of the planet is α

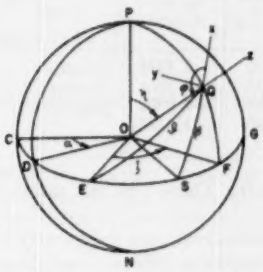

FIG. 2.—The co-ordinate systems on a planet

For $\alpha = 0°$ these equations give $\varphi = 180°$.

The element of area, $d\sigma$, at the point Q is given by

$$d\sigma = \rho^2 \sin \eta \, d\eta d\zeta . \tag{13}$$

The flux density, D, at the earth due to illumination from the planetary crescent is given by

$$D = \frac{1;}{\Delta^2} \iint I (0; \vartheta, \varphi) \cos \vartheta \, d\sigma , \tag{14}$$

where the integration is extended over the visible crescent. Introducing the planetary co-ordinates as variables, we have

$$D = \left(\frac{\rho}{\Delta}\right)^2 \int_0^{\pi} d\eta \sin^2 \eta \int_{\alpha - \pi/2}^{\pi/2} d\zeta \, I (0; \eta, \zeta) \cos \zeta = \left(\frac{\rho}{\Delta}\right)^2 j (\alpha), \tag{15}$$

where $j(\alpha)$ represents the double integral.

The stellar magnitude, m, of the planet is related to the flux density by the equation

$$m = -2.5 \log D ; \tag{16}$$

and, since πF is the flux density incident on the planet from the sun, this equation may be written

$$\begin{aligned} m - m_{\odot} &= -2.5 \log \left(D \frac{R^2}{\pi F r^2} \right) \\ &= -2.5 \log \left[\frac{j(\alpha)}{F} \right] - 2.5 \log \left[\frac{R^2}{\pi r^2} \left(\frac{\rho}{\Delta} \right)^2 \right], \end{aligned} \tag{17}$$

where $m_{\odot}$ is the magnitude of the sun. It is seen that $j(\alpha)/F$ has to be computed in order to get m. The method for doing this is explained in the next section.

The observational data for the inferior planets are usually reduced to the standard distances r = semi-major axis of the planet's orbit, $R = \Delta = 1$ A.U. For the superior planets the observations are reduced to "mean opposition," r = semi-major axis, $R = 1$ A.U., $\Delta = (r - 1)$ A.U. Russell's values[10] have been adopted for the magnitude of the sun, viz., m (visual) $= -26.72$, and m (photographic) $= -25.93$ on the system

TABLE 1

GEOMETRIC DATA FOR THE PLANETS

Planet	Radius $\rho \times 10^4$ (A.U.)	Semi-major Axis, r (A.U.)	$\log [1/r (R\rho/r\Delta)^2]$	Planet	Radius $\rho \times 10^4$ (A.U.)	Semi-major Axis, r (A.U.)	$\log [1/r (R\rho/r\Delta)^2]$
Mercury	0.1673	0.38710	−9.2258	Saturn	3.851	9.53884	−11.1478
Venus	0.4149	0.72333	−8.9801	Uranus	1.706	19.19098	−13.1191
Mars	0.2265	1.52369	−9.5909	Neptune	1.673	30.07067	−13.9333
Jupiter	4.669	5.20280	−9.8383				

of the *Harvard Revised Photometry*. Table 1 gives a summary of the geometric data for the planets.

The Bond or the spherical albedo is used frequently in planetary problems. It is defined in the following way: Consider a sphere of radius ρ illuminated by a parallel beam of light of flux density πF. The Bond albedo, A_B, is the ratio of the total flux sent by this sphere in all directions to the total incident flux. Applying this definition to a planet and using the usual notation, we obtain

$$\begin{aligned} A_B &= \frac{1}{\pi \rho^2 \pi F} \int_0^{\pi} \left[\left(\frac{\rho}{\Delta} \right)^2 j(\alpha) \right] 2\pi \Delta^2 \sin \alpha \, d\alpha \\ &= \frac{2}{\pi} \int_0^{\pi} \left[\frac{j(\alpha)}{F} \right] \sin \alpha \, d\alpha . \end{aligned} \tag{18}$$

It is obvious that, in order to compute A_B, we must be able to determine $j(\alpha)/F$ for all phase angles. If the magnitude of a planet can be measured at most phase angles, then A_B can be easily computed from the observed phase-curve (the graph of magnitude versus phase angle) without making any assumptions regarding the law of reflection; this is the case for Mercury, Venus, and the moon. However, for the superior planets it is necessary to find some way to construct the phase-curve. This can be done, provided that a model atmosphere can be found for the planet. Now, as we have seen, it is, in

[10] *Ap. J.*, **43**, 105, 1916.

principle, possible to find such a model atmosphere, provided that we know the magnitude and limb darkening at mean opposition. This is the method which we shall use.

IV. THE CUBATURE FORMULA

In order to perform the double integration for $j(\alpha)/F$, it is necessary to use numerical methods. The most convenient way appears to be the following. Now

$$\frac{j(\alpha)}{F} = \frac{1}{F}\int_0^{\pi} d\eta \, \sin^2 \eta \int_{\alpha-\pi/2}^{\pi/2} d\zeta \, I(0; \eta, \zeta) \cos \zeta \,. \tag{19}$$

In order to make this double integral amenable to integration by cubature, it is necessary to make changes in the variables such that the integration limits become -1 and $+1$. Thus, letting $\sin \zeta = \nu$ and $\cos \eta = \psi$, we have

$$\frac{j(\alpha)}{F} = \frac{1}{F}\int_{-1}^{+1} d\psi \, \sqrt{1-\psi^2} \int_{-\cos\alpha}^{+1} d\nu \, I(0; \psi, \nu) \,. \tag{20}$$

Also let

$$\xi = \left(\frac{2}{\cos\alpha + 1}\right)\nu + \left(\frac{\cos\alpha - 1}{\cos\alpha + 1}\right). \tag{21}$$

Then

$$\frac{j(\alpha)}{F} = \frac{\cos\alpha + 1}{2}\int_{-1}^{+1} d\psi \, \sqrt{1-\psi^2} \int_{-1}^{+1} d\xi \, \frac{I(0; \psi, \xi)}{F} \,. \tag{22}$$

This double integral now has a form such that the usual quadrature methods are applicable (cf. *Radiative Transfer*, chap. ii), and we can write

$$\frac{j(\alpha)}{F} = \tfrac{1}{2}(\cos\alpha + 1) \sum_{i=1}^{n} \sum_{j=1}^{n} a_i b_j \frac{I(0; \psi_i, \xi_j)}{F} \,, \tag{23}$$

where a_i and ψ_i are the Tschebichev weights and divisions[11] and b_j and ξ_j are the Gaus-

TABLE 2

TSCHEBICHEV AND GAUSSIAN DIVISIONS AND WEIGHTS

$n = 4$	
$\psi_1 = 0.30902$	$a_1 = 0.56832$
$\psi_2 = 0.80902$	$a_2 = 0.21708$
$\xi_1 = 0.33998$	$b_1 = 0.65214$
$\xi_2 = 0.86114$	$b_2 = 0.34786$
$n = 6$	
$\psi_1 = 0.22252$	$a_1 = 0.42658$
$\psi_2 = 0.62349$	$a_2 = 0.27433$
$\psi_3 = 0.90096$	$a_3 = 0.08450$
$\xi_1 = 0.23862$	$b_1 = 0.46791$
$\xi_2 = 0.66121$	$b_2 = 0.36076$
$\xi_3 = 0.93247$	$b_3 = 0.17132$
$\psi_i = -\psi_{n-i+1}$	$a_i = a_{n-i+1}$
$\xi_i = -\xi_{n-i+1}$	$b_i = b_{n-i+1}$

[11] G. Szegö, *Orthogonal Polynomials* (New York: American Mathematical Society, 1939), p. 344.

sian weights and divisions.[12] These quantities are tabulated in Table 2 for the two cases $n = 4$ and $n = 6$, where n is the number of divisions.

The sixteen-point cubature ($n = 4$) was found to be sufficiently exact by computing $j(\alpha)/F$ for Lambert's law of diffuse reflection, $I = \varpi_0 F \mu_0$, and comparing with the exact integration.[13] The results are shown in Table 3 for the case $\varpi_0 = 1$. The thirty-six-point

TABLE 3

COMPARISON OF EXACT INTEGRATION WITH MECHANICAL CUBATURE

CUBATURE	PHASE ANGLE		
	20°	80°	140°
Exact integration	1.977	0.8585	0.07198
16 points	1.989	.8609	.07194
36 points	1.980	0.8591	0.07197

cubature ($n = 6$) was adopted in the calculations for $\alpha = 0°$, and the sixteen-point cubature was used elsewhere.

Table 4 gives the following quantities for phase angles 0°, 20°, 40°, 60°, 80°, 100°, 120°, 140°, and 160°: (1) the cubature divisions (ψ, ξ); (2) the sine of the planetary co-ordinate ζ of the cubature points ($\sin \zeta = \nu$); (3) the cosine of the angle of incidence (μ_0); (4) the cosine of the angle of reflection (μ); and (5) the cosine and sine of the azimuthal angle of the reflected ray ($\cos \varphi$, $\sin \varphi$). The azimuthal angle for an incident ray is always taken to be 0°. It should be noticed that the cubature for phase angle 0° can be obtained by calculating $j(0)/F$ for one quadrant only and multiplying the result by 4. At other phase angles it is necessary to compute $j(\alpha)/F$ for one of the hemispheres determined by the intensity equator and then to multiply the result by 2.

V. THE OBSERVATIONAL DATA

There has not been much published on solar-system photometry in recent years, and we are forced to rely on rather old data. It is to be hoped that photoelectric photometers will be employed in the near future to give results of high accuracy.

The limb-darkening measurements that we shall use were determined photographically by Barabascheff and Semejkin. They used the 20-cm Zeiss refractor of the Karkov Observatory with a sun-moon camera which possessed a magnifying system. The planets Saturn,[14] Mars,[15] Jupiter,[16] and Venus[17] were photographed through three different color filters which had intensity maxima at 4610, 5630, and 6490 A. Exposure times ranged from a few seconds on Venus to 40–120 seconds on Saturn. The images were small, being around 1.3 mm in diameter for Saturn. Instrumental errors were eliminated as far as possible by photographing a uniformly illuminated flat disk and determining corrections empirically. These corrections were particularly important near the limb, owing to the diffraction caused by the circular opening of the telescope.

The visual and photographic magnitudes of the planets compiled by Russell[18] have

[12] *Radiative Transfer*, p. 62.

[13] E. Schoenberg, *Theoretische Photometrie* (*Tafeln*) (Berlin: J. Springer, 1929), p. 255.

[14] N. Barabascheff and B. Semejkin, *Zs. f. Ap.*, **7**, 290, 1933.

[15] N. Barabascheff and B. Semejkin, *ibid.*, **8**, 44, 1934.

[16] N. Barabascheff and B. Semejkin, *ibid.*, p. 179.

[17] N. Barabascheff and B. Semejkin, *Pub. Karkov Obs.*, No. 5, p. 29, 1935.

[18] *Ap. J.*, **43**, 111, 1916.

TABLE 4

Data for Performing Mechanical Cubature at Various Phase Angles

$a=0°$			$a=0°$		
ψ	$\xi=\sin\zeta$	$\mu=\mu_0$	ψ	$\xi=\sin\zeta$	$\mu=\mu_0$
0.22252	0.23862	0.9468	0.90096	0.66121	0.3255
.62349	.23862	.7592	.22252	.93247	.3522
.90096	.23962	.4214	.62349	.93247	.2824
.22252	.66121	.7314	0.90096	0.93247	0.1568
0.62349	0.66121	0.5865			

$a=20°$

ψ	ξ	ν	μ_0	μ	$\cos\varphi$	$\sin\varphi$
0.30902	+0.33998	+0.3599	0.9509	0.8873	−0.6721	0.7405
.80902	+ .33998	+ .3599	.5877	.5484	− .9125	.4090
.30902	+ .86114	+ .8653	.7294	.4767	− .9844	.1758
.80902	+ .86114	+ .8653	.4508	.2946	− .9459	.3244
.30902	− .33998	− .2996	.7552	.9074	− .9235	.3836
.80902	− .33998	− .2996	.4668	.5608	− .9258	.3779
.30902	− .86114	− .8050	.2683	.5642	− .9911	.1329
0.80902	−0.86114	−0.8050	0.1658	0.3487	−0.9542	0.2994

$a=40°$

0.30902	+0.33998	+0.4172	0.9172	0.8643	+0.1332	0.9911
.80902	+ .33998	+ .4172	.5668	.5342	− .6652	.7467
.30902	+ .86114	+ .8774	.8859	.4563	− .8766	.4812
.80902	+ .86114	+ .8774	.5475	.2820	− .7619	.6477
.30902	− .33998	− .1832	.6042	.9350	− .7115	.7027
.80902	− .33998	− .1832	.3734	.5778	− .7268	.6869
.30902	− .86114	− .6434	.1644	.7280	− .9559	.2938
0.80902	−0.86114	−0.6434	0.1016	0.4500	−0.8108	0.5853

$a=60°$

0.30902	+0.33998	+0.5050	0.8264	0.8209	+0.5546	0.8322
.80902	+ .33998	+ .5050	.5107	.5073	− .3251	.9457
.30902	+ .86114	+ .8959	.9492	.4226	− .3466	.9380
.80902	+ .86114	+ .8959	.5866	.2612	− .4436	.8962
.30902	− .33998	− .0050	.4714	.9510	− .1895	.9819
.80902	− .33998	− .0050	.2914	.5878	− .4248	.9053
.30902	− .86114	− .3959	.1106	.8734	− .8333	.5529
0.80902	−0.86114	−0.3959	0.0684	0.5398	−0.5514	0.8342

$a=80°$

0.30902	+0.33998	+0.6127	0.7044	0.7516	+0.7599	0.6500
.80902	+ .33998	+ .6127	.4353	.4645	+ .0358	.9994
.30902	+ .86114	+ .9185	.9256	.3761	+ .4973	.8676
.80902	+ .86114	+ .9185	.5720	.2324	− .0510	.9988
.30902	− .33998	+ .2137	.3615	.9291	+ .4703	.8826
.80902	− .33998	+ .2137	.2234	.5742	− .0569	.9984
.30902	− .86114	− .0922	.0781	.9470	− .3112	.9503
0.80902	−0.86114	−0.0922	0.0483	0.5853	−0.1795	0.9838

TABLE 4—*Continued*

ψ	ξ	r	μ_0	p	$\cos\varphi$	$\sin\varphi$
			$\alpha = 100°$			
0.30902	+0.33998	0.7273	0.5678	0.6527	0.8729	0.4880
.80902	+ .33998	.7273	.3510	.4034	.3679	.9299
.30902	+ .86114	.9426	.8278	.3175	.8203	.5720
.80902	+ .86114	.9426	.5116	.1962	.3253	.9456
.30902	− .33998	.4464	.2703	.8511	.7985	.6020
.80902	− .33998	.4464	.1670	.5260	.3119	.9500
.30902	− .86114	.2310	.0557	.9253	.5948	.8039
0.80902	−0.86114	0.2310	0.0344	0.5719	0.2358	0.9718
			$\alpha = 120°$			
0.30902	+0.33998	0.8350	0.4261	0.5233	0.9378	0.3471
.80902	+ .33998	.8350	.2633	.3234	.6410	.7675
.30902	+ .86114	.9653	.6708	.2484	.9280	.3726
.80902	+ .86114	.9653	.4146	.1535	.6268	.7792
.30902	− .33998	.6650	.1926	.7103	.9219	.3874
.80902	− .33998	.6650	.1190	.4390	.6190	.7854
.30902	− .86114	.5347	.0386	.8037	.8930	.4501
0.80902	−0.86114	0.5347	0.0238	0.4967	0.5899	0.8075
			$\alpha = 140°$			
0.30902	+0.33998	0.9228	0.2834	0.3664	0.9749	0.2226
.80902	+ .33998	.9228	.1752	.2265	.8402	.5423
.30902	+ .86114	.9838	.4706	.1707	.9735	.2285
.80902	+ .86114	.9838	.2909	.1055	.8374	.5466
.30902	− .33998	.8432	.1239	.5112	.9725	.2329
.80902	− .33998	.8432	.0766	.3160	.8353	.5497
.30902	− .86114	.7823	.0244	.5924	.9691	.2466
0.80902	−0.86114	0.7823	0.0151	0.3662	0.8292	0.5589
			$\alpha = 160°$			
0.30902	+0.33998	0.9801	0.1414	0.1888	0.9941	0.1087
.80902	+ .33998	.9801	.0874	.1167	.9601	.2797
.30902	+ .86114	.9958	.2422	.0869	.9940	.1094
.80902	+ .86114	.9958	.1497	.0537	.9599	.2803
.30902	− .33998	.9596	.0606	.2676	.9940	.1099
.80902	− .33998	.9596	.0375	.1654	.9598	.2808
.30902	− .86114	.9439	.0118	.3142	.9938	.1113
0.80902	−0.86114	0.9439	0.0073	0.1942	0.9594	0.2821

been adopted. The variation of magnitude with phase angle for Mercury and Venus has been investigated visually by Müller[19] and Danjon.[20] Table 5 and Figure 3 give their results for Venus with the magnitudes expressed on the system of the *Revised Harvard Photometry*. Danjon published his results in the International System; however, we have shifted Danjon's phase-curve horizontally until the best fit with Müller's curve was obtained.

[19] *Photometrie der Gestirne* (Leipzig: W. Engelmann, 1897).

[20] *C.R.*, **227**, 652, 1948.

TABLE 5

THE VISUAL PHASE-CURVE OF VENUS

α	Observed*		$\varpi_0 = 0.95$		$\varpi_0 = 0.975$		$\varpi_0 = 0.975$ $x = 0.500$	
	m	$j(\alpha)/F$	m	$j(\alpha)/F$	m	$j(\alpha)/F$	m	$j(\alpha)/F$
20°	−4.55	+1.236	−4.42	+1.153	−4.63	+1.39	−4.48	+1.22
40°	−4.27	+0.947	−4.24	+0.970	−4.41	+1.14	−4.32	+1.05
60°	−3.91	+0.699	−3.95	+0.743	−4.12	+0.87	−4.06	+0.826
80°	−3.48	+0.488	−3.54	+0.512	−3.71	+0.60	−3.70	+0.592
100°	−2.95	+0.316	−3.01	+0.313	−3.16	+0.36	−3.20	+0.375
120°	−2.37	+0.187	−2.28	+0.160	−2.40	+0.18	−2.52	+0.200
140°	−1.72	+0.098	−1.23	+0.061	−1.32	+0.07	−1.51	+0.079
160°	−1.00	+0.045	+0.53	+0.012	.....	.....	+0.19	+0.016
A_B	0.59		0.59		0.69		0.66	

* The mean of Müller's and Danjon's observations are given here.

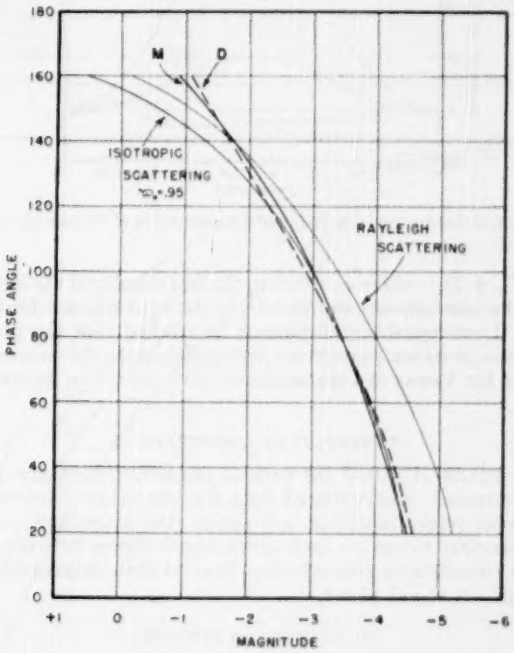

FIG. 3.—Observed and computed phase-curves for Venus. Curve *M* was obtained from the observations by Müller and curve *D* from the observations by Danjon. Two theoretical curves are shown, one for isotropic scattering with $\varpi_0 = 0.95$, the other for Rayleigh scattering.

Müller made his measurements with Zöllner-type photometers. Danjon used the method of "superposed fields," whereby two telescopes sent the image of Venus and a reduced image of the sun into the same field of view. All measurements were made near noon, so that the extinction corrections were reduced to a minimum. A calibrated neutral wedge was used to diminish the light of the sun to equality with Venus. The color index was determined by making observations through red and green filters.

At large phase angles, visual-magnitude observations are difficult to make, since Venus is near the sun and is crescent-shaped. It is difficult to compare visually such a crescent with a comparison or artificial star or with the sun, as the case may be. Furthermore, the refraction at large phases becomes very important. As α increases, the cusps gradually extend until they completely encircle the planet. In a more rigorous theoretical treatment than we intend to make, this effect would have to be taken quantitatively into account.

Very extensive and accurate polarization measurements of the planets have been made by Lyot.[21] The degree of polarization for the total light of a planet is defined by

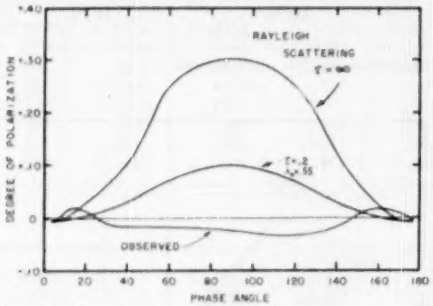

FIG. 4.—Comparison of the observed degree-of-polarization-curve of Venus with two theoretical curves for Rayleigh scattering.

$p = (D_r - D_l)/(D_r + D_l)$, where D_r refers to the flux density of the light which vibrates perpendicular to the intensity equator and D_l to the light which vibrates parallel to the intensity equator. Lyot found for all planets he studied that the plane of maximum polarization is oriented either parallel or perpendicular to the intensity equator. His measurements of p for Venus at various phases give the curve marked "Observed" in Figure 4.

VI. RESULTS OF COMPUTATIONS

The calculated values of $j(0)/F$ for various phase functions are given in Table 6. For comparison purposes, observational data for the major planets are also shown. Since many different phase functions will satisfy the magnitude condition at mean opposition, it is necessary to use the limb darkening to choose between various possibilities. This requires considerable computation. Several limb-darkening-curves are shown in Figure 5 for a planet at full phase.

a) URANUS AND NEPTUNE

The disks of Uranus and Neptune are so small, as seen from the earth, that limb darkening cannot be measured (the possibility of making occultation observations should be considered, however); and under these circumstances it is simplest to assume the law of reflection to be given by isotropic scattering in a semi-infinite atmosphere with an albedo

[21] *Ann. Obs. Paris* (Meudon), Vol. **8**, 1929.

TABLE 6

RESULTS OF COMPUTATIONS FOR ISOTROPIC SCATTERING AND FOR THE PHASE FUNCTION $\varpi_0(1+x \cos \Theta)$

A. THEORETICAL VALUES OF $j(0)/F$

Phase Function	$j(0)/F$	Phase Function	$j(0)/F$
$\varpi_0=1.000$	2.168	$1+\cos \Theta$	1.921
$\varpi_0=0.975$	1.454	$0.985\ (1+\cos \Theta)$	1.218
$\varpi_0=0.950$	1.234	$.985\ (1+0.9 \cos \Theta)$	1.265
$\varpi_0=0.925$	1.086	$0.925\ (1+0.65 \cos \Theta)$	0.850
$\varpi_0=0.900$	0.974		

B. OBSERVED MAGNITUDES AND VALUES OF $j(0)/F$ FOR THE MAJOR PLANETS

Planet	Visual		Photographic	
	$m(0)$	$j(0)/F$	$m(0)$	$j(0)/F$
Jupiter	−2.23	1.108	−1.79	1.528
Saturn	+0.89	1.272	+2.01	0.936
Uranus	+5.74	1.368	.....	.....
Neptune	+7.65	1.528	.....	.....

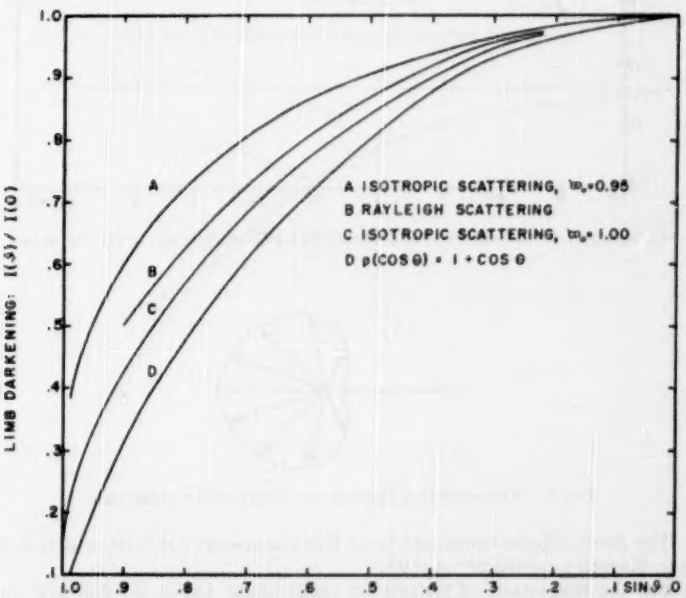

FIG. 5.—The limb-darkening-curves for four different phase functions

ϖ_0. In this way we obtain for Uranus $\varpi_0 = 0.97$ and for Neptune $\varpi_0 = 0.98$. The phase-curves and Bond albedos can then be computed, giving A_B (Uranus) = 0.64 and A_B (Neptune) = 0.71. These results are almost exactly the same as those given by Russell.[22]

b) SATURN

Computations for Saturn show that a semi-infinite atmosphere with phase function $0.985(1 + 0.9 \cos \Theta)$ gives fair agreement with the observed results in yellow light (Fig. 6 and Table 7). The scattering diagram (graph of the phase function) is shown in Figure 7. The entire phase-curve can now be constructed. The results are shown in Table 8 and

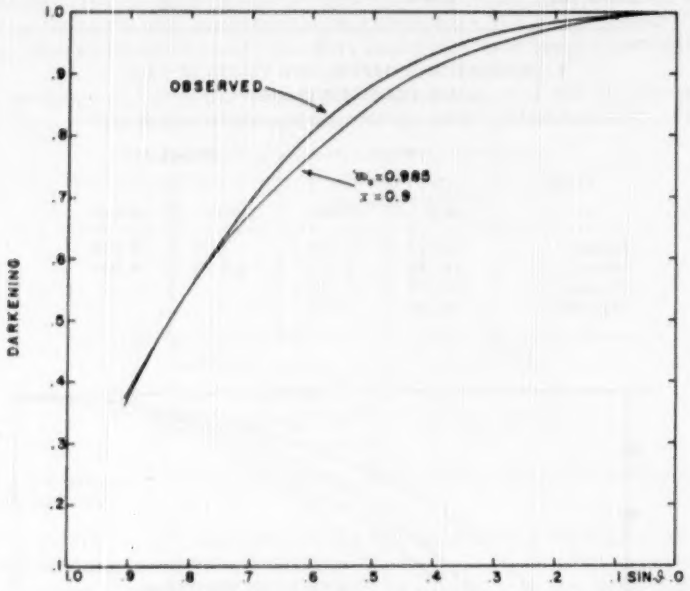

FIG. 6.—Comparison of the observed and theoretical limb-darkening-curves for Saturn in yellow light.

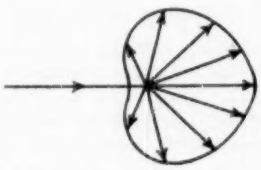

FIG. 7.—The scattering diagram for Saturn in the visual case

Figure 8. The Bond albedo computed from this phase-curve is 0.70, which is somewhat higher than Russell's estimate[22] of 0.63.

Sometimes the magnitude of Saturn for small phase angles is expressed as follows: $m(\alpha) = m(0) + a^*\alpha$, where $m(0)$ is the magnitude at mean opposition, a^* is the "phase

[22] *Ap. J.*, **43**, 190, 1916.

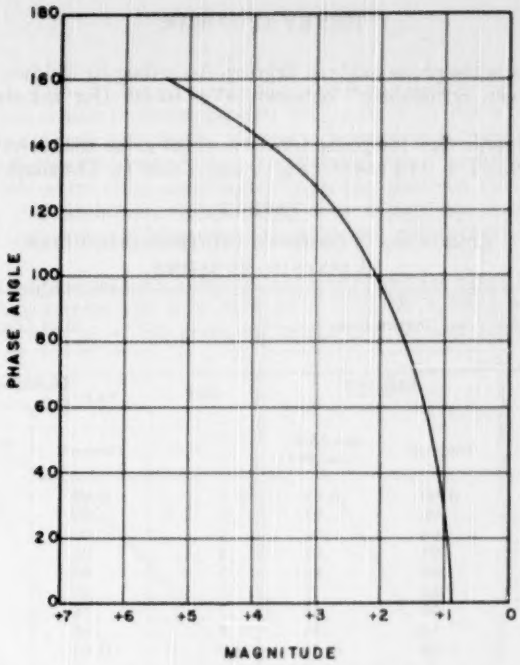

FIG. 8.—The theoretical visual phase-curve for Saturn

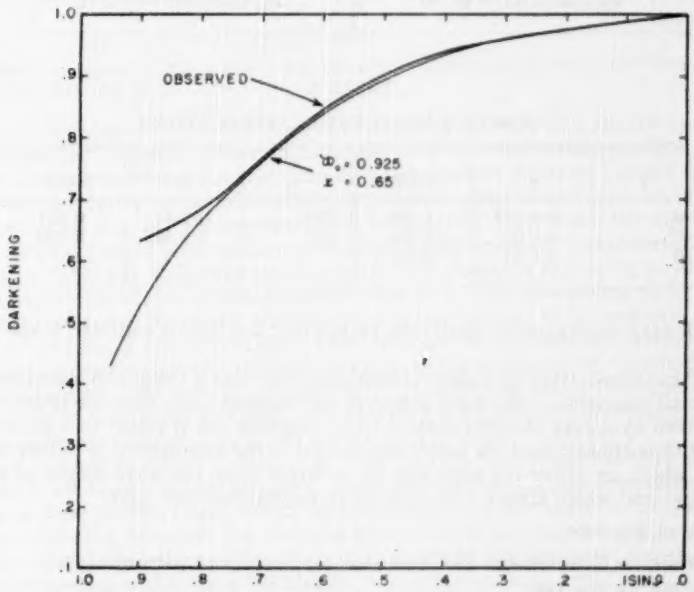

FIG. 9.—Comparison of the observed and theoretical limb-darkening-curves for Saturn in blue light

coefficient," and α is the phase angle in degrees. According to Baldwin's observations,[23] a^* is zero; however, Schoenberg[24] obtained $a^* \sim 0.010$. Our calculations give $a^* \sim 0.005$.

In the photographic case the phase function which gives the closest agreement with observation is $0.925(1 + 0.65 \cos \Theta)$ (Fig. 9 and Table 7). The shape of the scattering

TABLE 7

COMPARISON OF OBSERVED AND THEORETICAL LIMB DARKENING ON SATURN

sin θ	Yellow Light		sin θ	Blue Light	
	Darkening			Darkening	
	Observed	$\omega_0 = 0.985$ $x = 0.900$		Observed	$\omega_0 = 0.925$ $x = 0.650$
0.1	0.99	0.99	0.1	0.99	0.99
.2	.98	.97	.2	.98	.98
.3	.96	.94	.3	.96	.96
.4	.93	.91	.4	.94	.94
.5	.89	.86	.5	.90	.90
.6	.81	.77	.6	.85	.84
.7	.70	.68	.7	.76	.76
.8	.56	.56	.8	.68	.67
0.9	0.40	0.38	0.9	0.63	0.52
m_{vis} (observed) $= +0.89$ m_{vis} (computed) $= +0.90$			m_{pg} (observed) $= +2.01$ m_{pg} (computed) $= +2.11$		

TABLE 8

THEORETICAL VISUAL PHASE-CURVE OF SATURN

α	m	$j(\alpha)/F$	α	m	$j(\alpha)/F$
0°	+0.895	1.265	120°	+2.74	0.231
40°	+1.08	1.066	160°	+5.40	0.020
80°	+1.63	0.641			

diagram is very similar to the visual case, except that less light is scattered in the forward direction.

Yang[25] has shown from very general considerations that if the size of a scattering particle is small compared to the wave length of the incident light, then the phase function will be given by a sum of terms each of which contains $\cos \Theta$ raised to a positive even power. It thus appears that the scattering of light in the atmosphere of Saturn is due to particles which are either the same size as, or larger than, the wave length of ordinary visible light and which absorb blue light more readily than red light.

[23] *M.N.*, **69**, 458, 1909.

[24] *Photometrische Untersuchungen über Jupiter und das Saturnsystem* (Helsingfors, 1921).

[25] *Phys. Rev.*, **74**, 764, 1948.

c) VENUS

The visual phase-curve of Venus can be fairly well represented for $\alpha < 130°$ by isotropic scattering in a semi-infinite atmosphere with $\varpi_0 = 0.95$. For $\alpha > 136°$ the planet is brighter than if its atmosphere obeyed the law of isotropic scattering (Fig. 3 and Table 5). The computed Bond albedo agrees with the observed value[22] of 0.59, even though the theoretical phase-curve deviates considerably from the observed curve at large phase angles. However, this deviation, though large on a logarithmic scale, is small on a flux-density scale, and hence the large phase angles do not influence the determination of A_B very much.

The limb-darkening-curves were computed at those phases for which Barabascheff and Semejkin[17] give their results, viz., $\alpha = 59°.4$, $67°.3$, $77°.2$, $90°.5$, $98°.3$, and $128°.9$. Again isotropic scattering with $\varpi_0 = 0.95$ gives fair results (Fig. 10 and Table 9), except that

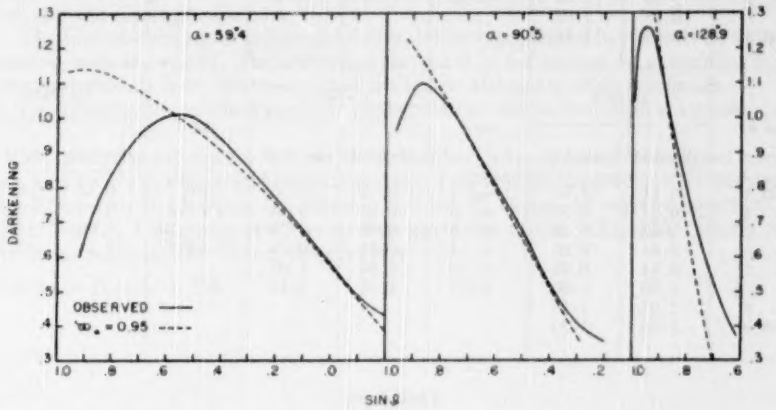

FIG. 10.—Comparison of the observed and theoretical limb-darkening-curves for Venus in yellow light at three phase angles.

close to the limb ($\sin \vartheta > 0.8$) the observed intensities decrease very rapidly and cannot be accounted for by theory. However, it is here that the observations are least reliable. The use of an asymmetric phase function does not improve matters (Table 5, last col.).

Rayleigh scattering by a semi-infinite atmosphere gives magnitudes which are too bright except for $\alpha > 140°$, where the reverse is true (Fig. 3 and Table 10); furthermore, the computed degree-of-polarization-curve is quite different from that observed by Lyot (Fig. 4 and Table 10). It is of interest to notice that Rayleigh scattering gives a nearly symmetrical curve, with a maximum polarization at $\alpha = 90°$ amounting to 30 per cent.

Rayleigh scattering by a finite atmosphere of optical depth $\tau = 0.2$ and with a ground surface which reflects light according to Lambert's law with a Lambert albedo $\lambda_0 = 0.55$ gives a good representation of the phase-curve up to phase angle 130° (Table 10) but is little improvement over isotropic scattering. The degree-of-polarization-curve is very similar in shape to that for Rayleigh scattering in a semi-infinite atmosphere, although the polarization is reduced by a factor of 3 or so (Fig. 4 and Table 10).

It is of interest to notice further that these polarization-curves are very similar to those which Lyot observed for Mercury, Mars, and the moon. It is conceivable that the surfaces of these planets might reflect light according to a law analytically the same as Rayleigh scattering. However, the observed albedos are so low that it would be necessary to assume that the scattering is by a very thin Rayleigh "atmosphere" situated on top of a ground surface which has a low albedo.

TABLE 9

Observed Limb Darkening of Venus at Six Phase Angles Compared with Isotropic Scattering

sin θ	$\alpha = 59°.4$		sin θ	$\alpha = 67°.3$		sin θ	$\alpha = 77°.2$	
	Observed	$\varpi_0 = 0.95$		Observed	$\varpi_0 = 0.95$		Observed	$\varpi_0 = 0.95$
−0.2	0.43	0.39	0.0	0.44	0.42	+0.2	0.37	0.39
− .1	0.49	0.48	+ .1	0.53	0.52	+ .3	0.46	0.51
.0	0.58	0.57	+ .2	0.65	0.63	+ .4	0.62	0.64
+ .1	0.68	0.66	+ .3	0.78	0.72	+ .5	0.78	0.78
+ .2	0.77	0.76	+ .4	0.88	0.81	+ .6	0.95	0.90
+ .3	0.84	0.83	+ .5	0.95	0.89	+ .7	1.00	1.00
+ .4	0.94	0.90	+ .6	1.00	0.96	+0.8	0.98	1.08
+ .5	1.00	0.97	+ .7	1.02	1.03			
+ .6	1.00	1.02	+0.8	1.01	1.09			
+ .7	0.95	1.07						
+0.8	0.84	1.12						

sin θ	$\alpha = 90°.5$		sin θ	$\alpha = 98°.3$		sin θ	$\alpha = 128°.9$	
	Observed	$\varpi_0 = 0.95$		Observed	$\varpi_0 = 0.95$		Observed	$\varpi_0 = 0.95$
+0.3	0.41	0.37	+0.4	0.48	0.36	+0.7	0.52	0.29
+ .4	0.52	0.52	+ .5	0.63	0.53	+ .8	0.79	0.69
+ .5	0.68	0.66	+ .6	0.78	0.70	+ .86	1.00	1.00
+ .6	0.81	0.80	+ .7	0.91	0.84	+0.9	1.16	1.19
+ .7	0.94	0.94	+ .8	1.04	1.02			
+ .74	1.00	1.00	+0.9	1.18	1.18			
+ .8	1.05	1.08						
+0.9	1.08	1.20						

TABLE 10

Results of Computations for Rayleigh Scattering

A. Semi-infinite atmosphere

Phase Angle	Degree of Polarization	$j_r(\alpha)$*/F	$j_l(\alpha)$†/F	m(Venus)‡
20°	0.022	1.169	1.118	−5.17
40°	.102	0.983	0.800	−4.90
80°	.298	0.498	0.269	−3.98
120°	.248	0.142	0.0857	−2.66
140°	.119	0.0512	0.0403	−1.67
160°	0.016	0.0110	0.0107	−0.11

B. Finite atmosphere with $\tau = 0.2$; ground surface with Lambert albedo $\lambda_0 = 0.55$

Phase Angle	Degree of Polarization	$j_r(\alpha)/F$	$j_l(\alpha)/F$	m(Venus)
20°	0.005	0.616	0.609	−4.49
80°	096	.262	.216	−3.47
140°	0.041	0.0327	0.0302	−1.27

* j_r refers to the light which vibrates perpendicular to the intensity equator.
† j_l refers to the light which vibrates parallel to the intensity equator.
‡ m(Venus) is the computed magnitude of Venus.

The photographic phase-curve can be represented by isotropic scattering (semi-infinite atmosphere) with $\varpi_0 = 0.95$. A color index of 0.8 was assumed. The agreement is exactly similar to that in the visual case, viz., the planet is too bright for $\alpha > 130°$. Unfortunately, an inconsistency arises. The limb-darkening-curves (in blue) require ϖ_0 to be around 0.2 or so!

Another possibility is to use the phase function $(1 + q \cos \Theta + p \cos^2 \Theta)/(1 + [p/3])$. The formula for this case has been derived by Chandrasekhar.[28] The writer made some calculations with various values of q and p but could not obtain agreement with observation.

The conclusions of the present work on Venus may be summarized as follows:

1. The visual and photographic phase-curves can be represented by known laws of diffuse reflection for $\alpha < 130°$. At larger phase angles the planet is much too bright. Isotropic scattering with $\varpi_0 = 0.95$ appears to give the closest agreement in both the visual and the photographic cases.
2. The limb darkening in yellow light can also be represented fairly well by isotropic scattering with $\varpi_0 = 0.95$. The darkening for $\sin \vartheta > 0.8$ cannot be accounted for by theory; however, it is in this region that the observations are most unreliable.
3. The polarization of the Venus atmosphere is not due to Rayleigh scattering.

I wish to express my thanks to Dr. Chandrasekhar, who suggested this line of research to me, and for his guidance and encouragement. I also greatly appreciate the discussions which I had with Dr. Kuiper, Dr. Münch, and Dr. T. D. Lee on various aspects of this subject. Finally, I must express a very deep gratitude to the "G.I. Bill," which made possible my study at the Yerkes Observatory.

[28] *Radiative Transfer*, p. 158.

O_2 EMISSION BANDS IN THE INFRARED SPECTRUM OF THE NIGHT SKY

A. B. MEINEL
Yerkes Observatory
Received July 14, 1950

ABSTRACT

A study of the profile of the (0, 1) 8645 A band of the atmospheric $^1\Sigma - {}^3\Sigma$ system of O_2 has indicated a normal rotational temperature of 150° ± 20° K. A temperature of 200° ± 10° K was obtained from a spectrogram that recorded a strong enhancement of this band on December 29, 1949. The temperature and a comparison with the *OH* emission bands places the oxygen-emission stratum at 80 km.

I. EMISSION-BAND INTENSITIES

Night-sky emission from the atmospheric $^1\Sigma - {}^3\Sigma$ system of O_2 was observed by the author in 1948.[1] These early observations clearly showed the *P* and *R* branches of this band at 8629 A and 8659 A, respectively, but with insufficient resolution to enable a study of the profile. Since the positions of other higher members of the atmospheric system of O_2 occur in near-by spectral regions containing emissions, it was thought that other bands of this system might be present in emission. A recent series of observations by the author at Yerkes Observatory, made with a spectrograph of higher resolution, has shown that *only the (0, 1) band appears in emission*. In this respect, the night-sky O_2 bands are similar to the O_2 bands obtained by Kaplan[2] in laboratory afterglow spectra, since the laboratory spectra show only the (0, 0) and (0, 1) bands in emission. In the case of the night sky, the (0, 0) emission band must be very intense in the stratum in which the radiation originates. According to the theoretical emission intensities for the $^1\Sigma - {}^3\Sigma$ O_2 bands computed by J. Hunaerts,[3] shown in Table 1, the (0, 0) band should be twenty-seven times as intense as the (0, 1) band. The great mass of O_2 in the ground state in the lower atmosphere, however, completely reabsorbs this radiation. The (0, 1) band is observable, since less than 10^{-3} of the O_2 molecules are in the $v'' = 1$ level at 300° K. Correspondingly, this band is not observed in absorption on solar spectrograms.

It is possible to place an upper limit on the population in the excited $^1\Sigma(v' = 1)$ level from the night-sky observations. The observations indicate an upper limit for the intensity of the (1, 1) band at 7708 A equal to one-fifteenth the intensity of the (0, 1) band. Consequently, the ratio of the populations in the $^1\Sigma(v' = 0)$ and the $^1\Sigma(v' = 1)$ levels is

$$\frac{N_{(v'=0)}}{N_{(v'=1)}} \geqslant 33$$

with the emission intensities given by Hunaerts.

The fact that the laboratory and night-sky spectra are so similar indicates that a common mechanism must be affecting the excitation. The mechanism populating the $v' = 0$ level, however, need not necessarily be the primary mechanism. D. R. Bates[4] has suggested that the selective population of the $v' = 0$ level could be brought about by an exchange of electronic excitation during collisions by means of the following process:

$$O_2{}^1\Sigma\,(v' > 0) + O_2{}^3\Sigma\,(v'' = 0) \rightarrow O_2{}^3\Sigma\,(v'' > 0) + O_2{}^1\Sigma\,(v' = 0)\,,$$

$$O_2{}^1\Sigma\,(v' = 0) \rightarrow O_2{}^3\Sigma + h\nu\,(0, n)\,.$$

[1] *Pub. A.S.P.*, **60**, 373, 1948; *Trans. Amer. Geophys. Union*, **31**, No. 1, 21, 1950.
[2] *Nature*, **159**, 673, 1947.
[3] Private communication by M. Nicolet. [4] Private communication.

This process would remove the restriction of a photochemical resonance phenomenon; however, the fact that this exchange process would operate for the oxygen emission, but for none of the other electronic bands observed in the night-sky airglow spectrum, opens the exchange suggestion to question.

II. TEMPERATURE OF THE O_2 STRATUM

The observations made at the Yerkes Observatory have provided spectra of sufficient resolution to enable the determination of the rotational temperature of the (0, 1) O_2 band. A rotational temperature determined from a homonuclear molecule like O_2 should be identical with the kinetic temperature of the molecules in the stratum, since rotational and vibrational transitions are forbidden. Even though these transitions are permitted for the *OH* molecule, whose emission originates from approximately the same elevation, the *OH* bands give a rotational temperature that must be very close to the kinetic temperature.[5] The lifetime of the $^1\Sigma - {}^3\Sigma$ O_2 bands is sufficiently long ($\sim$7 sec.) to allow a

TABLE 1

EMISSION INTENSITIES FOR THE $^1\Sigma - {}^3\Sigma$ ATMOSPHERIC BANDS OF OXYGEN

v'	v''				
	0	1	2	3	4
0	7619.3 A 1.00000	8644.7 A 0.03762	9965.6 A 0.00213	11730 A 0.00081	14208 A 0.000003
1	6882.5 0.10350	7708.4 0.82982	8741.5 0.06389	10071 0.00561	11843 0.00029
2	6286.6 0.00043	6968.7 0.19302	7802.3 0.68567	8844.3 0.08041	10183 0.00980
3	5795.1 0.00021	6369.8 0.00144	7059.2 0.26875	7901.5 0.55769	8953.7 0.09853
4	5383.1 0.00001	5875.4 0.00076	6457.1 0.00314	7154.7 0.33067	8006.7 0.45063

redistribution of the rotational states in accordance with the rotational constant for the excited state, even if the above electronic exchange mechanism is operative. It is important that the validity of the rotational temperature for O_2 be stressed, since the resulting temperatures are quite low.

The intensity of a rotational line is given by an equation of the form

$$I = cie^{-B_v J(J+1)/0.7T} \qquad (B_v = 1.392 \text{ cm}^{-1}),$$

where c is approximately constant over the small range of frequency of a molecular band, i is the intensity factor for the particular line, and Bv is the rotational constant for the upper vibrational level of the transition. The intensity factors for the intercombination $^1\Sigma - {}^3\Sigma$ bands, derived by R. J. Schlapp,[6] are as follows:

$$i(P_2) = \tfrac{1}{2}(J+2); \quad i({}^PQ) = \tfrac{1}{2}J; \quad i({}^RQ) = \tfrac{1}{2}(J+1); \quad i(R_2) = \tfrac{1}{2}(J-1),$$

[5] A. B. Meinel, *Ap. J.*, **112**, 120, 1950. [6] *Phys. Rev.*, **39**, 806, 1932.

where J is the numbering for the upper ($^1\Sigma$) state. In the case of the O_2 bands, rotational lines originate only from the even J-values.

The rotational-line positions for the (0, 1) O_2 band were computed for the P_2 and R_2 branches by means of the molecular constants given by Sponer. The line positions for the ^PQ and ^RQ branches were then obtained from the spacing observed for the (0, 0) band, as follows:

$$^PQ(J) - P(J) \cong -2.0 \text{ cm}^{-1}, \qquad ^RQ(J) - R(J) \cong +2.0 \text{ cm}^{-1}.$$

The resultant profile for the (0, 1) band was obtained by summing the individual rotational line intensities over an idealized profile of the slit and camera. It should be noted that the minimum of the O_2 band profile is displaced 2.4 cm^{-1} to the blue of the actual band origin.

Six spectra obtained at the Yerkes Observatory on different nights were microphotometered to obtain the profile of the (0, 1) O_2 band. During five nights this emission

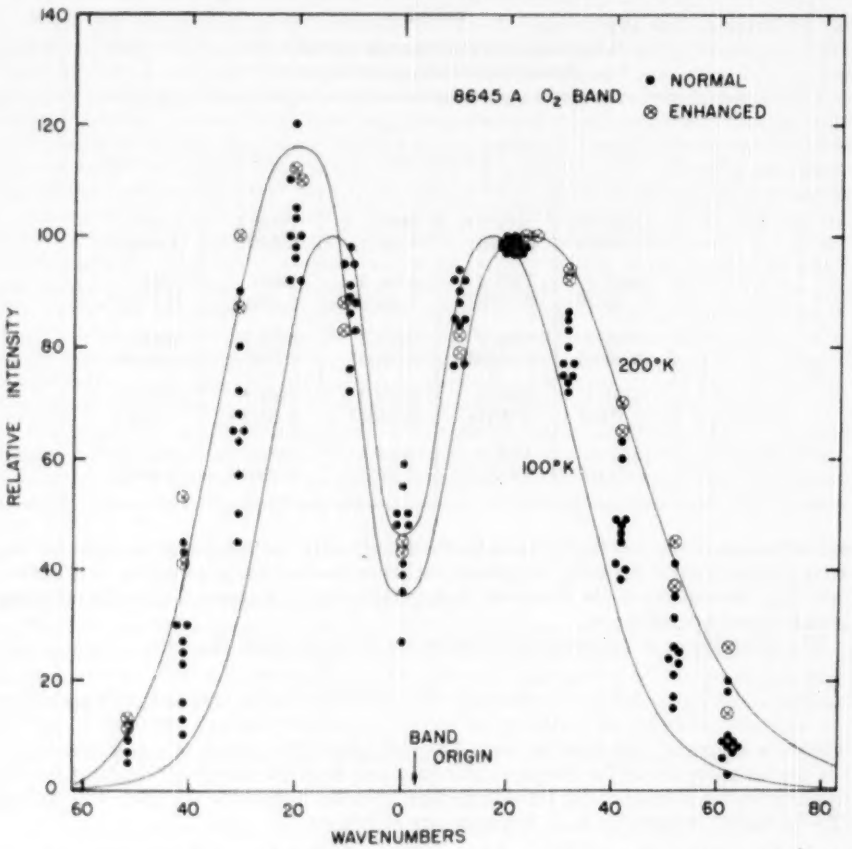

FIG. 1.—Temperature-profile relationship as observed and as computed for the (0, 1) 8645 A O_2 band.

appeared to be of approximately constant intensity; however, on December 29, 1949, the intensity was more than five times as great. No auroral emissions were observed, and the *OH* bands were unchanged. The cause of this oxygen "aurora" is not known. Each spectrum, covering a vertical angle of 30° in the sky, was microphotometered at two zenith distances. The ordinates of the tracings, measured at intervals of approximately 10 cm^{-1}, are plotted in Figure 1. The ordinates for the enhanced band are indicated by crosses. Superimposed on this figure are theoretical profiles for $T = 100°$ K and 200° K. The scatter in the points may be largely the result of a real scatter in the temperatures, since the points for any one profile tend to fall either high or low. From this diagram it is evident, however, that the O_2 band indicates a low temperature. The average for the five normal nights is 150° ± 20° K. When the band was enhanced, the temperature was 200° ± 10° K.

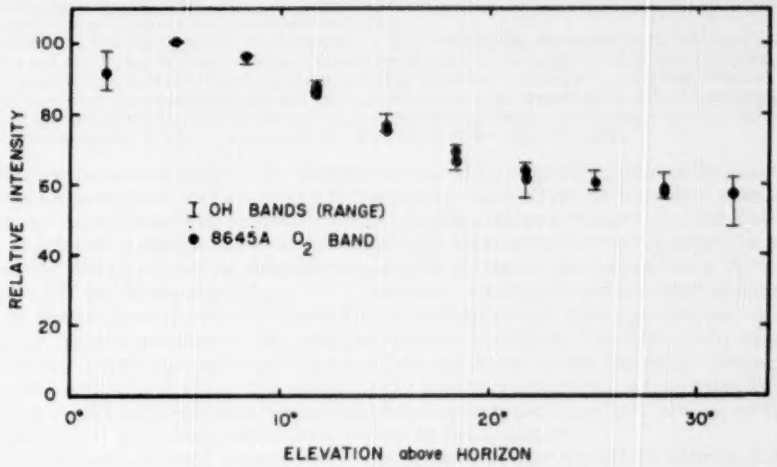

FIG. 2.—Observed variation of intensity with elevation above the horizon for the infrared *OH* bands and the (0, 1) 8645 A O_2 band.

III. HEIGHT OF THE O_2 EMISSION STRATUM

The temperature of 150° K appears to locate uniquely the height of the emission stratum in view of recent V-2 flights. The V-2 observations recorded a minimum temperature approaching 150° K at a height of 80 km.

A second method of establishing the height of the O_2 emission stratum is to measure the variation of intensity of the emission with zenith distance and then to apply the modified van Rhijn method. A direct determination of the zenith-distance intensity variation is difficult. Photoelectric techniques cannot be used, since it would be difficult to isolate in wave lengths the O_2 emission because of the strong *OH* bands on each side. The recent determination of height for the *OH* stratum of 70 km by F. E. Roach, H. B. Pettit, and D. Williams,[7] however, makes it feasible to intercompare the zenith-distance intensity variation of the O_2 and *OH* emissions in order to establish a relative height for the O_2 emission. Tracings were made of the (0, 1) O_2 band, the *Q* and *R* branches of the (7, 3) 8830 A *OH* band, and the *Q* and *P* branches of the (6, 2) 8347 A *OH* band. The or-

[7] *J. Geophys. Res.*, **55**, No. 2, 183, 1950.

dinates, normalized to unity at the maximum, are shown in Figure 2. This diagram shows that, to within the low accuracy of this procedure, the O_2 emission originates from the same region as does the *OH* emission. This result would then be in agreement with a height of 80 km, as is indicated by the temperature.

The author is indebted to F. E. Roach and his colleagues for information in advance of publication. This investigation has been supported by the Office of Naval Research in co-operation with the Lick Observatory and the Yerkes Observatory.

PHOTOELECTRIC MAGNITUDES AND COLORS OF STARS IN SELECTED AREAS 57, 61, AND 68

JOEL STEBBINS, A. E. WHITFORD, AND H. L. JOHNSON
Mount Wilson and Palomar Observatories and Washburn Observatory
Received July 24, 1950

ABSTRACT

Magnitudes and colors of 102 stars in three Selected Areas have been obtained from photoelectric observations at the 60-inch and 100-inch telescopes on Mount Wilson. The range covered extends from photographic magnitude 9.0 to 19.3. Comparison with the North Polar Sequence gave data for converting all magnitudes and colors to the International System.

In all three Selected Areas the difference $P_{g_p} - P_{g_{int}}$ between the photoelectrically determined magnitudes and the *Mount Wilson Catalogue* values is nearly zero at the bright end but shows progressively larger positive values as the faint limit is reached. The difference ranges up to +0.6 mag. Various tests confirm the linear response of the photoelectric apparatus and point toward an error in the photographic scale. If the trend found in the Selected Areas should prove applicable to the nebular counts, the calculated nebular density would be lowered in the outer parts of the explored region.

The magnitudes of stars in the Selected Areas, while originally intended by Kapteyn as data for analysis of stellar density in the galaxy, have served as secondary standards for many studies involving globular clusters, stars in resolved galaxies, and the distribution of galaxies in space. Errors in the magnitude scale would obviously affect the scale of galactic distances and the absolute magnitudes of stars in resolved galaxies. A. S. Eddington,[1] P. ten Bruggencate,[2] and W. Fricke[3] have all emphasized the effect of scale errors in the analysis of nebular counts and have pointed out that cosmological conclusions are quite dependent on the precision of the magnitudes. The desirability of a recalibration of the magnitude scale in a few Selected Areas by the inherently linear photoelectric method is obvious. The advent of the photomultiplier tube has so extended the working magnitude limit that almost all the photographic range can now be covered, leaving only about 2 mag. at the faint end to be extrapolated.

The observations here reported were undertaken at the request of Messrs. Edwin Hubble and Walter Baade, both of whom gave assistance at the telescope in the initial stages. The work was begun by Stebbins during a visit to Mount Wilson in 1947, continued by Whitford in 1948, and extended by Whitford and Johnson in 1949. Both the 60-inch and the 100-inch telescopes were used.

The same refrigerated 1P21 multiplier and field-lens combination employed in the study of the colors of faint nebulae[4] was used for the stars measured in 1947 and 1948. Spectral sensitivity-curves and effective wave lengths as measured after the 1947 season are given in the report on the nebulae. A new multiplier in a different mounting was substituted in 1949. Since the compound field lens in the latter contained only fused-quartz components, a Corning No. 7380 glass was added to the filters to give about the same ultraviolet cutoff as the flint glass did in the previous arrangement. The spectral sensitivity-curves for the 1949 combination are given in another paper by H. L. Johnson.[5] The same filters were used in all three years. These were Schott BG12, 1 mm thick, for blue, and Schott GG7, 2 mm thick, for yellow.

The observing procedure for faint stars was finally adopted as a standard for all, re-

[1] *M.N.*, **97**, 156, 1937.
[2] *Naturwiss.*, **25**, 565, 1937.
[3] *Zs. f. Ap.*, **14**, 56, 1937.
[4] Stebbins and Whitford, *Mt. W. Contr.*, No. 753; *Ap. J.*, **108**, 413, 1948.
[5] *Ap. J.*, **112**, 240, 1950.

gardless of brightness. The star was centered in a focal-plane diaphragm with an aperture 0.7 mm in diameter (11″ at the 100-inch telescope). The difference between star and sky was recorded by moving the hole off the star and back again. In the course of the work it became apparent that the working limit was set not by the photometer but by the observer's ability to put a star near the limit of visibility in the center of a small aperture and to keep it there during a series of deflections. A guiding and offset mechanism designed to facilitate this operation was constructed at the observatory shop in Pasadena from plans drawn up by E. C. Nichols. It was completed in time for use during the 1949 observations and made possible accurate centering on objects too faint to be seen.

The faintest object yet measured is Star No. 57 in SA 68, for which the derived photographic magnitude was found to be 19.26. Figure 1 shows a tracing of the actual record

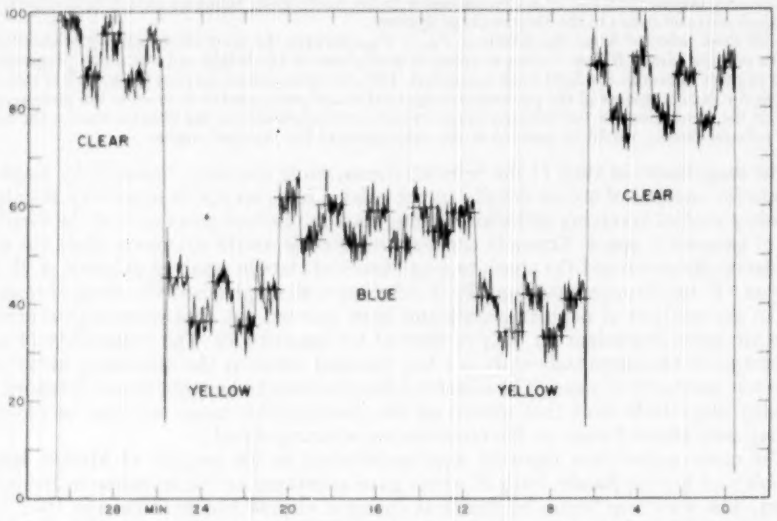

FIG. 1.—Tracing of milliammeter record for faintest star observed. Star No. 57 in SA 68, $Pg_p = 19.26$

of deflections. The sky gave more than a full-scale deflection, and the zero of intensity, representing "dark," was put well off the sheet. The on-off shifts between star and sky comparison area therefore represent a change of only about 7 per cent in the total light. The noise is mainly shot noise generated by the light of the sky; the noise arising from the dark current of the multiplier itself was much smaller. Probably the limit has not yet been reached. A smaller diaphragm and a darker sky would reduce the noise level. Good seeing and careful guiding would be needed.

The "clear" deflections were used for a system of photoelectric magnitudes and the yellow-blue magnitude differences for a system of photoelectric colors. Extinction corrections to reduce the observed magnitudes and colors to no atmosphere were derived to fit the following equations:

$$C_0 = C_z - (k_1 - k_2 C_0) \sec z \,, \tag{1}$$

$$\log d_0 = \log d_z + (f_1 - f_2 C_p) \sec z \,, \tag{2}$$

where C_z is the observed photoelectric color at zenith distance z, and C_0 is the color out-

side the atmosphere. Similarly, d_z and d_0 are the observed and corrected clear deflections, and C_p is the color on the International System derived from C_0 in a manner explained below. The values of the coefficients are summarized along with others in Table 1. In

TABLE 1

EXTINCTION, MAGNITUDE, AND COLOR COEFFICIENTS

Coefficient	1947	1948	1949	Coefficient	1947	1948	1949
k_1	0.129	0.121	0.112	a	0.96	1.03	1.08
k_2	.045	.033	.026	b	1.03	1.07	1.12
f_1	.123	.107	.110	g	0.29	0.25	0.20
f_2	0.024	0.022	0.033				

general, mean coefficients were used, since with a large, slow-moving telescope complete nightly determinations would consume a large fraction of the observing time. In the Selected Areas, magnitudes are relative to one or more local reference stars, and departures from the mean extinction cause only small differential errors. Any deviation from the normal color of a reference star is quickly noted and suitable corrections applied. By 1949, however, enough data on standard stars had accumulated so that nightly adjustments of the coefficients could usually be made.

Data for converting photoelectric magnitudes and colors to the International photographic system were obtained in each season by observations of the North Polar Sequence. Close correlation between the two systems of colors and magnitudes is probable only if both the photographic and the photovisual scales are correct over the interval compared. For stars fainter than the seventh photographic magnitude this turns out to be the case. But the errors in the photographic scale first found in 1938,[6] with a Kunz potassium hydride cell and a shorter base line for colors, again appeared in the present study with a wider range of wave lengths. O. J. Eggen[7] has very recently noted a similar deviation. Since it is unlikely that parallel errors have been made in both the photographic and the photovisual scales, the published colors of the bright NPS stars must also be questioned. Therefore, stars brighter than magnitude 7.0 were excluded from the comparison.

The following equations were used for establishing the relation between photoelectric colors and magnitudes and the International photographic system:

$$C_p = a + bC_0 , \tag{3}$$

$$Pg_p = Pe + gC_p , \tag{4}$$

where Pe is the photoelectric magnitude, and Pg_p and C_p are the photographic magnitude and the color index on the International System derived from photoelectric measures. The coefficients in these equations, as well as the extinction coefficients, are summarized in Table 1. Slight season-to-season changes will be noticed. In particular, it is apparent that the color sensitivity of the photomultiplier used in 1947 and 1948 shifted slightly toward the blue after the response-curves were measured.[4] Since the comparison with the North Polar Sequence was made separately in each year, the photoelectrically determined magnitudes and colors on the International System are not affected.

The final results for the North Polar Sequence are in Table 2. The values for C_{int} are the revised values given by Seares and Joyner.[8] The photographic magnitudes Pg_{int} are

[6] Stebbins and Whitford, *Mt. W. Contr.*, No. 586; *Ap. J.*, **87**, 237, 1938.

[7] *Ap. J.*, **111**, 65, 1950.

[8] *Mt. W. Contr.*, No. 701; *Ap. J.*, **101**, 15, 1945.

those of the Rome Report,[9] adjusted by dividing the revision in C_{int} equally between the Pg and the Pv magnitudes. In general, there is very satisfactory agreement between the two methods of determining magnitude and color. The magnitude differences are plotted at the top of Figure 2. For the nine stars observed in all three seasons (shown as filled dots in the figure) the mean differences are as follows:

$$\overline{Pg_p - Pg_{int}} = \pm 0.018 \text{ mag.},$$

$$\overline{C_p - C_{int}} = \pm 0.019 \text{ mag.}$$

These nine stars may be considered the standard stars upon which the magnitudes and colors of the paper are based. As pointed out by H. L. Johnson,[8] the values of C_p derived from the particular NPS stars here used differ slightly from those derived by O. J. Eggen[7] from a comparison involving another selection including the brightest NPS stars. Apparently, these bright stars have errors predominantly of one sign, not only in

TABLE 2

NORTH POLAR SEQUENCE

NPS	Pg_p	Pg_{int}	$Pg_p - Pg_{int}$	C_p	C_{int}	$C_p - C_{int}$	Class*
6	7.15	7.12	+0.03	+0.06	+0.06	0.00	1
2r	7.90	7.91	− .01	+1.56	+1.57	− .01	1
10	9.17	9.15	+ .02	+0.12	+0.12	.00	1
4r	9.24	9.23	+ .01	+1.02	+1.02	.00	1
13	10.51	10.55	− .04	+0.24	+0.22	+ .02	2
8r	11.43	11.43	.00	+1.02	+0.96	+ .06	2
16	11.56	11.57	− .01	+0.32	+0.34	− .02	1
19	12.66	12.68	− .02	+0.41	+0.44	− .03	1
12r	13.80	13.78	+ .02	+1.27	+1.30	− .03	2
426	13.87	13.89	− .02	+0.51	+0.51	.00	3
25	14.16	14.12	+ .04	+0.57	+0.56	+ .01	3
26	14.67	14.65	+ .02	+1.01	+1.00	+ .01	3
277	15.35	15.32	+0.03	+0.68	+0.74	−0.06	3

* Class 1, well observed in all three seasons; class 2, observed in two seasons; class 3, only one observation or discordant.

Pg_{int} but also in C_{int}; since they are nearly all blue stars, this affects the values of both a and b in equation (3).

The magnitudes and colors of stars in the three Selected Areas are given in Tables 3–5. The star numbers and photographic magnitudes Pg_{int} are those of the *Mount Wilson Catalogue*.[10] Each season's results were reduced independently, and the results were combined with no seasonal corrections on the basis of unit weight for each night. Systematic season-to-season differences averaged 0.012 mag. for both Pg_p and C_p.

Star No. 59 in SA 68, for which $Pg_p = 18.56$, $C_p = +0.14$, is the bluest star measured in the Selected Areas. Probably it is a white dwarf, since a main-sequence star of this magnitude and color would lie far outside the galaxy.

The differences between the new magnitudes and the catalogue values are shown graphically in Figure 2. A rather serious divergence appears between the photoelectric and photographic scales in all three Selected Areas. It is so large that random photoelectric errors are of no consequence. On the basis of internal night-to-night consistency, the

[9] *Trans. I.A.U.*, 1, 69, 1922.

[10] Seares, Kapteyn, and van Rhijn, *Mount Wilson Catalogue of Photographic Magnitudes in Selected Areas 1–139* (Washington: Carnegie Institution of Washington, 1930).

probable error of one Pg_p on a single night is

$$\pm 0.012 \text{ mag. for } Pg_p < 17.0\,; \quad \pm 0.025 \text{ mag. for } Pg_p > 17.0\,.$$

In considering the possibility of systematic error in the photoelectric results, nonlinearity of the amplification beyond the 1P21 can be ruled out. Beginning in 1948, observations were by a recording milliammeter. The d.c. amplifiers (different in 1948 and 1949)

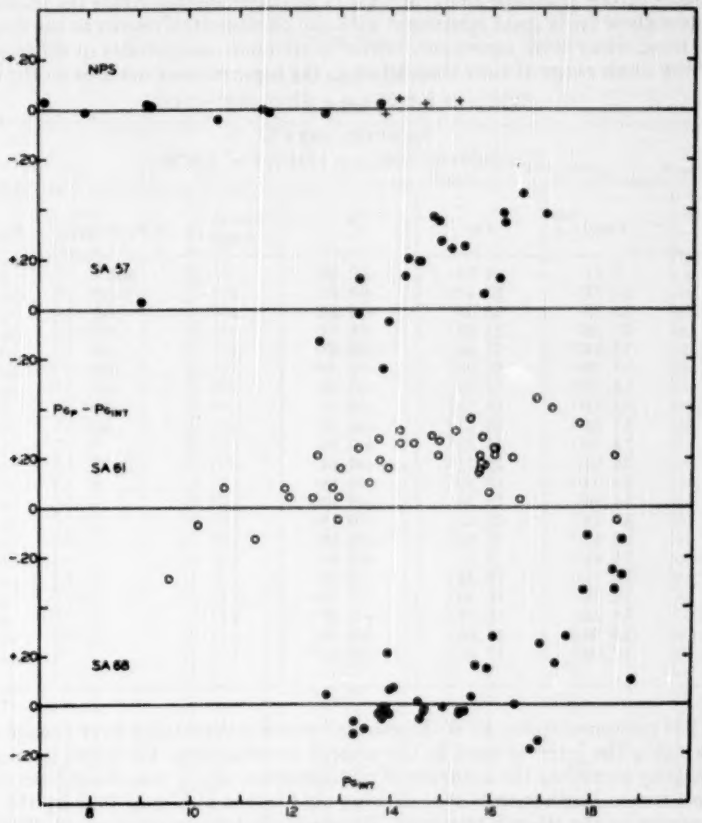

FIG. 2.—Difference between photoelectrically determined magnitudes and previous photographic magnitudes. The crosses represent Class 3 stars in Table 2.

between the multiplier and the milliammeter incorporated so much feedback that their linearity was beyond question, and the gain depended only on resistance ratios. Periodic calibrations, by injecting measured voltage, checked the linearity of the scale and the constancy of the attenuator ratios. The latter showed variations of a few tenths of 1 per cent at most. In 1947 a one-stage VX41 amplifier between the multiplier and the galvanometer was necessary beyond magnitude 13.0 on the 100-inch telescope. Here the results did depend on the linearity and constancy of VX41 characteristics, but these were

adequately checked. There is no systematic trend in the magnitude scale between the 1947 and 1948 seasons.

Internal evidence arguing for the correctness of the photoelectric scale would include the following: (1) the NPS measures on the 60-inch telescope show agreement with the photographic scale at the same intensity level that the 100-inch measures (1.1 mag. fainter) in both SA 57 and SA 61 show disagreement; (2) 60-inch and 100-inch measures on the same stars down to the sixteenth magnitude show as good internal agreement as do measures on one telescope alone; and (3) in all three Selected Areas the photographic magnitudes show fairly good agreement with the photoelectric results at the bright end, but the trend away from agreement begins at different magnitudes in different areas.

Over the whole range of more than 10 mag., the basic reliance must be on the linearity

TABLE 3

SELECTED AREA 57

Central Star (1950); $\alpha = 13^h6^m2$; $\delta = +29°39'$

No.	P_{Stat}	P_{Ep}	C_p	No. of Nights	A.D. of P_{Ep}	$P_{Ep}-P_{Stat}$
57	9.01	9.04	+0.46	.....	std	+0.03
29	12.57	12.44	+0.75	3	±0.02	− .13
11	13.35	13.33	+0.40	4	.02	− .02
52	13.36	13.48	+1.18	2	.04	+ .12
8	13.84	13.60	+0.47	3	.03	− .24
77	13.95	13.90	+0.69	3	.01	− .05
16	14.25	14.38	+0.90	2	.01	+ .13
54	14.32	14.52	+0.51	2	.00	+ .20
59	14.53	14.72	+0.55	2	.02	+ .19
58	14.59	14.78	+0.71	1	.....	+ .19
7	14.84	15.21	+0.44	2	±0.02	+ .37
72	14.95	15.30	+0.28	1	.....	+ .35
40	14.99	15.26	+0.28	1	.....	+ .27
82	15.18	15.42	+0.15	1	.....	+ .24
25	15.44	15.69	+0.65	1	.....	+ .25
36	15.81	15.87	+0.81	1	.....	+ .06
15	16.12	16.24	+0.49	1	.....	+ .12
61	16.21	16.59	+0.77	1	.....	+ .38
63	16.24	16.58	+0.87	1	.....	+ .34
74	16.59	17.05	+0.48	1	.....	+ .46
17	17.08	17.46	+0.36	1	.....	+0.38

of the 1P21 photomultiplier. R. W. Engstrom[11] tested several tubes over a range of intensities bridging the interval used in the present investigation. He found no departures from linearity exceeding the accuracy of measurement, which was about 3 per cent over the whole range. Further tests of scale were obtained in 1947 and 1949 by the use of a 3-mag. screen on the 60-inch telescope. The screen factor was constant to ±0.015 mag. (p.e.) over the magnitude range from 6.0 to 14.7 unscreened. With the screen the lowest intensity corresponded to magnitude 18.8 on the 100-inch telescope. A special laboratory check down through the intensity levels used for the faintest stars showed a constant absorption factor for a neutral filter of 2.87 ± 0.008 (p.e.) mag. In both tests, the residuals showed no significant trend with changing intensity.

We are forced to conclude, therefore, that a scale error has crept into the photographic magnitudes in the Selected Areas. W. Baade,[12] working from a photographic recalibration of SA 68, has given corrections to magnitudes of stars in the M31 field amounting

[11] *J. Opt. Soc. America*, **37**, 420, 1947.

[12] *Mt. W. Contr.*, No. 696; *Ap. J.*, **100**, 137, 1944.

to about half those found here at $Pg_{int} = 18.3$, and in the same sense. In the same M31 field he found that the scale down to $Pg_{int} = 20.0$ ran off in the same sense found in this paper, i.e., the photographic magnitude scale is too compressed. A scale error in this sense, if generally applicable to counts of faint nebulae, would counteract the outward increasing density found by Hubble[13] on the assumption that the red shift is a real recession. Since the argument over the run of the nebular-density function hinges on counts in the range between the eighteenth and twenty-first magnitudes, the photoelectric magnitudes here presented are clearly inadequate to permit any rediscussion of the

TABLE 4

SELECTED AREA 61

Central Star (1950); $\alpha = 17^h0^m8$; $\delta = +29°53'$

No.	P_{Est}	P_{Ep}	C_p	No. of Nights	A.D. of P_{Ep}	$P_{Ep} - P_{Est}$
80	9.56	9.27	+0.29	.....	std	−0.29
4s	10.14	10.07	+0.27	3	±0.02	− .07
34s	10.68	10.76	+0.43	1	.....	+ .08
52s	11.29	11.16	+0.24	1	.....	− .13
123s	11.89	11.97	+0.47	3	.02	+ .08
19	11.98	12.02	+0.93	1	.....	+ .04
30	12.43	12.47	+1.08	4	.02	+ .04
96	12.52	12.73	+0.21	3	.01	+ .21
89s	12.84	12.92	+1.20	2	.02	+ .08
108s	12.94	12.87	+1.51	4	.01	− .07
129s	12.96	13.00	+1.54	2	.03	+ .04
44	13.00	13.16	+0.56	4	.02	+ .16
48	13.33	13.57	+0.74	7	.01	+ .24
23s	13.56	13.66	+0.54	3	.01	+ .10
11	13.74	14.02	+0.68	3	.01	+ .28
32	13.77	13.96	+0.74	3	.02	+ .19
21	13.93	14.09	+0.85	2	.03	+ .16
66	14.15	14.46	+0.85	3	.02	+ .31
100	14.17	14.43	+0.50	5	.02	+ .26
88	14.43	14.69	+0.92	4	.03	+ .26
7	14.80	15.09	+0.57	3	.01	+ .29
143	14.92	15.13	+0.77	2	.00	+ .21
117	14.94	15.21	+0.68	3	.01	+ .27
130	15.27	15.58	+0.85	3	.01	+ .31
97	15.56	15.92	+0.45	2	.01	+ .36
20	15.73	15.87	+0.84	1	.....	+ .14
121	15.74	15.95	+0.44	2	.03	+ .21
124	15.76	15.92	+0.39	1	.....	+ .16
116	15.78	15.96	+0.57	1	.....	+ .18
36	15.80	16.09	+0.34	2	.00	+ .29
63	15.83	16.00	+0.71	2	.02	+ .17
99	15.92	15.98	+0.64	8	.02	+ .06
95	16.03	16.27	+0.78	1	.....	+ .24
94	16.05	16.26	+0.56	2	.01	+ .21
59	16.07	16.31	+0.54	1	.....	+ .24
51	16.40	16.60	+0.57	1	.....	+ .20
103	16.56	16.59	+0.56	1	.....	+ .03
123	16.88	17.32	+0.33	2	±0.01	+ .44
76	17.18	17.58	+0.59	1	.....	+ .40
101	17.73	18.07	+0.76	1	.....	+ .34
102	18.42	18.63	+1.43	1	.....	+ .21
79	18.47	18.42	+0.90	1	.....	−0.05

[13] *Mt. W. Contr.*, No. 557; *Ap. J.*, **84**, 517, 1936.

problem. But the results thus far suggest the need for much further work on the faint end of the magnitude scale before undertaking any such rediscussion.

This investigation was supported in part by the Research Committee of the Graduate School of the University of Wisconsin from funds supplied by the Wisconsin Alumni Research Foundation. The construction of the photometer used in the latter part of the observations was aided by support from the Office of Naval Research.

TABLE 5

SELECTED AREA 68

Central Star (1950); $\alpha = 0^h14^m0$; $\delta = +15°34'$

No.	P_{Stat}	P_{Ep}	C_p	No. of Nights	A.D. of P_{Ep}	$P_{Ep}-P_{Stat}$
18	12.71	12.75	+0.54	3	±0.01	+0.04
16	13.27	13.20	+0.43	2	.02	− .07
8s	13.27	13.15	+1.47	1	.....	− .12
72	13.47	13.37	+1.34	.....	std	− .10
76	13.76	13.72	+0.41	.....	std	− .04
45	13.81	13.80	+0.80	1	.....	− .01
12s	13.82	13.76	+0.42	1	.....	− .06
91	13.83	13.80	+0.86	2	.01	− .03
14	13.91	13.90	+0.84	2	.00	− .01
84	13.93	14.14	+0.44	2	.00	+ .21
99	13.97	14.03	+0.53	1	.....	+ .06
106	13.97	13.93	+0.76	1	.....	− .04
119	14.05	14.12	+0.55	1	.....	+ .07
137	14.54	14.55	+0.75	1	.....	+ .01
71	14.58	14.52	+0.58	2	.00	− .06
83	14.66	14.63	+0.82	3	.02	− .03
120	14.67	14.65	+0.51	1	.....	− .02
51	15.03	15.02	+0.64	2	.00	− .01
110	15.36	15.33	+0.40	1	.....	− .03
39	15.37	15.33	+0.58	1	.....	− .04
122	15.37	15.34	+0.62	1	.....	− .03
61	15.48	15.45	+0.63	1	.....	− .03
132	15.60	15.63	+0.92	2	.02	+ .03
23	15.68	15.84	+0.34	3	.01	+ .16
50	15.92	16.07	+1.34	2	.00	+ .15
73	16.01	16.29	+0.66	1	.....	+ .28
85	16.49	16.49	+0.60	1	.....	.00
129	16.79	16.61	+0.50	1	.....	− .18
94	16.96	16.81	+0.83	1	.....	− .15
27	16.96	17.21	+0.69	1	.....	+ .25
87	17.27	17.44	+0.44	2	.00	+ .17
60	17.48	17.76	+0.68	2	.02	+ .28
44	17.81	18.28	+1.19	1	.....	+ .47
59	17.87	18.56	+0.14	2	.02	+ .69
63	18.40	18.95	+1.16	2	.08	+ .55
56	18.44	18.91	+0.80	3	.02	+ .47
55	18.80	18.90	+1.15	1	.....	+ .10
64	18.59	19.12	+0.82	1	.....	+ .53
57	18.59	19.26	+1.12	2	±0.06	+0.67

PHOTOMETRIC INVESTIGATIONS OF THE WOLF-RAYET BINARY CQ CEPHEI*

W. A. HILTNER
Yerkes and McDonald Observatories
Received June 22, 1950

ABSTRACT

Three types of photoelectric photometric observations have been made on CQ Cephei: integrated light-curves at effective wave lengths of λ 5300 and λ 3550, polarization, and a light-curve of *He* II 4686. The two light-curves are identical except that both minima are deeper in the ultraviolet. Both curves show a pronounced asymmetry and a broader secondary than primary (Wolf-Rayet component eclipsed). The polarization observations show no variation of polarization (because of the binary nature of the system) greater than 0.005 mag. The light-curve of *He* II 4686 shows two maxima, and these two maxima correspond to the times of conjunctions.

INTRODUCTION

The Wolf-Rayet binary star CQ Cephei, in which one component is a Wolf-Rayet star of class WN5, was first observed in 1941 to show binary motion.[1] These early observations indicated a period of 6.4 days. However, a subsequent investigation showed that this period was too large by a factor of 4, the correct period being 1.641 days.[2] The latter observations further showed pronounced spectral variations. Later, Gaposchkin,[3] using the correct period, showed that the star is also an eclipsing system with two well-defined minima. This system, however, has not met with much favor by investigators working on the formal aspect of Wolf-Rayet stars. The reasons for this are probably obvious. From the spectrographic observations we immediately infer that the system shows remarkable changes with phase and with time. Also, the early light-curve indicated that the system will not lend itself so readily to a photometric interpretation as, for example, will V 444 Cyg. However, to encourage investigations of a theoretical nature on this system, a series of observations was planned in 1946 and has now progressed sufficiently to present some useful material.

Three types of photometric observations were undertaken. Although further spectrographic observations are seriously needed, only occasional spectrograms were obtained. In 1947 two light-curves at two different effective wave lengths were obtained. To secure two light-curves with a significantly different effective wave length seemed especially desirable in view of the work on V 444 Cyg.[4] In 1948 observations were made for the detection of polarization. Since Chandrasekhar[5] showed that we should expect polarization of the radiation from the limb of a star where the opacity is a consequence of electron scattering, it seemed especially desirable to observe a Wolf-Rayet star, since there is good evidence that electron scattering plays an important role in these systems.[6] In 1949 the light-curve of a single emission line (*He* II 4686) was obtained. It was hoped that, if such a curve could be accurately established, we should have some information regarding the distribution of emission about the Wolf-Rayet star.

* *Contributions from the McDonald Observatory, University of Texas*, No. 195.

[1] Dean B. McLaughlin and W. A. Hiltner, *Pub. A.S.P.*, **53**, 328, 1941.

[2] W. A. Hiltner, *Ap. J.*, **99**, 273, 1944.

[3] *Ap. J.*, **100**, 242, 1944.

[4] See Kron and Gordon, *A.J.*, **52**, 154, 1947; and W. A. Hiltner, *Ap. J.*, **110**, 95, 1949.

[5] *Ap. J.*, **103**, 365, 1946.

[6] See Z. Kopal and M. B. Shapley, *Ap. J.*, **104**, 160, 1946.

OBSERVATIONS AT λ 3550 AND λ 5300

All the observations were made with the 82-inch reflector of the McDonald Observatory. Also a 1P21 phototube multiplier was used for the measurement of the radiation. The output from the phototube multiplier was measured directly by a galvanometer, the period of which was 7.1 seconds and the sensitivity 1.8×10^{-10} amperes per millimeter at 2 meters. An Arytron shunt controlled the sensitivity by factors of 2. Deflections employed were such that the maximum deflection never exceeded 140 mm. Two filters were used: a Schott UG2 filter isolated the ultraviolet with an estimated effective wave length of 3550 A, and a Corning No. 3385 isolated the yellow with an effective wave length near 5300 A. The former filter was tested for a red leak, but none was present with the cell employed. The 1947 observing technique was such that three deflections on the comparison star were alternated with three deflections on the variable. The deflections for the comparison star were then used in conjunction with the variable on either side. This procedure, however, does not make succeeding observations entirely independent. The photometer is equipped with a standard radioactive source,[7] so that the over-all sensitivity of the photometer, and hence the extinction, can be easily obtained. This assumes, of course, that the reflectivity of the mirror remains unchanged. For the present investigations, however, small use was made of this feature. For the observations under discussion an accurate knowledge of the extinction was not necessary, and hence a mean extinction was employed. A standard is invaluable when working on a routine color program.

Two comparison stars were used in 1947. Since it was anticipated that the Wolf-Rayet system might show intrinsic variations and that their reality could be established only by a check on the comparison star, BD+56°2813 was employed as a check on BD+56°2815, the star with which CQ Cephei was always compared in the ultraviolet as well as the yellow. Data for the comparison stars and variable are given in Table 1. The two comparison stars were intercompared only in the ultraviolet region. The results of these observations, a total of 24 on 15 different nights, are given in Table 2. If we as-

TABLE 1

Star	α(1900)	δ(1900)	Mag. (HD)	Spec.
BD+56°2813	22^h31^m7	+56° 28′	8.9	A3
BD+56°2815	22^h31^m9	+56° 53′	8.6	A0
CQ Cephei	22^h32^m9	+56° 23′	8.92	WN5

TABLE 2

COMPARISON OF BD+56°2815 AND BD+56°2813, 1947 (ULTRAVIOLET)

Julian Day 2432000+	BD+56°2815 − BD+56°2813 (Mag.)	Julian Day 2432000+	BD+56°2815 − BD+56°2813 (Mag.)	Julian Day 2432000+	BD+56°2815 − BD+56°2813 (Mag.)
430.740	+0.047	448.778	+0.037	453.783	+0.037
439.715	+ .038	449.715	+ .032	454.710	+ .040
444.806	+ .031	449.718	+ .030	456.757	+ .038
445.706	+ .034	451.622	+ .035	456.761	+ .035
445.774	+ .041	451.626	+ .034	457.723	+ .038
447.644	+ .040	451.821	+ .041	457.728	+ .041
447.835	+ .023	451.825	+ .041	458.751	+ .040
448.706	+0.039	452.776	+0.040	459.776	+0.037

[7] V. B. Nikonov kindly suggested to the author in 1946 the use of a radioactive standard light-source for extinction measurements.

sume no variation of the two stars, we find that the probable error of a single observation is 0.0031 mag., which is entirely satisfactory, especially for the ultraviolet, where the extinction is appreciably greater.

A total of 382 and 188 observations in the yellow and ultraviolet, respectively, are listed in Tables 3 and 4. The heliocentric Julian Day of the observation, the observed difference in magnitude (correction for differential extinction applied), the difference in magnitude corrected for intrinsic variation, and the phase are given in these tables. The phases given in these and other tables in this paper were computed on the basis that a primary maximum occurred as follows:

Sept. 28.168, 1947 = JD 2432456.668 and a period of 1.641272 .

OBSERVATIONS FOR POLARIZATION

Although it has been shown previously that the polarization of the radiation from CQ Cephei is sensibly constant, the details of the observations have not been published. The technique employed has been described elsewhere.[8] The individual observations for polarization are given in Table 5. The Julian Day of the observation, the phase, the polarization in magnitude, and the position angle are given.

OBSERVATIONS OF *He* II 4686

In 1949 a series of observations was undertaken to obtain a light-curve of CQ Cephei from the radiation of one emission line. In order to do this, one must first isolate the emission line, preferably with a monochromator, and then compare this line with the neighboring continuum. The equipment employed here consisted of the Cassegrain spectrograph[9] used sensibly as a slitless spectrograph. Although a slight improvement might be expected if seeing were compensated for, no attempt was made to compensate. Compensation for seeing is necessary only when one is interested in high resolution. At such times a narrow entrance slit must be used, and hence fluctuations caused by variations in seeing are fatal unless compensation is employed.[10] In the present investigation the emission line is so broad that a wide second slit is necessary, removing the need for a narrow entrance slit. The Cassegrain spectrograph was used in its CG arrangement, that is, two glass prisms and a 500-mm camera. This combination gives a linear dispersion of 35.3 A/mm at λ 4686. The spectrograph was fitted with an exit slit in the focal plane of the camera which could be moved between two stops; one stop centered the *He* II 4686 line, while the other stop isolated the continuum free of emission lines to the red of *He* II 4686. This slit had a width of 2.06 mm or 72.7 A and a travel between stops of 2.18 mm or 77.0 A. The entrance slit of the spectrograph was set at 0.80 mm, or a projected width of 14.1 A. A field lens was placed back of the exit slit. This lens focused an image of the spectrograph camera lens on the cathode of a 1P21(F) phototube multiplier. The output of this cell was fed to a direct-coupled amplifier, which, in turn, drove a Brown recorder. With the second slit-width noted above, the deflection of the emission was approximately 40 per cent of the underlying continuum. Hence the equivalent width of *He* II is of the order of 20 A. The observing routine was such that a single observation consisted of three deflections, 20 seconds each, on the continuum to the red of *He* II 4686 separated by two deflections of *He* II 4686 plus the underlying continuum. A second star, BD+56°2815, was selected to serve as a check on the extinction and consequently was observed at all wave lengths and on all nights that CQ Cephei was observed.

In order to reduce the observations, some assumption must be made regarding the intensity of the continuum underlying the *He* II 4686 emission. We assume here that if

[8] *Ap. J.*, **109**, 471, 1949. [9] *Contr. McDonald Obs.*, No. 1, p. 74.

[10] See W. A. Hiltner and A. D. Code, *J. Opt. Soc. America*, **40**, 149, 1950.

TABLE 3

Photometric Observations of CQ Cephei, 1947 (Yellow)

Julian Day (Helioc.) 2432000+	CQ Cep - BD+56°2816 (observed)	CQ Cep - BD+56°2816 (corrected)	Phase (Days)	Julian Day (Helioc.) 2432000+	CQ Cep - BD+56°2816 (observed)	CQ Cep - BD+56°2816 (corrected)	Phase (Days)
430.753	+0.035	+0.005	0.345	445.841	-0.144	+0.143	0.662
430.756	+ .045	+ .018	0.348	445.844	+ .146	+ .145	0.665
430.758	+ .043	+ .013	0.350	446.710	+ .222	+ .252	1.531
430.762	+ .038	+ .008	0.354	446.713	+ .227	+ .257	1.534
430.765	+ .038	+ .008	0.357	446.715	+ .230	+ .260	1.536
430.797	+ .028	- .002	0.389	446.722	+ .250	+ .280	1.543
430.807	+ .017	- .013	0.399	446.725	+ .253	+ .283	1.546
430.811	+ .019	- .011	0.403	446.728	+ .255	+ .285	1.549
430.815	+ .021	- .009	0.407	446.763	+ .352	+ .382	1.584
430.818	+ .017	- .013	0.410	446.766	+ .363	+ .393	1.587
430.822	+ .015	- .015	0.414	446.769	+ .361	+ .391	1.590
439.703	+ .145	+ .145	1.089	447.622	+ .356	+ .356	0.802
439.706	+ .138	+ .138	1.092	447.625	+ .357	+ .357	0.805
439.709	+ .136	+ .136	1.095	447.628	+ .359	+ .359	0.808
439.712	+ .130	+ .130	1.098	447.631	+ .363	+ .363	0.811
439.717	+ .126	+ .126	1.103	447.654	+ .373	+ .373	0.834
444.647	+ .119	+ .119	1.109	447.656	+ .374	+ .374	0.836
444.650	+ .116	+ .116	1.112	447.659	+ .367	+ .367	0.839
444.652	+ .114	+ .114	1.114	447.668	+ .373	+ .373	0.848
444.655	+ .110	+ .110	1.117	447.671	+ .373	+ .373	0.851
444.729	+ .041	+ .041	1.191	447.674	+ .369	+ .369	0.854
444.732	+ .035	+ .035	1.194	447.695	+ .363	+ .363	0.875
444.735	+ .032	+ .032	1.197	447.698	+ .370	+ .370	0.878
445.649	- .012	- .013	0.470	447.700	+ .366	+ .366	0.880
445.652	- .008	- .009	0.473	447.703	+ .355	+ .355	0.883
445.654	- .010	- .011	0.475	447.706	+ .356	+ .356	0.886
445.657	- .006	- .007	0.478	447.709	+ .359	+ .359	0.889
445.684	.000	- .001	0.505	447.727	+ .345	+ .345	0.907
445.687	- .002	- .003	0.508	447.729	+ .338	+ .338	0.909
445.689	+ .002	+ .001	0.510	447.732	+ .333	+ .333	0.912
445.782	+ .068	+ .067	0.603	447.735	+ .326	+ .326	0.915
445.784	+ .069	+ .068	0.605	447.737	+ .341	+ .341	0.917
445.833	+ .133	+ .132	0.654	447.740	+ .329	+ .329	0.920
445.836	+ .139	+ .138	0.657	447.759	+ .308	+ .308	0.939
445.838	+0.133	+0.132	0.659	447.762	+0.301	+0.301	0.942

TABLE 5 (Cont'd).

Julian Day (Helioc.) 2432000+	CQ Cep - BD+56°2816 (observed)	CQ Cep - BD+56°2816 (corrected)	Phase (Days)	Julian Day (Helioc.) 2432000+	CQ Cep - BD+56°2816 (observed)	CQ Cep - BD+56°2816 (corrected)	Phase (Days)
447.765	+0.304	+0.304	0.945	449.627	+0.067	+0.055	1.165
447.777	+ .287	+ .287	0.957	449.631	+ .068	+ .056	1.169
447.779	+ .285	+ .285	0.959	449.634	+ .063	+ .051	1.172
447.782	+ .281	+ .281	0.962	449.638	+ .060	+ .048	1.176
447.802	+ .261	+ .261	0.982	449.661	+ .050	+ .038	1.199
447.805	+ .254	+ .254	0.985	449.663	+ .043	+ .031	1.201
447.808	+ .253	+ .253	0.988	449.666	+ .036	+ .024	1.204
447.811	+ .252	+ .252	0.991	449.669	+ .021	+ .009	1.227
447.813	+ .249	+ .249	0.993	449.692	+ .022	+ .010	1.230
447.816	+ .242	+ .242	0.996	449.695	+ .013	+ .001	1.233
447.819	+ .239	+ .239	0.999	449.697	+ .018	+ .006	1.235
447.844	+ .213	+ .213	1.024	449.700	+ .015	+ .003	1.238
447.847	+ .212	+ .212	1.027	449.746	- .004	- .016	1.284
447.850	+ .205	+ .205	1.030	449.749	- .003	- .015	1.287
447.852	+ .205	+ .205	1.032	449.752	- .007	- .019	1.290
447.854	+ .198	+ .198	1.034	451.601	+ .169	+ .169	1.499
447.857	+ .198	+ .198	1.037	451.604	+ .172	+ .172	1.501
447.859	+ .196	+ .196	1.039	451.606	+ .175	+ .175	1.503
447.862	+ .192	+ .192	1.042	451.609	+ .185	+ .185	1.506
448.618	+ .247	+ .229	0.156	451.611	+ .193	+ .193	1.508
448.621	+ .241	+ .223	0.159	451.614	+ .246	+ .246	1.511
448.624	+ .238	+ .220	0.162	451.637	+ .257	+ .257	1.534
448.627	+ .235	+ .217	0.165	451.640	+ .259	+ .259	1.537
448.645	+ .206	+ .188	0.183	451.647	+ .282	+ .282	1.544
448.648	+ .202	+ .184	0.186	451.650	+ .290	+ .290	1.547
448.684	+ .149	+ .131	0.222	451.652	+ .292	+ .292	1.549
448.687	+ .147	+ .129	0.225	451.655	+ .297	+ .297	1.552
448.690	+ .136	+ .118	0.228	451.669	+ .333	+ .333	1.566
448.693	+ .135	+ .117	0.231	451.672	+ .343	+ .343	1.569
448.714	+ .113	+ .095	0.252	451.676	+ .349	+ .349	1.573
448.718	+ .107	+ .089	0.256	451.678	+ .351	+ .351	1.575
448.719	+ .101	+ .083	0.257	451.681	+ .366	+ .366	1.578
448.785	+ .039	+ .021	0.323	451.695	+ .403	+ .403	1.592
448.788	+ .041	+ .023	0.326	451.698	+ .407	+ .407	1.595
448.791	+ .034	+ .016	0.329	451.725	+ .452	+ .452	1.622
448.793	+0.030	+0.012	0.331	451.728	+0.457	+0.457	1.625

TABLE 3 (Cont'd)

Julian Day (Helioc.) 2432000+	CQ Cep − BD+56°2816 (observed)	CQ Cep − BD+56°2816 (corrected)	Phase (Days)	Julian Day (Helioc.) 2432000+	CQ Cep − BD+56°2816 (observed)	CQ Cep − BD+56°2816 (corrected)	Phase (Days)
451.731	+0m.455	+0m.455	1.628	452.637	+0m.324	+0m.324	0.893
451.733	+ .459	+ .459	1.630	452.673	+ .322	+ .322	0.929
451.736	+ .458	+ .458	1.633	452.676	+ .316	+ .316	0.932
451.738	+ .453	+ .453	1.635	452.679	+ .310	+ .310	0.935
451.752	+ .460	+ .460	0.008	452.750	+ .217	+ .217	1.006
451.755	+ .455	+ .455	0.011	452.753	+ .222	+ .222	1.009
451.758	+ .455	+ .455	0.014	452.756	+ .215	+ .215	1.012
451.761	+ .447	+ .447	0.017	452.758	+ .213	+ .213	1.014
451.763	+ .448	+ .448	0.019	452.761	+ .206	+ .206	1.017
451.765	+ .446	+ .446	0.021	452.822	+ .138	+ .138	1.078
451.768	+ .440	+ .440	0.024	452.825	+ .136	+ .136	1.081
451.771	+ .440	+ .440	0.027	452.827	+ .134	+ .134	1.083
451.775	+ .437	+ .437	0.031	452.829	+ .128	+ .128	1.085
451.777	+ .443	+ .443	0.033	452.831	+ .126	+ .126	1.087
451.780	+ .432	+ .432	0.036	453.598	+ .149	+ .149	0.213
451.783	+ .428	+ .428	0.039	453.601	+ .148	+ .148	0.216
451.786	+ .420	+ .420	0.042	453.603	+ .141	+ .141	0.218
451.789	+ .422	+ .422	0.045	453.707	+ .034	+ .034	0.322
451.793	+ .413	+ .413	0.049	453.710	+ .032	+ .032	0.325
451.796	+ .404	+ .404	0.052	453.713	+ .031	+ .031	0.328
451.800	+ .399	+ .399	0.056	453.715	+ .029	+ .029	0.330
451.803	+ .400	+ .400	0.059	453.762	− .001	− .001	0.377
451.806	+ .390	+ .390	0.062	453.765	− .005	− .005	0.380
451.835	+ .343	+ .343	0.091	453.767	− .002	− .002	0.382
451.838	+ .335	+ .335	0.094	453.770	− .005	− .005	0.385
451.848	+ .319	+ .319	0.104	453.772	− .008	− .008	0.387
451.851	+ .314	+ .314	0.107	453.793	− .013	− .013	0.408
451.854	+ .313	+ .313	0.110	453.796	− .018	− .018	0.411
451.958	+ .299	+ .299	0.114	453.833	− .019	− .019	0.448
451.961	+ .296	+ .296	0.117	453.835	− .026	− .026	0.450
451.965	+ .289	+ .289	0.121	453.837	− .022	− .022	0.452
452.600	+ .371	+ .371	0.858	453.839	− .022	− .022	0.454
452.605	+ .375	+ .375	0.861	453.842	− .024	− .024	0.457
452.609	+ .374	+ .374	0.864	451.616	− .012	+ .003	1.231
452.631	+ .356	+ .356	0.887	451.619	− .010	+ .005	1.234
452.634	+0.359	+0.359	0.890	451.622	−0.012	+0.003	1.237

TABLE 3 (Cont'd)

Julian Day (Helioc.) 2432000+	CQ Cep - BD+56°2816 (observed)	CQ Cep - BD+56°2816 (corrected)	Phase (Days)	Julian Day (Helioc.) 2432000+	CQ Cep - BD+56°2816 (observed)	CQ Cep - BD+56°2816 (corrected)	Phase (Days)
454.613	-0.017	-0.002	1.245	455.746	+0.241	+0.241	0.719
454.633	- .015	.000	1.248	455.750	+ .243	+ .243	0.723
454.636	- .016	- .001	1.251	455.779	+ .287	+ .287	0.752
454.690	- .030	- .015	1.305	455.781	+ .293	+ .293	0.754
454.693	- .036	- .016	1.308	455.784	+ .299	+ .299	0.757
454.696	- .038	- .013	1.311	455.786	+ .303	+ .303	0.759
454.698	- .034	- .019	1.313	455.788	+ .307	+ .307	0.761
454.736	- .033	- .018	1.351	455.799	+ .319	+ .319	0.772
454.738	- .027	- 0.12	1.353	455.801	+ .316	+ .316	0.774
454.741	- .028	- .013	1.356	455.804	+ .323	+ .323	0.777
454.769	- .013	+ .002	1.384	455.806	+ .325	+ .325	0.779
454.772	- .014	+ .001	1.387	455.809	+ .332	+ .332	0.782
454.775	- .011	+ .004	1.390	455.811	+ .334	+ .334	0.784
454.777	- .009	+ .006	1.392	455.814	+ .336	+ .336	0.787
454.780	- .006	+ .009	1.395	455.816	+ .339	+ .339	0.789
454.804	+ .023	+ .038	1.419	455.819	+ .341	+ .341	0.792
454.807	+ .025	+ .040	1.422	455.822	+ .338	+ .338	0.795
454.810	+ .025	+ .040	1.425	455.836	+ .359	+ .359	0.809
454.818	+ .034	+ .049	1.433	455.839	+ .356	+ .356	0.812
454.821	+ .052	+ .067	1.436	455.842	+ .360	+ .360	0.815
454.824	+ .035	+ .050	1.439	455.845	+ .362	+ .362	0.818
454.827	+ .044	+ .059	1.442	455.847	+ .360	+ .360	0.820
454.831	+ .052	+ .067	1.446	456.602	+ .341	+ .362	1.575
455.619	+ .052	+ .052	0.592	456.606	+ .346	+ .367	1.579
455.622	+ .050	+ .050	0.595	456.609	+ .355	+ .376	1.582
455.625	+ .058	+ .058	0.598	456.612	+ .362	+ .383	1.585
455.627	+ .054	+ .054	0.600	456.615	+ .375	+ .396	1.588
455.629	+ .058	+ .058	0.602	456.619	+ .380	+ .401	1.592
455.670	+ .117	+ .117	0.643	456.623	+ .386	+ .407	1.596
455.673	+ .120	+ .120	0.646	456.626	+ .392	+ .413	1.599
455.676	+ .122	+ .122	0.649	456.629	+ .400	+ .421	1.602
455.678	+ .130	+ .130	0.651	456.638	+ .413	+ .434	1.611
455.716	+ .190	+ .190	0.689	456.641	+ .415	+ .436	1.614
455.719	+ .194	+ .194	0.692	456.644	+ .416	+ .437	1.617
455.721	+ .196	+ .196	0.694	456.647	+ .423	+ .444	1.620
455.745	+0.232	+0.232	0.718	456.651	+0.424	+0.445	1.624

TABLE 3 (Cont'd)

Julian Day (Heliocc.) 2432000+	CQ Cep - BD+56°2816 (observed)	CQ Cep - BD+56°2816 (corrected)	Phase (Days)	Julian Day (Heliocc.) 2432000+	CQ Cep - BD+56°2816 (observed)	CQ Cep - BD+56°2816 (corrected)	Phase (Days)
456.654	+0.428	+0.449	1.627	456.822	+0.213	+0.234	0.154
456.658	+ .423	+ .444	1.631	456.825	+ .207	+ .228	0.157
456.665	+ .432	+ .453	1.638	456.829	+ .199	+ .220	0.161
456.669	+ .430	+ .451	0.001	456.831	+ .196	+ .217	0.163
456.672	+ .431	+ .452	0.004	457.627	+ .259	+ .284	0.959
456.675	+ .427	+ .448	0.007	457.629	+ .253	+ .278	0.961
456.678	+ .427	+ .448	0.010	457.632	+ .251	+ .276	0.964
456.682	+ .428	+ .449	0.014	457.635	+ .247	+ .272	0.967
456.685	+ .425	+ .446	0.017	457.638	+ .243	+ .268	0.970
456.688	+ .423	+ .444	0.020	457.657	+ .228	+ .253	0.989
456.692	+ .417	+ .438	0.024	457.660	+ .220	+ .245	0.992
456.695	+ .416	+ .437	0.027	457.700	+ .179	+ .204	1.032
456.699	+ .414	+ .435	0.031	457.703	+ .180	+ .205	1.035
456.702	+ .409	+ .430	0.034	457.707	+ .165	+ .190	1.039
456.705	+ .403	+ .424	0.037	457.711	+ .166	+ .191	1.043
456.709	+ .402	+ .423	0.041	457.741	+ .135	+ .160	1.073
456.712	+ .396	+ .417	0.044	457.745	+ .140	+ .165	1.077
456.727	+ .371	+ .392	0.059	457.757	+ .118	+ .143	1.089
456.729	+ .374	+ .395	0.061	457.761	+ .112	+ .137	1.093
456.733	+ .371	+ .392	0.065	457.764	+ .107	+ .132	1.096
456.736	+ .360	+ .381	0.068	457.768	+ .107	+ .132	1.100
456.740	+ .356	+ .377	0.072	457.771	+ .103	+ .128	1.103
456.743	+ .347	+ .358	0.075	458.670	+ .028	+ .006	0.361
456.746	+ .340	+ .361	0.078	458.674	+ .030	+ .008	0.365
456.770	+ .299	+ .320	0.102	458.677	+ .022	.000	0.368
456.774	+ .288	+ .309	0.106	458.681	+ .022	.000	0.372
456.777	+ .288	+ .309	0.109	458.684	+ .019	- .003	0.375
456.781	+ .279	+ .300	0.113	458.734	+ .002	- .020	0.425
456.784	+ .274	+ .295	0.116	458.736	+ .005	- .017	0.427
456.798	+ .248	+ .269	0.130	458.760	+ .001	- .021	0.451
456.802	+ .240	+ .261	0.134	458.763	+ .003	- .018	0.454
456.805	+ .238	+ .259	0.137	458.767	+ .006	- .016	0.458
456.809	+ .231	+ .252	0.141	459.604	- .013	- .013	1.295
456.812	+ .223	+ .244	0.144	459.607	- .020	- .020	1.298
456.815	+ .219	+ .240	0.147	459.611	- .013	- .013	1.302
456.818	+0.211	+0.232	0.150	459.613	-0.012	-0.012	1.304

TABLE 3 (Concluded)

Julian Day (Helioc.) 2432000+	CQ Cep − HD+56°2816 (observed)	CQ Cep − HD+56°2816 (corrected)	Phase (Days)	Julian Day (Heliоc.) 2432000+	CQ Cep − HD+56°2816 (observed)	CQ Cep − HD+56°2816 (corrected)	Phase (Days)
459.615	−0.012	−0.012	1.306	459.723	+0.033	+0.033	1.414
459.638	− .015	− .015	1.329	459.751	+ .066	+ .066	1.442
459.640	− .011	− .011	1.331	459.753	+ .069	+ .069	1.444
459.666	− .012	− .012	1.357	459.756	+ .073	+ .073	1.447
459.669	− .003	− .003	1.360	459.783	+ .112	+ .112	1.474
459.684	+ .004	+ .004	1.375	459.786	+ .117	+ .117	1.477
459.686	+ .005	+ .005	1.377	459.788	+ .121	+ .121	1.479
459.688	+ .008	+ .008	1.379	459.813	+ .176	+ .176	1.504
459.713	+ .027	+ .027	1.404	459.816	+ .186	+ .186	1.507
459.715	+ .028	+ .028	1.406	459.818	+ .186	+ .186	1.509
459.718	+ .028	+ .028	1.409	459.821	+ .196	+ .196	1.512
459.720	+0.033	+0.033	1.411	459.824	+0.204	+0.204	1.515

TABLE 4

Photometric Observations of CQ Cephei, 1947 (Ultraviolet)

Julian Day (Heliоc.) 2432000+	CQ Cep − HD+56°2816 (observed)	CQ Cep − HD+56°2816 (corrected)	Phase (Days)	Julian Day (Heliоc.) 2432000+	CQ Cep − HD+56°2816 (observed)	CQ Cep − HD+56°2816 (corrected)	Phase (Days)
430.731	−0.405	−0.435	0.323	444.860	−0.496	−0.496	1.322
430.736	− .414	− .444	0.328	445.695	− .471	− .472	0.516
430.740	− .417	− .447	0.332	445.697	− .465	− .466	0.518
430.745	− .417	− .447	0.337	445.700	− .459	− .460	0.521
430.788	− .444	− .474	0.380	445.704	− .462	− .463	0.525
430.792	− .446	− .476	0.384	445.706	− .462	− .463	0.527
439.728	− .337	− .337	1.114	445.768	− .413	− .414	0.589
444.706	− .409	− .409	1.168	445.771	− .411	− .412	0.592
444.709	− .413	− .413	1.171	445.774	− .412	− .413	0.595
444.713	− .413	− .413	1.175	445.817	− .345	− .346	0.638
444.715	− .418	− .418	1.177	445.820	− .339	− .340	0.641
444.797	− .432	− .432	1.259	445.822	− .336	− .337	0.643
444.800	− .430	− .430	1.262	445.826	− .337	− .338	0.647
444.804	− .483	− .483	1.266	446.732	− .172	− .142	1.553
444.806	− .484	− .484	1.268	446.735	− .166	− .136	1.556
444.854	− .499	− .499	1.316	446.738	− .158	− .128	1.559
444.857	−0.513	−0.513	1.319	446.780	−0.028	+0.002	1.601

TABLE 4 (Cont'd)

Julian Day (Helioc.) 2432000+	CQ Cep − BD+56°2816 (observed)	CQ Cep − BD+56°2816 (corrected)	Phase (Days)	Julian Day (Helioc.) 2432000+	CQ Cep − BD+56°2816 (observed)	CQ Cep − BD+56°2816 (corrected)	Phase (Days)
446.784	-0.033	-0.003	1.605	448.706	-0.348	-0.366	0.284
446.786	- .025	+ .005	1.607	448.770	- .420	- .438	0.308
446.789	- .019	+ .011	1.610	448.773	- .422	- .440	0.311
447.637	- .088	- .088	0.817	448.775	- .423	- .441	0.313
447.640	- .082	- .082	0.820	448.778	- .427	- .445	0.316
447.643	- .076	- .076	0.823	448.813	- .447	- .465	0.351
447.645	- .066	- .066	0.825	448.816	- .451	- .469	0.354
447.680	- .078	- .078	0.860	448.819	- .457	- .475	0.357
447.683	- .077	- .077	0.863	448.821	- .451	- .469	0.359
447.686	- .077	- .077	0.866	449.643	- .413	- .425	1.181
447.689	- .077	- .077	0.869	449.646	- .409	- .421	1.184
447.713	- .102	- .102	0.893	449.650	- .416	- .428	1.188
447.716	- .102	- .102	0.896	449.709	- .464	- .476	1.247
447.719	- .103	- .103	0.899	449.711	- .462	- .474	1.249
447.722	- .115	- .115	0.902	449.713	- .466	- .478	1.251
447.746	- .130	- .130	0.926	449.716	- .466	- .478	1.254
447.749	- .136	- .136	0.929	449.720	- .461	- .473	1.258
447.752	- .134	- .134	0.932	449.756	- .481	- .493	1.294
447.754	- .141	- .141	0.934	449.759	- .481	- .493	1.297
447.788	- .182	- .182	0.968	449.762	- .484	- .496	1.300
447.790	- .183	- .183	0.970	451.618	- .245	- .245	1.515
447.793	- .182	- .182	0.973	451.621	- .239	- .239	1.518
447.796	- .189	- .189	0.976	451.623	- .231	- .231	1.520
447.825	- .220	- .220	1.005	451.627	- .228	- .228	1.524
447.828	- .228	- .228	1.008	451.660	- .130	- .130	1.557
447.831	- .235	- .235	1.011	451.663	- .128	- .128	1.560
447.833	- .231	- .231	1.013	451.665	- .112	- .112	1.562
447.836	- .256	- .256	1.016	451.686	- .058	- .058	1.583
448.633	- .234	- .252	0.171	451.689	- .047	- .047	1.586
448.635	- .240	- .258	0.173	451.691	- .040	- .040	1.588
448.638	- .233	- .251	0.176	451.743	+ .019	+ .019	1.640
448.640	- .238	- .256	0.178	451.745	+ .021	+ .021	0.001
448.696	- .330	- .348	0.234	451.747	+ .022	+ .022	0.003
448.699	- .336	- .354	0.237	451.813	- .060	- .060	0.069
448.701	- .340	- .358	0.239	451.818	- .065	- .065	0.074
448.704	-0.339	-0.357	0.242	451.821	-0.077	-0.077	0.077

TABLE 4 (Cont'd)

Julian Day (Helioc.) 2432000+	QQ Cep - BD+56°2816 (observed)	QQ Cep - BD+56°2816 (corrected)	Phase (Days)	Julian Day (Helioc.) 2432000+	QQ Cep - BD+56°2816 (observed)	QQ Cep - BD+56°2816 (corrected)	Phase (Days)
451.326	-0.081	-0.081	0.082	454.763	-0.492	-0.477	1.378
452.642	- .101	- .101	0.898	455.636	- .394	- .394	0.609
452.645	- .108	- .108	0.901	455.638	- .385	- .335	0.611
452.647	- .107	- .107	0.903	455.641	- .396	- .396	0.614
452.684	- .153	- .153	0.940	455.644	- .382	- .382	0.617
452.686	- .165	- .165	0.942	455.682	- .326	- .326	0.655
452.688	- .163	- .163	0.944	455.685	- .323	- .323	0.658
452.765	- .255	- .255	1.021	455.688	- .323	- .323	0.661
452.768	- .261	- .261	1.024	455.690	- .315	- .315	0.663
452.771	- .261	- .261	1.027	455.726	- .255	- .255	0.699
452.774	- .256	- .256	1.030	455.728	- .247	- .247	0.701
452.777	- .266	- .266	1.033	455.731	- .242	- .242	0.704
452.812	- .315	- .315	1.068	455.769	- .173	- .173	0.742
452.814	- .315	- .315	1.070	455.771	- .172	- .172	0.744
452.817	- .319	- .319	1.073	455.774	- .172	- .172	0.747
453.720	- .447	- .447	0.335	455.827	- .099	- .099	0.800
453.722	- .452	- .452	0.337	455.829	- .096	- .096	0.802
453.725	- .449	- .449	0.340	455.831	- .090	- .090	0.804
453.777	- .481	- .481	0.392	456.754	- .103	- .081	0.086
453.780	- .481	- .481	0.395	456.757	- .117	- .096	0.089
453.783	- .490	- .490	0.398	456.763	- .130	- .109	0.095
453.788	- .490	- .490	0.403	457.644	- .226	- .211	0.976
453.822	- .491	- .491	0.437	457.647	- .237	- .222	0.979
453.825	- .495	- .495	0.440	457.650	- .224	- .209	0.982
453.827	- .499	- .499	0.442	457.652	- .225	- .210	0.984
454.641	- .497	- .482	1.256	457.712	- .302	- .287	1.044
454.644	- .503	- .488	1.259	457.720	- .305	- .290	1.052
454.646	- .497	- .482	1.261	457.723	- .314	- .299	1.055
454.649	- .501	- .486	1.264	457.729	- .313	- .298	1.061
454.703	- .517	- .502	1.318	457.734	- .325	- .310	1.066
454.706	- .516	- .501	1.321	458.698	- .459	- .477	0.389
454.709	- .517	- .502	1.324	458.702	- .464	- .482	0.393
454.711	- .512	- .497	1.326	458.705	- .464	- .482	0.396
454.755	- .501	- .486	1.370	458.745	- .474	- .492	0.436
454.758	- .496	- .481	1.373	458.749	- .468	- .486	0.440
454.761	-0.499	-0.484	1.376	458.752	-0.467	-0.485	0.443

TABLE 4 (Concluded)

Julian Day (Helioc.) 2432000+	CQ Cep − BD+56°2816 (observed)	CQ Cep − BD+56°2816 (corrected)	Phase (Days)	Julian Day (Helioc.) 2432000+	CQ Cep − BD+56°2816 (observed)	CQ Cep − BD+56°2816 (corrected)	Phase (Days)
459.727	−0.438	−0.438	1.418	459.775	−0.369	−0.369	1.466
459.729	− .436	− .436	1.420	459.777	− .369	− .369	1.468
459.731	− .439	− .439	1.422	459.804	− .308	− .308	1.495
459.734	− .424	− .424	1.425	459.806	− .306	− .306	1.497
459.772	−0.378	−0.378	1.463	459.809	−0.293	−0.293	1.500

TABLE 5

POLARIZATION OF CQ CEPHEI

Julian Day (Heliоc.) 2432000+	Phase (Days)	Polarization (Mag.)	Position Angle	Julian Day (Heliоc.) 2432000+	Phase (Days)	Polarization (Mag.)	Position Angle
740.802	0.194	0.095	60°0	743.882	1.633	0.105	63°5
741.833	1.225	.095	58.5	744.844	0.953	.102	61.0
741.868	1.260	.100	61.0	744.889	0.998	.097	60.0
741.920	1.312	.100	62.0	767.876	1.008	.098	62.0
742.816	0.567	.098	62.5	769.796	1.286	.095	62.0
742.906	0.657	.102	62.0	769.949	1.439	.100	63.0
742.934	0.685	0.100	62.0	770.845	0.694	0.102	63.0

the emission were not present, then the difference in magnitudes of the two spectral regions would be the same as for BD+56°2815. This assumption is probably not significantly in error and will enter the observations only as a scale error. After the observations are reduced on the above assumption, they must be corrected for variation of the continuum to which the emission is compared. For this, one must refer to the integrated light-curve. Although it will be shown later that this eclipsing system shows a small intrinsic variation, the mean light-curve as determined at λ 5300 was used to transfer the *He* II 4686 observations to an absolute scale. The observations are recorded in Table 6. The first column gives the heliocentric Julian Day, the second the difference in magnitude of *He* II 4686 and the neighboring continuum, the third gives the intensity of *He* II 4686 after the correction for the variation of the continuum, and the fourth gives the phase in days computed by the formula given previously. A correction by 0.020 day in phase is indicated by a few photometric observations at λ 5300 taken in 1948–1949. This correction in phase was considered in applying the integrated light-curve to the *He* II 4686 observations.

OBSERVATIONS AT λ 5300 (1948–1949)

These observations were made only for checking the phase of the binary system. The 1948 observations were made with the same filter, cell, and telescope as those in 1947. However, the 1949 observations were made with a 13-inch Cassegrain reflector. A different photocell, 1P21(E), but the same filter, was used in 1949. Although the effective wave length in 1949 may be slightly different, it will be of little consequence, since the character of the light-curve is nearly independent of wave length. These observations were not used in the present investigation except to give a correction for phase and are reproduced here in Table 7 primarily as a matter of record.

TABLE 6

Photometric Observations of CQ Cephei, 1949 (He II 4686)

Julian Day (Helioc.) 2433000+	He II 4686 - Continuum (observed)	He II 4686 Intensity	Phase (Days)	Julian Day (Heliocc.) 2433000+	He II 4686 - Continuum (observed)	He II 4686 Intensity	Phase (Days)
180.658	0.753	0.912	0.209	180.813	1.106	1.107	0.364
180.661	.781	.929	0.212	180.815	.102	.102	0.366
180.663	.794	.937	0.214	180.819	.096	.095	0.370
180.666	.816	.956	0.217	180.822	.088	.086	0.373
180.670	.804	.937	0.221	180.826	.108	.104	0.377
180.671	.805	.937	0.222	180.829	.109	.104	0.380
180.674	.810	.938	0.225	180.834	.096	.090	0.385
180.685	.846	.959	0.236	180.838	.095	.088	0.387
180.688	.866	0.973	0.239	180.840	.129	.121	0.391
180.690	.910	1.015	0.241	180.846	.114	.109	0.397
180.693	.866	0.966	0.244	180.850	.143	.131	0.401
180.696	.874	.972	0.247	180.853	.180	.167	0.404
180.699	.873	.967	0.250	180.856	.099	.085	0.407
180.702	.888	.979	0.253	180.860	.142	.127	0.411
180.705	.882	.970	0.256	180.863	.161	.145	0.414
180.708	.910	.993	0.259	180.867	1.117	.100	0.418
180.724	.931	.997	0.275	184.780	0.885	.069	1.049
180.727	.914	0.976	0.278	184.784	.851	.031	1.053
180.730	.944	1.004	0.281	184.789	.845	.020	1.058
180.733	.905	0.962	0.284	184.793	.870	.040	1.062
180.736	.957	1.010	0.287	184.796	.907	.075	1.065
180.740	.961	1.011	0.291	184.799	.921	.085	1.068
180.743	.941	0.988	0.294	184.803	.897	.057	1.072
180.746	.901	0.945	0.297	184.811	.944	.096	1.080
180.754	.996	1.033	0.305	184.814	.944	.093	1.083
180.758	.997	1.031	0.309	184.816	.958	.105	1.085
180.761	0.966	0.998	0.312	184.820	.946	.088	1.089
180.765	1.001	1.030	0.316	184.826	.889	.024	1.095
180.783	.023	.041	0.334	184.829	.898	.030	1.098
180.786	.051	.067	0.337	184.831	.978	.108	1.100
180.790	.066	.078	0.341	184.834	.928	.055	1.103
180.793	.062	.073	0.344	184.836	.919	.043	1.105
180.797	.046	.055	0.348	184.841	0.939	.057	1.110
180.806	.053	.057	0.357	184.859	1.049	.147	1.128
180.809	1.028	1.031	0.360	184.861	1.025	1.121	1.130

TABLE 6 (Cont'd)

Julian Day (Helioc.) 2433000+	He II 4686 - Continuum (observed)	He II 4686 Intensity	Phase (Days)	Julian Day (Helioc.) 2433000+	He II 4686 - Continuum (observed)	He II 4686 Intensity	Phase (Days)
188.963	0.981	1.075	1.132	188.777	0.596	0.881	0.122
188.970	1.028	.115	1.139	188.784	.626	.896	0.129
188.972	1.003	1.087	1.141	188.787	.625	.892	0.132
188.573	0.621	0.913	1.556	188.790	.646	.906	0.135
188.578	.617	.942	1.561	188.793	.643	.897	0.138
188.581	.585	.919	1.564	188.797	.670	.918	0.142
188.584	.606	.946	1.567	188.904	.665	.902	0.149
188.587	.585	.930	1.569	188.907	.677	.909	0.152
188.673	.419	.867	0.015	188.910	.687	.915	0.155
188.677	.406	.852	0.019	188.913	.664	.887	0.158
188.680	.385	.828	0.022	188.916	.704	.924	0.161
188.681	.393	.832	0.027	188.919	.688	.905	0.164
188.685	.406	.843	0.030	188.926	.714	.919	0.171
188.688	.411	.844	0.033	188.931	.729	.928	0.176
188.693	.417	.840	0.040	188.934	.738	.932	0.179
188.697	.439	.859	0.042	188.937	.709	.899	0.182
188.704	.454	.866	0.049	188.940	.687	.873	0.185
188.707	.428	.836	0.052	188.943	.724	.905	0.188
188.710	.433	.837	0.055	188.945	.749	.927	0.190
188.713	.442	.841	0.058	189.610	.660	.951	0.955
188.715	.440	.836	0.060	189.613	.685	.972	0.958
188.718	.470	.861	0.063	189.619	.654	.934	0.964
188.720	.467	.855	0.065	189.623	.711	0.986	0.968
188.728	.488	.861	0.073	189.629	.738	1.006	0.974
188.731	.497	.864	0.076	189.631	.711	0.976	0.976
188.736	.530	.885	0.083	189.635	.733	0.994	0.980
188.742	.517	.864	0.087	189.639	.761	1.018	0.984
188.745	.537	.880	0.090	189.648	.742	0.989	0.993
188.751	.589	.920	0.096	189.654	.798	1.038	0.999
188.754	.573	.898	0.099	189.656	.799	.036	1.001
188.756	.557	.879	0.101	189.665	.789	.017	1.010
188.760	.583	.898	0.105	189.668	.824	.049	1.013
188.763	.545	.855	0.108	189.670	.786	.009	1.015
188.767	.594	.897	0.112	189.675	.800	.016	1.020
188.770	.578	.875	0.115	189.677	.812	.027	1.022
188.773	0.577	0.868	0.118	189.683	0.796	1.003	1.028

TABLE 6 (Cont'd)

Julian Day (Helioc.) 2433000+	He II λ686 - Continuum (observed)	He II λ686 Intensity	Phase (Days)	Julian Day (Helioc.) 2433000+	He II λ686 - Continuum (observed)	He II λ686 Intensity	Phase (Days)
189.686	0.819	1.023	1.011	189.835	1.108	1.153	1.180
189.688	.823	.025	1.033	189.841	.106	.146	1.186
189.692	.854	.052	1.037	189.844	.115	.152	1.189
189.695	.881	.074	1.040	189.846	.159	.195	1.191
189.701	.891	.079	1.046	191.640	.118	.104	1.344
189.704	.864	.048	1.049	191.643	.172	.159	1.347
189.707	.864	.045	1.052	191.649	.129	.118	1.353
189.711	.900	.077	1.056	191.652	.131	.121	1.356
189.716	.876	.048	1.061	191.658	.117	.109	1.362
189.720	.931	.098	1.065	191.661	.142	.135	1.365
189.724	.881	.045	1.069	191.663	.104	.099	1.367
189.728	.936	.095	1.073	191.668	.111	.109	1.373
189.735	.906	.058	1.080	191.673	.138	.139	1.377
189.738	.920	.069	1.083	191.675	.062	.164	1.379
189.742	.927	.072	1.087	191.697	.093	.113	1.401
189.745	.933	.074	1.090	191.700	.089	.112	1.404
189.748	.890	.027	1.093	191.704	.076	.104	1.408
189.754	.954	.085	1.099	191.710	.058	.091	1.414
189.758	.977	.104	1.103	191.713	.073	.109	1.417
189.761	.965	.088	1.106	191.718	.071	.113	1.422
189.769	0.963	.077	1.114	191.725	.075	.124	1.429
189.775	1.002	.109	1.120	191.727	.080	.131	1.431
189.779	0.986	.089	1.124	191.731	.083	.138	1.435
189.782	1.002	.100	1.127	191.738	.031	.096	1.442
189.788	.021	.113	1.133	191.740	1.011	.079	1.444
189.792	1.036	.124	1.137	191.745	0.996	.069	1.449
189.795	0.960	.045	1.140	191.749	.997	.075	1.453
189.798	1.048	.130	1.143	191.752	.961	.043	1.456
189.805	.045	.120	1.150	191.754	.997	.082	1.458
189.810	.111	.181	1.155	191.761	.969	.065	1.465
189.812	.073	.141	1.157	191.763	.949	.049	1.467
189.815	.093	.158	1.160	191.770	.942	.053	1.474
189.818	.070	.132	1.163	191.777	.941	.065	1.481
189.826	.108	.154	1.171	191.780	.886	.018	1.484
189.829	.079	.129	1.174	191.786	.918	.065	1.490
189.832	1.128	1.176	1.177	191.789	0.878	1.029	1.493

TABLE 6 (Cont'd)

Julian Day (Helioc.) 2433000+	He II 4686 - Continuum (observed)	He II 4686 Intensity	Phase (Days)	Julian Day (Helioc.) 2433000+	He II 4686 - Continuum (observed)	He II 4686 Intensity	Phase (Days)
191.793	0.844	1.026	1.497	192.658	0.672	0.712	0.720
191.798	.837	.012	1.502	192.661	.649	.994	0.723
191.802	.850	.034	1.506	192.667	.645	.899	0.729
191.804	.827	.015	1.508	192.670	.640	.898	0.732
191.808	.825	.021	1.512	192.675	.644	.910	0.737
191.813	.793	.003	1.517	192.677	.630	.870	0.739
191.816	.784	.002	1.520	192.683	.594	.873	0.745
191.819	.792	1.016	1.523	192.686	.588	.872	0.748
191.822	.754	0.989	1.526	192.689	.585	.875	0.751
191.828	.732	.985	1.532	192.695	.584	.884	0.757
191.831	.737	.997	1.535	192.700	.568	.875	0.762
191.834	.727	.997	1.538	192.702	.582	.892	0.764
191.840	.675	.961	1.544	192.709	.562	.881	0.771
191.844	.672	.968	1.548	192.712	.536	.858	0.774
191.846	.662	.960	1.550	192.715	.554	.879	0.777
191.848	.679	0.981	1.552	192.718	.561	.890	0.780
192.570	.966	1.065	0.632	192.725	.529	.866	0.787
192.572	.953	.055	0.634	192.727	.539	.878	0.789
192.578	.922	.032	0.640	192.731	.547	.891	0.793
192.581	.920	.036	0.643	192.736	.520	.870	0.798
192.588	.895	.020	0.650	192.738	.518	.870	0.800
192.591	.886	1.016	0.653	192.742	.505	.860	0.804
192.602	.852	0.998	0.664	192.747	.519	.878	0.809
192.604	.853	1.003	0.666	192.751	.517	.879	0.813
192.607	.842	0.996	0.669	192.757	.518	.883	0.819
192.612	.827	.990	0.674	192.760	.503	.870	0.822
192.615	.796	.965	0.677	192.766	.488	.858	0.828
192.618	.814	.986	0.680	192.769	.490	.861	0.831
192.621	.805	.984	0.683	192.775	.492	.866	0.837
192.627	.751	.941	0.689	192.778	.486	.860	0.840
192.630	.750	.944	0.692	192.784	.515	.890	0.846
192.634	.745	.945	0.696	192.790	.541	.916	0.852
192.637	.769	.974	0.699	192.794	.545	.920	0.856
192.642	.758	.972	0.704	192.797	.520	.895	0.859
192.645	.721	.940	0.707	192.801	.530	.904	0.863
192.656	0.689	0.925	0.718	192.806	0.547	0.919	0.868

TABLE 6 (Cont'd)

Julian Day (Helioc.) 2433000+	He II 4686 - Continuum (observed)	He II 4686 Intensity	Phase (Days)	Julian Day (Helioc.) 2433000+	He II 4686 - Continuum (observed)	He II 4686 Intensity	Phase (Days)
192.810	0.538	0.909	0.872	193.689	0.543	0.849	0.110
192.813	.553	.922	0.875	193.694	.556	.852	0.115
192.817	.544	.911	0.879	193.698	.602	.892	0.119
192.822	.584	.948	0.884	193.705	.669	.944	0.126
192.826	.551	.912	0.888	193.709	.633	.902	0.130
192.829	.566	.925	0.891	193.711	.623	.889	0.132
192.832	.567	.924	0.894	193.715	.636	.894	0.136
192.836	.588	.941	0.898	193.719	.631	.882	0.140
192.838	.591	.941	0.900	193.732	.695	.925	0.153
192.845	.574	.919	0.907	193.735	.668	.893	0.156
192.847	.620	.963	0.909	193.741	.707	.926	0.162
193.563	.369	.819	1.625	193.747	.721	.931	0.168
193.565	.364	.816	1.627	193.751	.740	.944	0.172
193.568	.354	.807	1.630	193.754	.727	.927	0.175
193.571	.393	.847	1.633	193.761	.765	.955	0.182
193.578	.379	.834	1.640	193.764	.750	.936	0.185
193.581	.365	.820	0.002	193.768	.756	.936	0.189
193.584	.368	.822	0.005	193.771	.782	.958	0.192
193.587	.401	.854	0.008	193.774	.759	.930	0.195
193.593	.348	.797	0.014	193.777	.756	.923	0.198
193.596	.381	.828	0.017	193.781	.801	.963	0.202
193.600	.368	.812	0.021	193.787	.792	.944	0.208
193.604	.389	.830	0.025	193.791	.807	.954	0.212
193.607	.400	.838	0.028	193.795	.797	.937	0.216
193.613	.407	.839	0.034	193.809	.830	.950	0.230
193.617	.413	.838	0.038	193.812	.830	.946	0.233
193.631	.447	.855	0.052	193.815	.873	.986	0.236
193.634	.423	.827	0.055	193.822	.863	.965	0.243
193.656	.490	.855	0.077	193.826	.895	0.992	0.247
193.659	.487	.847	0.080	193.831	.910	1.002	0.252
193.668	.496	.841	0.089	193.871	.975	1.024	0.292
193.670	.512	.852	0.091	194.562	.705	0.972	0.983
193.675	.516	.846	0.096	194.567	.665	.918	0.988
193.679	.551	.875	0.100	194.571	.721	.969	0.992
193.682	.530	.853	0.103	194.592	.753	.978	1.013
193.686	0.537	0.900	0.107	194.594	0.749	0.972	1.015

TABLE 6 (Cont'd)

Julian Day (Helioc.) 2433000+	He II 4686 - Continuum (observed)	He II 4686 Intensity	Phase (Days)	Julian Day (Helioc.) 2433000+	He II 4686 - Continuum (observed)	He II 4686 Intensity	Phase (Days)
194.597	0?730	0?949	1.018	194.825	1?077	1?070	1.246
194.601	.752	.966	1.022	194.827	.045	.042	1.248
194.611	.747	.950	1.032	194.830	.065	.060	1.251
194.613	.779	.979	1.034	195.571	.051	.059	0.351
194.620	.784	.977	1.041	195.575	.069	.074	0.355
194.623	.796	.986	1.043	195.577	.242	.046	0.357
194.627	.731	.966	1.048	195.580	.075	.078	0.360
194.630	.792	.974	1.051	195.586	.078	.078	0.366
194.634	.838	0.986	1.055	195.588	.072	.071	0.368
194.640	.846	1.018	1.061	195.597	.100	.096	0.377
194.645	.789	0.955	1.066	195.600	.067	.062	0.380
194.649	.825	0.987	1.070	195.606	.091	.084	0.386
194.668	.876	1.018	1.089	195.609	.134	.126	0.389
194.671	.873	.011	1.092	195.612	.099	.090	0.392
194.675	.870	.004	1.096	195.616	.128	.117	0.396
194.679	.876	.006	1.100	196.563	.112	.096	1.343
194.683	.919	1.045	1.104	196.566	.168	.153	1.346
194.686	.876	0.998	1.107	196.570	.099	.086	1.350
194.690	.888	1.004	1.111	196.576	.102	.091	1.356
194.693	.869	0.983	1.114	196.579	.084	.074	1.359
194.697	.920	1.030	1.118	196.586	.134	.128	1.366
194.700	.887	0.993	1.121	196.590	.118	.114	1.370
194.706	.923	1.022	1.127	196.595	.110	.110	1.375
194.709	.930	.026	1.130	196.598	1.082	1.084	1.378
194.712	.939	.031	1.133	196.751	0.703	0.954	1.531
194.715	.951	.040	1.136	196.754	.718	.975	1.534
194.719	.954	.039	1.140	196.759	.692	.963	1.539
194.722	.929	.011	1.143	196.761	.711	.987	1.541
194.727	0.958	.035	1.148	196.771	.631	.931	1.551
194.734	1.028	.053	1.205	196.775	.603	.913	1.555
194.793	0.985	.003	1.214	196.778	.614	.933	1.558
194.806	1.202	.028	1.227	196.783	.532	.912	1.563
194.809	.051	.058	1.230	196.787	.536	.876	1.567
194.811	.075	.080	1.232	196.795	.557	.917	1.575
194.814	.070	.073	1.235	196.799	.518	.888	1.579
194.819	1.081	1.081	1.240	196.803	0.519	0.900	1.583

TABLE 6 (Concluded)

Julian Day (Helioc.) 2433000+	He II 4686 - Continuum (observed)	He II 4686 Intensity	Phase (Days)	Julian Day (Helioc.) 2433000+	He II 4686 - Continuum (observed)	He II 4686 Intensity	Phase (Days)
196.807	0.694	0.885	1.587	197.700	0.503	0.876	0.838
197.568	.733	.950	0.706	197.711	.503	.878	0.849
197.571	.699	.920	0.709	197.714	.518	.893	0.852
197.575	.692	.922	0.713	197.730	.553	.925	0.868
197.578	.679	.913	0.716	197.734	.534	.905	0.872
197.581	.668	.900	0.719	197.737	.562	.932	0.875
197.586	.642	.890	0.724	197.740	.549	.918	0.878
197.593	.652	.909	0.731	197.745	.542	.907	0.883
197.597	.637	.901	0.735	197.747	.561	.924	0.885
197.601	.689	.929	0.739	197.752	.562	.927	0.890
197.611	.601	.886	0.749	197.761	.570	.922	0.899
197.614	.577	.868	0.752	197.765	.596	.944	0.903
197.619	.601	.901	0.757	197.770	.590	.934	0.908
197.622	.611	.916	0.760	197.774	.592	.932	0.912
197.625	.571	.880	0.763	197.778	.615	.951	0.916
197.636	.554	.875	0.774	197.784	.626	.954	0.922
197.640	.569	.895	0.778	197.793	.645	.964	0.931
197.645	.538	.870	0.783	197.802	.662	.971	0.940
197.648	.522	.958	0.786	197.805	.655	0.961	0.943
197.671	.530	.389	0.309	197.809	.700	1.001	0.947
197.675	.495	.858	0.813	197.813	.719	1.014	0.951
197.679	.494	.858	0.817	197.815	.692	0.985	0.953
197.684	.509	.876	0.822	197.819	.698	.986	0.957
197.686	.509	.877	0.824	197.822	.705	.989	0.960
197.694	.513	.884	0.832	197.828	.704	.981	0.966
197.697	0.516	0.888	0.835	198.538	0.494	0.850	0.082

TABLE 7

Photometric Observations of CQ Cephei, 1948 and 1949 (Yellow)

Julian Day (Helioc.)	CQ Cep - BD+56°2815 (observed)	Phase (Days)	Julian Day (Helioc.)	CQ Cep - BD+56°2815 (observed)	Phase (Days)
2432751.835	-0.035	1.379	2432766.939	+0.351	0.071
751.838	- .049	1.382	770.938	+ .302	0.787
751.841	- .039	1.385	770.741	+ .308	0.790
752.782	+ .159	0.685	2432770.943	+ .316	0.792
752.784	+ .167	0.687	2433243.587	+ .304	0.750
752.788	+ .167	0.691	243.589	+ .306	0.752
752.790	+ .172	0.693	243.592	+ .304	0.755
757.831	+ .338	0.810	243.594	+ .313	0.757
757.833	+ .344	0.812	243.597	+ .313	0.760
757.836	+ .347	0.815	243.600	+ .322	0.763
757.950	+ .260	0.929	243.603	+ .339	0.846
757.952	+ .263	0.931	243.685	+ .360	0.848
757.955	+ .260	0.934	243.688	+ .355	0.851
757.958	+ .260	0.937	244.566	+ .295	0.087
757.961	+ .259	0.940	244.569	+ .295	0.090
757.963	+ .257	0.942	244.571	+ .314	0.092
758.799	+ .238	0.137	244.574	+ .308	0.095
758.802	+ .229	0.140	245.561	+ .105	1.082
758.804	+ .220	0.142	245.565	+ .102	1.086
758.807	+ .226	0.145	245,569	+ .114	1.090
758.810	+ .212	0.148	245.572	+ .093	1.093
758.840	+ .172	0.178	246.549	- .026	0.429
758.843	+ .167	0.181	246.553	- .050	0.433
758.845	+ .161	0.183	246.556	- .031	0.436
765.884	+ .089	0.657	246.560	- .039	0.440
765.887	+ .097	0.660	246.563	- .034	0.443
766.933	+ .354	0.065	246.567	- .032	0.447
2432766.936	+0.347	0.068	250.545	+ .027	1.143
			2433250.549	+0.026	1.147

THE RESULTS

We will first discuss the 1947 observations. If the differences in magnitude of the comparison star and CQ Cephei are plotted against phase, it will immediately be obvious that successive cycles do not necessarily coincide. Either the comparison star is variable, or CQ Cephei is, in addition, an intrinsic variable. From the checks on the comparison star given in Table 2 it appears that this star is not variable. Consequently, it is assumed that CQ Cephei shows intrinsic variations from cycle to cycle.

Because of the relatively short period (39.4 hours) and because the star was frequently observed for a period of 6 hours, it is possible to reconstruct a good light-curve by the overlapping of runs on different nights. The assumption must be made that during the period of 6 hours there are no intrinsic variations. In addition, we implicitly assume that the character of the eclipse will be independent of the intrinsic brightness of the star. The former assumption may not be entirely correct. Such an analysis gives a set of corrections to be applied to the observed magnitudes. These corrections, given in Table 8, are applied to the observed magnitudes in Table 3 in order to obtain the corrected magnitudes. These corrections, which were obtained from the consideration of the observations at λ 5300 only, were also applied to the observed ultraviolet observations in Table 4, in order to obtain the corrected differences in magnitude given in this table. This assumes, of course, that the intrinsic variations are, to a first approximation, independent of wave length.

TABLE 8

CORRECTIONS FOR INTRINSIC VARIATIONS OF CQ CEPHEI, 1947

Julian Day Limits (Helioc.) 2432000+	Correction (Mag.)	Phase Limits (Days)	Julian Day Limits (Helioc.) 2432000+	Correction (Mag.)	Phase Limits (Days)
430.753–430.822	−0.030	0.345–0.414	452.602–452.831	0.000	0.858–1.087
439.703–439.717	.000	1.089–1.103	453.598–453.842	.000	0.213–0.457
444.647–444.735	.000	1.109–1.197	454.616–454.831	+ .015	1.231–1.446
445.649–445.844	− .001	0.470–0.665	455.619–455.847	.000	0.592–0.820
446.710–446.769	+ .030	1.531–1.590	456.602–456.831	+ .021	1.575–0.163
447.622–447.862	.000	0.802–1.042	457.627–457.771	+ .015	0.959–1.103
448.618–448.793	− .018	0.156–0.331	458.670–458.767	− .018	0.361–0.458
449.627–449.752	− .012	1.165–1.290	459.604–459.824	0.000	1.295–1.515
451.601–451.865	0.000	1.498–0.121			

The corrected differences in magnitude are plotted in Figures 1 and 2. It is seen that the analysis gave not only a smooth light-curve at λ 5300 but also one of nearly equal quality for the ultraviolet.

In addition to the more obvious characteristics of the light-curve, the following remarks can be made:

1. The primary eclipse corresponds to the eclipse of the Wolf-Rayet component.[11]
2. The ultraviolet curve shows a greater depth of either minimum, as given in the accompanying tabulation.

Minimum	λ 5300 (Mag.)	Ultraviolet (Mag.)
Primary	0.474	0.520
Secondary	0.391	0.425

[11] Recent greatly widened spectrograms show some of the higher members of the Balmer series in absorption. Presumably, these lines are associated with the secondary star.

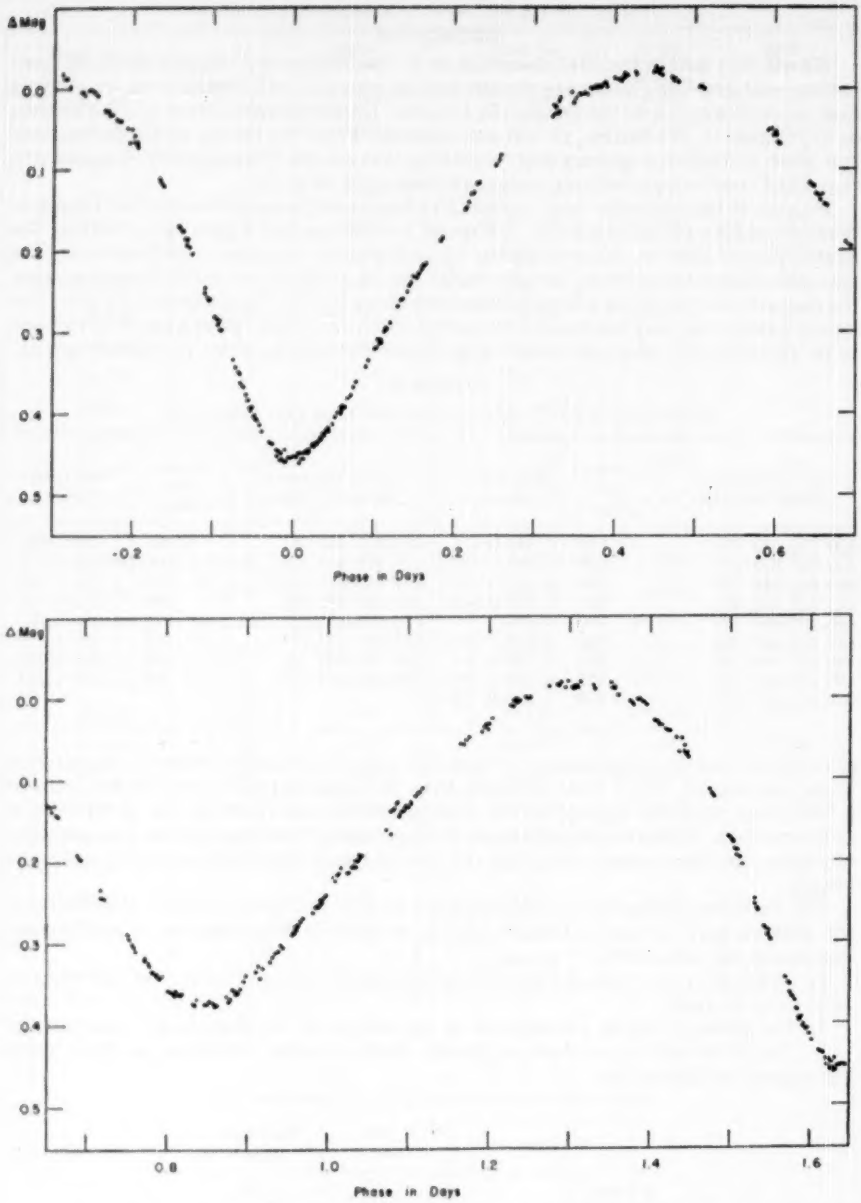

FIG. 1.—The light-curve of CQ Cephei at an effective wave length λ 5300. The observations have been corrected for an intrinsic variation of the system.

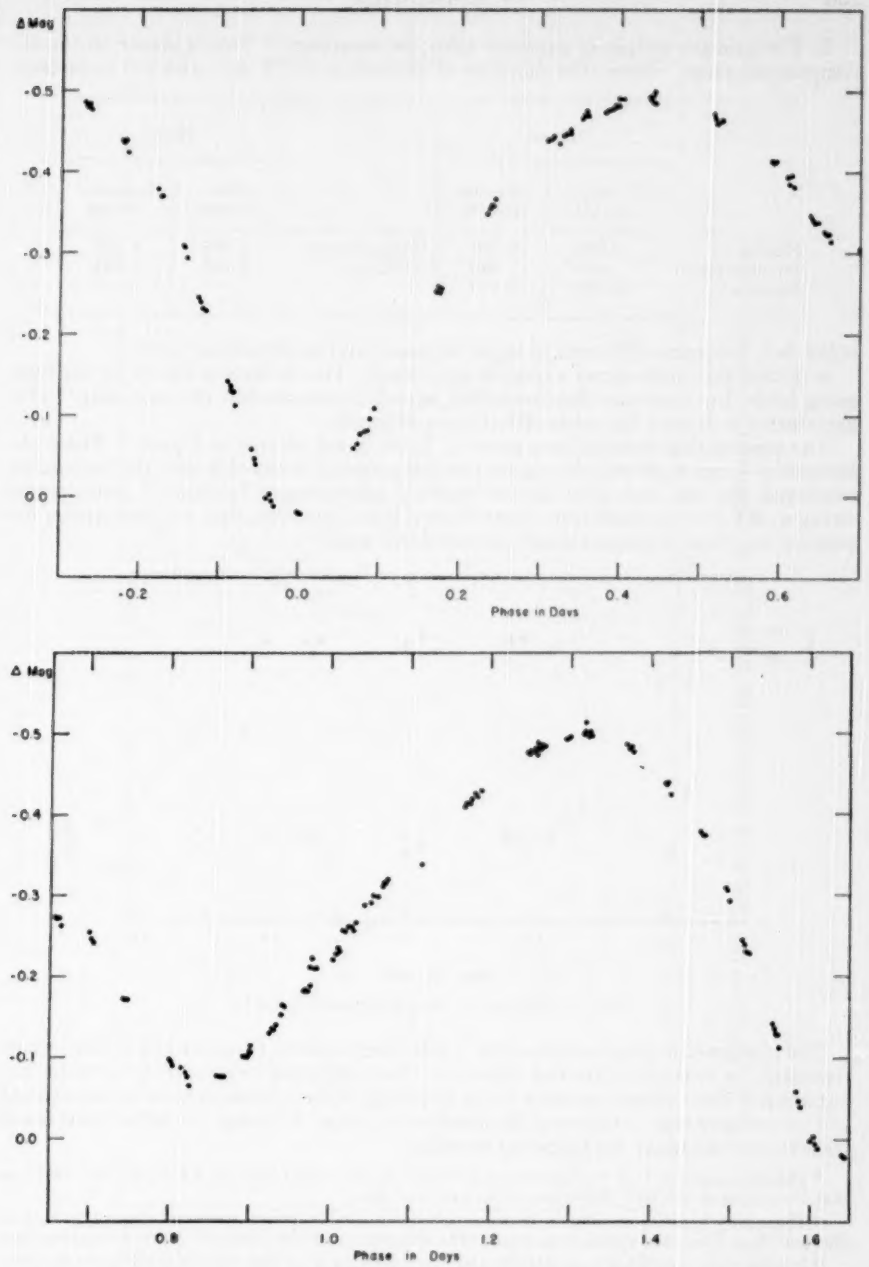

FIG. 2.—The light-curve of CQ Cephei in the ultraviolet. The same correction has been applied for intrinsic variation as that determined for λ 5300.

3. The primary eclipse is narrower than the secondary.[12] This is shown in the accompanying table. Hence, the duration of primary is 0.772 day, and the secondary,

	Phase			Phase	
	Obs. (λ 5300)	Computed ($e=0.00$)		Obs. (λ 5300)	Computed ($e=0.00$)
Primary	0.000	0.000	3d quadrature	1.312	1.232
1st quadrature	.443	.410	Primary	1.641	1.641
Secondary	0.850	0.821			

0.869 day. The same difference in width is present in the ultraviolet curve.

4. Either minimum shows a marked asymmetry. This is likewise shown by the foregoing table. In either case the descending branch is steeper than the ascending.[13] This asymmetry is present for either effective wave-length.

The polarization observations, given in Table 5, are plotted in Figure 3. These observations do not represent the highest possible accuracy obtainable with the instrument employed, for the ones here are not entirely homogeneous because of instrumental changes. We can conclude from these observations, however, that no polarization dependent on phase is present which exceeds 0.005 mag.[14]

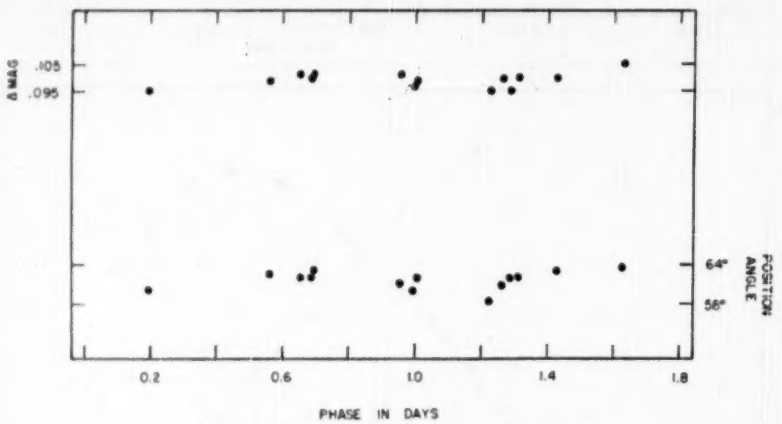

FIG. 3.—Polarization observations of CQ Cephei

The photometric observations of *He* II 4686 are plotted in Figures 4 and 5. The former represent the intensity of the line relative to the neighboring continuum uncorrected for variation of this continuum, while in the latter figure the intensities have been corrected so that we have true variation of *He* II 4686 with phase. Although the entire cycle is not covered, we can make the following remarks:

[12] This is in common with the light-curve of V 444 Cyg (Kron and Gordon, *Ap. J.*, **97**, 311, 1945), in that the eclipse of the Wolf-Rayet star is the narrower one.

[13] There may be some correlation between this asymmetry and the presence of absorption lines of *He* I and *He* II. These absorption lines appear to be strengthened at the phases of the ascending branches.

[14] It is not to be concluded from this that electron scattering is not important in Wolf-Rayet stars but that in this case the geometry is not favorable for polarization.

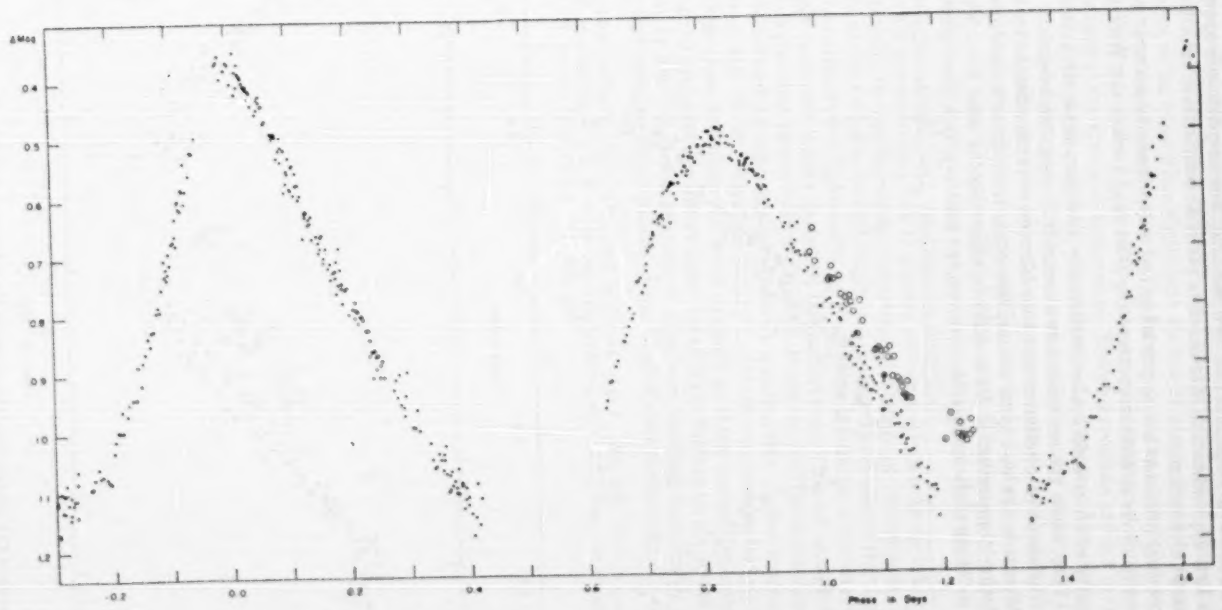

FIG. 4.—Light-curve of CQ Cephei from the emission line *He* II 4686 uncorrected for the eclipses

1. The curve shows two maxima and two minima. The amplitude is approximately 0.35 mag. To a first approximation, the maxima occur at conjunction (at either eclipse) and the minima at elongation.

2. The descending branches are appreciably less steep than the ascending branches.

3. The intensity of *He* II 4686 is greatest (by 0.04 mag.) when the Wolf-Rayet star is eclipsed.

4. The intensity of *He* II 4686 is also intrinsically variable, as shown by the observation on JD 2433194, when the emission was at least 0.10 mag. too bright.

The question arises as to whether or not the observed curve is affected by absorption in *He* II 4686. We can make no logical assumption other than the one mentioned earlier, that the absorption component of *He* II 4686 in either star is near zero. Thus far we have observed no trace of the comparison star except possibly by a few higher members

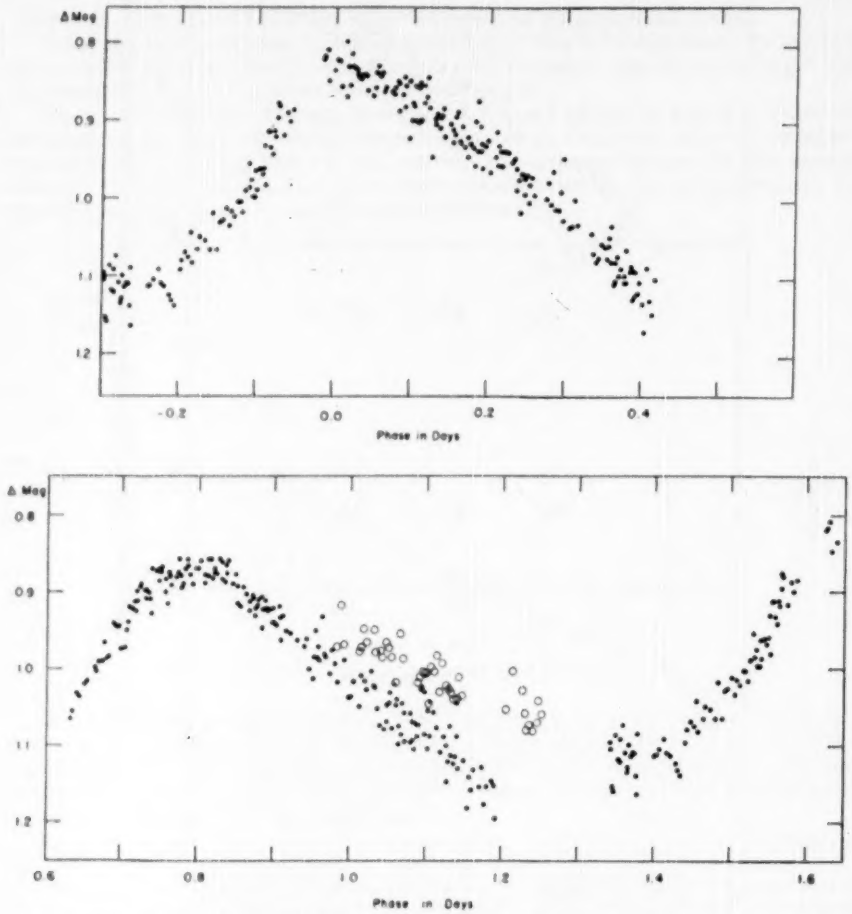

FIG. 5.—Light-curve of CQ Cephei from the emission *He* II 4686 corrected for the eclipses. As in Figure 4, the open circles represent one night when the emission was abnormally strong.

of the Balmer series. No violet-edge absorption of *He* II 4686 is observed at any phase. However, we can consider two different cases for the presence of absorption: first, that one component of the binary has significant *He* II 4686 absorption and, second, that both components have equal absorption. In the former case the absorption would have the effect of lowering the observed intensity of the emission at that conjunction corresponding to the eclipse of the star with absorption. The observations are not informative as to whether or not such is the case; but, since the two maxima are of nearly equal intensity, we suspect that the distortion of the observed light-curve by absorption in one component only is not significant. However, the evidence cannot be conclusive. The second case is that in which the absorption component has the same equivalent width in either star. The consequence of absorption in either component will be that of lowering the observed intensity of the emission at either conjunction, and hence the curve computed on the above assumption would have too small an amplitude.

At present it is not obvious how this series of observations must be interpreted in order to add materially to our knowledge regarding the origin of the emission lines in Wolf-Rayet stars. If the emission had its origin in a compact shell about the parent-star, then we should have observed a light-curve with only one minimum. Likewise, if the emission has its origin in a shell large relative to the parent-star, then we should have expected a more or less constant intensity of *He* II 4686. However, neither is the case, for the emission is more intense at conjunctions than at quadratures. A few similar observations were made of HD 211853, another binary in which one component is a Wolf-Rayet star; and from these few observations it appears as if the same phenomenon is present. If one wishes to interpret the above behavior of *He* II 4686 in terms of a model, then this model must be such that the amount of observed emitting material is greater at the advancing and receding hemispheres of the Wolf-Rayet component.[15]

[15] A somewhat similar model was invoked by Struve (*Ap. J.*, **106**, 255, 1947) in order to explain the spectroscopic peculiarities of UX Mon. In late-type binaries, such as RZ Cnc, the emission is localized at the areas of low gravity (*Pub. A.S.P.*, **55**, 166, 1946).

THE LIGHT-CURVE OF UX MONOCEROTIS*

W. A. Hiltner, O. Struve, and P. D. Jose
Yerkes and McDonald Observatories
Received July 29, 1950

ABSTRACT

The light-curve of UX Mon has been determined at an effective wave length of λ 5300. The primary minimum has a depth of 0.94 mag., and a secondary with a depth of the order of 0.24 mag. may be present. Intrinsic fluctuations as great as 0.16 mag. have been observed. These fluctuations are associated with the brighter component.

The eclipsing binary UX Monocerotis is unique among the eclipsing binaries thus far investigated spectrographically. The system consists of a small A-type star and a large and more massive G-type star. The spectrum is characterized by variable emission lines of *H* and peculiar absorption lines of *H* and *Ca* II.[1] The variation in light was discovered by Miss Ida E. Woods in 1926.[2] A primary minimum of 1.74 mag. and a secondary of 0.14 were reported. Because of the dispersion shown in the individual observations, she concluded "that either the maximum light is not constant, or that one of the comparison stars varies slightly." An orbit computed by Mrs. M. B. Shapley is given in the same reference. A second photometric investigation has been made by Gaposchkin.[3] His observations show a primary minimum of 1.03 mag. and a secondary of 0.04 mag. Some of the conclusions he drew regarding the system, such as the eccentricity of the photometric orbit and the greater width of the secondary, do not appear to be justified by the material at hand.

Because of its position (1900, $\alpha = 7^h54^m$; $\delta = -7°14'$) and period (5.90 days), the system does not lend itself readily to photometric observations, and it was not until a small reflecting telescope was erected at the McDonald Observatory[4] that it appeared possible to observe the star adequately.

During the period from November 26, 1949, to April 10, 1950, a total of 486 observations on 45 different nights was obtained with a photoelectric photometer on a 13-inch reflector. All the observations were made through a Corning No. 3385 filter, 2 mm thick. The radiation receiver was an RCA 1P21 (E) multiplier phototube. The effective wave length given by this combination is near λ 5300. The output from the phototube was fed to a direct-coupled amplifier, which, in turn, drove a Brown recorder. One observation consisted of three deflections of 25-second duration each on the variable and the same on the comparison.

Because of variation of maximum light suspected by Miss Woods[2] and since we might well expect measurable fluctuations from cycle to cycle associated with the spectroscopic variations, two comparison stars were selected, BD−7°2310 and BD−6°2402. The latter served as a check on the former. These check observations were made on 40 of the 45 nights on which settings were made on UX Mon. As a matter of record these check observations are listed in Table 1. The probable error of a single observation, −0.005, is larger than normal for so bright a star. The larger error may be attributed to a variety of causes; one is that the principal criterion, as to whether or not observations were made, was the clearness of the sky, to a great extent independent of the seeing.

* *Contributions from the McDonald Observatory, University of Texas*, No. 196.

[1] For a detailed discussion of the system see O. Struve, *Ap. J.*, **106**, 255, 1947.

[2] *Bull. Harvard Obs.*, No. 854, 1928.

[3] *Ap. J.*, **105**, 264, 1947.

[4] See appendix to this article.

The observations of UX Mon are listed in Table 2. All observations have been corrected for differential extinction by a mean coefficient, 0.20 mag. The phases, in the second column, were computed by the formula given in the 1941 edition of Schneller's catalogue of variable stars:

$$\text{Principal minimum} = \text{JD } 2418602.84 + 5.904604E.$$

This is the same formula used by Struve in his spectroscopic investigation. Our observed principal minimum occurs at phase −0.067 days. Two figures of the light-curve

TABLE 1

COMPARISON OF BD−7°2310 AND BD−6°2402

JD 2433000+	ΔM	JD 2433000+	ΔM	JD 2433000+	ΔM	JD 2433000+	ΔM
246.923	−0.418	303.810	−0.434	328.624	−0.422	346.712	−0.420
249.877	− .431	303.839	− .425	328.652	− .430	346.761	− .430
264.847	− .419	303.869	− .432	328.670	− .424	346.789	− .420
264.908	− .409	314.710	− .422	328.719	− .412	346.817	− .428
268.811	− .417	314.713	− .425	328.747	− .415	347.685	− .418
268.837	− .421	314.763	− .421	328.774	− .403	348.712	− .426
273.798	− .420	314.811	− .414	328.801	− .415	349.717	− .415
273.809	− .422	314.833	− .406	330.713	− .419	353.683	− .422
274.783	− .416	315.653	− .433	330.765	− .422	353.751	− .420
274.793	− .413	317.694	− .426	330.792	− .423	356.715	− .413
277.854	− .415	317.725	− .402	334.608	− .416	356.741	− .432
278.790	− .421	317.774	− .424	334.660	− .434	357.692	− .425
278.969	− .425	318.699	− .422	334.710	− .421	357.740	− .412
299.699	− .410	320.687	− .423	334.737	− .404	358.637	− .418
300.706	− .420	320.747	− .426	334.776	− .413	358.681	− .433
300.765	− .426	321.682	− .422	334.805	− .406	358.721	− .412
301.726	− .425	321.734	− .418	336.620	− .419	358.766	− .417
301.771	− .432	321.797	− .424	336.719	− .429	358.787	− .426
301.842	− .424	321.826	− .409	336.747	− .413	361.755	− .426
302.703	− .406	322.778	− .422	336.798	− .425	365.742	− .430
302.745	− .423	322.799	− .412	340.640	− .432	369.658	− .416
302.772	− .413	327.697	− .410	340.698	− .425	370.765	− .394
303.741	− .401	327.699	− .422	340.812	− .418	374.689	− .425
303.787	−0.425	328.595	−0.428	346.651	−0.427	381.653	−0.422

are given. Figure 1 shows the whole light-curve except for primary minimum, while Figure 2 shows the principal minimum.

The following remarks can be made regarding the light-curve of UX Mon:

1. The principal minimum, A-type star eclipsed, has a depth of approximately 0.94 mag. Consequently, at λ 5300 the A-type star contributes not less than 58 per cent of the radiation of the system. This is at variance with the spectroscopic observations, in which Struve estimated that the total luminosities of the two components are about the same at λ 4231.

2. A depression of approximately 0.24 mag. at phase near 3 days is, in all likelihood, the secondary minimum. There is no evidence from the present observations that the secondary minimum is broader than the principal minimum and that the photometric orbit is eccentric.

3. Well-pronounced intrinsic rapid fluctuations are present. These variations may be as great as 0.16 mag.[5] Spectrographic observations may prove fruitful in interpreting these fluctuations.

[5] At the June, 1950, meeting of the American Astronomical Society at Bloomington, Indiana, similar fluctuations were reported by Dr. Bradshaw Wood.

TABLE 2

Photometric Observations of UX Monocerotis

JD (Helio.) 2455000+	Phase	ΔM	JD (Helio.) 2455000+	Phase	ΔM	JD (Helio.) 2455000+	Phase	ΔM
246.909	0.681	-0.002	274.780	4.904	- .074	299.882	0.483	- .002
246.912	0.684	- .006	274.785	4.907	- .065	300.696	1.297	- .031
246.916	0.688	- .010	274.788	4.912	- .059	300.708	1.304	- .031
246.919	0.691	.000	274.792	4.916	- .056	300.760	1.361	- .027
246.924	0.696	- .002	274.796	4.920	- .061	300.764	1.365	- .025
249.851	3.616	+ .027	277.851	2.070	.000	300.771	1.372	- .024
249.858	3.598	+ .028	277.854	2.073	+ .007	301.721	2.322	- .027
249.860	3.602	+ .029	277.859	2.078	+ .014	301.725	2.326	- .028
249.865	3.606	+ .027	277.862	2.081	+ .010	301.753	2.354	- .045
249.867	3.609	+ .029	278.777	2.996	+ .174	301.762	2.363	- .054
249.870	3.612	+ .018	278.780	2.999	+ .175	301.766	2.367	- .054
249.874	3.616	+ .020	278.784	3.003	+ .165	301.780	2.381	- .057
249.881	3.623	+ .016	278.788	3.007	+ .174	301.821	2.422	- .072
249.884	3.626	+ .027	278.790	3.009	+ .180	301.825	2.426	- .066
249.887	3.629	+ .052	278.961	3.180	+ .150	301.829	2.430	- .067
264.836	0.864	+ .026	278.965	3.184	+ .132	301.837	2.438	- .082
264.840	0.868	+ .021	278.968	3.187	+ .125	301.848	2.449	- .092
264.844	0.872	+ .025	295.764	2.265	+ .014	301.853	2.454	- .001
264.847	0.875	+ .038	296.752	3.240	+ .089	302.691	3.292	+ .022
264.901	0.929	+ .048	296.759	3.244	+ .082	302.695	3.296	+ .044
264.905	0.933	+ .061	296.763	3.258	+ .092	302.698	3.299	+ .042
264.909	0.937	+ .041	297.726	4.251	- .049	302.702	3.303	+ .018
268.817	4.845	- .021	297.752	4.257	- .060	302.706	3.306	+ .047
268.821	4.849	- .025	298.762	5.287	- .001,	302.729	3.330	+ .020
268.825	4.853	- .024	298.787	5.292	- .007	302.734	3.335	+ .015
268.828	4.856	- .028	298.892	5.377	+ .017	302.739	3.340	+ .016
268.832	4.860	- .026	299.696	0.297	+ .253	302.742	3.343	+ .023
268.835	4.863	- .032	299.700	0.301	+ .245	302.746	3.347	+ .030
273.795	3.219	- .041	299.729	0.330	+ .185	302.758	3.359	+ .039
273.798	3.922	- .041	299.815	0.416	+ .058	302.761	3.362	+ .024
273.802	3.927	- .044	299.819	0.420	+ .040	302.765	3.366	+ .032
273.808	3.932	- .038	299.873	0.474	+ .012	302.769	3.370	+ .029
273.812	3.936	-0.040	299.878	0.479	+0.006	302.774	3.375	+0.038

TABLE 2 (Cont'd)

JD (Helio.) 2435000+	Phase	ΔM	JD (Helio.) 2435000+	Phase	ΔM	JD (Helio.) 2435000+	Phase	ΔM
302.799	3.400	+0.058	314.806	3.597	+0.034	320.679	3.566	+0.000
302.804	3.405	+ .059	314.810	3.601	+ .046	320.682	3.569	+ .007
303.735	4.336	- .066	314.813	3.604	+ .052	320.688	3.575	+ .064
303.739	4.340	- .082	314.821	3.612	+ .049	320.689	3.576	+ .067
303.742	4.343	- .077	314.824	3.615	+ .059	320.735	3.622	+ .066
303.796	4.397	- .086	314.827	3.618	+ .056	320.738	3.625	+ .077
303.801	4.402	- .090	314.851	3.642	+ .052	320.742	3.629	+ .080
303.804	4.405	- .103	314.855	3.646	+ .064	320.745	3.632	+ .088
404.808	4.409	- .087	315.639	4.430	- .069	320.749	3.636	+ .062
303.812	4.413	- .099	315.643	4.433	- .079	320.763	3.650	+ .049
303.826	4.427	- .106	315.647	4.438	- .076	320.767	3.654	+ .065
303.829	4.430	- .102	315.650	4.441	- .078	320.770	3.657	+ .081
303.833	4.434	- .100	315.654	4.445	- .087	320.774	3.661	+ .085
303.836	4.437	- .099	317.682	0.569	- .007	321.670	4.557	- .070
303.840	4.441	- .092	317.686	0.573	- .008	321.673	4.560	- .082
303.856	4.457	- .110	317.690	0.576	- .018	321.677	4.564	- .064
303.859	4.460	- .096	317.693	0.579	- .011	321.680	4.567	- .081
303.863	4.464	- .094	317.696	0.582	- .018	321.685	4.570	- .069
303.867	4.468	- .092	317.720	0.607	- .008	321.7[illegible]	4.609	- .089
303.870	4.471	- .101	316.724	0.611	- .005	321.725	4.612	- .073
314.697	3.488	+ .032	317.728	0.615	- .005	321.728	4.615	- .065
314.701	3.492	+ .028	317.729	0.616	- .008	321.731	4.618	- .062
314.704	3.495	+ .025	317.739	0.626	+ .003	321.736	4.623	- .060
314.708	3.499	+ .046	317.742	0.629	+ .010	321.784	4.671	- .050
314.711	3.502	+ .030	317.746	0.633	+ .008	321.788	4.675	- .046
314.749	3.540	+ .026	317.749	0.636	- .005	321.792	4.679	- .055
314.752	3.543	+ .027	317.752	0.639	- .001	321.795	4.682	- .040
314.756	3.547	+ .040	314.463	0.650	.000	321.799	4.686	- .047
314.760	3.551	+ .038	317.766	0.653	+ .004	321.815	4.702	- .058
314.763	3.554	+ .038	317.770	0.657	+ .005	321.817	4.704	- .052
314.772	3.563	+ .032	317.772	0.659	+ .001	321.822	4.709	- .062
314.775	3.566	+ .042	317.776	0.663	+ .005	321.825	4.712	- .050
314.779	3.570	+ .042	318.692	1.579	- .069	321.828	4.715	- .048
314.783	3.574	+ .033	318.696	1.582	- .068	322.763	5.650	+ .706
314.786	3.577	+ .042	318.698	1.585	- .064	322.766	5.653	+ .724
314.789	3.580	+ .041	318.701	1.588	- .068	322.770	5.657	+ .719
314.803	3.594	+0.047	320.675	3.562	+0.069	322.775	5.660	+0.735

TABLE 2 (Cont'd)

JD (Helio.) 2433000+	Phase	Δm	JD (Helio.) 2433000+	Phase	Δm	JD (Helio.) 2433000+	Phase	Δm
322.776	5.663	+0.746	328.747	5.729	+0.841	334.654	5.732	+0.850
322.780	5.667	+ .774	328.750	5.732	+ .847	334.657	5.735	+ .849
322.795	5.682	+ .810	328.764	5.746	+ .857	334.660	5.738	+ .859
322.798	5.685	+ .800	328.768	5.750	+ .865	334.663	5.741	+ .843
322.802	5.689	+ .805	328.771	5.753	+ .854	334.700	5.778	+ .855
327.684	4.666	- .034	328.774	5.756	+ .859	334.705	5.783	+ .863
327.688	4.670	- .035	328.777	5.759	+ .861	334.707	5.785	+ .844
327.691	4.673	- .027	328.792	5.774	+ .863	334.710	5.788	+ .858
328.587	5.569	+ .427	328.795	5.777	+ .869	334.714	5.792	+ .869
328.590	5.572	+ .435	328.798	5.760	+ .854	334.728	5.806	+ .855
328.614	5.596	+ .540	328.801	5.783	+ .878	334.730	5.808	+ .862
328.616	5.598	+ .563	328.804	5.786	+ .862	334.733	5.811	+ .852
328.621	5.603	+ .592	328.817	5.799	+ .861	334.737	5.815	+ .853
328.623	5.605	+ .594	328.862	5.844	+ .862	334.739	5.817	+ .835
328.627	5.609	+ .612	328.866	5.848	+ .867	334.766	5.844	+ .859
328.641	5.623	+ .665	328.869	5.951	+ .857	334.769	5.847	+ .857
328.645	5.627	+ .666	330.705	1.783	- .080	334.773	5.851	+ .848
328.648	5.630	+ .683	330.707	1.785	- .074	334.775	5.853	+ .845
328.651	5.633	+ .690	330.710	1.788	- .078	334.778	5.856	+ .848
328.655	5.637	+ .702	330.713	1.791	- .776	334.793	5.871	+ .855
328.662	5.644	+ .730	330.716	1.794	- .080	334.797	5.875	+ .855
328.665	5.647	+ .736	330.752	1.830	- .069	334.800	5.878	+ .856
328.668	5.650	+ .745	330.755	1.833	- .062	334.803	5.881	+ .852
328.672	5.654	+ .757	330.758	1.836	- .053	334.808	5.886	+ .845
328.690	5.672	+ .783	330.761	1.839	- .065	334.814	5.892	+ .846
328.693	5.675	+ .777	330.766	1.844	- .053	334.817	5.895	+ .846
328.696	5.678	+ .791	330.767	1.845	- .059	334.821	5.899	+ .850
328.699	5.681	+ .793	330.784	1.862	- .066	334.824	5.902	+ .857
328.703	5.685	+ .801	330.787	1.865	- .050	336.610	2.260	- .089
328.707	5.689	+ .807	330.789	1.867	- .057	336.614	2.264	- .097
328.711	5.693	+ .828	330.792	1.870	- .054	336.617	2.267	- .084
328.715	5.697	+ .830	334.599	5.677	+ .769	336.620	2.270	- .090
328.718	5.700	+ .809	334.602	5.680	+ .771	336.623	2.273	- .095
328.722	5.704	+ .823	334.605	5.683	+ .762	336.708	2.358	- .081
328.737	5.719	+ .840	334.608	5.686	+ .769	336.713	2.363	- .072
328.741	5.723	+ .853	334.611	5.689	+ .779	336.715	2.365	- .084
328.743	5.725	+0.838	334.650	5.728	+0.848	336.718	2.368	-0.077

TABLE 2 (Cont'd)

JD (Helio.) 2433000+	Phase	Δu	JD (Helio.) 2433000+	Phase	Δu	JD (Helio.) 2433000+	Phase	Δu
336.721	2.371	+0.078	346.706	0.070	+0.820	353.681	1.140	-0.065
336.737	2.387	- .071	346.709	0.073	+ .811	353.684	1.143	- .060
336.739	2.389	- .075	346.714	0.078	+ .821	353.737	1.196	- .076
336.743	2.393	- .086	346.750	0.114	+ .739	353.740	1.199	- .072
336.746	2.396	- .087	346.753	0.117	+ .735	353.745	1.204	- .065
336.749	2.399	- .077	346.756	0.120	+ .735	353.748	1.207	- .060
336.786	2.436	- .063	346.760	0.124	+ .719	353.752	1.211	- .061
336.790	2.440	- .054	346.764	0.128	+ .709	356.697	4.156	+ .015
336.793	2.443	- .067	346.777	0.141	+ .660	356.701	4.160	+ .023
336.797	2.447	- .068	346.780	0.144	+ .655	356.705	4.164	+ .005
340.629	5.302	+ .867	346.784	0.148	+ .642	356.708	4.167	+ .015
340.632	5.305	+ .860	346.788	0.152	+ .624	356.712	4.171	+ .012
340.636	5.309	+ .848	346.791	0.155	+ .608	356.715	4.174	+ .013
340.639	5.312	+ .851	346.805	0.169	+ .584	356.727	4.186	+ .024
340.642	5.315	+ .861	346.808	0.172	+ .569	356.731	4.190	+ .031
340.689	5.362	+ .850	346.812	0.176	+ .559	356.734	4.193	+ .034
340.694	5.367	+ .851	346.816	0.180	+ .537	356.738	4.197	+ .034
340.695	5.368	+ .848	346.819	0.183	+ .519	356.742	4.201	+ .037
340.698	5.371	+ .846	347.710	1.074	- .102	357.676	5.136	- .002
340.701	5.374	+ .854	347.715	1.079	- .092	357.679	5.138	- .007
340.773	0.041	+ .836	347.721	1.085	- .106	357.683	5.142	- .029
340.777	0.045	+ .837	347.725	1.089	- .097	357.686	5.145	- .010
340.780	0.048	+ .837	347.728	1.092	- .103	357.690	5.149	- .016
340.783	0.051	+ .834	348.685	2.049	- .061	357.693	5.152	- .015
340.800	0.068	+ .807	348.692	2.056	- .052	357.727	5.186	- .010
340.804	0.072	+ .809	348.698	2.062	- .059	357.731	5.190	.000
340.807	0.075	+ .809	348.705	2.069	- .055	357.735	5.194	+ .010
340.812	0.080	+ .791	348.711	2.075	- .052	357.738	5.197	- .015
340.815	0.083	+ .784	348.723	2.092	- .053	357.742	5.201	- .013
340.832	0.100	+ .750	349.714	3.078	+ .119	358.615	0.170	+ .583
346.639	0.003	+ .837	349.718	3.082	+ .111	358.619	0.174	+ .571
346.642	0.006	+ .845	349.728	3.092	+ .128	358.622	0.177	+ .551
346.646	0.010	+ .851	349.733	3.097	+ .125	358.626	0.181	+ .548
346.650	0.014	+ .846	351.688	5.052	- .073	358.629	0.184	+ .522
346.653	0.017	+ .828	353.670	1.129	- .066	358.632	0.187	+ .523
346.699	0.063	+ .821	353.673	1.132	- .062	358.636	0.191	+ .523
346.703	0.067	+0.811	353.677	1.136	- .063	358.639	0.194	+0.505

TABLE 2 (Concluded)

JD (Helio.) 2433000+	Phase	Δv	JD (Helio.) 2433000+	Phase	Δv	JD (Helio.) 2433000+	Phase	Δv
358.660	0.215	+0.425	358.785	0.340	+0.101	369.725	5.675	+0.040
358.671	0.226	+ .411	358.790	0.345	+ .087	370.754	0.499	- .003
358.675	0.230	+ .401	361.738	3.293	+ .111	370.758	0.503	- .004
358.679	0.234	+ .391	361.741	3.296	+ .107	370.762	0.507	+ .001
358.682	0.237	+ .370	361.745	3.300	+ .106	370.766	0.511	+ .008
358.706	0.261	+ .305	361.748	3.303	+ .115	374.672	4.417	+ .021
358.711	0.266	+ .294	361.752	3.307	+ .122	374.677	4.422	+ .027
358.714	0.269	+ .290	361.756	3.311	+ .111	374.680	4.425	+ .027
358.718	0.273	+ .265	365.733	1.383	- .053	374.685	4.430	+ .027
358.722	0.277	+ .253	365.736	1.386	- .039	374.688	4.433	+ .033
358.752	0.307	+ .174	365.740	1.390	- .042	374.718	4.463	+ .044
358.756	0.311	+ .176	365.743	1.393	- .039	374.721	4.466	+ .033
358.760	0.315	+ .174	369.647	5.297	+ .009	374.726	4.471	+ .032
358.763	0.318	+ .154	369.652	5.302	+ .016	381.635	5.476	+ .155
358.767	0.322	+ .140	369.655	5.305	+ .011	381.639	5.480	+ .178
358.775	0.330	+ .131	369.658	5.308	+ .023	381.644	5.485	+ .169
358.779	0.334	+ .120	369.718	5.368	+ .046	381.648	5.489	+ .193
358.782	0.337	+0.118	369.722	5.672	+0.043	381.653	5.494	+0.181

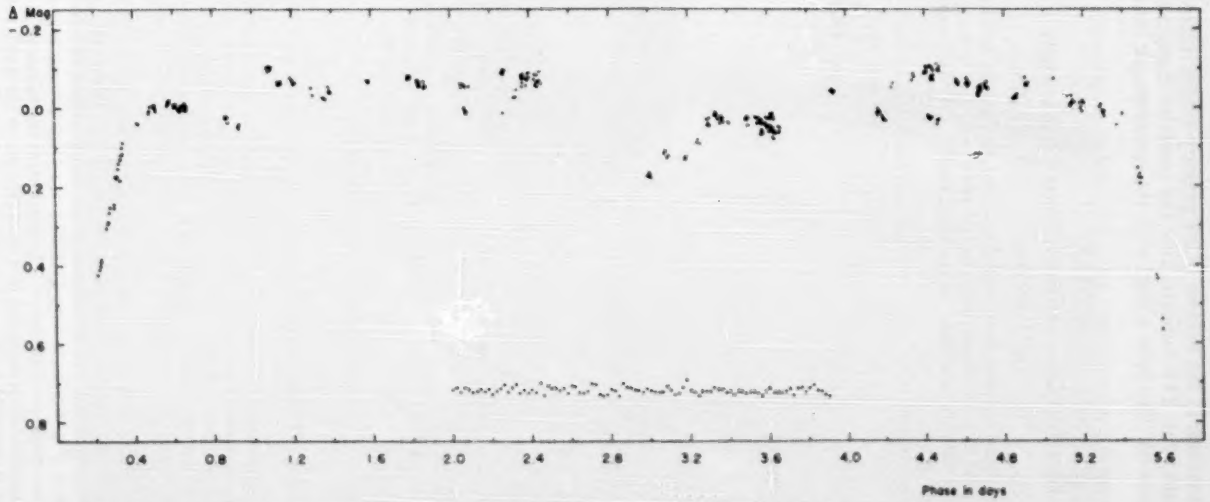

FIG. 1.—Light-curve of UX Mon. The principal minimum is not shown. Note that the rapid and the cycle-to-cycle fluctuations are greater at total light than at principal minimum (see Fig. 2). For comparison, a random plot of the intercomparison of BD−7°2310 and BD−6°2402 is given in the lower section of the figure.

4. The intrinsic fluctuations at the bottom of the primary eclipse appear to be much smaller than at maximum light. This indicates that the irregular changes are associated with the brighter component. This is in accord with the spectroscopic observations.[1]

APPENDIX

The 13-Inch Reflector of the McDonald Observatory

W. A. HILTNER

The 13-inch Cassegrain telescope was constructed and installed at the McDonald Observatory for the explicit purpose of promoting photoelectric photometry. For many observations the larger instrument is unnecessary and often unavailable, particularly for programs of any ex-

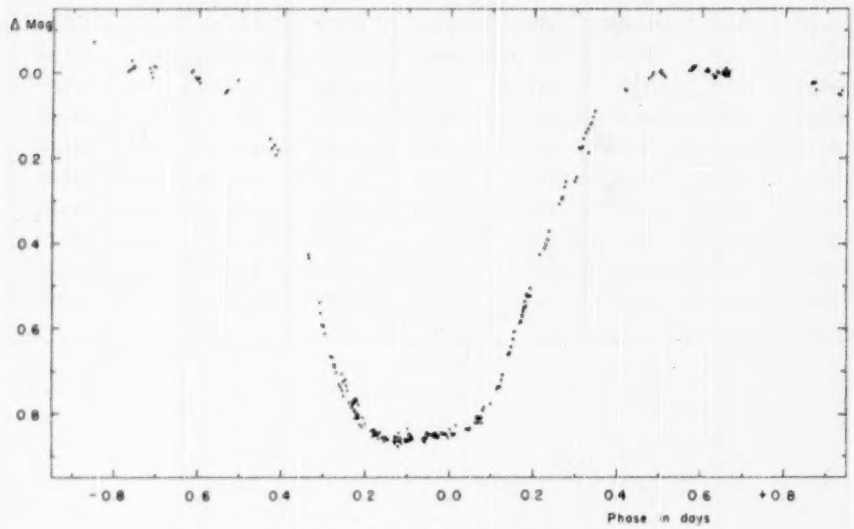

FIG. 2.—Principal minimum of UX Mon

tended length, such as the one discussed above; and hence the need for a small instrument had become acute.

The optics of the telescope were made by B. Schmidt and had been previously used on occasion at McDonald in a temporary mounting. The equivalent focal length of the Cassegrain focus has not been determined but is of the order of 20 feet. This gives an especially desirable *f*-ratio for photometry. The primary mirror has a central hole, which permits a normal Cassegrain arrangement. The telescope, of course, was diaphragmed so that the photocell would see the secondary mirror only.

The new mounting was made in part by the late Mr. H. H. Porter, Sr., of Lake Geneva, Wisconsin. The changes introduced in the mechanical shop by Mr. C. Ridell at Yerkes Observatory were primarily the electrical fast and slow motions on either axis. A fast motion of 1° per second and a slow motion of 1° per minute were installed. A switch system is provided so that the same control buttons are used for either speed. The position of the telescope is not read from conventional circles but from two dials mounted in a steel cabinet on the north side of the dome (see Fig. 3). Sidereal time is supplied to the right-ascension dial, so that this dial reads right ascension directly. This same cabinet contains a crystal-controlled drive for the telescope and a power supply for the photometer amplifier attached to the telescope.

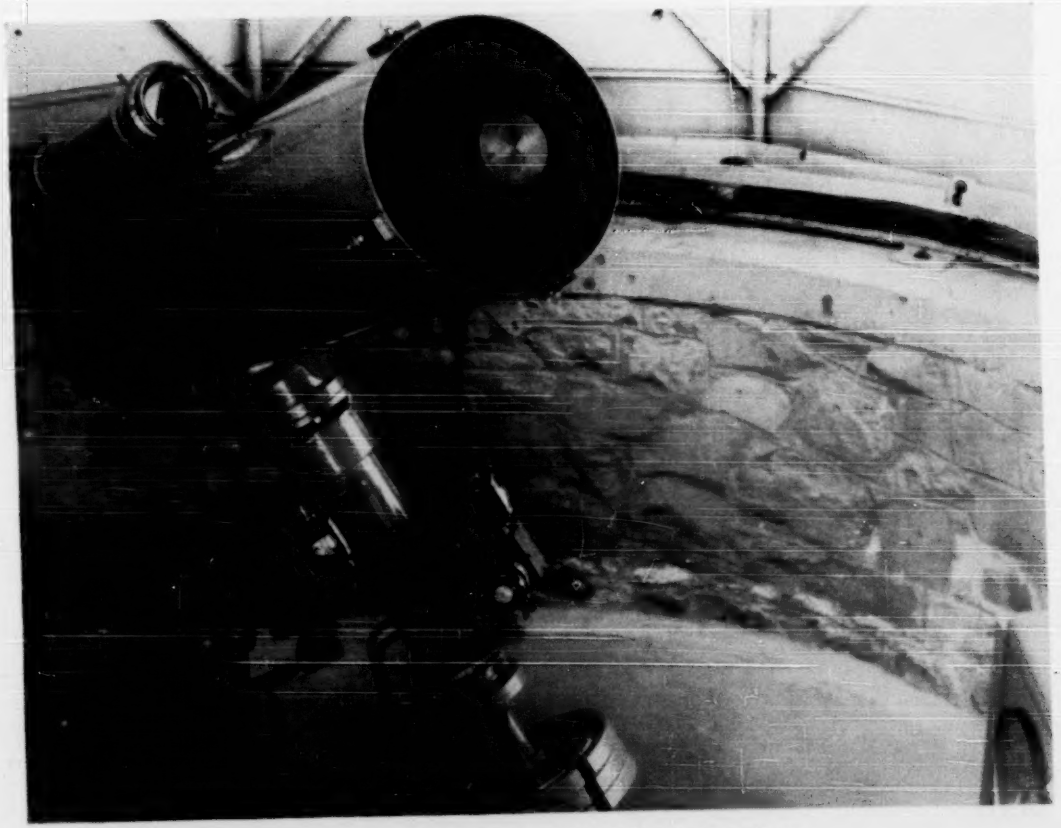

FIG. 3.—The 13-inch reflector of the McDonald Observatory

The entire telescope and dome are controlled by a single small control box. All electrical wires, such as power and controls for the telescope and power for the amplifier and its output, are all carried by underfloor conduits.

The photometer used on this telescope is the same instrument as that used on the 82-inch reflector.

NOTE ADDED IN PROOF.—The scale of the Cassegrain focus has now been measured. It is 1 mm = 28″, corresponding to a focal length of 24 feet.

It is a pleasure to thank Mr. A. Shatzel for assistance in the design of the mounting, Dr. P. D. Jose for assistance in its installation.

THE SPECTRUM OF R AQUARII, 1936–1949

PAUL W. MERRILL
Mount Wilson and Palomar Observatories
Received June 29, 1950

ABSTRACT

Fifty spectrograms of R Aquarii, including fifteen with dispersion 10 A/mm, have been obtained from 1936 to 1949. During this interval the red variable has continued to exhibit the striking periodic changes characteristic of Me variables. The "companion" or nuclear star seems to have made little direct contribution to the photographed spectrum. The nebular lines were weak in 1936, increased in intensity toward 1940, and have since remained strong.

The radial velocities from various groups of lines were studied in some detail. The displacement of the absorption lines, -22 km/sec, probably represents the actual velocity of the red variable. Emission lines definitely associated with the variable yield a velocity of -33 km/sec. The nebular lines exhibit variable velocities, those arising in regions of lowest density yielding the largest changes. The curve for λ 4363 [*O* III] resembles that of a spectroscopic binary of period 26.7 years, $e = 0.5$. The orbital interpretation is dubious. R Aquarii might be characterized as a "simmering nova."

The red long-period variable star R Aquarii, 2338*15*, is remarkable because of its close association with an object which might be called an "atypical planetary nebula." The red variable has a period of 387 days; its color, light-curve, and spectroscopic behavior appear to be normal for a variable of that period.

The nebula may be considered to have three parts: (1) nucleus; (2) inner nebulosity; (3) outer nebulosity. The *nucleus* is hypothetical in the sense that it has never been resolved optically from the red variable. The spectrum, however, seems to indicate its existence as an independent source of light. It must be small, if not actually stellar. In my earlier papers this object was called the "companion." It is variable in total light, but its variations have no certain relationship to those of the red star. In 1932 and 1933 it was unusually bright, and the maxima of the red star were unusually faint; this may or may not have been a coincidence. Its spectrum has been subject to radical changes, being classified at times as Ofp with bright lines of *N* III and *He* II or as Bep with a strong continuous spectrum and numerous bright lines of *Fe* II.

The *inner nebulosity* consists of small, rather definitely bounded clouds very near the nucleus, if not actually projecting from it. These small clouds vary in appearance from year to year. The *outer nebulosity* shows long, faint arcs with intricate structure, the whole slowly expanding. Both nebulosities were discovered by Dr. C. O. Lampland at the Lowell Observatory. Illustrations and a brief discussion will be found in my monograph, *Spectra of Long-Period Variable Stars*.[1]

The behavior of the spectrum of the red variable and of the apparently coincident "companion" star during the period 1919–1934 were described in earlier articles.[2,3] Three low-dispersion spectrograms taken in 1935 were mentioned in another article.[4] Observations from 1936 to 1949 are discussed in the present article.

The light-curve, kindly supplied by Mrs. Margaret Mayall, of the Harvard Observatory, is shown in Figure 1. Because the companion has been faint, this curve is practically that of the red long-period variable. A valuable comparison of the visual and photo-

[1] (Chicago: University of Chicago Press, 1940), pp. 87–89.
[2] P. W. Merrill, *Mt. W. Contr.*, No. 206; *Ap. J.*, **53**, 375, 1921.
[3] P. W. Merrill, *Mt. W. Contr.*, No. 513; *Ap. J.*, **81**, 351, 1935.
[4] P. W. Merrill, *Mt. W. Contr.*, No. 539; *Ap. J.*, **83**, 272, 1936.

graphic light-curves prior to 1944 has been made by Cecilia Payne-Gaposchkin and Constance Boyd.[5]

Spectrograms taken at Mount Wilson from 1936 to 1949 are listed in Table 1. The points on the light-curve at which most of them fall are indicated in Figure 1.

The spectrum of the red variable.—The striking periodic changes in the Me spectrum are typical of long-period variables; hence it is unnecessary to describe them in detail. The measured radial velocities of absorption and emission lines, summarized in Tables 1 and 2, exhibit the usual differences. It is somewhat uncertain whether the bright lines of *Fe* II, [*Fe* II], [*Fe* III], and [*S* II] should be ascribed to the Me star or to the nebula. Perhaps the question is without meaning. Lines of *Fe* II, [*Fe* II], and [*S* II] have been ob-

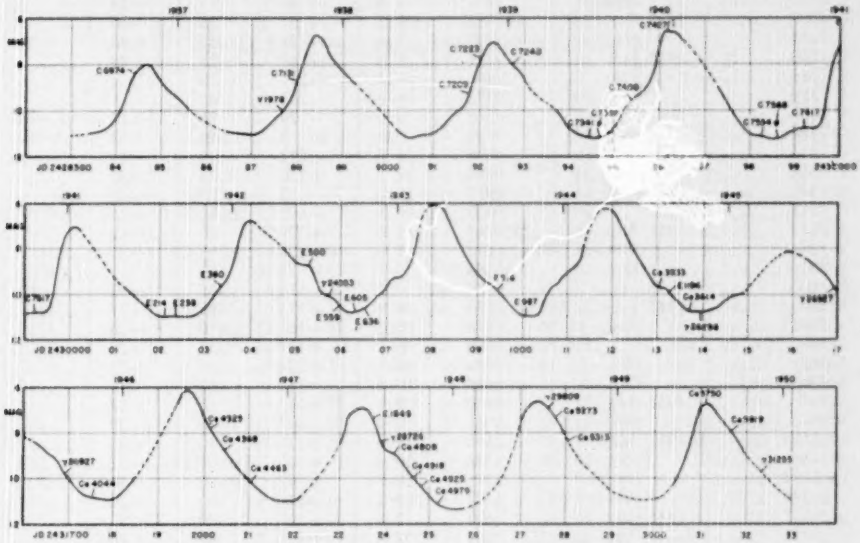

FIG. 1.—Light-curve of R Aquarii showing dates of spectrograms (see Table 1)

served in the spectra of other long-period variables and may indeed be typical. Thus the features that make the system of R Aquarii resemble a planetary nebula may exist weakly or partially in many or all long-period variables.

The nebular spectrum.—Throughout the interval 1936–1949 the companion seems to have made little contribution to the photographed spectra. At least, its continuous spectrum and the conspicuous features recorded in earlier years[3] have not been in evidence. Thus all the bright lines have been ascribed either to the Me variable or to the nebula. It is possible, however, that bright lines of *H* and *He* I considered nebular in the following discussion may at times have been due in part to the companion or nucleus. On my spectrograms the nebular lines must have come very largely from a region extremely near the nucleus. The so-called "inner nebulosity," visible on direct photographs, was probably too faint to make a substantial contribution.

The nebular lines were weak in 1936 but increased in intensity during the next four years. Since 1940 they have remained strong. Most of them are noticeably widened (with dispersion 10 A/mm) but have different widths on various plates; on one or two plates they appear slightly unsymmetrical. These effects indicate an appreciable range of mo-

[5] *Ap. J.*, **104**, 357, 1946.

TABLE 1

JOURNAL OF OBSERVATIONS

PLATE	DATE	JD	MAG.	PHASE (DAYS)	DISP. AT $H\gamma$ (A/MM)	RAD. VEL. ME (KM/SEC)	
						Em.	Abs.
C 6974	1936 Sept. 30	2428442	8.4	− 19	40	−42	.....
V 1978	1937 Aug. 22	8768	10.0	− 74	65	.....	.....
C 7106	27	8773	10.0	− 69	75	.....	.....
C 7131	Sept. 25	8802	8.6	− 40	75	−24	.....
C 7209	1938 Oct. 10	9182	9.2	− 51	75	−40	.....
C 7223	Nov. 6	9209	7.6	− 24	75	−33	−29
C 7240	1939 Jan. 12	9276	8.0	+ 43	75	−48	.....
C 7341	July 5	9450	11.2	+217	75	.....	.....
C 7359	30	9475	11.2	+242	40	.....	.....
C 7400	Oct. 5	9542	9.6	− 74	75	−25	(−24)
C 7427	Dec. 22	9620	6.6	+ 4	40	−33	−23
C 7534	1940 July 19	9830	11.2	+214	75	−42	.....
C 7568	Aug. 24	9866	11.2	+250	75	−30	.....
C 7592	Oct. 14	9917	10.8	− 97	75	−35	.....
C 7617	20	9923	10.8	− 91	40	−27	.....
E 214	1941 Aug. 6	2430213	11.0	+199	65	−18	.....
E 238	31	0238	11.0	+224	65	−25	.....
E 351	Dec. 5	0334	9.7	− 76	65	.....	.....
E 360	7	0336	9.7	− 74	65	−33	−23
E 500	1942 June 22	0533	8.8	+123	65	−27	.....
γ 24353	Aug. 4	0576	10.1	+166	110	−30	.....
E 559	31	0603	10.5	+193	65	−28	.....
E 605	Oct. 1	0634	10.7	+224	65	−21	.....
E 636	Oct. 22	0655	10.6	−149	65	−31	.....
E 916	1943 Aug. 12	0949	9.8	+145	65	−32	.....
E 987	Oct. 13	1011	10.9	+207	65	−29	.....
Ce 3533	1944 Aug. 3	1306	9.6	+125	10	−38	.....
E 1186	Aug. 25	1328	10.0	+147	65	−34	.....
Ce 3614	Oct. 9	1373	10.7	+192	10	−36	.....
γ 26296	Nov. 2	1397	10.7	+216	40	−24	.....
γ 26927	1945 Aug. 25	1693	9.8	+117	40	−23	.....
γ 26931	Aug. 26	1694	9.8	+118	40	−40	.....
Ce 4044	Oct. 26	1755	10.8	+179	10	−31	.....
Ce 4325	1946 July 14	2016	7.9	+ 47	10	−40	.....
Ce 4368	Aug. 15	2048	8.8	+ 79	10	−34	−22
Ce 4456	Oct. 11	2105	10.1	+136	10	−33	.....
Ce 4463	Oct. 13	2107	10.1	+138	10	−35	.....
E 1848	1947 July 5	2372	7.6	+ 31	65	−22	.....
γ 28726	July 25	2392	8.4	+ 51	40	−27	.....
Ce 4808	Aug. 25	2423	8.9	+ 82	10	−31	−21.2
Ce 4918	Oct. 7	2466	10.0	+125	10	−34	.....
Ce 4925	Oct. 23	2482	10.3	+141	10	−32	.....
Ce 4979	Nov. 29	2519	11.1	+178	10	−26	.....
γ 29809	1948 July 30	2763	7.0	+ 29	80	.....	.....
Ce 5273	Aug. 15	2779	7.4	+ 45	10	−33	−21.5
Ce 5313	Sept. 11	2806	8.4	+ 72	10	−34	.....
Ce 5750	1949 July 12	3110	6.8	− 4	10	−31	−23.4
Ce 5919	Sept. 9	3169	8.0	+ 55	10	−33	−20.7
γ 31250	Nov. 12	3233	9.7	+119	80	−29	.....
γ 31255	Nov. 13	3234	9.7	+120	40	−28	.....

TABLE 2

RADIAL VELOCITIES FROM VARIOUS GROUPS OF LINES

	Coudé		Low-Disp		*Mt. W. Contr.*, No. 513		Wt'd. Mean (Km/Sec)
	Km/Sec	Wt.	Km/Sec	Wt.	Km/Sec	Wt.	
Absorption	−21.7	10	−25.2	2	−19.1	1	−22.0
Emission Normal Me, *H*, *Fe* I, *Si* I, etc.	−33.4	3	−30.9	1	−29.5	1	−33.2
Fe II	−29.4	5	−22.4	1	−31.8	2	−29.1
[*Fe* II]	−26.4	1	−21.2	1	−34.6	1	−27.4

TABLE 3

RADIAL VELOCITIES FROM NEBULAR LINES (KM/SEC)

Plate	Date	*H*	*He* I	[*O* III]		[*Ne* III]	[*Fe* III]	[*S* II]	[*Fe* II]
				λ 4959, λ 5007	λ 4363				
V 1978	1937 Aug. 22	(−57)	.....	.....	.....	.....	.....	.....	.....
C 7106	27	−52	.....	(− 69)	.....	.....	.....	.....	.....
C 7341	1939 July 5	−64	.....	(−124)	(−79)	(−80)	.....	.....	.....
C 7359	30	−41	.....	(− 39)	.....	.....	.....	.....	.....
C 7400	Oct. 5	−31	.....	− 73	−35	−59	.....	.....	.....
C 7534	1940 July 19	−58	−36	(−109)	(−54)	.....	−45	−51	−55
C 7568	Aug. 24	−44	−53	−105	−48	(−63)	−44	−48	−27
C 7592	Oct. 14	−33	−30	− 87	−44	.....	−54	(−20)	−49
C 7617	20	−33	−38	− 41	−41	(−42)	−23	−18	(−26)
E 214	1941 Aug. 6	−16	− 4	− 23	−21	−11	(0)	−16	−11
E 238	31	−21	−15	− 26	−21	−16	−16	−16	−14
E 351	Dec. 5	−19	−20	− 40	−15	−15	−14	− 4	−21
E 360	7	−20	−18	− 28	−26	−22	−14	−20	−23
E 500	1942 June 22	(− 8)	− 2	− 31	−26	−16	.....	(− 4)	−10
γ 24353	Aug. 4	.....	(−12)	.....	−18	−21	.....	−34	−20
E 559	31	−14	−17	− 28	−21	−17	−25	−23	−22
E 605	Oct. 1	−16	−22	− 11	− 8	−12	−14	−12	−15
E 636	22	−15	−26	− 15	−27	−11	−10	−16	−11
E 916	1943 Aug. 12	−14	−12	− 16	−17	−14	− 8	−16	−15
E 987	Oct. 13	−14	−14	− 34	−24	−16	−18	−18	−19
Ce 3533	1944 Aug. 3	−13	.....	− 13	−16	−16	.....	.....	.....
E 1186	25	−22	−24	− 22	−13	−15	−12	−17	−19
Ce 3614	Oct. 29	−17	.....	− 20	−19	−23	−14	−14	−22
γ 26296	Nov. 2	− 7	− 1	− 6	− 6	−12	− 5	−12	−13
γ 26927	1945 Aug. 25	(− 2)	−25	0	− 3	+ 1	−11	− 6	−16
γ 26931	26	(− 8)	.....	− 11	−13	.....	.....	.....	.....
Ce 4044	Oct. 26	−12	−15	− 7	−12	−10	.....	.....	−28
Ce 4325	1946 July 14	.....	.....	− 10	.....	.....	.....	.....	.....
Ce 4368	Aug. 15	(− 9)	−18	− 10	−20	−20	−18	−31	−28
Ce 4456	Oct. 11	−17	(−30)	− 10	−21	−19	−14	−18	−28
Ce 4463	13	−19	−19	− 10	−23	−21	−18	−26	−26
γ 28726	1947 July 25	.....	.....	− 12	−12	−18	.....	−22	.....
Ce 4808	Aug. 25	.....	−19	− 19	−21	−22	−18	−25	−26
Ce 4918	Oct. 7	−22	.....	− 22	−22	−20	.....	.....	.....
Ce 4925	23	−24	−21	− 18	−24	−24	−20	−27	−27
Ce 4979	Nov. 29	−20	−24	− 18	−23	−25	−20	−22	−27
Ce 5273	1948 Aug. 15	.....	.....	− 13	−21	−27	.....	.....	.....
Ce 5313	Sept. 11	−16	.....	− 17	−25	−26	−23	−29	.....
Ce 5750	1949 July 12	.....	.....	− 19	.....	−29	.....	.....	.....
Ce 5919	Sept. 29	−22	.....	− 22	−24	−24	.....	−30	.....
γ 31250	Nov. 12	.....	.....	.....	−27	−18	.....	−24	.....
γ 31255	13	.....	−22	− 24	−24	−30	−12	−29	−18

tion in the tenuous gases producing the lines and also changes in these motions from time to time.

Radial velocities from nebular lines.—The radial velocities measured from various groups of lines are recorded in Table 3. Yearly normal places, Table 4, are plotted in Figure 2. The [*O* III] lines λ 4959, λ 5007 show the largest changes; [*O* III] λ 4363 and [*Ne* III] λ 3869, λ 3968 show smaller changes in the same direction; while lines of *H* and *He* I and lines of [*Fe* II], [*Fe* III], and [*S* II] show still smaller changes. From this it ap-

TABLE 4

ANNUAL MEANS OF VARIOUS GROUPS OF NEBULAR LINES (KM/SEC)

JD	*H*, *He* I	[*O* III] λ 4959, λ 5007	[*O* III] λ 4363, [*Ne* III]	[*Fe* II], [*Fe* III], [*S* II]
2428771	−54	(−69)	.....	.....
9506	−45	−77	−65	.....
9885	−40	−82	−48	−40
2430280	−17	−29	−18	−15
0610	−15	−21	−18	−17
0980	−14	−25	−18	−16
1354	−14	−16	−16	−15
1725	−14	− 6	− 9	−15
2087	−19	−10	−21	−23
2452	−22	−18	−22	−24
2797	−16	−15	−25	−26
3177	−22	−21	−25	−24

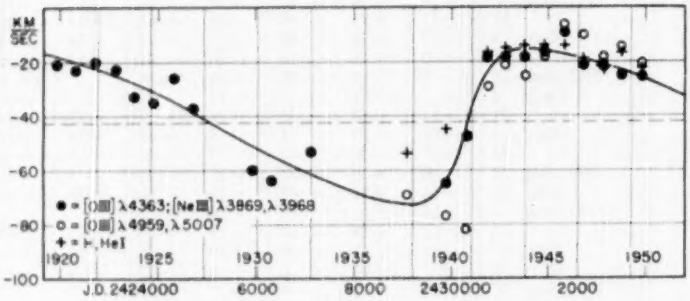

FIG. 2.—Radial velocities derived from the nebular lines

pears that lines originating in regions of highest density exhibit the smallest range of velocity.

For earlier years[3] the data are less satisfactory because the measures were not so accurate and because at times the spectrum of the companion was superposed on the nebular lines. The most reliable velocities are probably those derived from λ 4363 [*O* III]; these are plotted in Figure 2. The curve drawn through the plotted displacements of λ 4363 (combined in recent years with results from [*Ne* III] lines) bears considerable resemblance to the velocity-curve of a spectroscopic binary having the elements in Table 5. It remains to be seen whether the curve will actually repeat itself. The orbital interpretation is, of course, decidedly dubious. An alternative hypothesis, albeit a vague one, is that of large-scale pulsations or currents in which the fastest motions oc-

cur in regions of lowest density. The fact that the γ-velocity is algebraically less by 20 km/sec than the velocity of the red variable may possibly be due to the circumstance that only the near side of the nuclear star is visible to us, rising gases on the far side being occulted.

General.—The outer expanding arcs of R Aquarii suggest a nova-like outburst from the nucleus some centuries ago. The changing inner nebulosity and the motions indicated

TABLE 5

ORBITAL ELEMENTS CORRESPONDING TO THE VELOCITY-CURVE DERIVED FROM λ 4363 [O III]

P	26.7 years	K	29 km/sec
T	JD 2429850	γ	−42 km/sec
ω	265°	$a \sin i$	3.4×10^9 km
e	0.5		

TABLE 6

STELLAR ERUPTIONS
(In Order of Decreasing Violence)

I. Supernovae
  a) Type I
  b) Type II
II. Novae
  a) Fast
  b) Slow
III. Recurring novae
IV. Planetary nebulae
V. Simmering novae
  a) Combination spectra (symbiotic stars)
  b) R Aquarii (and other long-period variables?)
VI. Be stars
  a) P Cygni type
  b) Shell stars
  c) Normal
VII. Flaring dwarf stars
VIII. Solar phenomena
  a) Eruptive prominences
  b) Flares
  c) Corona

by the nebular lines that arise very near the nucleus reflect continuing activity. A detailed explanation of all the phenomena of R Aquarii is remote. But at least this object can be placed in the group of stars with active, expanding atmospheres; we might go further and call the nucleus a "simmering nova." This leads to the attempt, Table 6, to list various stellar eruptions in order of decreasing violence.

W. F. MEYER'S WORK ON BETA CANIS MAJORIS*

OTTO STRUVE
Lick Observatory, University of California
Received July 5, 1950

ABSTRACT

Table 1 lists the radial velocities of β Canis Majoris from 698 three-prism plates obtained with the Mills spectrograph of the Lick Observatory between 1904 and 1948. The star's radial-velocity-curve is characterized by three periods. $P_1 = 0.25002246$ day and $K_1 = 5.8$ km/sec were constant over the entire interval. P_2 varied from 0.2513015 to 0.2513003 day, with a corresponding change in K_2 from 4.2 to 2.0 km/sec. This variable period represents the variation in the contours of the absorption lines. Finally, P_3, the beat period of P_1 and P_2, varied from 49.09 to 49.17 days. This latter variation is probably accounted for by the variation of P_2.

There is no entirely satisfactory explanation of the variation in radial velocity, but the behavior of all stars of the β Cephei class differs so markedly from that of the cluster-type variables that pulsations *alone* are probably not sufficient. It is therefore suggested that we return, tentatively, to the consideration of a close binary whose invisible satellite is very small and dense. Perhaps P_1 represents the orbital period of this satellite, while P_2 may correspond to a pulsation induced by the satellite in the atmosphere of the principal star.

If very close binaries exist, one component of which is a normal star while the other is an object related to the white dwarfs, we should probably look for them among the β Cephei objects. Among the known spectroscopic binaries there are no other possible candidates. It would therefore be important to consider theoretically whether such systems could exist without disruption.

In 1930 Professor W. F. Meyer, of the Berkeley Astronomical Department of the University of California, undertook a study of the spectrum and radial velocity of β Canis Majoris that lasted until his premature death in August, 1948. Thereafter Dr. J. H. Moore, retired from the directorship of the Lick Observatory, took over the responsibility for completing this work, but he, too, died before he could finish it. In an obituary for Dr. Meyer, J. H. Moore wrote:

> He became interested in β Canis Majoris whose complex variations in radial velocity arise from causes other than orbital motions and to which he devoted an extended investigation based upon a long series of observations made in different years. Assuming that the observed velocity-curve was the resultant of two velocity-curves of different amplitudes and slightly different periods, he was able to derive a formula which satisfactorily represented all observations available to him in 1932, and it appeared that at least the first step had been taken toward a solution of the problem. More recent observations, and in particular those of this last year, indicated further complexities; and it was upon these he was working this past summer.[1]

Unfortunately, Mr. Moore, who was fully acquainted with Mr. Meyer's ideas, took with him to his grave what he knew of the "complexities" of β Canis Majoris. All Meyer's radial-velocity measurements have been preserved, but there are no notes concerning his final conclusions. Some forty Mills three-prism spectrograms had not yet been measured by him. This work has now been completed, and the final results of all the Lick Observatory measurements are given in Table 1. Figures 1 and 2 show some of the individual velocity-curves, which illustrate in a striking manner the 49-day variation in the amplitude, K.

Meyer's earlier results were published in abstract form.[2] Apparently he had been working, from time to time, on a more extensive paper; but the measurements of the long 1947–1948 series of plates were not discussed. I am greatly indebted to Director C. D.

* *Contributions from the Lick Observatory*, Ser. II, No. 31.

[1] *Pub. A.S.P.*, **60**, 287, 1948.

[2] *Pub. A.S.P.*, **46**, 202, 1934.

Table 1

RADIAL VELOCITIES OF β CANIS MAJORIS

Date	J.D. 241+	Velocity	Date	J.D.	Velocity
1904 Jan. 13	6493.808	+39.8	1909 Mar. 1	8367.746	+37.2
Feb. 1	6512.731	30.6	" 1	8367.761	38.3
1907 Nov. 10	7881.014	39.9	" 1	8367.775	42.2
Dec. 17	7927.856	28.2	" 1	8367.790	41.4
1908 Jan. 11	7952.805	30.6	" 1	8367.805	41.2
Feb. 24	7996.669	32.5	" 1	8367.822	40.5
Sep. 11	8196.042	31.9	" 11	8377.613	36.1
Oct. 5	8220.051	40.2	" 11	8377.629	31.8
" 9	8224.062	40.0	" 12	8378.611	34.2
" 13	8228.061	37.4	" 15	8381.635	35.8
Nov. 6	8252.049	36.5	" 16	8382.642	33.9
" 10	8286.096	27.0	" 17	8383.744	37.0
" 19	8265.003	40.8	" 17	8383.763	37.7
" 28	8274.962	29.0	Apr. 1	8398.619	29.3
" 29	8275.906	27.3	" 1	8398.636	25.6
Dec. 5	8281.910	34.1	" 1	8398.653	28.2
" 11	8287.811	33.3	1910 Feb. 11	8714.697	24.9
" 17	8293.892	30.5	" 11	8714.709	27.9
" 20	8296.819	31.5	" 11	8714.790	36.6
" 20	8296.969	38.6	" 11	8714.814	40.3
" 24	8300.777	39.9	Apr. 15	8777.629	32.4
" 24	8300.943	35.0	" 15	8777.640	32.9
1909 Feb. 22	8360.675	25.2	" 15	8777.655	33.1
" 22	8360.695	29.1	" 17	8779.637	33.5
" 22	8360.760	41.6	" 17	8779.649	35.7
" 22	8360.778	42.8	" 17	8779.663	34.0
Mar. 1	8367.600	36.5	" 20	8782.656	29.2
" 1	8367.615	33.6	" 20	8782.674	33.3
" 1	8367.634	27.7	" 21	8783.643	32.4
" 1	8367.646	25.6	" 21	8783.656	32.5
" 1	8367.657	24.2	" 21	8783.685	29.6
" 1	8367.668	23.2	" 22	8784.640	35.2
" 1	8367.706	29.6	" 22	8784.651	32.5
" 1	8367.718	30.2	" 22	8784.663	29.8
1909 " 1	8367.730	+34.0	1910 " 28	8790.630	+33.2

Table 1 (continued)

Date	J.D.	Velocity	Date	J.D. 242+	Velocity
1910 Apr. 28	2418790.644	+31.7	1917 Dec. 21	1584.779	+39.2
" 28	8790.658	29.0	" 21	1584.797	37.4
May 1	8793.653	24.2	" 21	1584.814	35.6
1917 Nov. 29	2421562.781	35.4	" 21	1584.831	39.1
" 29	1562.806	41.5	" 21	1584.848	36.1
" 29	1562.826	43.1	" 21	1584.865	37.2
" 29	1562.922	33.4	" 21	1584.882	33.2
" 29	1562.940	31.0	" 21	1584.899	30.1
" 29	1562.958	32.6	" 21	1584.915	31.2
" 30	1563.058	40.8	" 21	1584.933	32.2
Dec. 2	1565.776	36.2	" 21	1584.951	33.8
" 2	1565.794	40.7	" 21	1584.970	37.7
" 2	1565.811	43.8	1918 Jan. 17	1611.695	31.4
" 3	1566.763	36.4	" 17	1611.712	27.4
" 3	1566.781	36.9	" 18	1612.623	37.9
" 3	1566.799	39.0	" 18	1612.647	37.9
" 3	1566.817	42.0	" 18	1612.672	29.9
" 3	1566.850	40.0	" 18	1612.696	28.1
" 3	1566.960	32.2	" 18	1612.719	27.9
" 3	1566.998	33.9	" 18	1612.742	26.6
" 4	1567.815	37.2	" 18	1612.764	30.5
" 5	1568.784	34.3	" 18	1612.788	36.6
" 5	1568.803	35.3	" 18	1612.815	39.1
" 5	1568.823	37.5	" 18	1612.840	41.2
" 5	1568.858	37.7	" 18	1612.865	38.2
" 5	1568.878	37.9	" 28	1622.646	38.1
" 5	1568.896	37.8	" 28	1622.671	37.2
" 5	1568.917	34.5	" 28	1622.693	34.0
" 5	1568.934	30.9	" 28	1622.719	35.2
" 5	1568.952	34.4	" 28	1622.741	35.5
" 5	1568.969	31.9	" 28	1622.767	35.5
" 5	1568.988	31.5	" 28	1622.795	35.9
" 6	1569.005	31.2	" 28	1622.822	36.6
" 6	1569.023	32.2	" 28	1622.845	35.3
1917 " 21	1584.741	+39.3	1918 " 28	1622.870	+37.4

Table 1 (continued)

Date	J.D. 242+	Velocity	Date	J.D. 242+	Velocity
1918 Jan. 30	1624.644	+30.8	1918 Feb. 28	1653.691	+27.0
" 30	1624.669	31.8	Mar. 8	1661.708	32.2
" 30	1624.699	31.7	" 9	1662.605	42.8
" 30	1624.725	33.5	" 13	1666.721	29.3
" 30	1624.749	34.9	" 14	1667.611	39.9
" 30	1624.773	35.8	" 14	1667.721	33.6
" 30	1624.798	38.7	" 14	1667.745	32.7
" 30	1624.823	40.3	1930 Feb. 12	6019.637	34.0
" 30	1624.863	35.3	" 12	6019.672	41.1
" 30	1624.890	34.0	" 12	6019.695	43.9
Feb. 11	1636.615	32.5	" 12	6019.751	37.5
" 11	1636.632	28.9	" 12	6019.772	31.9
" 11	1636.651	28.1	" 12	6019.794	30.3
" 11	1636.667	27.6	" 12	6019.817	26.2
" 11	1636.682	27.7	" 14	6021.632	29.7
" 11	1636.696	31.8	" 14	6021.656	35.7
" 11	1636.713	33.7	" 14	6021.678	41.8
" 11	1636.749	41.7	" 14	6021.701	44.8
" 11	1636.769	43.7	" 14	6021.771	33.2
" 11	1636.788	46.9	" 14	6021.793	26.9
" 11	1636.811	41.2	" 14	6021.815	26.2
" 11	1636.833	41.8	" 11	6046.617	33.8
" 26	1651.648	34.1	" 11	6046.636	36.0
" 26	1651.667	30.0	" 11	6046.654	33.8
" 26	1651.686	25.2	" 11	6046.672	35.2
" 26	1651.706	25.7	" 11	6046.689	32.5
" 26	1651.803	42.8	" 11	6046.707	32.5
Feb. 27	1652.638	30.1	" 11	6046.728	33.2
" 27	1652.657	27.5	" 11	6046.749	31.3
" 27	1652.679	24.4	" 11	6046.771	31.6
" 27	1652.704	21.8	1931 Oct. 14	6628.998	35.1
" 27	1652.735	26.3	" 14	6629.018	36.6
" 28	1653.604	44.1	" 14	6629.035	35.8
" 28	1653.619	39.6	" 14	6629.050	35.9
1918 " 28	1653.672	+27.9	1931 Oct. 14	6629.068	+35.3

Table 1 (continued)

Date	J.D. 242+	Velocity
1931 Oct. 17	6631.931	+33.7
" 17	6631.951	31.9
" 17	6631.970	33.3
" 17	6631.986	35.7
" 17	6632.002	36.3
" 17	6632.020	35.2
" 17	6632.034	35.4
" 17	6632.047	36.2
" 17	6632.069	35.5
" 24	6638.888	30.8
" 24	6638.906	34.4
" 24	6638.920	34.3
" 24	6638.938	37.4
" 24	6638.950	40.9
" 24	6638.967	41.7
" 24	6638.980	40.5
" 24	6638.998	39.2
" 24	6639.018	36.8
" 24	6639.036	33.5
" 24	6639.056	30.4
" 24	6639.074	28.7
" 28	6642.896	30.7
" 28	6642.915	33.4
" 28	6642.936	37.3
" 28	6642.958	40.5
" 28	6642.979	40.7
" 28	6642.997	39.9
" 28	6643.014	39.8
" 28	6643.033	35.1
" 28	6643.052	31.8
" 28	6643.068	30.4
Nov. 1	6645.892	30.0
" 1	6645.920	34.2
" 1	6645.946	36.2
1931 " 3	6648.870	+25.9
1931 Nov. 3	6648.880	+27.4
" 3	6648.901	29.2
" 3	6648.922	31.7
" 3	6648.935	36.2
" 3	6648.953	39.2
" 3	6648.965	44.3
" 3	6648.977	42.9
" 3	6648.982	43.5
" 3	6648.994	44.2
" 3	6649.015	43.4
" 3	6649.027	40.2
" 3	6649.050	34.2
" 3	6649.067	31.6
" 3	6649.085	27.2
" 6	6651.848	25.5
" 6	6651.865	25.6
" 6	6651.883	27.2
" 6	6651.889	25.8
" 6	6651.917	28.7
" 6	6651.926	31.8
" 6	6651.945	35.4
" 6	6651.955	37.4
" 6	6651.969	40.7
" 6	6651.980	42.7
" 6	6651.991	41.8
" 6	6652.003	42.3
" 6	6652.027	40.2
" 6	6652.038	37.1
" 6	6652.054	37.4
" 6	6652.065	33.7
" 6	6652.077	28.9
" 6	6652.088	25.9
" 9	6654.837	27.2
" 9	6654.856	24.4
1931 " 9	6654.880	+23.4

Table 1 (continued)

Date	J.D. 242+	Velocity	Date	J.D. 242+	Velocity
1931 Nov. 9	6654.906	+25.3	1931 Nov. 24	6669.816	+39.6
" 9	6654.931	30.7	" 24	6669.840	33.2
" 9	6654.951	35.4	" 24	6669.866	28.1
" 9	6654.973	40.8	" 24	6669.894	26.7
" 9	6654.995	41.8	" 24	6669.917	25.9
" 9	6655.013	43.6	" 24	6669.946	30.0
" 9	6655.037	39.7	" 24	6669.965	35.2
" 9	6655.066	32.8	" 24	6669.988	39.4
" 9	6655.091	27.4	" 24	6670.024	41.2
" 12	6657.826	33.9	" 24	6670.047	40.9
" 12	6657.849	27.0	" 24	6670.067	39.2
" 12	6657.876	24.2	" 30	6675.781	37.7
" 12	6657.904	24.3	" 30	6675.800	38.9
" 12	6657.933	29.7	" 30	6675.828	34.8
" 12	6657.963	35.7	" 30	6675.856	31.0
" 12	6657.989	42.4	" 30	6675.884	30.1
" 12	6658.014	45.9	" 30	6675.908	30.2
" 12	6658.033	41.2	" 30	6675.932	28.1
" 12	6658.052	38.1	" 30	6675.960	29.5
" 12	6658.073	34.7	" 30	6675.981	35.5
" 12	6658.090	31.5	" 30	6676.008	36.6
" 19	6664.809	40.8	" 30	6676.033	37.7
" 19	6664.832	35.1	" 30	6676.058	38.2
" 19	6664.855	26.1	Dec. 6	6681.763	35.6
" 19	6664.882	25.7	" 6	6681.788	37.3
" 19	6664.903	24.3	" 6	6681.820	36.1
" 19	6664.920	25.8	" 6	6681.849	32.3
" 19	6664.939	28.8	" 6	6681.879	31.0
" 19	6664.966	34.3	" 6	6681.909	32.0
" 19	6664.992	41.1	" 6	6681.935	33.2
" 19	6665.023	40.7	" 6	6681.962	33.3
" 19	6665.044	39.2	" 6	6681.986	37.5
" 19	6665.062	37.5	" 6	6682.022	35.9
" 19	6665.080	32.9	" 10	6685.759	35.5
1931 " 24	6669.793	+42.1	1931 Dec. 10	6685.781	+33.7

Table 1 (continued)

Date	J.D. 242+	Velocity	Date	J.D. 242+	Velocity
1931 Nov. 10	6685.804	+34.0	1932 Mar. 21	6787.656	+31.5
" 16	6691.726	41.0	" 21	6787.683	35.9
" 16	6691.758	40.0	" 21	6787.712	39.4
" 16	6691.783	36.4	" 21	6787.745	39.7
" 16	6691.810	30.4	Nov. 8	7019.872	37.2
" 16	6691.834	27.3	" 8	7019.897	34.2
" 16	6691.859	26.9	" 8	7019.925	33.3
" 16	6691.881	31.4	" 8	7019.953	31.1
" 16	6691.909	31.5	" 8	7019.979	32.0
" 16	6691.935	36.2	" 8	7020.007	33.3
" 16	6691.963	38.9	" 8	7020.032	38.3
" 16	6691.983	39.1	" 8	7020.059	40.1
" 16	6692.010	40.2	" 8	7020.081	38.5
Dec. 19	6694.720	42.3	1934 Jan. 30	7466.630	34.4
" 19	6694.741	41.2	" 30	7466.646	32.5
" 19	6694.762	39.8	" 30	7466.661	33.7
" 19	6694.792	32.9	" 30	7466.676	34.1
" 19	6694.826	29.1	" 30	7466.691	31.5
" 19	6694.857	28.5	" 30	7466.703	33.6
" 19	6694.874	27.4	" 30	7466.715	32.7
" 19	6694.891	28.0	" 30	7466.731	31.0
" 19	6694.923	32.5	" 30	7466.744	32.4
" 19	6694.945	40.2	" 30	7466.761	31.8
" 19	6694.967	41.2	" 30	7466.779	33.4
1932 Jan. 6	6712.717	33.5	" 30	7466.797	34.0
" 6	6712.742	40.9	" 30	7466.816	33.5
" 6	6712.768	42.3	" 30	7466.836	35.1
" 6	6712.789	41.9	" 30	7466.853	35.8
" 6	6712.807	39.9	" 31	7467.629	33.8
" 6	6712.828	36.1	" 31	7467.645	33.8
" 6	6712.855	30.5	" 31	7467.659	34.6
" 6	6712.910	23.6	" 31	7467.674	31.9
" 6	6712.933	26.6	" 31	7467.688	33.6
" 6	6712.956	30.4	" 31	7467.703	33.2
1932 Mar. 21	6787.620	+27.4	1934 " 31	7467.716	+31.1

Table 1 (continued)

Date	J.D.	Velocity	Date	J.D. 243+	Velocity
1934 Jan. 31	2427467.730	+32.3	1942 Jan. 13	0372.857	+34.0
" 31	7467.744	33.1	" 13	0372.876	33.5
" 31	7467.757	35.6	" 13	0372.891	33.7
" 31	7467.769	32.8	" 13	0372.907	29.8
" 31	7467.783	36.0	Feb. 12	0402.605	42.6
" 31	7467.795	35.0	" 12	0402.620	43.0
" 31	7467.809	33.8	" 12	0402.635	40.8
" 31	7467.823	33.7	" 12	0402.650	37.9
" 31	7467.843	33.7	" 12	0402.663	32.1
1939 Feb. 15	9309.730	43.4	" 12	0402.676	31.0
" 15	9309.753	43.1	" 12	0402.689	28.0
" 15	9309.785	40.0	" 12	0402.703	24.4
" 16	9310.612	24.5	" 12	0402.715	26.8
" 16	9310.629	26.4	" 12	0402.728	24.8
" 16	9310.646	23.7	" 12	0402.740	24.4
" 16	9310.664	26.5	" 12	0402.753	24.8
" 16	9310.681	32.4	" 12	0402.766	27.0
" 16	9310.698	37.0	" 12	0402.780	27.6
" 16	9310.716	41.3	" 12	0402.795	31.4
" 16	9310.735	41.4	" 12	0402.808	32.6
" 16	9310.755	45.8	" 12	0402.823	35.0
" 16	9310.776	41.5	" 12	0402.846	42.2
" 16	9310.796	34.9	Mar. 6	0424.630	32.8
" 16	9310.818	30.4	" 6	0424.642	33.8
1942 Jan. 13	2430372.673	33.8	" 6	0424.661	30.2
" 13	0372.684	32.8	" 6	0424.672	29.7
" 13	0372.703	32.8	" 6	0424.682	31.5
" 13	0372.721	32.8	" 6	0424.695	30.7
" 13	0372.737	31.1	" 6	0424.705	32.6
" 13	0372.752	30.8	" 6	0424.716	28.4
" 13	0372.767	30.9	" 6	0424.727	29.9
" 13	0372.782	32.2	" 6	0424.738	30.0
" 13	0372.796	33.0	" 6	0424.749	30.0
" 13	0372.810	33.2	" 6	0424.761	30.4
" 13	0372.825	35.7	" 6	0424.773	29.8
1942 Jan. 13	2430372.840	+35.5	1942 Mar. 6	0424.786	+32.8

Table 1 (continued)

Date	J.D. 243+	Velocity	Date	J.D. 243+	Velocity
1942 Mar. 6	0424.799	+32.6	1947 Dec. 13	2532.788	+36.8
" 6	0424.813	39.7	" 13	2532.799	37.7
1947 Nov. 21	2510.861	33.0	" 13	2532.812	37.4
" 21	2510.900	27.6	" 13	2532.822	36.9
" 21	2510.931	24.5	" 13	2532.831	35.3
" 21	2510.948	26.6	" 13	2532.841	34.2
" 21	2510.963	27.9	" 13	2532.851	33.8
" 21	2510.976	30.8	" 13	2532.860	35.8
" 21	2510.993	32.4	" 13	2532.869	31.4
" 21	2511.007	35.5	" 13	2532.898	29.9
" 21	2511.021	38.1	" 13	2532.909	28.8
" 21	2511.036	40.6	" 13	2532.918	31.2
" 24	2513.853	38.2	" 13	2532.930	29.5
" 24	2513.867	35.3	" 13	2532.941	29.2
" 24	2513.880	29.9	" 13	2532.954	30.1
" 24	2513.893	29.8	" 13	2532.964	28.7
" 24	2513.907	26.8	" 13	2532.978	29.6
" 24	2513.918	24.8	" 13	2532.993	31.4
" 24	2513.932	25.4	" 13	2533.009	31.4
" 24	2513.956	27.0	" 19	2538.784	37.5
" 24	2513.969	28.4	" 19	2538.798	39.6
" 24	2513.984	32.0	" 19	2538.812	38.9
" 24	2514.018	34.4	" 19	2538.824	37.2
" 24	2514.033	38.5	" 19	2538.836	33.5
" 24	2514.049	40.2	" 19	2538.850	33.2
Dec. 3	2522.809	38.6	" 19	2538.865	33.0
" 3	2522.820	37.9	" 19	2538.905	32.9
" 3	2522.832	37.7	" 24	2543.762	40.0
" 3	2522.842	38.6	" 24	2543.776	39.7
" 3	2522.857	37.5	" 24	2543.793	37.2
" 3	2522.872	35.0	" 24	2543.807	36.8
" 3	2522.899	31.2	" 24	2543.820	34.6
" 3	2522.911	29.0	" 24	2543.832	32.5
" 13	2532.767	34.0	" 24	2543.843	32.8
1947 Dec. 13	2532.777	+35.4	1947 Dec. 24	2543.857	+29.2

Table 1 (continued)

Date	J.D. 243+	Velocity	Date	J.D. 243+	Velocity
1947 Dec. 24	2543.870	+31.5	1948 Jan. 11	2561.902	+26.5
" 24	2543.882	30.2	" 11	2561.943	25.9
" 24	2543.891	28.3	" 18	2568.656	30.6
" 24	2543.918	27.3	" 18	2568.673	28.2
" 24	2543.930	28.2	" 18	2568.689	26.6
" 24	2543.944	29.3	" 18	2568.705	27.0
" 24	2543.960	30.2	" 18	2568.719	26.6
" 24	2543.972	31.8	" 18	2568.730	26.8
" 24	2543.984	34.3	" 18	2568.743	30.4
" 30	2549.727	34.0	" 18	2568.764	34.6
" 30	2549.749	35.3	" 18	2568.776	34.6
" 30	2549.765	40.2	" 18	2568.788	34.9
" 30	2549.782	41.2	" 18	2568.802	38.8
" 30	2549.802	39.6	" 18	2568.817	38.1
" 30	2549.821	37.2	" 18	2568.830	37.8
" 30	2549.842	33.2	" 18	2568.841	37.0
" 30	2549.858	30.7	" 18	2568.855	36.3
" 30	2549.893	26.2	" 18	2568.873	33.9
" 30	2549.913	24.9	" 18	2568.886	36.7
" 30	2549.932	27.0	Dec. 25	2575.637	33.4
" 30	2549.951	26.9	" 25	2575.654	31.6
1948 Jan. 11	2561.682	23.7	" 25	2575.669	28.6
" 11	2561.697	24.5	" 25	2575.683	28.2
" 11	2561.711	28.5	" 25	2575.694	27.2
" 11	2561.729	28.9	" 25	2575.708	27.3
" 11	2561.742	32.5	" 25	2575.717	28.4
" 11	2561.753	34.5	" 25	2575.727	27.6
" 11	2561.769	37.8	" 25	2575.739	30.0
" 11	2561.794	39.7	" 25	2575.756	31.4
" 11	2561.808	41.5	" 25	2575.768	32.3
" 11	2561.822	40.9	" 25	2575.778	34.4
" 11	2561.839	39.3	" 25	2575.799	37.5
" 11	2561.854	35.1	" 25	2575.810	38.5
" 11	2561.872	33.4	" 25	2575.821	38.3
1948 " 11	2561.887	+28.9	1948 Dec. 25	2575.838	+37.9

Table 1 (continued)

Date	J.D. 243+	Velocity	Date	J.D. 243+	Velocity
1948 Dec. 25	2575.847	+36.9	1948 Feb. 17	2598.679	+25.4
" 25	2575.862	34.8	" 17	2598.693	26.5
Jan. 30	2580.628	37.5	" 17	2598.705	28.1
" 30	2580.642	35.2	" 17	2598.722	34.6
Feb. 11	2592.651	27.6	" 17	2598.735	34.8
" 11	2592.667	28.2	" 17	2598.744	35.3
" 11	2592.685	30.4	" 17	2598.755	37.4
" 11	2592.735	34.8	" 17	2598.802	40.0
" 11	2592.750	36.3	" 17	2598.819	37.2
" 11	2592.766	35.4	" 24	2605.635	29.3
" 11	2592.809	40.7	" 24	2605.651	29.5
" 11	2592.834	33.6	" 24	2605.666	27.9
" 11	2592.852	33.3	" 24	2605.681	27.2
" 15	2596.615	34.6	" 24	2605.697	27.6
" 15	2596.630	28.6	" 24	2605.711	29.3
" 15	2596.643	29.4	" 24	2605.725	37.0
" 15	2596.659	30.2	" 24	2605.739	32.4
" 15	2596.670	30.0	" 24	2605.758	38.0
" 15	2596.686	28.7	" 24	2605.776	38.5
" 15	2596.697	28.1	" 24	2605.805	44.4
" 15	2596.708	30.1	" 24	2605.829	39.3
" 15	2596.719	30.2	Mar. 1	2611.643	31.2
" 15	2596.736	34.6	" 1	2611.656	27.7
" 15	2596.753	34.8	" 1	2611.668	28.3
" 15	2596.767	36.5	" 1	2611.681	25.2
" 15	2596.778	36.7	" 1	2611.693	22.0
" 15	2596.795	38.4	" 1	2611.704	22.5
" 15	2596.810	36.8	" 1	2611.740	29.7
" 15	2596.827	33.8	" 1	2611.753	30.9
" 17	2598.633	25.2	" 1	2611.771	35.0
" 17	2598.644	24.2	" 1	2611.785	37.8
" 17	2598.654	23.3	" 1	2611.807	40.7
1948 Feb. 17	2598.668	+24.8	1948 Mar. 1	2611.821	+39.8

Shane for encouraging me to prepare this work for publication and to Drs. G. H. Herbig and H. F. Weaver for assistance in locating most of the original spectrograms. My own interest in this star dates from the time when I was observing β Cephei at the Yerkes Observatory. Later, several series of coudé spectrograms of β Canis Majoris were obtained at the McDonald Observatory.[2] Some slight discrepancies between the results of the

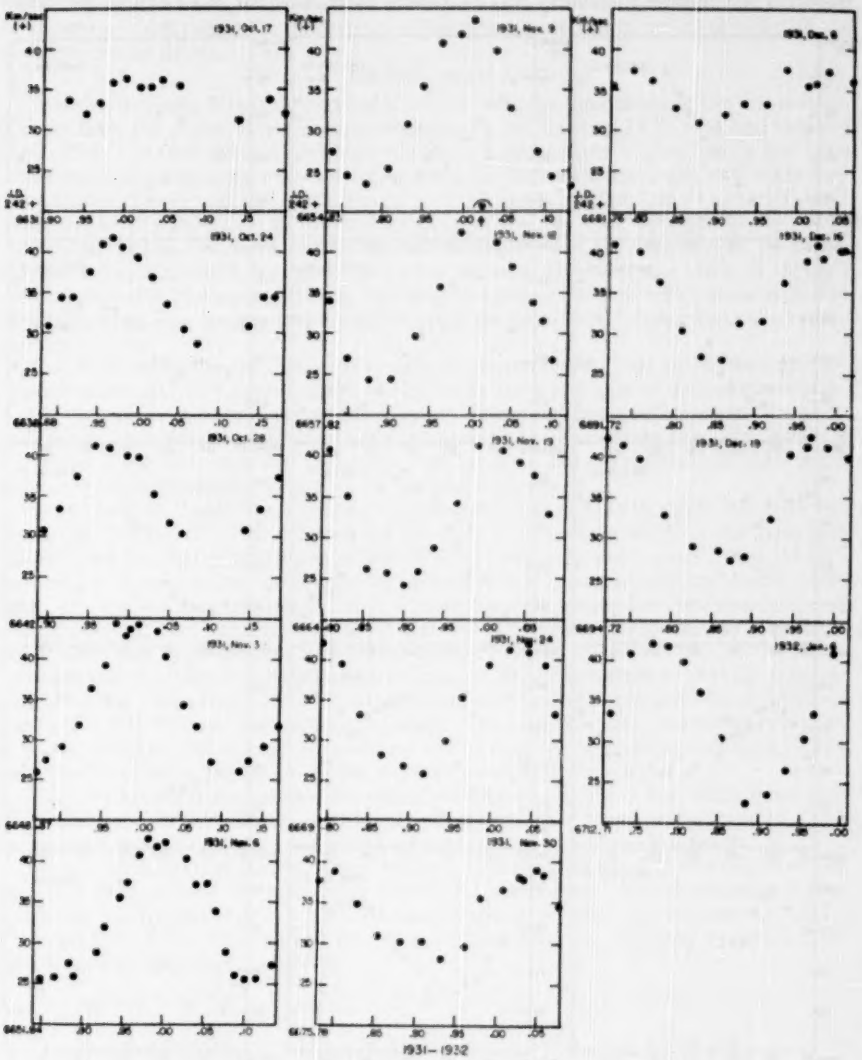

FIG. 1.—Velocity-curves of β Canis Majoris

[2] O. Struve and P. Swings, *Ap. J.*, **94**, 99, 1941; A. B. Underhill, *Ap. J.*, **104**, 388, 1946.

McDonald measurements and the predictions based upon Meyer's earlier work led to renewed observational effort at the Lick Observatory in 1942 and especially in 1947–1948. The seeds of the "complexities" to which Dr. Moore referred were probably first noticed when the McDonald results were compared with those obtained at the Lick Observatory.

The earlier literature concerning β Canis Majoris was referred to in Meyer's 1934 paper.[2] The variation in velocity was discovered by S. Albrecht in 1908, and the varia-

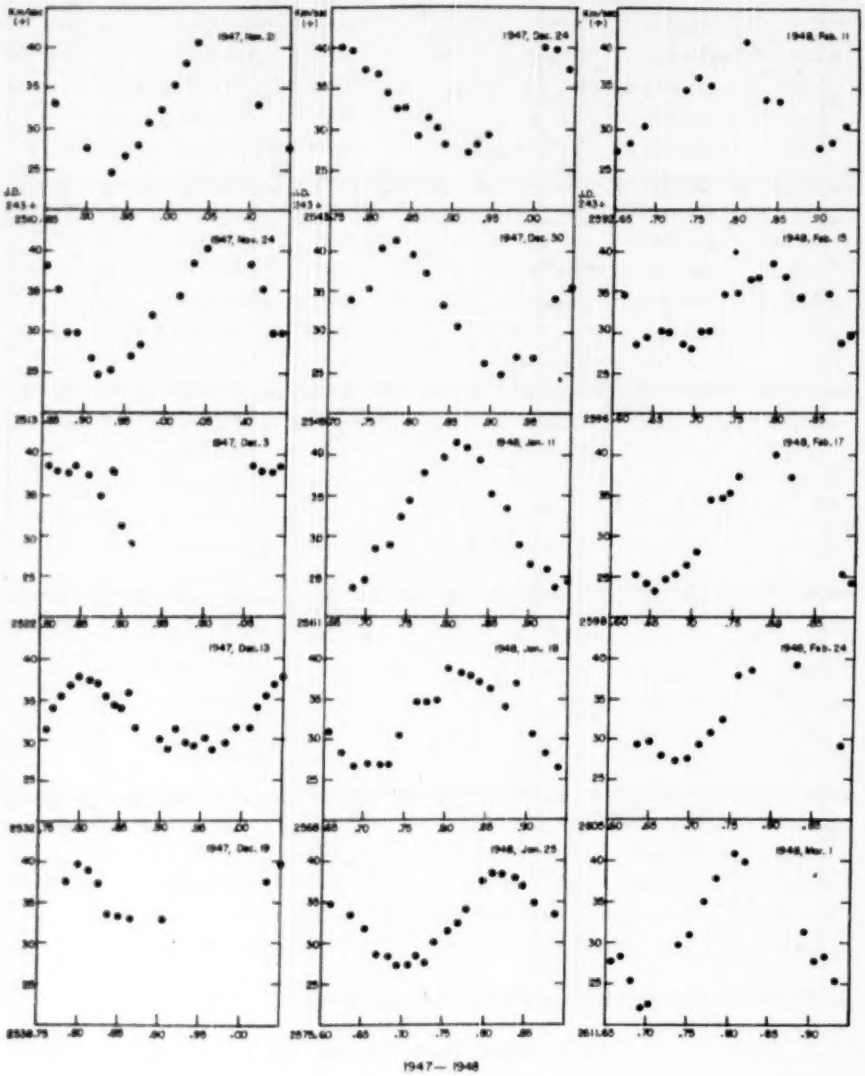

FIG. 2.—Velocity-curves of β Canis Majoris

tion in line width by F. Henroteau in 1918. The latter also proposed the interpretation of the velocity-curve, later adopted by Meyer, as the sum of two harmonic oscillations with slightly different periods. Henroteau's later work at Ottawa[4] was not accurate enough to be of use in connection with the present discussion.

The light-curve of β Canis Majoris was investigated by E. A. Fath,[5] and evidence of variation was obtained, with an amplitude of 0.03 mag., but the period of this variation is uncertain; Fath concluded that more observations are necessary before this part of the problem can be solved.

THE LINE WIDTHS

In order to verify Meyer's period of 0.2513015 day for the change in the line widths, I chose from the material two groups of spectrograms: those of 1930–1934 and those of 1947–1948. For each date on which a sufficiently large number of good plates had been obtained I estimated separately the times when the lines were narrowest and when they were widest. I next took the mean epochs of "wide" and "narrow" ($w \rightarrow n$) and Table 2 gives the results. Adopting as the best mean epochs of ($w \rightarrow n$), obtained from smooth curves, JD 2426669.942 and 2432510.916, for Groups I and II, respectively, we find a new period of 0.2513003 day, which gives the values of O − C in the table. If Meyer's old period is used, the two epochs are represented within 0.037 day, which is not regarded as satisfactory. But the result confirms the single periodicity of the phenomenon of varying line widths.

The departures (O − C) have no systematic character. In particular, they are not related to the 49.1-day period of the oscillation in the amplitude of the velocity-curve.

For the earlier material, we can use Meyer's discussion. In accordance with the work of Henroteau, Meyer measured with the micrometer the line widths in half-millimeters for seven absorption lines and took their sum for each plate. Variations in these sums represent fairly accurately variations in the line contours.

As an example, Table 3 lists the line widths on November 8, 1931. From this table the epoch JD 2426654.935 was deduced for the time of minimum width of the lines and 2426655.060 for that of maximum width. With these epochs and a period of 0.2513015 day for the line variation, the epochs for maximum widths were calculated for all dates when line widths were measured. Table 4 gives the comparison between observed and computed epochs for maximum widths of Henroteau's measures from the 1917 and 1918 plates and from those measured by Meyer on more recent plates.

We have a total interval including more than 43,000 cycles. The two periods differ by 0.0000012 day. Over the entire interval the use of each period would produce an accumulated error of 0.060 day, which is not admissible. The suspicion arises that this period has changed. Perhaps this change accounts for the change in the period of 49 days of the variation in velocity amplitude, which we shall consider later.

There is a strong suspicion that the amplitude of the variation in line width is not constant. Table 5 lists those dates on which the effect was "very large" or "very small," the comparison in each case referring to the *average effect* observed in each season.

There is no indication that these epochs are connected with the 49.1-day period of the variation in amplitude of the velocity-curve. But the *average effect* of variation of line width was less conspicuous in 1947–1948 than in the other well-observed seasons, 1917–1918 and 1931–1932. This may be related to the fact that the curves of variation in K show a similar difference, as follows:

In 1917–1918 : $2K_{max} = 20$ km/sec ; $2K_{min} = 4$ km/sec ;

In 1930–1934 : $2K_{max} = 20$ km/sec ; $2K_{min} = 4$ km/sec ;

In 1947–1948 : $2K_{max} = 17$ km/sec ; $2K_{min} = 8$ km/sec .

[4] *Pub. Dom. Obs. Ottawa*, **8**, 31, 1922. [5] *Lick Obs. Bull.*, **17**, 116, 1935.

In terms of Meyer's double sinusoidal waves this would mean:

For 1917–1918 : $2K_1+2K_2=20$; $2K_1-2K_2=4$;

For 1930–1934 : $2K_1+2K_2=20$; $2K_1-2K_2=4$;

For 1947–1948 : $2K_1+2K_2=17$; $2K_1-2K_2=8$.

Solving these three sets, we have

For 1917–1918 : $K_1=6$; $K_2=4$ km/sec ;

For 1930–1934 : $K_1=6$; $K_2=4$ km/sec ;

For 1947–1948 : $K_1=6$; $K_2=2$ km/sec .

TABLE 2

AVERAGE TIMES OF SUCCESSIVE WIDEST AND NARROWEST LINES

DATE	OBS. (w→n)	COMP. (w→n)	(O−C)
	Group I		
1930 Feb. 12	2426019.819	0.824	−0.005
Feb. 14	6021.826	.834	− .008
Mar. 11	6046.692	.713	− .021
1931 Oct. 13	6628.970	.979	− .009
Oct. 17	6632.010	.995	+ .015
Oct. 24	6639.043	.032	+ .011
Oct. 28	6643.072	.053	+ .019
Nov. 3	6649.083	.084	− .001
Nov. 6	6652.096	.100	− .004
Nov. 9	6654.882	.864	+ .018
Nov. 12	6657.894	.880	+ .014
Nov. 19	6664.899	.916	− .017
Nov. 24	6669.932	.942	− .010
Nov. 30	6675.975	.973	+ .002
Dec. 6	6681.774	.753	+ .021
Dec. 10	6685.742?	.774	− .032?
Dec. 16	6691.834	.805	+ .029
Dec. 19	6694.808	.821	− .013
1932 Jan. 6	6712.890?	.915	− .025?
Mar. 21	6787.558?	.552	+ .006?
Nov. 8	7019.992	.967	+ .025
1934 Jan. 30	7466.814	.821	− .007
Jan. 31	7467.806	0.826	−0.020
	Group II		
1947 Nov. 21	2432510.931	0.916	+0.015
Nov. 24	2513.938	.932	+ .006
Dec. 13	2532.758	.779	− .021
Dec. 24	2543.868	.837	+ .031
1948 Jan. 11	2561.643	.653	− .010
Jan. 18	2568.713	.715	− .002
Jan. 24	2575.778	.762	+ .016
Feb. 11	2592.605	.589	+ .016
Feb. 15	2596.860	.861	− .001
Feb. 17	2598.861	.872	− .011
Feb. 24	2605.883	.908	− .025
Mar. 1	2611.672	0.688	−0.016

TABLE 3

LINE WIDTHS ON NOVEMBER 8, 1931
(Unit = 0.5 mm)

PLATE	JD	*He* I 4388	*O* II		*He* I 4471	*Si* III			Σ
			4415	4417		4552	4567	4574	
1	2426654.837	0.210	0.155	0.160	0.215	0.170	0.145	0.160	1.215
2	6654.856	.200	.175	.160	.200	.150	.160	.162	1.207
3	6654.880	.225	.145	.155	.190	.122	.115	.110	1.062
4	6654.906	.180	.145	.115	.180	.130	.105	.115	0.970
5	6654.931	.180	.125	.130	.175	.100	.095	.095	0.900
6	6654.951	.175	.115	.145	.170	.100	.125	.105	0.935
7	6654.973	.170	.122	.125	.150	.120	.130	.105	0.922
8	6654.995	.205	.165	.165	.185	.120	.105	.110	1.075
9	6655.013	.200	.155	.155	.180	.145	.115	.135	1.088
10	6655.037	.210	.175	.160	.195	.170	.160	.140	1.210
11	6655.066	.215	.170	.170	.195	.155	.145	.140	1.190
12	6655.091	0.230	0.165	0.150	0.195	0.140	0.145	0.135	1.160

TABLE 4

EPOCHS FOR MAXIMUM WIDTH OF LINES
(T_0 = 2426655.060; Period = $0^d.2513015$)

Observed	Computed	O−C	No. of Cycles	Observed	Computed	O−C	No. of Cycles
2421562.940	.938	+0.002	−20,263	2426643.000	.998	+0.002	− 48
1566.956	.959	− .003	−20,247	6649.025	.029	− .004	− 24
1568.967	.969	− .002	−20,239	6664.860	.860	.000	+ 39
1584.795	.800	− .005	−20,176	6669.875	.887	− .012	+ 59
1612.693	.695	− .002	−20,065	6691.745	.750	− .005	+ 146
1622.743	.747	− .004	−20,025	7019.970	.965	+ .005	+ 1452
1624.755	.758	− .003	−20,017	7466.770	.764	+ .006	+ 3230
1636.824	.823	+ .001	−19,969	9310.805	.810	−0.005	+10,568
6638.980	.977	+0.003	− 64				

TABLE 5

RANGE IN LINE WIDTHS

VERY LARGE		VERY SMALL	
Date	JD	Date	JD
1931 Nov. 3	2406649	1930 Feb. 12	2426019
1931 Dec. 16	2426691	1931 Oct. 24	2426639
1948 Feb. 15	2432596	1931 Oct. 28	2426643
		1931 Dec. 6	2426681
		1947 Dec. 13	2432532

There is no appreciable change in K_1; but the decrease in the amplitude of that wave whose period of 0.25130 day is identical with the period of change in line contour is distinctly suggestive. If the value of K_2 is correlated with the amplitude of the variation in line width, it is probable that the entire secondary velocity variation is caused by the changing shapes of the lines.

THE VARIATION OF K

In order to describe this variation, we have listed in Table 6 the observed values of

TABLE 6

VALUES OF $2K$ FROM INDIVIDUAL VELOCITY-CURVES

Date	JD	Observed $2K$ (Km/Sec)	Date	JD	Observed $2K$ (Km/Sec)
1909 Mar. 2	2418367	18	1934 Jan. 30	2427466	4
1909 Feb. 23	2418361	20	1934 Jan. 31	2427467	2.5
1917 Nov. 30	2421563	12	1939 Feb. 16	2429310	20
1917 Dec. 6	2421569	8	1941 Jan. 24	2430018	11.5 (McDonald)
1917 Dec. 22	2421585	9.5			
1918 Jan. 19	2421613	13	1942 Jan. 13	2430373	5
1918 Jan. 29	2421623	4	1942 Feb. 12	2430402	17.5
1918 Jan. 31	2421625	4	1942 Feb. 13	2430403	19.5 (McDonald)
1918 Feb. 12	2421637	16			
1918 Feb. 27	2421652	18.5	1942 Mar. 4	2430422	7.5 (McDonald)
1918 Feb. 28	2421653	20			
1930 Feb. 12	2426020	20	1942 Mar. 6	2430424	5
1930 Feb. 14	2426022	18.5	1947 Nov. 21	2432510	18
1931 Oct. 17	2426632	4	1947 Nov. 24	2432513	16
1931 Oct. 24	2426639	12	1947 Dec. 3	2432522	10
1931 Oct. 28	2426643	12.5	1947 Dec. 13	2432532	8
1931 Nov. 3	2426649	19	1947 Dec. 19	2432538	9
1931 Nov. 6	2426652	18	1947 Dec. 24	2432543	13
1931 Nov. 9	2426655	19	1947 Dec. 30	2432549	16
1931 Nov. 12	2426658	20	1948 Jan. 11	2432561	17
1931 Nov. 19	2426665	16.5	1948 Jan. 18	2432568	11.5 (McDonald)
1931 Nov. 24	2426670	14.5			
1931 Nov. 30	2426676	8	1948 Jan. 25	2432575	10
1931 Dec. 6	2426682	5	1948 Feb. 11	2432592	12
1931 Dec. 16	2426692	13	1948 Feb. 15	2432596	12.5
1931 Dec. 19	2426695	14.5	1948 Feb. 17	2432598	16
1932 Jan. 6	2426713	17	1948 Feb. 24	2432605	14.5
1932 Mar. 21	2426788	12	1948 Mar. 1	2432611	17.5
1932 Nov. 8	2427019	9			

$2K$ for all well-observed cycles. Figure 3 shows these values plotted, with a period of 49.1 days, in three groups. There is a marked change in the most recent curve from the two earlier ones. As we shall see, all three curves agree reasonably well, in shape, with Meyer's theoretical expression. We derive three epochs of minimum K, as shown in the accompanying tabulation. The two periods are not reconcilable within the errors of the

Epoch (JD)	Interval (Days)	No. of Cycles	P_2 (Days)	No. of Cycles	P_2 (Days)
2421576	5056	103	49.087	223	49.130
2426632					
2426632	5900	120	49.167		
2432533					

observations. If we use Meyer's adjusted value, 49.126 days, we obtain a departure of 4 days in 103 cycles. It is not possible that any of the three epochs is in error by such a large amount. We conclude that P_2 has changed appreciably in 33 years.

The theoretical expression for the variation of K is given by

$$K = \sqrt{(K_1 + K_2 \cos x)^2 + (K_2 \sin x)^2},$$

where

$$x = (\omega_1 - \omega_2)\, t - (\phi_1 - \phi_2),$$

and the observed velocity at any moment is

$$V = K_1 \sin(\omega_1 t - \phi_1) + K_2 \sin(\omega_2 t - \phi_2).$$

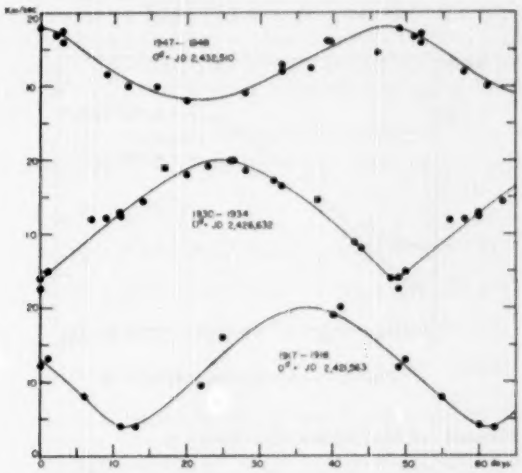

FIG. 3.—Observed oscillation of $2K$

The shift of the observed maximum (or minimum) radial velocity from the maximum value of $K_1 \sin(\omega_1 t - \phi_1)$ is given by

$$\phi = \text{arc } tg \frac{K_2 \sin x}{K_1 + K_2 \cos x}.$$

Figure 4 gives the theoretical curves computed as follows:

$$K_1 = 5.8 \text{ km/sec}; \qquad K_2 = 4.2 \text{ km/sec}, \tag{1}$$

$$K_1 = 5.8 \text{ km/sec}; \qquad K_2 = 2.0 \text{ km/sec}. \tag{2}$$

These curves almost coincide with the observed curves of Figure 3. The first set of values for K_1 and K_2 satisfies the observations made in 1917–1918 and in 1930–1934. The second set satisfies those made in 1947–1948.

We shall next explore the behavior of that period of velocity variation which has the larger amplitude of 6 km/sec. We shall therefore select three epochs during each of the intervals, 1917–1918, 1931–1934, and 1947–1948, as recorded in Table 6, when K was near its maximum value, and we shall add three epochs from the years 1909, 1939, and

1942, when this was also the case. Maximum radial velocity occurred as in the accompanying tabulation. The approximate period, P_1, is known from Meyer's work as about

Date	Epoch JD	Date	Epoch JD
1909 Mar. 2.....	2418367.78	1939 Feb. 16.....	2429310.75
1918 Feb. 28	2421652.83	1942 Feb. 13.....	2430403.61
1931 Nov. 12.....	2426658.01	1948 Jan. 11.....	2432561.81

0.2500222 day, and was derived by him from the relation

$$\frac{1}{49.11} = \frac{1}{P_1} - \frac{1}{0.2513015}.$$

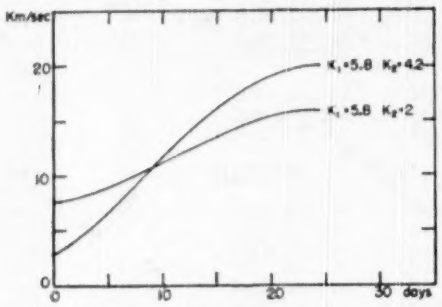

FIG. 4.—Computed oscillation of $2K$

Meyer's resulting formula for the combined velocity is

$$V = 4.2 \sin\left[\frac{2\pi}{0.2513015}(t-T_1)\right] + 5.8 \sin\left[\frac{2\pi}{0.2500222}(t-T_2)\right],$$

where T_1 = JD 2426660.210 and T_2 = JD 2426660.948. We use the second and last epochs to give us a revised period, P_1 = 0.25002246, which represents an interval of 10,908.98 days or 43,632 cycles. We then obtain the representation of the intervals given in the accompanying tabulation. This representation is entirely within the precision with

Epoch JD	Interval Obs. (Days)	Comp. (Decimal Day)	Difference O−C (Day)	Epoch JD	Interval Obs. (Days)	Comp. (Decimal Day)	Difference O−C (Day)
2418367.78				2429310.75			
	3285.05	0.045	+0.005		1092.86	0.848	+0.012
2421652.83				2430403.61			
	5005.18	.200	− .020		2158.20	0.194	+0.006
2426658.01				2432561.81			
	2652.74	0.738	+0.002				

which the epochs can be estimated on the velocity-curves; the period of the oscillation having the larger K (and smaller P) was constant over the interval of 39 years, from

1909 to 1948. This result confirms our previous suspicion that the variable period is the one associated with the variation in line width.

If we use the formulas

$$\frac{1}{P_3'} = \frac{1}{0.25002246} - \frac{1}{0.2513015} \qquad \text{(for 1917–1931)},$$

$$\frac{1}{P_3''} = \frac{1}{0.25002246} - \frac{1}{0.2513003} \qquad \text{(for 1931–1948)},$$

we find

$$P_3' = 49.1236 \text{ days}; \qquad P_3'' = 49.1695 \text{ days}.$$

The second value agrees almost precisely with the value 49.167 days which we had found from Figure 3 of the variation in K. The former agrees well with Meyer's original value of 49.11 days and is but slightly larger than the value of 49.09 which we had derived from Figure 3. This discrepancy of about 0.03 day may be due to the fact that $P_2' = 0.2513015$ was taken from Meyer's work and was not rediscussed by going directly to the observations.

SUMMARY OF THE OBSERVATIONS

We thus have a star which is characterized by three periods in its radial velocity-curve:

$$P_1 = 0.25002246 \text{ day},$$

$$P_2 \begin{cases} P_2' = 0.2513015 \text{ day} & \text{(for 1909–1931)} \\ P_2'' = 0.2513003 \text{ day} & \text{(for 1931–1948)}, \end{cases}$$

$$P_3 \begin{cases} P_3' = 49.1236 \text{ days} & \text{(for 1909–1932)} \\ P_3'' = 49.1695 \text{ days} & \text{(for 1931–1948)}. \end{cases}$$

The first, P_1, represents a harmonic oscillation of the radial velocity with $K_1 = 5.8$ km/sec, and it is constant over the interval covered by the observations.

The second, P_2, represents a change of the line contours, and it is associated with a periodic shift of the measured centers of the varying (and sometimes unsymmetrical) lines. This period is slightly variable, and its variation is associated with a change in the amplitude K_2 between 4.2 and 2.0 km/sec and also with a corresponding change in the conspicuousness of the variation of the line contours.

The third period, P_3, is the beat period of P_1 and P_2 and is variable by virtue of the variation of P_2.

THE CAUSE OF THE VARIATION

The cause of the variation in line width is obscure. Meyer had already found that the lines are broadest when the sine-curve of smaller amplitude and longer period crosses the γ-axis from plus to minus. If this variation represented orbital motion, it might indicate some kind of eclipsing effect. But there are no other reasons for supposing that the lines would be broad when the hypothetical eclipse is central. The light-curve by Fath shows no eclipses.

On the other hand, the broadening might also be attributed to some unknown effect of pulsation. The radial-velocity observations would then indicate that the lines are broadest at the time of maximum contraction of the star. Although this idea is suggestive, it finds no support in the case of ordinary cepheids, RR Lyrae variables, or even such a star as β Cephei. On the other hand, R. M. Petrie[6] found a similar variation in HD 199140.

[6] *J.R.A.S. Canada*, **40**, 149, 1946.

J. H. Moore and W. F. Meyer both suspected that the lines of β Canis Majoris are unsymmetrical at certain times. This may also be the case on the McDonald spectrograms measured photometrically by Struve and Swings,[7] but the material is inadequate to follow up this point.

The McDonald plates[8] had already shown that the central absorptions of the lines vary with their widths, being greatest when the lines are narrowest. The equivalent widths of the lines probably undergo a very small variation, in the sense that they are greatest when the lines are sharpest. The change in line contour is greatest for *O* II; is intermediate for *Mg* II, *Si* III, *N* II, and *C* III; and is least conspicuous for *H* and *He* I. This dependence upon atom is probably unrelated to the fact that, on the average, the lines of *H* and *He* I are strongest. For example, the weak *He* I lines 4437 and 4169 appear to vary less than the *O* II lines of similar intensity.

All this information suggests that the phenomenon is not caused by rotation or by any other, purely mechanical, Doppler effect. Although there is no clear indication of a change in spectral class, such a change was suspected by Petrie in HD 199140. Nor does the effect resemble anything that can be explained as a simple change in turbulence.

If we compare β Canis Majoris to the best-known of the other stars assigned to the β Cephei class, we can derive the following results:

1. It would seem that the periods P_1 and P_2 are excited differently in different stars: β Cephei shows only P_1; HD 199140 shows only P_2; β Canis Majoris shows both P_1 and P_2; 12 Lacertae probably shows both P_1 and P_2; and σ Scorpii probably also shows both P_1 and P_2. This comparison may mean that the amplitudes corresponding to P_1 and P_2 have very different ratios, the P_1 oscillation alone being sufficiently pronounced in β Cephei to be observable, while the P_2 oscillation alone is noticeable in HD 199140.

2. The amplitudes K_1 and K_2 are different in different stars. If we can generalize from the observations of β Canis Majoris, we conclude that K_1 is constant in any one star, while K_2 may be variable.

3. The total amplitude, $K_1 + K_2$, has a large range; it may be as small as 2 km/sec (in β Canis Majoris) or as large as 60 km/sec (in HD 199140).

4. The light is usually variable, and there is a pronounced correlation (found by Hellerich) between the amplitudes of the light-curve and those of the velocity-curve in different stars.

5. The light-curve shows no eclipses. Maximum light falls near the point where the velocity-curve crosses the mean axis from positive to negative values.

Perhaps we must go back to an idea which, in a somewhat different form, was proposed by Meyer. The P_1 variation in velocity may represent binary motion, the satellite being an object of small mass and size. It is not unreasonable to suggest a mass ratio $a = m_1/m_2 = 100$ and a diameter sufficiently small to prevent us from detecting the eclipses in the light-curve. In other words, the satellite may be a very dense object—something resembling a white dwarf. Revolving around the primary, not far above its photosphere, it could conceivably excite that overtone, P_2, of the natural pulsation of this primary which is closest to the orbital period P_1. The intensity with which such an overtone is excited will probably depend upon $1/(P_1 - P_2)^2$. This consideration may explain why in some objects of the same class, like β Cephei, the overtone P_2 is not appreciably excited, while in others it may exceed the P_1 variation.

The marked spectroscopic differences between β Canis Majoris—a very luminous B1 star—and β Cephei—a normal main-sequence B1 star—suggest differences of internal

[7] *Ap. J.*, **94**, 99, 1941.

[8] A. B. Underhill, *Ap. J.*, **104**, 388, 1946.

constitution and therefore differences in the overtone periods P_2.[9] It is principally because of this difference that a simple pulsational mechanism is not sufficient to explain all the observations.

I am grateful to Dr. R. M. Petrie for information regarding his unpublished observations of HD 199140.

[9] O. Struve and P. Swings, *Ap. J.*, **94**, 108, 1941; *Contr. McDonald Obs.*, No. 36, 1941.

A STUDY OF THE SPECTROSCOPIC BINARY U CEPHEI*

ROBERT H. HARDIE
Yerkes Observatory
Received August 22, 1950

ABSTRACT

Two velocity-curves have been determined for U Cephei which are characterized by eccentricities of 0.0 and 0.15; this has been accomplished through correction of the radial-velocity measurements for asymmetries displayed by the *H* lines. A large discrepancy in the velocities of the center of mass as determined from 1943 and 1949–1950 data has been pointed out. The two components in this system appear to obey the mass-luminosity relation.

I. INTRODUCTION

Many investigations have been carried out on the eclipsing binary U Cephei[1] of both a spectroscopic and a photometric nature. Two fairly complete surveys and discussions were made in recent years by Struve[2] and Dugan,[3] the first dealing principally with the spectroscopic observations and the second with the photometric work. From the latter it appears that the orbital eccentricity is very small ($e < 0.1$), and, moreover, the period is so short that one could hardly expect the eccentricity to be very different from zero. However, the spectroscopically derived values for this quantity are between 0.2 and 0.5; these are indicated by the pronounced asymmetries in the velocity-curves in Figure 1, *a* and *b*, by Carpenter[4] (1923–1925), and by Struve[2] (1943). This large discrepancy between the values of the eccentricity determined photometrically and spectroscopically and the discrepancies between the two observed radial-velocity-curves suggested that a re-examination of the early data might be advisable, together with the gathering of some new observations. These latter were obtained in December, 1949, and January, 1950, at the McDonald Observatory with the Cassegrain quartz spectrograph and the 82-inch reflector by Dr. Struve; these are represented in Figure 1, *c*.

If reference is made to Struve's discussion of this binary system, one notes that just around primary minimum the rotational effect is more pronounced for the lines of *He* I, *Mg* II, and *Ca* II than for the lines of *H;* furthermore, he pointed out that he suspected asymmetries in the *H*-line contours at maximum velocity, in the sense that the cores were to the red of the centers of the underlying lines, whereas during the first partial phase of eclipse there were pronounced asymmetries in the opposite sense. These effects were taken as a starting point in this investigation; they will be taken up presently in the following discussion.

In 1943 Struve noted that "the existence at partial phases of superposed lines, originating in a stream of gas, links the problem with that of SX Cassiopeiae and suggests that the asymmetry of the velocity-curve may be produced by the same stream." However, he also pointed out important differences between the two systems; the absence of the dilution effect in the lines outside primary eclipse and of strong emission features during eclipse, both of which effects are conspicuous in SX Cassiopeiae, seemed to be evidence against the existence of a shell, although a stream hypothesis might still be applicable. It has since become clear that some other mechanism would be required to

* *Contributions from the McDonald Observatory, University of Texas*, No. 197.

[1] HD 5679; $\alpha = 0^h53^m4$; $\delta = +81°20'$ (1900); Sp. B9, gG2.

[2] *Ap. J.*, **99**, 221, 1944.

[3] *Contr. Princeton U. Obs.*, No. 5, 1920.

[4] *Ap. J.*, **72**, 205, 1930.

explain the broad features of this system; this has been largely due to the recognition as real of the phenomenon of the reversal of the asymmetries in the profiles of the *H* lines at and after maximum velocity, the interpretation of which in terms of streams alone would require an outer stream which moves in the same sense as the system, to-

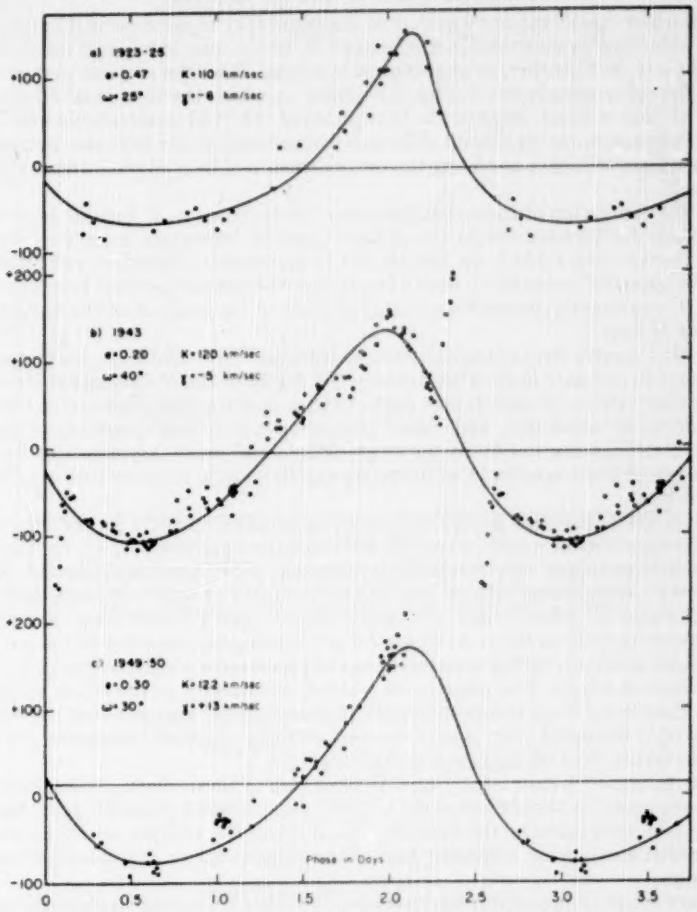

FIG. 1.—Three velocity-curves of U Cephei. *a*, Carpenter's; *b*, Struve's; *c*, derived from plates recently obtained at McDonald Observatory.

gether with an inner stream which moves in the opposite sense. Such a case was also observed in RW Tauri and a reinspection of the plates of U Cephei revealed that the asymmetries were present over an even wider range of phases than Struve had suspected originally. The similarities between the two systems were pointed out in a recent investigation;[5] perhaps further spectra taken of U Cephei at primary minimum will reveal the presence of emission lines, which are occasionally present in the spectra of RW Tauri

[5] W. A. Hiltner and R. H. Hardie, *Ap. J.*, **110**, 438, 1949.

and which form the most significant difference presently recognized between the two stars. A comparison of the characteristics of the systems U Cephei and U Sagittae was made and the similarities pointed out and discussed by Struve.[6]

II. INTERPRETATION OF THE 1943 SPECTRA

One of the first considerations was that of the possibility of systematic differences between the velocities as measured in the lines of *H*, on the one hand, and those of *He* I, *Mg* II, and *Ca* II, on the other, at phases outside eclipse. It will be recalled that such systematic differences were noted during the phases in which the rotational effect is observed. With this in mind, some of the best plates of the 1943 observations were examined and remeasured. No significant differences were found either between Struve's and the author's measurements or among the measurements of lines of the various elements named above.

During the measuring of these spectra under the microscope, it became increasingly apparent that the asymmetries in the *H* lines must be intimately associated with the spurious velocity-curves which we had set out to investigate; indeed, it was noted that that *H* lines appeared asymmetric over a larger range of phases than had heretofore been suspected. Consequently, attention was then shifted to the analysis of the varying contours of the *H* lines.

All the 1943 spectra were examined visually with both low- and high-power eyepieces in an attempt to estimate in an arbitrary way the degree of the *H*-line asymmetries. The results are illustrated in Figure 2; here open circles indicate a core displaced to the violet of the underlying broad line, and closed circles indicate a core displaced to the red. Strong asymmetries are indicated by large circles, and weak asymmetries by small circles; crosses indicate spectra in which no asymmetries were to be noticed in an inspection of this kind.

The asymmetric features go through some remarkable changes in the course of a cycle. Immediately after eclipse, when the velocities are determined by a large rotational effect, the *H* lines appear very markedly asymmetric, with the cores to the red. Shortly after this the asymmetries become less distinct, only to change to pronounced violet asymmetries around phase 0.5 day. Between phases 0.7 and 1.8 days there are no significant asymmetries to be noticed. At phase 2.0 days strong asymmetries to the red are to be seen, which gradually disappear and change to pronounced violet asymmetries during the first stages of eclipse. The presence of a strong asymmetry to the red in the spectra at phases close to 2.0 days and to the violet at phase 0.5 day suggests that the velocity-curve has been distorted from one of zero eccentricity through measurements of the sharp cores rather than of the broad underlying lines.

In order to obtain a more nearly quantitative idea of these effects, microphotometer tracings were made for the portion of the velocity-curve around phase 2.0 days. Measurements on these were made on the lines $H\gamma$, $H\delta$, $H\epsilon$, and $H8$, and the results appeared so promising that most of the remaining part of the velocity-curve was investigated in the same fashion.

In Figure 3 two typical contours have been illustrated, in order to show the manner in which the measurements were made. For this purpose an estimated continuum was drawn across the top of the line profile. A second line, parallel to this, was drawn through the profile at a depth of one-quarter the total depth, and the points where this cut the profile were taken, somewhat arbitrarily, to represent the width of the underlying broad line. Thus the difference between the center of this straight line and the center of the deepest part of the contour was taken as a measurement of the skewness or asymmetry of the contour. The irregularities introduced by the grain in the spectra were smoothed over where necessary, although this was avoided when possible. The results of the corrections due to the asymmetries are listed in Table 1.

[6] George Darwin Lecture, *M.N.*, **109**, 487, 1949.

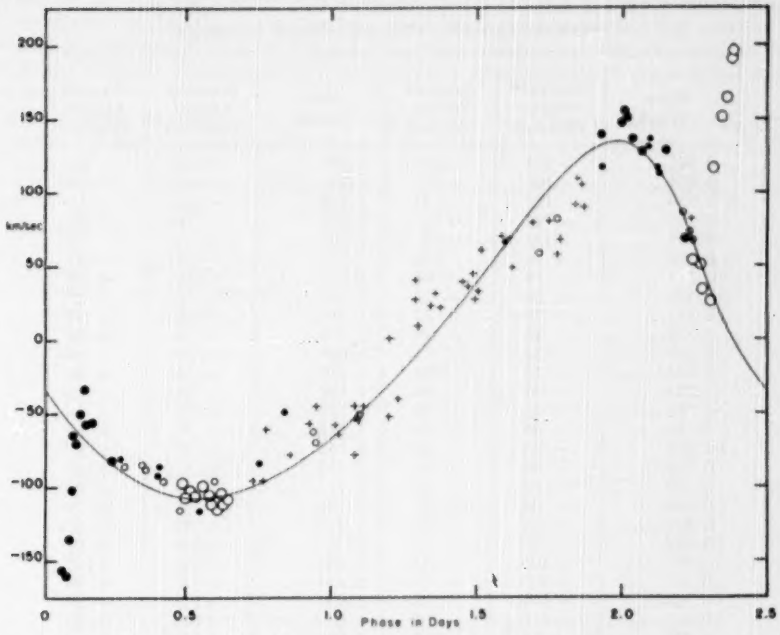

FIG. 2.—Distribution of spectra with asymmetric *H* lines as noted through visual inspection. Open circles represent violet-displaced cores; closed circles represent red-displaced cores; crosses represent undisplaced cores. Strong asymmetries are indicated by large circles, weak asymmetries by small circles.

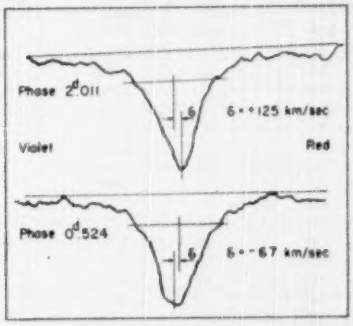

FIG. 3.—Two microphotometer tracings of *Hδ* illustrate asymmetry. The top line is from a spectrum at phase 2.011 days, and the bottom line is from a spectrum at phase 0.524 day. The measure of the asymmetry is taken as the difference between the center of the core and the center of the line drawn at one-quarter of the depth.

TABLE 1

CORRECTED RADIAL VELOCITIES OF U CEPHEI

Phase (Days)	Observed* Velocity (Km/Sec)	Corrected Velocity (Km/Sec)	Phase (Days)	Observed* Velocity (Km/Sec)	Corrected Velocity (Km/Sec)
0.041	−194	−225	1.097	− 53	− 60
0.064	−160	−228	1.104	− 51	− 23
0.070	−122	−190	1.114	− 44	− 45
0.081	−103	−151	1.195	− 54	− 57
0.091	−101	−130	1.207	+ 2	− 3
0.102	− 84	−126	1.225	− 38	− 47
0.116	− 74	− 96	1.500	+ 28	+ 39
0.130	− 59	− 75	1.508	+ 32	+ 22
0.141	− 59	− 70	1.516	+ 62	+ 58
0.158	− 48	− 71	1.596	+ 71	+ 68
0.169	− 52	− 71	1.605	+ 69	+ 64
0.253	− 82	−100	1.615	+ 69	+ 69
0.263	− 81	− 99	1.624	+ 49	+ 45
0.273	− 83	− 89	1.709	+ 80	+ 83
0.342	− 85	− 64	1.718	+ 59	+ 62
0.353	− 86	− 63	1.752	+ 80	+ 87
0.366	− 95	− 94	1.773	+ 82	+123
0.395	− 93	− 87	1.777	+ 59	+ 92
0.404	− 86	− 91	1.786	+ 68	+ 79
0.471	−115	− 85	1.851	+ 93	+ 95
0.482	− 98	− 84	1.857	+108	+ 99
0.495	−106	− 66	1.860	+108	+107
0.509	−105	− 97	1.864	+ 90	+ 84
0.524	−104	− 68	1.931	+118	+ 65
0.541	−116	−106	1.939	+140	+ 68
0.557	− 98	− 70	2.002	+148	+ 86
0.570	−106	− 41	2.011	+154	+ 68
0.583	−112	− 73	2.015	+151	+ 79
0.592	− 95	− 91	2.038	+137	+ 68
0.605	−114	−100	2.067	+128	+ 48
0.613	−104	− 64	2.088	+131	+ 82
0.621	−111	−105	2.097	+135	+103
0.631	−108	−120	2.117	+117	+ 76
0.736	− 95	− 56	2.131	+113	+ 47
0.755	− 84	− 86	2.150	+128	+ 77
0.764	− 94	−111	2.216	+ 86	+ 74
0.771	− 59	− 93	2.226	+ 70	+ 18
0.832	− 47	− 64	2.229	+ 72	+ 72
0.843	− 70	− 92	2.236	+ 74	+ 73
0.856	− 79	− 63	2.236	+ 66	+ 59
0.923	− 57	− 76	2.248	+ 85	+ 92
0.934	− 62	− 25	2.262	+ 63	+ 96
0.942	− 44	− 42	2.278	+ 67	+ 76
0.950	− 69	− 39	2.297	+ 92	+153
1.015	− 58	− 30	2.318	+ 80	+157
1.025	− 63	− 34	2.344	+108	+224
1.086	− 45	− 50	2.364	+109	+228
1.088	− 77	− 37	2.374	+ 90	+248
1.096	− 54	− 54	2.378	+ 37	+137

* Velocities are taken from Tables 2 and 3, *Ap. J.*, **99**, 221, 1944.

It was found that the contributions of the lines other than *H* were of small weight, since on many spectra the *Ca* K line was the only other measurable line and the behavior of this line and of those of *He* and *Mg*, where measurable, was so erratic as to be of little importance.[7] Consequently, the corrections were applied to the original velocities directly.

Figure 4 shows the resulting radial-velocity-curve. It is at once evident that the asymmetries have indeed been responsible for the distortion in the uncorrected curve, for the

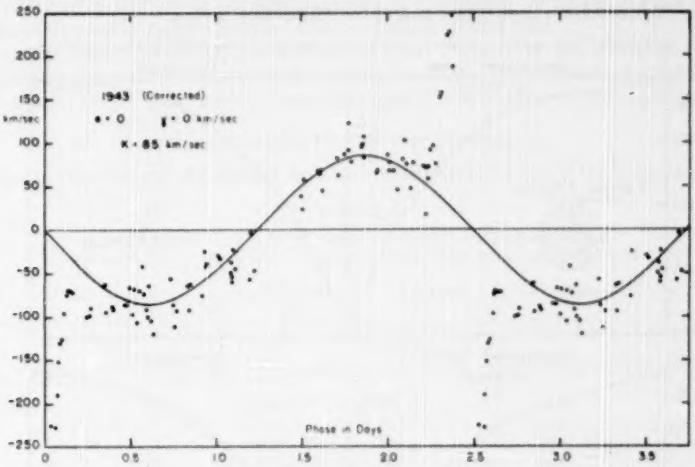

FIG. 4.—Velocity-curve after applying corrections for the asymmetries in the *H* lines, using the 1943 spectra.

TABLE 2

CORRECTED ORBITAL ELEMENTS OF U CEPHEI FROM 1943 SPECTRA

$P = 2.493$ days (assumed)	$i = 90°$ (assumed)
$e = 0 \pm 0.1$	$K_1 = 85 \pm 4$ km/sec
$\gamma = 0 \pm 5$ km/sec	$a_1 = 2.9 \times 10^6$ km

$$\frac{m_2^3 \sin^3 i}{(m_1 + m_2)^2} = 0.16 M_\odot$$

corrected curve is one for a circular orbit; thus the spectroscopic and photometric data are in better agreement. A summary of the orbital elements thus derived is presented in Table 2.

As to the cause of the peculiar asymmetries in the *H* lines at phases not thought to be disturbed by streams, Struve[8] has given a hypothesis that combines rotational and Stark effects. In order to look into this in a somewhat quantitative manner, the following calculations were carried out.

A spherical star having no limb darkening and no gravity darkening was considered. Although this model must be remote from reality, it will be clear that it provides the best

[7] Struve, *Ap. J.*, **99**, 228, n. 20, 1944.

[8] Address of the retiring president of the American Astronomical Society, December, 1949, *Pop. Astr.*, **58**, 7, 1950.

conditions for the production of the desired effect. If we imagine that the star has some portions of its surface in which, for one reason or another, the gravity and pressure are lower, then these portions will give rise to absorption lines having narrower contours. In this calculation we have taken three different cases, illustrated in the figures, in which we have assigned to several of the vertical strips (zones having common radial velocity) narrow line profiles.

For a dwarf profile, that of $H\delta$ of α Lyrae was employed, as provided in the *Photometric Atlas of Stellar Spectra* of Williams and Hiltner. For the narrow profile this was arbitrarily reduced by a factor of 2 along the dispersion axis.

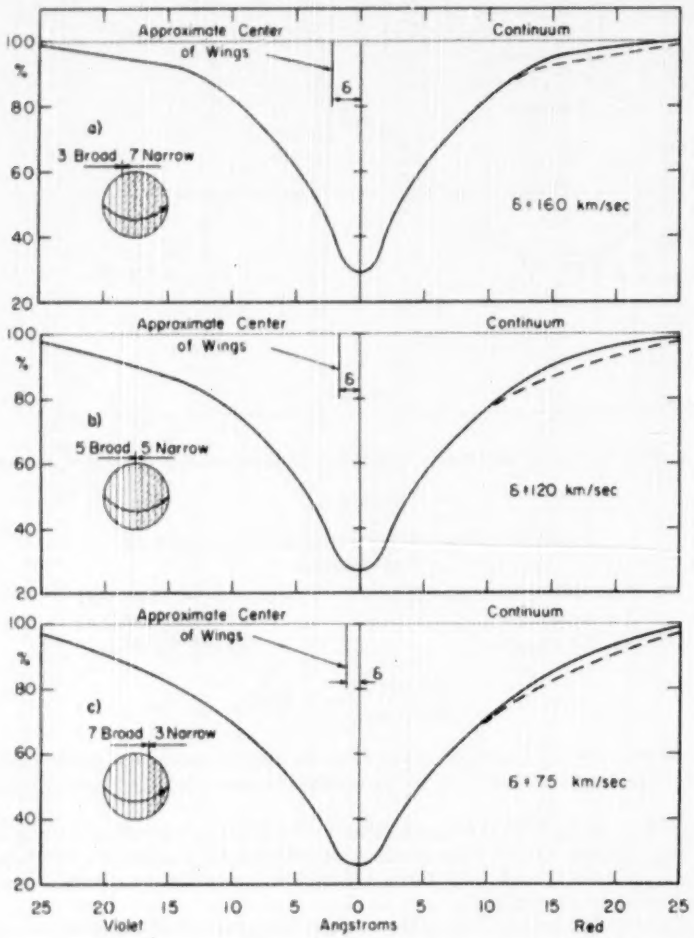

FIG. 5.—Graphically constructed contours of $H\delta$ in a star with an equatorial rotational velocity of 220 km/sec. In each case the star's projected disk was divided into ten zones of common radial velocity. Three different combinations of broad and narrow line profiles were used to characterize the absorption lines arising in the zones. The dotted line on the red side is a reflection about the center of the core of the violet wing.

An equatorial velocity of 220 km/sec was taken, and the component of this in the line of sight for the center of each of ten zones across the star was assigned. The usual procedure of graphically integrating a contour for the rotating star was carried out; however, in this case some of the zones were taken with the narrow line contours.

The results are shown graphically in Figure 5, with the approximate amount of shift of the wings relative to the core indicated. Of the three examples illustrated, all indicate the order of magnitude of asymmetry observed in U Cephei during the partial phases; in cases *a* and *b* the asymmetry appears somewhat farther out in the wings than could be measured on a tracing of the line contours in U Cephei. Thus we are led to accept case *c* as more nearly approximating the conditions in this star.

The larger portion of the star's surface produces absorption-line contours consistent with its dwarf characteristics, whereas a small area facing the companion, perhaps in the form of a tidal bulge, produces line contours suggestive of reduced pressure conditions.

III. DISCUSSION OF THE 1949–1950 SPECTRA

In order to supplement the earlier data and to attempt to verify the foregoing results,

TABLE 3

STAR LINES USED IN RADIAL-VELOCITY DETERMINATION

Element	Wave Length	Element	Wave Length
	B8 Star		
$H\gamma$	4340.47	*Mg* II	4481.23
$H\delta$	4101.74	*He* I	4471.48
*H*8	3889.05	*He* I	4387.93
*H*9	3835.39	*He* I	4026.19
*H*10	3797.90	*Ca* II	3933.68
	G2 Star		
Fe I	4045.82	$H\gamma$	4340.47
Fe I	4071.75	*Fe* I	4383.55
Fe I	4143.87		

a new series of spectra was obtained. From these spectra it was possible to measure fifty-six plates and to obtain radial velocities; although they were somewhat overexposed to facilitate the microscope measurements, they were also standardized for total absorption measurements.

The radial velocities determined from these plates are presented in Table 4, and the resulting velocity-curve is illustrated in Figure 1, *c*. The phases were computed by a new ephemeris kindly provided by Dr. Huffer, of the Washburn Observatory:

$$t_1 = \text{JD } 2432168.7030 + 2^d.492934 \, E .$$

The lines used in these measurements are given in Table 3.

A direct comparison of these data with the 1943 data is made in Figure 6; the open circles represent the 1949–1950 velocities, and the closed circles represent the 1943 velocities. There is a pronounced difference in their behavior. That this is not due to systematic personal errors is fairly certain: several plates, chosen at random, were kindly remeasured by Mr. Henry Horak, whose results showed substantial agreement with the

TABLE 4

1949–1950 RADIAL VELOCITIES OF U CEPHEI

Date JD 2433+	Phase (Days)	Velocity (Km/Sec)	Date JD 2433+	Phase (Days)	Velocity (Km/Sec)
274.535	1.459	+ 23.6	278.651	0.588	− 76.0
.548	1.472	+ 30.1	.674	0.611	− 66.5
.574	1.498	+ 21.6	.698	0.635	− 74.9
.604	1.528	+ 41.8	.714	0.651	− 82.5
.627	1.551	+ 41.8	.728	0.665	− 91.8
.651	1.575	+ 32.5	279.534	1.471	− 10.4
.681	1.605	+ 25.7	.564	1.501	− 13.6
.713	1.637	+ 59.7	.645	1.582	+ 38.5
.737	1.661	+ 56.4	281.533	0.977	− 50.4
.819	1.743	+ 52.7	.550	0.994	− 32.2
.838	1.762	+ 83.5	.568	1.012	− 22.0
.859	1.783	+101.4	.596	1.040	− 27.2
.910	1.834	+100.7	.748	1.192	− 36.5
275.582	0.012	− 3.2*	.769	1.213	− 6.2
276.618	1.049	− 62.9	282.525	1.986	+168.7
.651	1.082	− 43.1	.540	2.001	+144.3
277.527	1.957	+159.3	.553	2.014	+147.2
.536	1.966	+152.2	.568	2.029	+147.1
.551	1.981	+174.7	.580	2.041	+177.9
.572	2.002	+159.0	283.678	0.630	− 88.8
.594	2.024	+161.3	285.815	0.274	− 43.1
.607	2.037	+169.5	.843	0.302	− 55.6
.628	2.058	+183.7	.866	0.325	− 53.0
.648	2.078	+149.8	286.546	1.005	− 29.9
.660	2.090	+160.9	.560	1.019	− 28.7
.677	2.107	+207.3	.574	1.033	− 35.4
278.532	0.469	− 76.0	.588	1.047	− 31.3
.545	0.482	− 93.2	.606	1.065	− 29.5

* Velocity of G2 star.

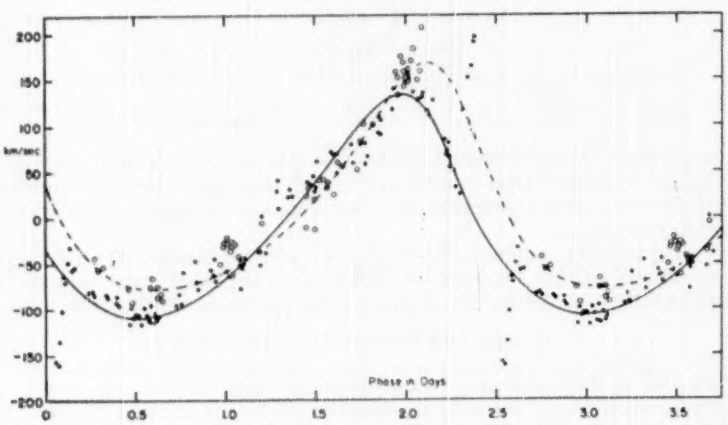

FIG. 6.—Uncorrected velocity-curves derived from spectra in 1943 and 1949–1950 superimposed. The closed circles and solid curve are for the 1943 data, the open circles and dashed curve for the 1949–1950 data.

author's; furthermore, those 1943 plates which were remeasured showed no significant differences between Struve's and the author's measures.

In spite of the 1949–1950 velocity-curve's greater departure from that of a circular orbit, the asymmetries in the *H* lines, which we have been accustomed to interpreting as the cause of the spurious values of the eccentricity, were not so conspicuous to the eye as in the earlier spectra. There is some suspicion that this effect may be influenced by the fact that the recent spectra were all denser than the earlier set, although an attempt to correlate dense and light spectra with the amount of asymmetry was not successful. The orbital elements as derived from the best-fitting velocity-curve are presented in Table 5.

TABLE 5

ORBITAL ELEMENTS OF U CEPHEI FROM 1949–1950 SPECTRA

$P = 2.493$ days (assumed)	$i = 90°$ (assumed)
$e = 0.30$	$K_1 = 122$ km/sec
$\gamma = +13$ km/sec	$a_1 = 4\times10^6$ km
$\omega = 30°$	$T = 2.22$ days

$$\frac{m_2^3 \sin^3 i}{(m_1 + m_2)^2} = 0.41 M_\odot$$

The radial velocities as determined from the elements *Mg*, *Ca*, and *He* were plotted individually and were found to have very little correlation with the curve in Figure 1, *c*.

The results of the corrections for the asymmetries in the *H* lines are tabulated in Table 6. The velocity-curve resulting from applying the corrections to the microscope measurements in the same manner as for the earlier data is drawn in Figure 7. The orbital elements as derived from the best-fitting velocity-curve are presented in Table 7.

One of the factors which causes the velocity-curve to have an appreciable eccentricity in spite of the corrections for asymmetries is the influence of the group of fifteen points around phase 2.0 days. About these points two interesting features are to be noticed: first, the group has an unusually large scatter; second, they represent two nights' observations, JD 2433277.5 and 2433282.5, in which those of the first night show considerably larger values of asymmetry than do those of the second. The average values are about 55 and 35 km/sec, respectively. The causes of these two features are not understood. On account of these uncertainties, it is felt that the value determined for *e* is not too significant and that these results are in fair agreement with those derived from the 1943 plates.

However, more significance may be attached to the value determined for γ, since it is not so sensitive to the behavior of individual groups of points. The change of γ from 0 to 22 km/sec in seven years may indicate the presence of a third body, although further observations will be required to verify the changes found in this investigation and to allow an interpretation to be drawn. It was not possible to investigate systematic instrumental errors which may account for the discrepancies, since no stars of known constant radial velocity were obtained at the same time.

Most of the spectra were further examined for any systematic changes in spectral type, and the ten best plates were examined for any systematic changes in the equivalent width of the *Hδ* line. No indication of changes was found within the phases covered by the recent observations.

IV. CONCLUSIONS

In the foregoing sections we have examined all the spectra of U Cephei that have been taken at the McDonald Observatory. The radial velocities determined in them have been altered to allow for the asymmetric features in the *H* lines, and these appear to yield velocity-curves that are more in keeping with the photometric data.

TABLE 6

CORRECTED RADIAL VELOCITIES OF U CEPHEI

Phase (Days)	Observed* Velocity (Km/Sec)	Corrected Velocity (Km/Sec)	Phase (Days)	Observed* Velocity (Km/Sec)	Corrected Velocity (Km/Sec)
0.274	− 43	− 27	1.501	− 14	+ 28
0.302	− 56	− 21	1.528	+ 42	+ 58
0.325	− 53	− 36	1.551	+ 42	+ 67
0.469	− 76	− 47	1.575	+ 33	+ 44
0.482	− 93	− 50	1.582	+ 39	+ 67
0.588	− 76	− 48	1.605	+ 26	+ 46
0.611	− 67	− 43	1.637	+ 60	+ 57
0.630	− 89	− 42	1.665	+ 56	+ 73
0.635	− 75	− 61	1.743	+ 53	+ 78
0.651	− 83	− 59	1.762	+ 84	+ 96
0.665	− 92	− 50	1.783	+101	+ 82
0.977	− 50	− 49	1.834	+101	+107
0.994	− 32	− 43	1.957	+159	+107
1.005	− 30	− 16	1.966	+152	+ 97
1.012	− 22	− 44	1.981	+175	+126
1.019	− 29	− 23	1.986	+169	+140
1.033	− 35	− 26	2.001	+144	+106
1.040	− 27	− 3	2.002	+159	+133
1.047	− 31	− 25	2.014	+147	+118
1.049	− 63	− 50	2.024	+161	+110
1.065	− 30	− 28	2.029	+147	+120
1.082	− 43	− 28	2.037	+170	+102
1.192	− 37	− 23	2.041	+178	+134
1.213	− 6	+ 5	2.058	+184	+117
1.459	+ 24	+ 43	2.078	+150	+ 71
1.471	− 10	+ 12	2.090	+161	+108
1.472	+ 30	+ 50	2.107	+207	+149
1.498	+ 22	+ 55			

* Velocities taken from Table 4.

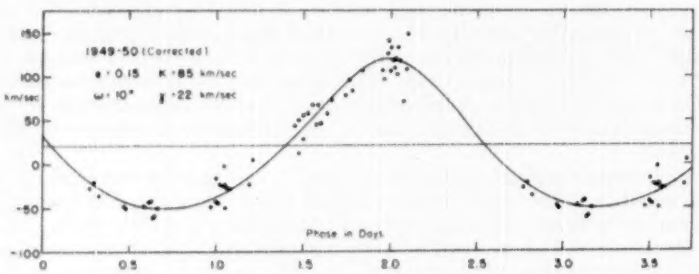

FIG. 7.—Velocity-curve after applying corrections for the asymmetries in the *H* lines, using the 1949–1950 spectra.

TABLE 7

CORRECTED ORBITAL ELEMENTS OF U CEPHEI FROM 1949–1950 SPECTRA

$P = 2.493$ days (assumed)	$i = 90°$ (assumed)
$e = 0.15 \pm 0.05$	$K_1 = 85 \pm 2$ km/sec
$\gamma = +22 \pm 3$ km/sec	$a_1 = 2.9 \times 10^6$ km
$\omega = 10° \pm 15°$	$T = 2.04 \pm 0.08$ days

$$\frac{m_2^3 \sin^3 i}{(m_1 + m_2)^2} = 0.16 M_\odot$$

There is still the unresolved problem concerning the irregular behavior of the velocities determined at the time of maximum velocity in the most recent spectra. Irregularities may reasonably be expected when there is evidence of streams or shells, as in the case of the occasional appearance of emission lines in the system RW Tauri. However, it is not clear why there should still remain the differences between the curves of 1943 and 1949–1950, when corrections have been applied which presumably allow for the influence of streams and other effects which reveal themselves spectrally through sharp lines. Further observations may point out the reasons for this and thus whether the change in γ is real.

Preliminary calculations were carried out to find whether the reversal of line asymmetries during the partial phases can be interpreted in terms of a tidal bulge where the absorption contours are narrower because of a lessened pressure effect. There is indication that this mechanism can account for the observations.

In Table 8 we have listed the approximate dimensions of the system, for which pur-

TABLE 8

MASSES AND RADII OF THE COMPONENTS OF U CEPHEI

$\frac{K_2}{K_1} = 2.5$	$m_1 = 4.7 M_\odot$
$a_2 = 7.3 \times 10^6$ km	$m_2 = 1.9\ M_\odot$
$a_1 + a_2 = 10.2 \times 10^6$ km	$r_1 = 2.9\ R_\odot$
$= 0.07$ A.U.	$r_2 = 4.7\ R_\odot$

pose we have determined K_2 from Struve's 1943 measurements of the G-type component during eclipse. Assuming that the B8 star has an absolute magnitude characteristic of its spectral type, namely, -0.5 mag., we may conclude that the G2 star has an absolute magnitude of 1.5, about that of a giant. The components show substantial agreement with the mass-luminosity relation.

The writer wishes to express his thanks to Dr. Struve for his suggestions and advice throughout this investigation and for donating a large part of his observing time to obtain new spectra of U Cephei. Grateful acknowledgment is also made to the staff of Yerkes Observatory for many illuminating discussions.

A CORRELATION BETWEEN THE SPECTROSCOPIC AND DYNAMICAL CHARACTERISTICS OF THE LATE F- AND EARLY G-TYPE STARS

NANCY G. ROMAN
Yerkes Observatory
Received July 22, 1950

ABSTRACT

Among the giants and dwarfs in the spectral range F5–G5, some stars have systematically weaker lines than others of the same spectral type and luminosity class. On this basis two groups of stars can be distinguished. An examination of the velocity distributions of the two groups shows definite differences. The velocities of the stars with weaker lines have a larger dispersion than those of the stars with stronger lines; the conventional "high-velocity" stars occur only in the weak-line group. The two types of stars are about equally numerous among the bright northern stars. Stars with velocities less than 70 km/sec are found in both groups.

It has long been known that there are many peculiar stars which cannot be placed uniquely on a two-dimensional Hertzsprung-Russell diagram. However, even such well-populated groups as the metallic-line stars are small compared with the normal stars of similar spectral types. Among the late F- and early G-type stars there appear to be two groups of stars which occur with comparable frequency and which can be distinguished spectroscopically, although they occupy the same region of the H-R diagram.

The stars in one of these groups have systematically weaker lines than those in the other group. This cannot be due to a difference in either spectral type or luminosity. In this region of the H-R diagram the hydrogen lines are weakening rapidly as the metallic lines are growing stronger. Thus the weakness of the hydrogen lines would indicate a later spectral type, while the weakness of the remaining lines would indicate an earlier type. The effect occurs in both giants and dwarfs, and, on the average, the lines have the same strength in the giants and in the dwarfs of the same spectral type.

The present discussion is based on ninety-four northern stars brighter than 5.50 mag. for which comparable plates are available. The spectra have a dispersion of 125 A/mm at $H\gamma$. The stars studied include giants and dwarfs in the spectral classes F5–G5, except that the G-type stars which show *CN* were arbitrarily excluded. Earlier than F5, the broadening of the star lines by rotation makes it difficult or impossible to detect the small differences between the two groups.

The conflicting types derived from the hydrogen lines and from the metallic lines lead to a problem in an attempt to classify the two groups of stars on the same system. In this paper the types are derived from line ratios, and thus it is assumed implicitly that all lines are weakened by approximately the same amount. The resulting type is thus a compromise between the types which would be derived from the absolute strengths of either the hydrogen lines or the metallic lines. It is also assumed that the same absolute-magnitude calibration can be used for the two groups of stars. That these assumptions are reasonable is indicated by the close agreement between the mean radial motion of the stars and the mean tangential motion divided by $\sqrt{2}$, as is shown in Table 1.

While the systematic difference in the intensity of the lines characterizes the two groups throughout the range in spectral types studied, some features can be used more readily than others to discriminate between them on plates of the dispersion used in this study. In the F5 and the F6 stars the metallic lines are fairly weak, and the most obvious difference between the two groups is that λ 4226 of *Ca* I stands out noticeably in the

weak-line stars but is merely one of a number of lines in the strong-line stars. By F8, the weakening of the general background of metallic lines is quite obvious in the dwarfs but not particularly striking in the giants. The strength of the hydrogen lines and the G band provide useful criteria throughout the range F5–G5 and are particularly valuable in the F8 and G0 giants. At G0 the ratio of the lines 4340/4325 is noticeably smaller in the weak-line stars for the same strength of λ 4226. The differences are small at best, and comparable plates of high quality are needed to detect them. Also, it is necessary to compare stars of very nearly the same spectral type.

The space velocity was computed for each of the ninety-four stars. These velocities were based on spectroscopic parallaxes and corrected for a solar motion of 20 km/sec toward $A = 271°$, $D = +28°$. The frequency distributions of the total space velocities

TABLE 1

CHARACTERISTICS OF THE MOTIONS OF THE TWO GROUPS OF STARS

Group	No. of Stars	Mean Radial Velocity (Km/Sec)	Mean Tangential Velocity/$\sqrt{2}$ (Km/Sec)	Mean Speed (Km/Sec)	Standard Deviation (Km/Sec)
Strong-line	47	14.5	13.6	28.1	13.8
Weak-line	47	22.2	21.9	43.9	23.4

are strikingly different for the two groups of stars. These are shown in Figure 1 and in Table 1. While the distributions overlap to a considerable extent, both the mean and the dispersion are larger for the weak-line stars than for the strong-line stars. However, it is important to note that the knowledge of the speed alone is not sufficient to determine the group to which a particular star belongs, with the possible exception of stars with speeds greater than 70 km/sec.

Table 2 lists the stars included in the strong-line group, together with their 1900 positions, apparent visual magnitudes, spectral types,[1] spectroscopic parallaxes, and space velocities. Table 3 gives the same data for the weak-line stars. In each table a number of visual and spectroscopic binaries have been included. These are described in the notes to the tables. They have no effect on the velocity characteristics found for the two groups of stars; identical values of the mean speeds and the standard deviations are obtained if the two-line spectroscopic binaries and the close visual binaries are excluded from the solution.

This work developed from several discussions with Dr. W. W. Morgan, to whom I am also indebted for the use of plates of many of the stars included in this paper.

[1] On the system of *An Atlas of Stellar Spectra* by Morgan, Keenan, and Kellman (Chicago: University of Chicago Press, 1943).

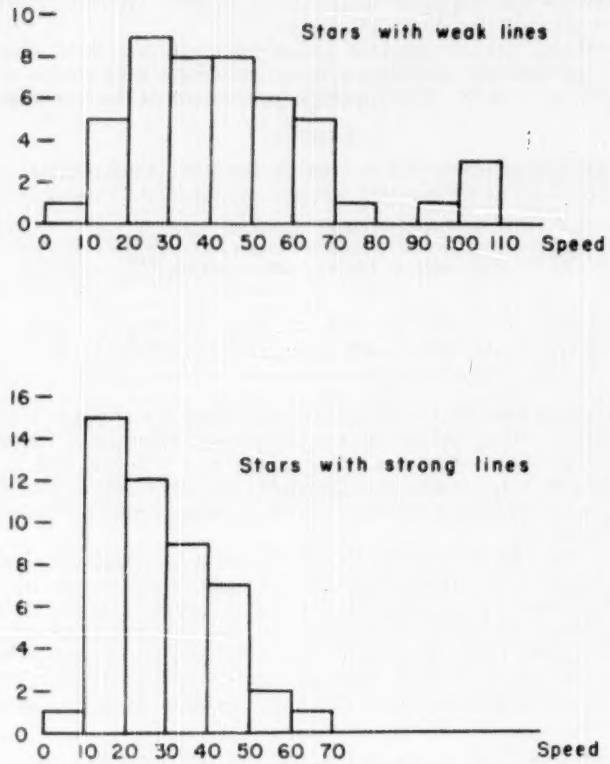

FIG. 1.—The frequency distributions of the speeds of the two groups of stars

TABLE 2

THE STRONG-LINE STARS

Name	$\alpha_{(1900)}$	$\delta_{(1900)}$	m	Spectral Type	π_{ap}	Speed (Km/Sec)
ρ And	$0^h 15^m.9$	$+37° 25'$	5.20	F5 III	0".018	14
ϕ^2 Cet	0 45.1	−11 11	5.24	F8 V	.060	56
HR 244	0 47.1	+60 34	4.93	F8 IV	.044	46
σ Cet	2 27.4	−15 41	4.82	F5 IV	.038	48
12 Per†	2 35.9	+39 46	4.99	F8 V	.048	30
τ^1 Eri	2 40.4	−19 0	4.61	F6 V	.069	17
κ Cet	3 14.1	+ 3 0	4.96	G5 V	.104	17
43 Per†	3 49.2	+50 24	5.47	F5 V	.029	26
π^3 Ori	4 44.4	+ 6 47	3.31	F6 V	.125	19
ξ Gem	6 39.7	+13 0	3.40	F5 III	.042	17
α CMi	7 34.1	+ 5 29	0.48	F5 IV	.276	20
9 Pup‡	7 47.1	−13 38	5.34	G1 V	.058	44
μ Cnc	8 1.9	+21 52	5.38	G2 IV	.038	49
ζ Cnc A§	8 6.5	+17 57	5.56	F8 V	.050	24
σ^3 UMa	9 1.6	+67 32	4.87	F6 IV	.040	16
HR 3750	9 22.8	− 5 38	5.44	G2 V	.072	39
HR 3881	9 42.1	+46 29	5.20	G2 V	.079	30
19 LMi*	9 51.6	+41 32	5.19	F5 V	.046	16
HR 4251	10 48.6	−19 36	5.28	F6 V	.050	33
47 UMa	10 53.9	+40 58	5.14	G0 V	.072	21
β Vir	11 45.5	+ 2 20	3.80	F8 V	.114	49
18 Com	12 24.5	+24 40	5.49	F5 III	.016	24
31 Com	12 46.8	+28 5	5.07	G0 III	.013	15
53 Vir	13 6.7	−15 40	5.09	F6 III–IV	.026	56
β Com	13 7.2	+28 23	4.32	G0 V	.104	52
59 Vir	13 11.8	+ 9 57	5.22	G0 V	.069	29
η Boo*	13 49.9	+18 54	2.80	G0 IV	.119	15
12 Boo†	14 5.8	+25 34	4.82	F8 IV	.032	25
ι Vir	14 10.8	− 5 31	4.16	F6 III	.029	64
18 Boo	14 14.4	+13 28	5.31	F5 IV	.030	33
ϵ Lib*	15 18.8	− 9 58	5.08	F5 V	.048	6
ξ Sco‖	15 58.9	−11 6	4.77	F6 IV	.042	21
θ Dra*	16 00.0	+58 50	4.11	F8 IV	.063	23
HR 6493†	17 21.3	− 5 0	4.61	F5 V	.043	19
ψ Dra A	17 43.7	+72 12	4.90	F5 V	.053	37
35 Dra	17 53.9	+76 59	5.04	F6 IV	.038	19
θ Cyg	19 33.8	+49 59	4.64	F5 IV	.041	25
HR 7496	19 37.9	−15 42	5.50	F6 IV	.030	35
β Del#	20 32.9	+14 15	3.72	F5 III	.030	11
δ Equ†	21 9.6	+ 9 36	4.61	F8 V	.057	20
κ Peg**	21 40.1	+25 11	4.27	F5 IV	.038	12
ι Peg*	22 2.4	+24 51	3.96	F5 V	.079	10
π Peg	22 5.5	+32 41	4.38	F5 II–III	.012	23
37 Peg††	22 24.9	+ 3 55	5.47	F5 III	.013	49
σ Peg	22 47.3	+ 9 18	5.30	F6 V	.050	41
υ Peg	23 20.4	+22 51	4.57	F8 III	.019	36
ω Psc*	23 54.2	+ 6 19	4.03	F4 III	0.032	10

* One-line spectroscopic binary.
† Two-line spectroscopic binary.
‡ Close visual binary. Δm = 0.9 mag.
§ Close visual binary. Δm = 0.70 mag.
‖ Close visual binary. Δm = 0.30 mag.
Close visual binary. Δm = 1.0 mag.
** Close visual binary. Δm = 0.5 mag.
†† Close visual binary. Δm = 1.4 mag.

TABLE 3

THE WEAK-LINE STARS

Name	$\alpha_{(1900)}$	$\delta_{(1900)}$	m	Spectral Type	π_{ap}	Speed (Km/Sec)
η Cas‡	0^h43^m0	+57° 17′	3.64	G0 V	0".144	27
ω And	1 21.7	+44 58	4.96	F5 III	.020	69
υ And	1 30.9	+40 54	4.18	F8 IV	.060	45
δ Tri	2 10.9	+33 46	5.07	G0 V	.072	62
θ Per	2 37.4	+48 48	4.22	F6 V	.083	28
ι Per	3 1.8	+49 14	4.17	G0 V	.109	66
10 Tau	3 31.8	+ 0 5	4.40	F8 V	.087	32
λ Aur	5 12.1	+40 1	4.85	G2 IV–V	.068	74
χ Cnc	8 14.0	+27 32	5.16	F6 V	.052	31
HR 3579§	8 54.2	+42 11	4.09	F5 V	.071	29
τ^1 Hya	9 24.1	− 2 20	4.78	F6 V	.063	11
θ UMa	9 26.2	+52 08	3.26	F6 III	.043	102
40 Leo	10 14.3	+19 59	4.97	F6 V	.058	7
HR 4084	10 18.9	+83 4	5.34	F5 III	.016	24
36 UMa	10 24.2	+56 30	4.84	F8 V	.072	17
ξ UMa‖	11 12.9	+32 6	4.41	G0 V	.090	26
HR 4439#	11 26.7	+61 38	5.47	F6 V	.035	43
β CVn	12 29.0	+41 54	4.32	G0 V	.104	22
α Com**	13 5.1	+18 4	5.22	F5 V	.032	55
61 Vir	13 13.2	−17 45	4.80	G5 V	.114	44
70 Vir	13 23.5	+14 19	5.16	G5 IV–V	.064	37
τ Boo	13 42.5	+17 57	4.51	F6 IV	.048	34
θ Boo	14 21.8	+52 19	4.06	F6 IV	.058	33
μ Vir•	14 37.8	− 5 13	3.95	F5 III	.032	50
α^1 Lib	14 45.2	−15 35	5.33	F5 IV	.030	16
45 Boo	15 2.9	+25 16	5.03	F5 V	.030	33
5 Ser	15 14.2	+ 2 9	5.18	F8 IV	.038	104
η CrB††	15 19.1	+30 39	5.58	G0 V	.058	28
λ Ser	15 41.6	+ 7 40	4.42	G0 V	.100	50
χ Her	15 49.2	+42 44	4.61	F8 V	.079	65
γ Ser	15 51.8	+15 59	3.86	F6 IV	.063	100
ζ Her‡‡	16 37.5	+31 47	3.00	G0 IV	.109	57
20 Oph	16 44.3	−10 36	4.73	F6 III	.023	43
19 Dra•	16 55.5	+65 17	4.82	F6 V	.063	25
72 Her	17 16.9	+32 36	5.36	G2 V	.072	92
26 Dra	17 34.0	+61 57	5.31	G2 V	.076	46
ω Dra•	17 37.5	+68 48	4.87	F5 V	.053	16
99 Her	18 3.2	+30 33	5.21	F8 V	.060	23
110 Her	18 41.4	+20 27	4.26	F5 IV	.048	51
11 Aql	18 54.5	+13 29	5.37	F8 III–IV	.022	40
17 Cyg	19 42.6	+33 30	5.03	F5 V	.050	49
HR 7955	20 42.9	+57 13	4.63	F8 IV	.050	39
ϵ Eql A§§	20 54.1	+ 3 55	5.29	F5 III	.014	68
μ Cyg A‖‖	21 39.7	+28 17	4.73	F6 V	.066	35
ζ Aqr##	22 23.7	− 0 32	4.42	F5 III	.024	44
ξ Peg	22 41.7	+11 40	4.31	F6 III–IV	.038	56
ι Psc	23 34.8	+ 5 5	4.28	F8 V	0.091	16

• One-line spectroscopic binary.

‡ Close visual binary. Δm = 3.8 mag.

§ Close visual binary. Δm = 2 mag.

‖ Close visual binary. Δm = 0.46 mag. Each component is a spectroscopic binary.

Close visual binary. Δm = 0.3 mag.

•• Close visual binary with equal components.

†† Close visual binary. Δm = 0.50 mag.

‡‡ Close visual binary. Δm = 3.5 mag.

§§ Close visual binary. Δm = 0.5 mag.

‖‖ Close visual binary. Δm = 1.35 mag.

Visual binary. Δm = 0.17; ρ = 3".

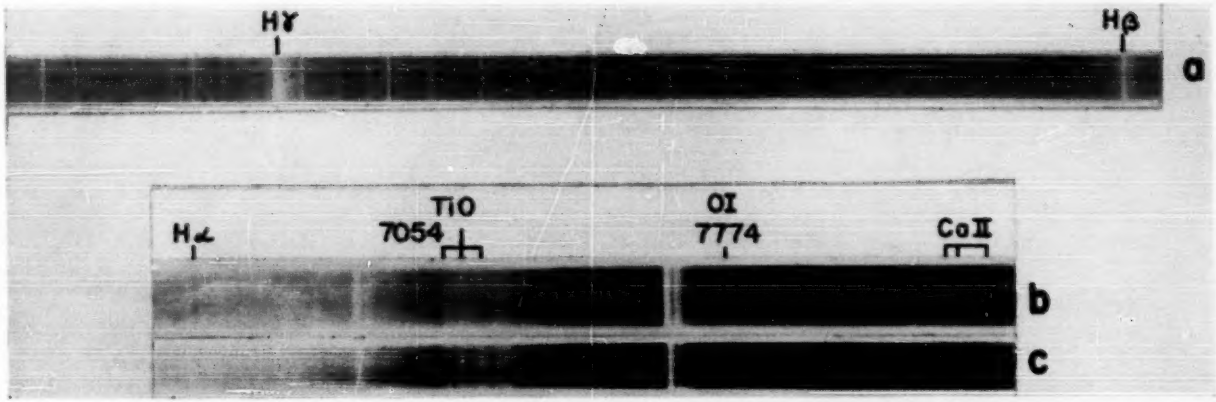

FIG. 1.—*a*, the spectrum of 17 Leporis in the blue region, taken on January 17, 1950; *b*, a portion of the infrared spectrum of 17 Leporis, taken on the same date; *c*, the M2 III star μ Coronae Borealis.

NOTES

NOTE ON THE INFRARED SPECTRUM OF 17 LEPORIS

The star 17 Leporis has been described by Struve,[1] Struve and Roach,[2] and Smith and Struve.[3] It is a shell star of type A in which *Hα* and sometimes *Hβ* are bright and in which the sharp metallic lines show a large violet displacement, corresponding to a velocity of expansion of between about −40 and −140 km/sec. This expanding shell gives rise to strong sharp lines of *H*, *Fe* II, *Ti* II, *Fe* I, *Sr* II, *Ca* I, *Ca* II, *Cr* II, *Sc* II, and possibly other atoms. According to Smith and Struve,[3] the lines arising from the shell undergo large variations in structure and in intensity. Sometimes they become double, evidently as a result of a new shell which has a larger velocity of expansion. These outbursts repeat themselves at intervals of approximately 150 days.

Figure 1, *a*, shows the blue spectrum of 17 Leporis, taken with the two-prism spectrograph attached to the 69-inch reflector of the Perkins Observatory. The star appears to have been between outbursts on January 17, 1950, as the shell lines are single, strong, and sharp and show no emission borders. Figure 1, *b*, taken with the same spectrograph on the same night, shows a portion of the infrared spectrum of 17 Leporis. The spectrum of the standard M2 giant, μ Coronae Borealis, is also shown for comparison. It will be seen that the spectrum of 17 Leporis is composite: the (0, 0) band of the γ system of *TiO* with head at λ 7054 is present and matches the corresponding band in μ Coronae Borealis quite well. The strength of the band would indicate that the companion is not far from spectral class M2. The blending of the two spectra makes the estimate of M2 only approximate, however. Nothing can be said about the luminosity of the late-type companion at this time.

Although the spectrogram illustrated is overexposed to the red of the 7054 band, the lines of *O* I at λ 7774 and λ 8446 and the *Ca* II triplet at λλ 8498, 8542, and 8662 can be seen as fairly strong absorption lines. The Paschen series of hydrogen is also present in absorption but is quite weak.

I am indebted to Dr. P. C. Keenan for the spectrogram of μ Coronae Borealis shown.

ARNE SLETTEBAK

PERKINS OBSERVATORY
July 1950

RADIAL VELOCITIES OF SIX STARS HAVING COMPOSITE SPECTRA

Three stars with composite spectra—45 Cnc (A3–G), HD 135774–5 (A2–G), and HD 159870 (F2 susp. comp.)—previously listed as constant in radial velocity have been found to have variable radial velocity. Three other composite-spectra stars—HD 39118–9 (G0–A0), HD 126269–70 (F5–A0), and HD 187982–3 (F5–A2)—are probably variable in radial velocity. Of the latter three stars, a previous velocity determination was available for only HD 126269–70.

Five to seven plates of each star were used in the velocity determinations, and an

[1] *Ap. J.*, **72**, 343, 1930; **76**, 85, 1932.

[2] *Ap. J.*, **90**, 727, 1939.

[3] *Ap. J.*, **95**, 468, 1942.

average of fourteen lines was measured on each plate. The spectrograms were taken by J. A. Hynek and the writer with the two-prism spectrograph attached to the 69-inch reflector of the Perkins Observatory. Cameras giving dispersions of 27 and 50 A/mm at $H\gamma$, respectively, were used.

Table 1 lists, in successive columns, the star, α and δ for 1900, magnitude, JD of observation, measured velocities with probable errors, and the previously adopted velocity.

TABLE 1

RADIAL VELOCITIES OF SIX STARS HAVING COMPOSITE SPECTRA

Star	α	δ	Mag.	JD	Measured Velocity	Previously Adopted Velocity
HD 39118-9	5^h45^m3	+ 2° 00′	6.26	2432120	+ 6.2±4.1	None
				139	+11.9 2.8	
				181	+ 2.0 1.5	
				504	+13.6 2.6	
				534	+18.3 3.4	
				33345	− 3.8 2.1	
				345	− 1.5 1.8	
45 Cnc	8 37.7	+13 03	5.67	2429576	+25.6 1.2	
				30797	+ 3.9 2.2	−18.8±1.2
				33336	−17.0 2.3	
				345	−21.8 2.4	
				345	−25.1 2.1	
HD 126269-70	14 19.4	+16 44	6.77	2432302	−17.9 6.3	
				340	−28.9 2.5	−19.8±1.4
				353	−27.2 3.0	
				353	−31.9 3.1*	
				33345	−12.7 1.4	
				371	−14.2 0.8	
				378	−13.7 0.8	
HD 135774-5	15 11.8	+10 04	6.64	2430479	−10.4 2.7	
				2349	−10.5 0.8	− 6.6±1.4
				2666	−16.5 2.4	
				33088	− 1.7 1.7	
				33088	− 6.9 1.7*	
				345	−53.3 0.9	
				345	−52.9 1.5*	
				378	−24.5 1.5	
HD 159870	17 31.9	+57 38	6.17	2432029	+ 7.9 4.0	+ 0.8±1.4
				302	− 9.6 2.2	
				392	+ 3.3 2.2	
				393	+ 2.1 2.7	
				33088	+ 7.5 1.0	
				399	−23.3 1.0	
				399	−25.4 0.9*	
HD 187982-3	19 47.8	+24 44	5.67	2432091	+ 2.6 2.1	None
				091	− 8.1 3.2	
				33056	− 0.6 3.9	
				088	−19.6 1.7	
				162	+ 2.4 1.1	
				399	− 9.0±2.1	

* Independent measure by J. A. Hynek.

WILLIAM C. WHITE, JR.

McMILLIN OBSERVATORY
OHIO STATE UNIVERSITY
July 1, 1950

NOTE ON THE PROTON-PROTON REACTION IN WHITE DWARF STARS

Owing to the high values of the Fermi threshold energy of the electrons in a white dwarf star, He^3 is unstable against the capture of an electron (inverse process of β-decay). The energy production by the proton-proton reaction involves the cycle

$$H^1 + H^1 \rightarrow H^2 + e^+ + \nu\,, \tag{1}$$

$$H^2 + H^1 \rightarrow He^3 + \gamma\,, \tag{2}$$

$$He^3 + e^- \rightarrow H^3 + \nu\,, \tag{3}$$

$$H^3 + H^1 \rightarrow He^4 + \gamma\,. \tag{4}$$

Reaction (3) is an endothermic process with a threshold energy equal to 11 ± 2 kv;[1] under the conditions in ordinary stars this reaction cannot take place and is replaced by[2]

$$He^3 + He^4 \rightarrow Be^7 + \gamma\,, \tag{5}$$

$$Be^7 + e^- \rightarrow Li^7 + \nu\,, \tag{6}$$

$$Li^7 + H^1 \rightarrow 2\,He^4\,. \tag{7}$$

The lifetime, τ, of He^3 against capture of electrons can be calculated by using the usual theory of β-decay;[3] it is given by

$$\frac{1}{\tau} = \frac{2}{\pi}\frac{|GM|^2}{\hbar^4 c^3}\int_{E_c}^{\infty} (E - E_c)^2 n_e(E)\, dE\,, \tag{8}$$

where $\hbar$ is $1/2\pi$ times the Planck constant, c the velocity of light, G the interaction constant of β-decay, and M the "nuclear matrix element" which measures the overlapping of the states of nucleons connected by this transition; also $n_e(E)dE$ is the number of electrons per unit volume having kinetic energy (including the rest-mass of the electron) between E and $E + dE$, and E_c is the sum of the threshold energy and the rest-energy of the electron.

Taking $n_e(E)$ as that given by a degenerate gas of maximum energy E_m, we have

$$\frac{1}{\tau} = \frac{2\,|GM|^2}{\pi^3\hbar^7 c^6}\int_{E_c}^{E_m} (E^2 - m^2c^4)^{1/2} E\,(E - E_c)^2 dE\,, \tag{9}$$

where m is the rest-mass of the electron. Setting $E_m = x_m mc^2$ and $E_c = x_c mc^2$, we find, for the lifetime τ,

$$\frac{1}{\tau} = \frac{2\,|GM|^2}{\pi^3\hbar^7}\, m^5 c^4\,[F(x_m) - F(x_c)]\,, \tag{10}$$

where

$$F(x) = (x^2-1)^{3/2}\left(\tfrac{1}{3}x^2 + \tfrac{2}{15} - \tfrac{1}{2}x x_c + \tfrac{1}{5}x^2\right) - \tfrac{1}{4}x x_c (x^2-1)^{1/2} + \tfrac{1}{4}x_c ln\,[x + \sqrt{(x^2-1)}]\,. \tag{11}$$

The rate of transformation of He^3 into Be^7 by He^4 has been calculated by Bethe.[4] A

[1] R. J. Watts and D. Williams, *Phys. Rev.*, **70**, 640, 1946.

[2] H. Bethe and C. L. Critchfield, *Phys. Rev.*, **54**, 248, 1938.

[3] E. Fermi, *Zs. f. Phys.*, **88**, 161, 1934. [4] *Phys. Rev.*, **55**, 434, 1939.

comparison of the lifetime of He^3 due to these two reactions is tabulated in Table 1 for degenerate matter with a temperature equal to 2×10^{7}° K. Calculations on white dwarfs[5] show that even in the envelope of the star, when the temperature becomes about

TABLE 1

LIFETIME OF He^3 IN DEGENERATE MATTER FOR $T = 2 \times 10^{7}$° K

$(E_m - mc^2)/kT$	LIFETIME OF He^3 DUE TO REACTION	
	$He^3 + e^- \rightarrow H^3 + \nu$	$He^3 + He^4 \rightarrow Be^7 + \gamma$
10	1.9 years	$5.16 \times 10^{4}/x_{H_e}\mu_e$ years
20	13 days	$1.8 \times 10^{4}/x_{H_e}\mu_e$ years
50	7.0 hours	$4.7 \times 10^{3}/x_{H_e}\mu_e$ years
500	1.9 sec.	$5.9 \times 10^{2}/x^{4}_{H_e}\mu_e$ years

* x_{H_e} is the concentration of He^4 by weight, and μ_e is the average number of nucleons per single electron.

10^{7}° K, $(E_m - mc^2)/kT$ is already about 10–20. Hence from Table 1 it is easily seen that the decay of He^3 into H^3 will always be much more probable than the transformation of He^3 by He^4 in a white dwarf star.

T. D. LEE

YERKES OBSERVATORY
July 31, 1950

A NEW BAND SYSTEM OF N_2^+ IN THE INFRARED AURORAL SPECTRUM

Several strong auroral bands near 8000 A have been ascribed by Vegard and Kvifte[1] to members of the first positive system of N_2. Bates, Massey, and Pearse[2] have questioned this identification, in spite of apparent wave-length coincidences, because of the absence of other first positive bands from the particular vibrational levels.

Spectra obtained by the author with a relatively high resolution during the auroral storm of August 18 and 19, 1950, showed that the detailed structure of these bands was very different from first positive bands of N_2. The unidentified bands have two or more maxima, with a sharp edge on the violet side.

The six bands listed in Table 1 appeared to belong to this new band system from their similar appearance. The two bands at 6858A and 7250A are superimposed on first positive bands of N_2. The characteristic two maxima, however, can readily be distinguished. The analysis of the six bands, when arranged to agree with a Franck-Condon intensity distribution, gave the molecular constants for the lower state of $\omega_e'' = 2205$ cm^{-1} and $\omega_e'' x_e'' = 17$ cm^{-1}. These values are very close to those for the ground state of N_2^+.

Assuming that the $X^2\Sigma$ state of N_2^+ is the lower level of these bands, the set of molecular constants are as follows:

$$\omega_e'' = 2207.2 \text{ cm}^{-1}, \qquad \omega_e'' x_e'' = 16.1 \text{ cm}^{-1},$$
$$\omega_e' = 1878.4 \text{ cm}^{-1}, \qquad \omega_e' x_e' = 16.0 \text{ cm}^{-1},$$

Doublet splitting $= 75$ cm^{-1},
$\nu_{00} = 10882.6$ cm^{-1}.

[5] T. D. Lee, *Ap. J.*, **111**, 625, 1950.

[1] *Geophys. Pub. Oslo*, Vol. **16**, No. 7, 1945.

[2] *Report to the Gassiot Committee: Emission Spectrum of the Night Sky and Aurorae* (London: Physical Society, 1948), p. 97.

The residuals with these constants are shown in Table 1. The excellent agreement of the lower-level constants and the obvious doublet structure establish that this new band system arises from the long-missing $A^3\Pi$ state of N_2^+.

TABLE 1

$A^3\Pi - X^2\Sigma$ BANDS OF N_2^+ IN THE AURORA

Wave Length (A_{air}) (Violet Head)	Residuals O−C (Mean)	Intensity	v', v''	Wave Length (A_{air}) (Violet Head)	Residuals O−C (Mean)	Intensity	v', v''
6858	−1	4	2, 0	7828	0	40	1, 0
7050	−3	7	3, 1	8057	+2	20	2, 1
7250	−2	4	4, 2	8298	+3	6	3, 2

A. B. MEINEL

YERKES OBSERVATORY
October, 1950